

DELFT UNIVERSITY OF TECHNOLOGY

MASTER THESIS

Wave radiation from offshore pile driving for non-symmetric force fields.

Author : Amal El-Ghalbzouri (4476263)

Thesis committee : Dr. ir. A. Tsouvalas (chair), Offshore Engineering
Ir. T. Molenkamp, Offshore Engineering
Msc. Y. Peng, Dynamics of Solids and Structures

October 19, 2022



Summary

Monopiles are by far the most chosen foundation option for most off-shore activities. The installation of the foundation is commonly done by impact pile driving. The biggest issue of the traditional pile driving method is the sound emission, which reaches levels that are harmful to the immediate environment. Partly because of this, an alternative pile driving method is being developed, namely the Gentle Driving of Piles [1], where the hydraulic hammer is replaced by a GDP-shaker, which drives the pile toe into the ground by means of a torsional force. This is an additional incentive for developing a predictive model for the underwater noise radiation due to a non-symmetric force field. The model proposed in this thesis is similar to the existing symmetric semi-analytical model SILENCE [2], where the model, as shown in [fig. 0.1](#), consists of two submodules, namely a pile module and a module that describes the acousto-elastic medium. In both submodules the displacement field of the subsystem is described using its modal field. The procedure for both systems are derived and explained in further detail in [chapter 3](#).

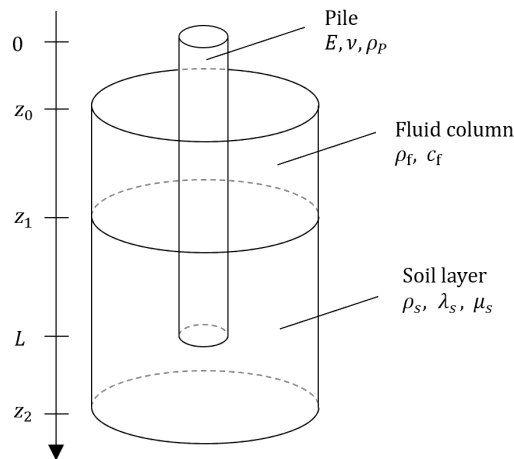


Figure 0.1: Model overview

To combine the submodules two different mode-matching methods, that account for the azimuthal direction, are developed in [chapter 4](#). One of these methods is the so-called Orthogonality method, which is, similar to [3], based on the orthogonality relations of the acousto-elastic medium. The other is referred to as the Point-Collocation method, which is loosely based on the reciprocity theorem. Both methods have proven to be sufficiently stable to achieve good convergence at least for lower frequencies.

The model is tested a small sized pile case study. The results are assessed in [chapter 5](#) through the frequency spectra of the acousto-elastic medium as well as the metrics. The time evolution of the response is also looked at, even though these are considered less reliable, due to the limited frequency range.

Acknowledgements

In front of you lies the final product of the Master Thesis in completion of my degree in Structural Engineering at the Technical University of Delft.

This report is the result of the research I conducted on noise emission prediction for off-shore pile driving, during which a semi-analytical model has been developed to assess underwater noise production due to piles driven by non-symmetrical impact forces.

I'd like to give thanks to all members of my committee, Dr. ir. A. Tsouvalas, Ir. T. Molenkamp and Msc. Y. Peng. In particular I would like to thank my daily supervisor T. molenkamp, for his feedback on my work as well as his guidance during the graduation process.

It is impossible to extend enough gratitude to my family and friends, who gave me the encouragement I needed throughout this process. Thank you all for your unwavering support during this time.

Now that this chapter has come to an end, I'm looking forward to what is coming next on my path.

Amal El-Ghalbzouri
Delft, October 2022

Contents

List of Figures	ix
List of Tables	xi
1 Introduction	1
1.1 Problem Statement, Relevance and Impact	1
1.2 Research goal and methodology	1
1.3 Thesis Outline	2
2 Background Literature	3
2.1 Underwater Acoustics	3
2.1.1 Underwater noise prediction models	3
2.1.2 Noise metrics	4
2.2 Shell dynamics	4
2.2.1 Cylindrical shell	4
2.2.2 The GDP-shaker	6
2.3 Soil and fluid dynamics	6
2.3.1 Complex rootfinder	6
3 Model description	7
3.1 The Pile: A circular cylindrical shell	8
3.1.1 Modal decomposition	8
3.1.2 Boundary value problem	8
3.1.3 Displacement and stress field	10
3.1.4 Forcing	12
3.1.5 In-vacuo response	13
3.2 The fluid & soil domain: An acousto-elastic medium	15
3.2.1 Modal Decomposition	15
3.2.2 Boundary Value Problem	18
3.2.3 Displacement and stress field	21
4 Mode-matching	25
4.1 Method description	25
4.2 The Orthogonality-method	30
4.3 The Point Collocation-method	32
4.4 Numerical considerations	36
4.4.1 Stability of the system	36
4.4.2 Matching error	37
4.4.3 Truncation	37
5 A case study	43
5.1 Basic forcing configurations	46
5.1.1 A vertical force	46
5.1.2 A horizontal force	49

5.1.3	A moment on the y -axis	54
5.2	Imperfect vertical force	57
6	Discussion	61
6.1	The method	61
6.2	The case study	65
7	Conclusions & Recommendations	69
7.1	The method	69
7.2	The case study	69
7.3	Recommendations	70
	Bibliography	71
A	The Pile	III
A.1	Constitutive & kinematic relations	III
A.2	Coefficient matrix & Characteristic relation	V
A.3	Displacement & stress field	VI
B	Fluid & soil domain	VII
B.1	Constitutive & kinematic relations	VII
B.2	Solution to the Helmholtz equation	IX
B.3	Coefficient matrix & Dispersion relation	X
B.4	Displacement & stress field	XI
B.4.1	For the non-symmetric case ($n > 0$)	XI
B.4.2	For the axi-symmetric case ($n = 0$)	XV
C	Modematching	XIX
C.1	Overview matching equations	XIX
C.1.1	Generic equations	XX
C.1.2	Orthogonality method	XXII
C.1.3	Point-Collocation method	XXIII
C.2	The extended orthogonality method for the non-symmetric case ($n > 0$)	XXVI
D	Casestudy	XXXVII
D.1	Error analysis	XXXVII
D.2	Time evolution	XXXVIII
D.2.1	A vertical force	XL
D.2.2	A horizontal force	XLI
D.2.3	A moment on the y -axis	XLII
D.2.4	Imperfect vertical force	XLIII

List of Figures

Figure 0.1	Model overview	iii
2 Background Literature		
Figure 2.1	Internal forces and coordinate system of an arbitrary shell	5
3 Model description		
Figure 3.1	Model overview	7
Figure 3.2	Eigenvalue analysis of the pile up to 500 Hz for $n = 0$ and $n = 1$	9
Figure 3.3	Displacements for the first three pile-modes	11
Figure 3.4	Basic force configurations	12
Figure 3.5	Normalized response to different basic force configurations	13
Figure 3.6	Geometry of the soil-fluid media (F1S1 configuration)	18
Figure 3.7	P-SV and SH wavenumbers in the complex plane	20
Figure 3.8	Orthogonality conditions for $f = 10$ Hz for the undamped values from table 3.3	21
Figure 3.9	Displacement and stress field for the first three modes for $f = 10$ Hz for the undamped values from table 3.3	23
4 Mode-matching		
Figure 4.1	The absolute mismatch and filtered relative error at $f = 200$ Hz	38
Figure 4.2	Convergence of the response due to a uniform vertical force	38
Figure 4.3	Local error of the response due to a uniform horizontal force (incl. ideal number of modes $N_{\{PSV,SH\}}$)	39
Figure 4.4	Local error of the response due to a uniform horizontal force (incl. ideal number of modes N_{PSV})	40
Figure 4.5	The local error per frequency due to a uniform horizontal force	40
Figure 4.6	The local error per continuity condition	41
Figure 4.7	Absolute mismatch in the radial direction at $f = 420$ Hz	42
5 A case study		
Figure 5.1	Forcing components of an imperfect load	43
Figure 5.2	Forcing spectrum	44
Figure 5.3	Local mismatch error δ_{Total} in the response to a vertical force per frequency	46
Figure 5.4	Amplitude spectrum $\tilde{p}_f(\omega)$ due to a vertical force	46
Figure 5.5	Amplitude spectra $\tilde{u}_{\{f,s\},\{r,z\}}(\omega)$ due to a perfect vertical force	47
Figure 5.6	Time signal $p_f(t)$ due to a perfect vertical force	47
Figure 5.7	Unfiltered time signal $u_{\{f,s\},\{r,z\}}(t)$ due to a perfect vertical force	47
Figure 5.8	Filtered time signal $u_{\{f,s\},\{r,z\}}(t)$ due to a perfect vertical force	48
Figure 5.9	Noise metrics due to a perfect vertical force	48
Figure 5.10	Contour plots $p_f(t)$ and $ u_s(t) $ due to a perfect vertical force	49
Figure 5.11	Polar plot $p_f(t)$ due to a perfect vertical force	50
Figure 5.12	Local mismatch error δ_{Total} in the response to a horizontal force per frequency.	50
Figure 5.13	Amplitude spectrum $\tilde{p}_f(\omega)$ due to a horizontal force	50
Figure 5.14	Unfiltered amplitude spectra $\tilde{u}_{\{f,s\},\{r,z\}}(\omega)$ due to a horizontal force	51
Figure 5.15	Filtered amplitude spectra $\tilde{u}_{\{f,s\},\{r,z\}}(\omega)$ due to a horizontal force	51
Figure 5.16	Time signal $p_f(t)$ due to a horizontal force	52

Figure 5.17	Velocities $v_{s,\{\theta,z\}}(t)$ due to a horizontal force	52
Figure 5.18	Noise metrics due to a horizontal force	53
Figure 5.19	Contour plots $p_f(t)$ and $ u_s(t) $ due to a horizontal force	53
Figure 5.20	Top view $ u_s(t) $ due to a horizontal force	54
Figure 5.21	Local mismatch error δ_{Total} in the response to a moment on the y -axis per frequency	55
Figure 5.22	Amplitude spectrum $\tilde{p}_f(\omega)$ due to a moment on the y -axis	55
Figure 5.23	Unfiltered amplitude spectra $\tilde{u}_{\{f,s\},\{r,\theta,z\}}(\omega)$ due to a moment on the y -axis	55
Figure 5.24	Unfiltered amplitude spectra $\tilde{u}_{\{f,s\},\{r,z\}}(\omega)$ due to a moment on the y -axis	56
Figure 5.25	Time signal $p_f(t)$ due to a moment on the y -axis	56
Figure 5.26	Noise metrics due to a moment on the y -axis	56
Figure 5.27	Contour plots $p_f(t)$ and $ u_s(t) $ due to a moment on the y -axis	57
Figure 5.28	The amplitude spectra of the fluid pressure due to an eccentric (a) vertical and (b) tilted force at a depth of 13.5 m.	58
Figure 5.29	Unfiltered amplitude spectra $\tilde{u}_{\{f,s\},\{r,\theta,z\}}(\omega)$ due to an imperfect force ($\varphi = 0^\circ, e = 3$ cm)	58
Figure 5.30	Unfiltered amplitude spectra $\tilde{u}_{\{f,s\},\{r,\theta,z\}}(\omega)$ due to an imperfect force ($\varphi = 3^\circ, e = 3$ cm)	59
Figure 5.31	Time signal $p_f(t)$ due to an imperfect force ($\varphi = 3^\circ, e = 3$ cm)	59
Figure 5.32	Noise metrics due to an imperfect force ($\varphi = 3^\circ, e = 3$ cm)	60
Figure 6.1	The convergence of the response to an uniform vertical force shown by plotting δ_{total} against $N_{\{\text{PSV},\text{SH}\}}$	63
Figure 6.2	Absolute mismatch in the radial direction at $f = 420$ Hz	63
Figure 6.3	(b)-(c) The ideal number of modes $N_{\{\text{PSV},\text{SH}\}}$ for the response to a uniform force and (a) the corresponding error	64
Figure 6.4	(b) The ideal number of modes N_{PSV} for the response to a uniform vertical force and (a) the corresponding error	64
6 Discussion		
Figure 6.5	Amplitude spectra $\tilde{p}_f(\omega)$	65
Figure 6.6	Eigenvalue analysis of the pile up to 500 Hz for $n = 0$ and $n = 1$	66
Figure 6.7	Amplitude spectra $\tilde{u}_{\{s\},\{r,z\}}(\omega)$ due to (a,b) a vertical and (c,d) a horizontal force	66
Figure 6.8	Contour plots $ p_f(t) $ and $ u_s(t) $ due to a horizontal force	67
B Fluid & soil domain		
Figure B.1	First three displacement modes for $n > 0$ and $f = 10$ Hz	XVI
Figure B.2	First three displacement modes for $n = 0$ and $f = 10$ Hz	XVI
Figure B.3	First three vertical stress modes for $n > 0$ and $f = 10$ Hz	XVII
Figure B.4	First three vertical stress modes for $n = 0$ and $f = 10$ Hz	XVII
Figure B.5	First three radial stress modes for $n > 0$ and $f = 10$ Hz	XVIII
Figure B.6	First three radial stress modes for $n = 0$ and $f = 10$ Hz	XVIII
C Modematching		
Figure C.1	Model overview	XIX
D Casestudy		
Figure D.1	Local mismatch error δ_{Total} in the response to a vertical force	XXXVII
Figure D.2	Local mismatch error δ_{Total} in the response to a horizontal force	XXXVIII
Figure D.3	Local mismatch error δ_{Total} in the response to a moment on the y -axis	XXXVIII
Figure D.4	Local mismatch error δ_{Total} in the response to a higher order torsional moment per frequency.	XXXVIII
Figure D.5	Contour plots $ p_f(t) $ and $ u_s(t) $ due to a perfect vertical force	XL
Figure D.6	Polar plot $p_f(t)$ due to a perfect vertical force	XL
Figure D.7	Contour plots $ p_f(t) $ and $ u_s(t) $ due to a horizontal force	XLI
Figure D.8	Polar plot $p_f(t)$ due to a uniform horizontal force	XLI
Figure D.9	Contour plots $ p_f(t) $ and $ u_s(t) $ due to a moment on the y -axis	XLII
Figure D.10	Polar plot $p_f(t)$ due to a moment on the y -axis	XLII
Figure D.11	Contour plots $ p_f(t) $ and $ u_s(t) $ due to an imperfect vertical force	XLIII
Figure D.12	Polar plot $p_f(t)$ due to an imperfect vertical force ($\varphi = 3^\circ, e = 3$ cm)	XLIII

List of Tables

3 Model description

Table 3.1	Frequency parameters for a C-C pile with the properties from pile A in table 3.2	9
Table 3.2	Pile properties	10
Table 3.3	Properties of the acousto-elastic medium per layer	19

4 Mode-matching

Table 4.1	Properties of the system	37
-----------	------------------------------------	----

5 A case study

Table 5.1	Properties of the system	44
Table 5.2	Pre-set properties of the basic forcing configurations, displayed in fig. 5.1	44
Table 5.3	The amplitudes of the force spectrum of a unit force and the forces per component of an imperfect impact load. Note $\hat{f}_{\{z,\theta,r\},\max} = \max(\hat{f}_{\{z,\theta,r\}}(t))$	45

D Casestudy

Table D.1	Properties of the system	XXXVII
-----------	------------------------------------	--------

Chapter 1

Introduction

1.1 Problem Statement, Relevance and Impact

For many applications steel monopiles are being used, both on- and offshore. The traditional way of installing these piles is by impulse hammering, where the pile is driven into the soil with multiple blows of the hammer. The disadvantage of this method is the loud noises it causes, which is detrimental to the environment and its inhabitants. To counteract this drawback a fair amount of applications have been developed to absorb and reduce the produced noise. However, these methods can become expensive and complicated to implement, especially on an offshore platform where resources are limited.

This is where Gentle Driving of Piles (GDP) comes in as a project to look for an alternative pile driving method where the pile is not driven solely by an impact force but also by wielding (torsional) vibrations to the pile head [1]. By activating these two different modes of motion, non-symmetrical displacements will take place, which brings with the coupling of the vertical and horizontal shear waves that exist in the soil medium. In contrast to the original method, where the horizontal shear waves do not influence the response.

Apart from the non-symmetrical forcing fields, the higher order response might also be interesting to delve deeper in the response to a vertical impact force. By comparing the pile modes to its response to a vertical impact force, one can derive that higher order circumferential pile modes are excited, this could be the result of an off-set of the impact force or an initial inclination of the pile. Thus these higher order modes must have an influence on the noise field generated [4]. A mathematical solution was proposed that takes this effect into consideration [3, 4], which is the stepping stone towards implementing higher order circumferential modes of the monopile, where the azimuthal dependence of the system is implemented. The latter seems to be even more present in the acoustic field caused by slightly inclined monopiles [5].

1.2 Research goal and methodology

As outlined in the previous section, there is a need for assessment of the non-symmetric response of the acousto-elastic field, independent of the pile driving technique used.

The aim of the thesis at hand is to create such an initial vibro-acoustic model that considers the non-symmetric response of the system in the near-field. Which is a stepping stone to mapping the noise emission of the novel pile driving technique.

The developed model is based on the modal fields of the pile, soil and fluid. The derivations of these fields are essentially embroidered on the work to develop SILENCE BASIC, a software to for modeling underwater noise from offshore pile-driving, where the same modal approach is used to obtain the symmetric response [2].

In this work a linear semi-analytical formulation of the response of the acousto-elastic medium is developed, in which non-symmetric force fields are accounted for. The motions of the acousto-elastic medium as well as the response of the pile are described using a modal approach. The pile-water-soil interaction is then modelled by matching the modes of the different subsystems, with a proposed mode-matching method, where the azimuthal direction is taken into account. Two stable mode-matching methods are developed, namely the point-collocation-method and the orthogonality-method. The latter is a continuation of the stub in Tsouvalas' dissertation [4], which is used as a starting point, while the point-collocation-method is a more systematic method, that has not yet been used in the acoustic field.

Scope

Unlike the SILENCE software, which consists of both near- and far-field modules, the scope of this thesis will be limited to the near-field response of the system. Essentially focusing on the first module of SILENCE, which should be able to be coupled to the far-field propagation through implementation of the boundary integral method [6].

Furthermore, the model is currently developed for the most simple configuration, one fluid-layer and one soil-layer. The latter is described as a three-dimensional elastic continuum while the fluid is assumed to be in-viscid compressible. In this configuration homogeneous fluid and soil properties are assumed. The model is implemented in such a way that there is room left for more extensive configurations for future development.

Limitations due to existing modules

For an initial model it would suffice to assume an undamped acousto-elastic medium, however, since for the derivation of its displacement field the root-finder-module of SILENCE is involved, where damping is readily implemented for frequencies higher than ± 300 Hz, this would lead to a small frequency range from which the time response can be obtained. Because of this limitation damping will be considered in the casestudies to maximize the frequency-range, and thus the length of the time signals.

Furthermore, the same root-finder has a limit for the number of pure imaginary roots that are obtained. This puts a constraint on the number of acousto-elastic modes that can be taken into account. For more elaboration on the root-finder the reader is referred to [section 2.3.1](#).

Time and frequency domain

All of the derivations in this work are done in the frequency domain. All signals will thus be transformed from the time domain to the frequency domain using the Fourier transform pair in [eqs. \(1.2.1a\) and \(1.2.1b\)](#). In sake of abbreviation and simplicity the marking of the transformed signals and their ω -dependence will be omitted throughout the body of the thesis. In [chapters 5 to 7](#), the transformed signals will be marked, as is traditionally done, to distinguish between the frequency spectra and the time-signals, since these are of importance in the assessment of the acoustic field and the associated noise emission. For the numerical implementation a backward discrete Fourier Transform is used using the Nyquist sampling theorem.

$$\tilde{g}(r, \theta, z, \omega) = \int_{-\infty}^{\infty} g(r, \theta, z, t) e^{-i\omega t} dt \quad (1.2.1a)$$

$$g(r, \theta, z, t) = \int_{-\infty}^{\infty} \tilde{g}(r, \theta, z, \omega) e^{i\omega t} d\omega \quad (1.2.1b)$$

1.3 Thesis Outline

First off the three-dimensional model is described in [chapter 3](#), where both the pile and soil-fluid media are modelled in [sections 3.1 and 3.2](#) respectively. For the basal theory fundamental to the models the reader is referred to [chapter 2](#).

The proposed methods for mode-matching are described in [chapter 4](#)¹. After this the model is used to conduct a casestudy, for which the obtained results are elaborated in [chapter 5](#). Finally both the method and results are discussed in [chapter 6](#) and conclusions, as well as recommendations for future research, are stated in [chapter 7](#).

¹ A final overview of the modematching equations is given in [appendix C.1](#)

Chapter 2

Background Literature

The aim of this research, as described in [section 1.2](#), essentially connects three different study fields. First and foremost the field of underwater acoustics and noise emission, of which the relevant material is briefly summarized in [section 2.1](#). Followed by a section on the dynamics of the shell [section 2.2](#) and a final section on the dynamics of the acousto-elastic field in [section 2.3](#).

2.1 Underwater Acoustics

A scala of methods and models have been developed with the sole purpose to predict the underwater noise emission caused by the off-shore driving of piles. The methods predecesing to the method developed in [\[3\]](#) and by extension to this thesis are briefly mentioned in [section 2.1.1](#). To form a base for the assessment of results, obtained with the model described in this thesis, the general quantities and metrics used in the underwater acoustics field are stated in [section 2.1.2](#)

For an overview and a more detailed summary of existing models, as well as noise mitigation systems, the reader is referred to [\[7\]](#).

2.1.1 Underwater noise prediction models

The acoustic response to various human activities in deep water has been researched thoroughly, partly due to military interests. However, this research does not easily translate to shallow water, where the small depth causes both the water-surface and the seabed to play a significant role in the propagation of sound. Between these two, the emphasis lays on the seabed, since characterising its composition contains the most uncertainty when developing a mathematical description of the sound source mechanism [\[7\]](#). The influence of the modelling of the seabed is further elaborated upon in chapter 6 of [\[4\]](#).

Currently, there are various ways to define and predict the underwater noise produced by off-shore pile driving. The most simple and straight-forward approach is to assign a sound level to the acoustic source. The acoustic field would then be determined with the domain characteristics by semi-empirical formulae. Logically, such procedures are referred to as so-called empirical models. Several of these models are mentioned in [\[7\]](#), with more light shed upon a fairly recent proposition by [\[8\]](#).

More extensive models often define the acoustic source by splitting it in two modules, namely the pile module and the soil and fluid module. The latter can be modelled in various ways: from a series of distributed springs and dashpots to a set of partial differential equations that confiscate the behaviour of the acousto-elastic medium.

In the literature review [\[7\]](#), a distinction is made between semi-analytical solutions on the one side, and numerical solutions on the other. The latter focuses on discretizing the field in the close range, while the former are focussed on analytically solving the differential equations. The numerical models are able to provide highly detailed results compared to the response obtained by semi-analytical models, which in turn have the advantage of being less time consuming.

2.1.2 Noise metrics

For the sake of uniformity, the underwater noise emission is assessed by standardized noise metrics as defined in [9]. Three of these metrics are used for the assessment of the results in chapter 5, namely the Sound Pressure Level (SPL, eq. (2.1.1)), Sound Exposure Level (SEL, eq. (2.1.2)), and the zero-to-peak pressure level (L_{peak} , eq. (2.1.3)). Note that the SPL differs from the other two metrics, as it uses the frequency spectrum $\tilde{p}_f(z, \theta, r, \omega)$ of the fluid pressure, while the SEL uses the time signal $p_f(z, \theta, r, t)$ and the L_{peak} completely reduces the signal to its peak.

$$\text{SPL} = 20 \cdot \log_{10} \left(\frac{1}{2} \sqrt{2} \frac{|\tilde{p}_f(r, \theta, z, \omega)|}{10^{-6}} \right) \quad \text{in} \quad \text{dB re } 1 \mu\text{Pa s} \quad (2.1.1)$$

$$\text{SEL} = 10 \log_{10} \left(\frac{1}{t_0} \int_{t_5}^{t_{95}} \frac{p_f^2(r, \theta, z, t)}{10^{-12}} dt \right) \quad \text{in} \quad \text{dB re } 1 \mu\text{Pa}^2 \text{ s} \quad (2.1.2)$$

$$L_{\text{peak}} = 20 \log_{10} \left(\frac{|p_{\text{peak}}(r, \theta, z)|}{10^{-6}} \right) \quad \text{in} \quad \text{dB re } 1 \mu\text{Pa} \quad (2.1.3)$$

$$\text{with} \quad p_{\text{peak}}(r, \theta, z) = \max(p_f(r, \theta, z, t))$$

2.2 Shell dynamics

When considering the dynamics of a wide variety of shell theories shell is available. The different theories are categorized into one of the following categories [10]:

1. Classical Shell Deformation Theory
2. First-order shear deformation Theory
3. Higher-order shear deformation theory

For the axi-symmetric case a lower-order or classical theory would suffice, since in the perfect scenario, the pile would not be loaded in a way that causes shear deformations. However when a non-symmetric force is considered, shear stresses will most certainly occur, thus a shear deformation theory would not be an unnecessary luxury.

In this thesis, a thin shell theory extended with shear deformation and rotary inertia for a perfect cylinder is used to represent the pile. Rotary inertia and shear deformation are of importance at high frequencies with short wavelength compared to the shell thickness. However, it should be mentioned that the added value of the rotary inertia and shear deformation is expected to be negligible for the proposed configuration ¹. A theory where the rotatory inertia is neglected would suffice since the pile thickness is rather small compared to the other dimensions of the pile. Thorough derivations of the theory are found in [11].

2.2.1 Cylindrical shell

The motion of an arbitrary deep shell are derived from its energy equilibrium, following Hamilton's principle. Since the model of choice includes shear deformation, the shear angles β_1, β_2 are additional degrees of freedom on top of the regular translational degrees of freedom u_1, u_2, u_3 . Therefore, five equations, eqs. (2.2.1a)

¹ The properties of the assessed configuration are given in table 3.2 on page 10

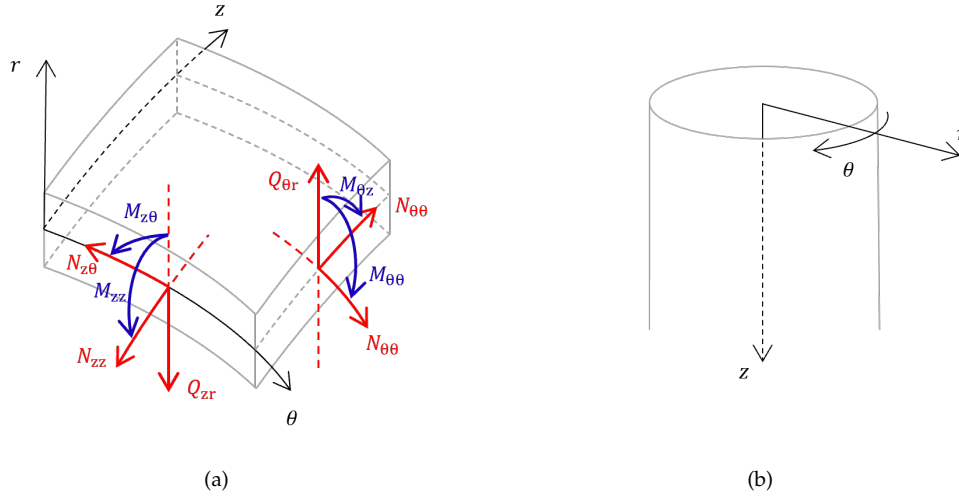


Figure 2.1: (a) The internal forces of an arbitrary shell. (b) The global coördinate system used to describe the pile in the proposed model.

to (2.2.1e), are needed to solve the motion of the dynamical system. The derivation of the shell equations is done in many previous literature and will thus be excluded from this work.

$$-\frac{\partial N_{11}A_2}{\partial \alpha_2} - \frac{\partial N_{21}A_1}{\partial \alpha_2} - N_{12} \frac{\partial A_1}{\partial \alpha_2} + N_{22} \frac{\partial A_2}{\partial \alpha_2} - A_1A_2 \frac{k'\varepsilon_{13}Gh}{R_1} + A_1A_2\rho h\ddot{u}_1 = A_1A_2q_1 \quad (2.2.1a)$$

$$-\frac{\partial N_{12}A_2}{\partial \alpha_1} - \frac{\partial N_{22}A_1}{\partial \alpha_2} - N_{21} \frac{\partial A_2}{\partial \alpha_1} + N_{11} \frac{\partial A_1}{\partial \alpha_2} - A_1A_2 \frac{k'\varepsilon_{23}Gh}{R_2} + A_1A_2\rho h\ddot{u}_2 = A_1A_2q_2 \quad (2.2.1b)$$

$$-k'Gh \frac{\partial \varepsilon_{13}A_2}{\partial \alpha_1} - k'Gh \frac{\partial \varepsilon_{23}A_1}{\partial \alpha_2} + A_1A_2 \left(\frac{N_{11}}{R_1} + \frac{N_{22}}{R_2} \right) + A_1A_2\rho h\ddot{u}_3 = A_1A_2q_3 \quad (2.2.1c)$$

$$\frac{\partial M_{11}A_2}{\partial \alpha_1} + \frac{\partial M_{21}A_1}{\partial \alpha_2} + M_{12} \frac{\partial A_1}{\partial \alpha_2} - M_{22} \frac{\partial A_2}{\partial \alpha_1} - A_1A_2Ghk'\varepsilon_{13} - A_1A_2 \frac{\rho h^3}{12} \ddot{\beta}_1 = 0 \quad (2.2.1d)$$

$$\frac{\partial M_{12}A_2}{\partial \alpha_1} + \frac{\partial M_{22}A_1}{\partial \alpha_2} + M_{21} \frac{\partial A_2}{\partial \alpha_1} - M_{11} \frac{\partial A_1}{\partial \alpha_2} - A_1A_2Ghk'\varepsilon_{23} - A_1A_2 \frac{\rho h^3}{12} \ddot{\beta}_2 = 0 \quad (2.2.1e)$$

In the case of a cylindrical shell, the coordinates are defined in the box below and shown in fig. 2.1b. With R being the radius of the cylinder.

$\alpha_1 \equiv z,$	$\alpha_2 \equiv \theta$
$\beta_1 \equiv \beta_z,$	$\beta_2 \equiv \beta_\theta$
$A_1 = 1,$	$A_2 = R$
$R_1 = \infty,$	$R_2 = R$

Substituting these into the arbitrary shell equations, eqs. (2.2.2a) to (2.2.2e), will give the equations that are specifically used for the work in this thesis. The internal forces and moments are depicted in fig. 2.1a.

$$-R \frac{\partial N_{zz}}{\partial z} - \frac{\partial N_{z\theta}}{\partial \theta} - \omega^2 R \rho h u_z = R q_z \quad (2.2.2a)$$

$$-R \frac{\partial N_{z\theta}}{\partial z} - \frac{\partial N_{\theta\theta}}{\partial \theta} - Q_{\theta r} - \omega^2 R \rho h u_\theta = R q_\theta \quad (2.2.2b)$$

$$-R \frac{\partial Q_{zr}}{\partial z} - \frac{\partial Q_{\theta r}}{\partial \theta} + N_{\theta\theta} - \omega^2 R \rho h u_r = R q_r \quad (2.2.2c)$$

$$R \frac{\partial M_{zz}}{\partial z} + \frac{\partial M_{z\theta}}{\partial \theta} - R Q_{zr} + \omega^2 R \rho \frac{h^3}{12} \beta_z = 0 \quad (2.2.2d)$$

$$R \frac{\partial M_{z\theta}}{\partial z} + \frac{\partial M_{\theta\theta}}{\partial \theta} - R Q_{\theta r} + \omega^2 R \rho \frac{h^3}{12} \beta_\theta = 0 \quad (2.2.2e)$$

2.2.2 The GDP-shaker

The shaker developed for the gentle pile driving technique works, as any vibratory device, with masses that rotate. In this case, two equal masses are used. When these rotate in opposite fashion a downward vibrating force is produced. Other forcing configurations are produced by asymmetrical rotation of the masses. In current noise pile driving models, however, the mechanism of the shaker is not modeled in detail, but a replacement with a force load on the top of the pile is chosen. As a result, certain uncertainties, related to the forces on the pile, are not included in current models. This is a gap to be assessed in future research [7].

2.3 Soil and fluid dynamics

One way to model the effect of the soil of the seabed onto the pile, is by capturing its elasticity and damping by distributed springs and dashpots respectively [12]. This offers a straightforward solution for modeling the resistance of the soil on the pile response. However, in practice the response of the system strongly depends on the chosen coefficients, on top of the fact that determining these coefficients with reliable accuracy proves to be a challenge [3].

A more intensive way to go about the description of soil behaviour is by use of the dynamics of an elastic continuum, eq. (2.3.1). The soil layer is then either cut-off to create a rigid boundary at the bottom of the layer, or modelled as a half-space [4]. For the application at hand it holds that a rigid boundary suffices when enough soil is left between the pile toe and the bottom of the soil layer.

$$\mu_s \nabla^2 \underline{\mathbf{u}}_s + (\lambda_s + \mu_s) \nabla \nabla \underline{\mathbf{u}} - \rho_s \omega^2 \underline{\mathbf{u}}_s = \mathbf{0} \quad (2.3.1)$$

The damping in a soil layer is expressed through the Lamè parameters, which become complex-valued. The damping itself can be defined in various ways, which are found in [13]. The definition used in this work is further elaborated upon in section 3.2.2.

The seawater is often modelled as an inviscid compressible fluid, the behaviour of which is captured with the wave equation, eq. (2.3.2), in terms of the velocity potential ϕ_f [3, 12].

$$\nabla^2 \phi_f(r, \theta, z, \omega) + \frac{\omega^2}{c_f^2} \phi_f(r, \theta, z, \omega) = 0 \quad (2.3.2)$$

Note that ∇^2 denotes the Laplacian operator in cylindrical coordinates: $\nabla^2 = \partial_r^2 + \frac{1}{r} \partial_r + \frac{1}{r^2} \partial_\theta^2 + \partial_z^2$

2.3.1 Complex rootfinder

The dynamics of the acousto-elastic medium, as any other dynamical system, is described by its modal field (i.e. eigenfunctions). Each mode corresponds to a wavenumber (i.e. eigenvalue), which is a root of the dispersion relation (i.e. characteristic equation) of the system.

In the case of the acousto-elastic medium, the dispersion relation has both real and complex roots. For this purpose, a complex rootfinder has been developed by Tsouvalas et al.. The algorithm itself is based on the Principle of the Argument. For a more detailed description of the rootfinder, the reader is referred to [14], where the method of the rootfinder is explained briefly.

Chapter 3

Model description

The model that is developed in this work essentially consists of two dynamical subsystems. The motion of each system is described by normal modes. The choice for a modal approach is necessary in order for the interface conditions between the pile and the acousto-elastic medium to be fulfilled using the modematching method, to be introduced in [Chapter 4](#).

The first subsystem is the monopile, which is modelled as a cylindrical thin shell. The motion of the pile is derived in [Section 3.1](#) using the equations introduced in [Section 2.2](#). The second subsystem is the acousto-elastic medium, of which the necessary equations were introduced in [Section 2.3](#), the problem is solved in [Section 3.2](#). The displacement and stress-fields for the pile and acousto-elastic system can be found in both systems are obtained using a modal expansion with the set of normal modes derived in the chapter at hand.

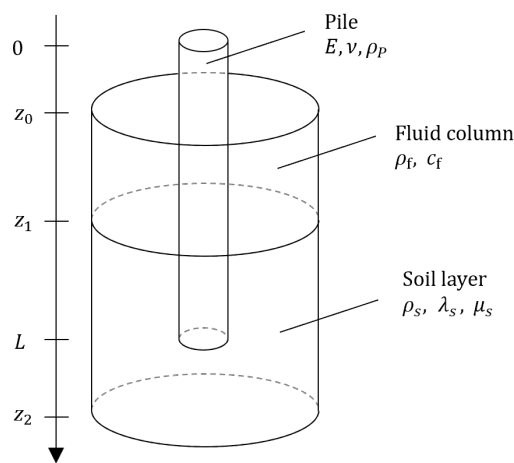


Figure 3.1: Model overview

3.1 The Pile: A circular cylindrical shell

In this section, the modal solution to for the pile equations are derived. The modal solution is hereafter verified with literature. The orthogonality relations are applied to find the modal forces. A variation of external loads at the top of the pile are described and the first axi-symmetric in-vacuo modes for the pile are shown.

3.1.1 Modal decomposition

The pile is modelled as a circular cylindrical shell with a higher order theory as described in [section 2.2](#). After substituting the internal forces into the equation of motion, [eq. \(3.1.1\)](#), a linear system of equations is formed, where the unknown vector \underline{u}_P consists of the degrees of freedom $u_{P,z}$, $u_{P,\theta}$, $u_{P,r}$, $\beta_{P,z}$, and $\beta_{P,\theta}$. The elements of the coefficient matrix $\underline{\underline{K}}$ and $\underline{\underline{M}}$ are found in [appendix A.2](#). Using these, the equation of motion is written in matrix notation:

$$\left(\omega^2 \underline{\underline{M}} + \underline{\underline{K}}\right) \underline{u}_P(z, \theta, \omega) = \underline{q}(z, \theta, \omega) \quad (3.1.1)$$

The modes of the pile are sought for in the form of [eq. \(3.1.2\)](#), where the elements of $\underline{\underline{C}}$ are the modal amplitudes and $\underline{\underline{R}}_n(\theta)$ is an extended version of the rotation matrix. Note that in [eq. \(3.1.2\)](#), the displacement is displayed per circular mode number n . It should go without saying that the final displacement is obtained by summation of the circular modes. That is $u_P(z, \theta, \omega) = \sum_n u_{P,n}(z, \theta, \omega)$.

$$\underline{u}_{P,n}(z, \theta, \omega) = \underline{\underline{R}}_n(\theta) \underline{\underline{A}}_n e^{kz} \quad \text{with} \quad \underline{\underline{R}}_n(\theta) = \text{diag} \left(\begin{array}{c} \cos(n\theta) \\ -\sin(n\theta) \\ \cos(n\theta) \\ \cos(n\theta) \\ -\sin(n\theta) \end{array} \right) \quad (3.1.2)$$

By substituting [eq. \(3.1.2\)](#) into [eq. \(3.1.1\)](#) and re-arranging, a linear set of equations with unknown $\underline{\underline{A}}$ is assembled. The characteristic equation of the homogeneous system will be a quintic equation ([\(3.1.3\)](#)) in terms of k^2 . This equation generally has ten roots $k(\omega_m)$ per eigenfrequency ω_m , which are found numerically by solving the eigenvalues of the companion matrix.

$$\text{Det} \left(\omega^2 \underline{\underline{M}} + \underline{\underline{K}} \right) = \sum_{i=1}^5 c_i \cdot k^{2i} = 0 \quad \longrightarrow \quad \begin{array}{l} \underline{u}_{P,n}(z, \theta, \omega) = C_P \cdot \underline{\underline{R}}_n(\theta) \cdot \hat{\underline{u}}_{P,n}(z) \\ \hat{\underline{u}}_{P,n}(z) = \sum_{i=1}^{10} \gamma_i \cdot e^{k_i z} \quad \text{with} \quad \underline{\underline{\gamma}} = \frac{1}{A_z} \cdot \underline{\underline{A}} \end{array} \quad (3.1.3)$$

The unknown constants in the system reduce to one unknown constant C_P for each root k . This is done by assuming a unit displacement in vertical direction $u_{P,z}$, which results into a known set of relative amplitudes γ_i per root $k_i(\omega_m)$. Note that the first element $\gamma_{P,z}$ is equal to one because of the assumed unit displacement.

3.1.2 Boundary value problem

In the case of offshore pile driving, it is often the case that the bottom of the pile is driven deep into the soil. The soil will then behave as a stiff spring at the bottom boundary of the pile [[10](#)]. In this work, a more simplified approach is taken, where the bottom of the pile is assumed to be clamped. This is equivalent to the springs being infinitely stiff, this leads to five homogeneous Dirichlet conditions, [eq. \(3.1.4b\)](#). The top of the pile is modelled as a free end, so the shaker can impose displacement on the top. The free end is modelled by prohibiting any initial internal forces at $z = 0$, [eq. \(3.1.4a\)](#). Another plausible configuration is allowing for displacements at the bottom of the pile, which is modelled the same as the free top.

$$\text{Free boundary:} \quad \hat{N}_{P,zz} = \hat{N}_{P,z\theta} + \frac{1}{R} \hat{M}_{P,z\theta} = \hat{Q}_{P,zr} + R \frac{\partial \hat{M}_{P,z\theta}}{\partial \theta} = \hat{M}_{P,zz} = \hat{M}_{P,z\theta} = 0 \quad (3.1.4a)$$

$$\text{Clamped boundary:} \quad \hat{u}_{P,z} = \hat{u}_{P,\theta} = \hat{u}_{P,r} = \hat{\beta}_{P,z} = \hat{\beta}_{P,\theta} = 0 \quad (3.1.4b)$$

Substituting the solution eq. (3.1.3) in the boundary conditions in eq. (3.1.4), results in a 10×10 -problem, with the unknowns being the relative amplitudes γ_i . To get the non-trivial solution the determinant must be zero, the characteristic equation is a polynomial in terms of ω^2 . The eigenfrequencies of the pile are the roots of this equation. Since eigenfrequencies per definition have real and positive values for undamped systems, the roots are numerically found by brute-force root finding over the real axis. Figure 3.2 shows the eigenvalue analysis for the 0th and 1st circular modes for frequencies up to 500 Hz.

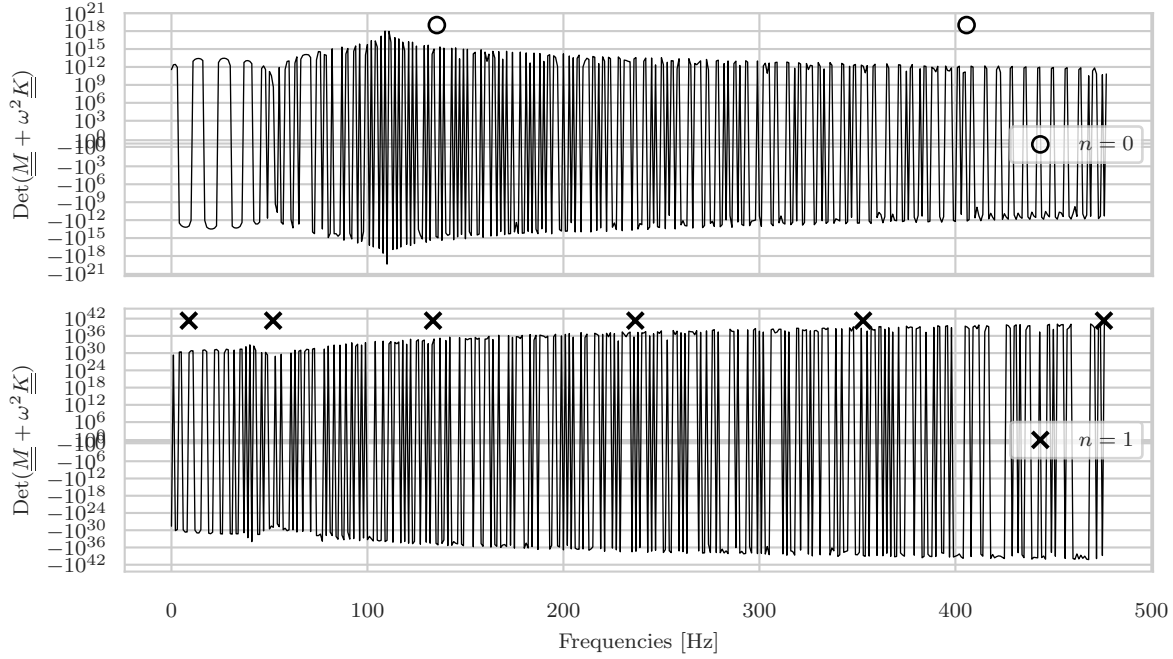


Figure 3.2: Eigenvalue analysis of the pile up to 500 Hz for $n = 0$ and $n = 1$

To validate the numerical model developed in this work, the obtained eigenfrequencies are compared through the dimensionless frequency parameter Ω_{nm} , eq. (3.1.5). In table 3.1 the frequency parameter is recorded from various literature for several modes of a C-C pile with properties A from table 3.2.

$$\Omega_{nm} = \omega_{nm} \cdot R \cdot \sqrt{\frac{\rho(1+\nu^2)}{E}} \quad (3.1.5)$$

Mode (n, m)	Present Ω_{nm} [-]	(Tsouvalas et al., 2014) [3] Ω_{nm} [-]	FEM (ANSYS) [3] Ω_{nm} [-]	(Zhou et al., 2012) [15] Ω_{nm} [-]
(1, 1)	0.032779	0.032791	0.032750	0.032781
(2, 1)	0.012145	0.013901	0.013891	0.013898
(3, 1)	0.012307	0.022664	0.022653	0.022666
(4, 1)	0.027229	0.042177	0.042088	0.041998
(2, 2)	0.030697	0.031472	0.031449	0.031464
(3, 2)	0.018641	0.026762	0.026743	0.026762
(3, 3)	0.03083	0.036468	0.036452	0.036465
(4, 2)	0.034984	0.043183	0.043071	0.043194

Table 3.1: Frequency parameters for a C-C pile with the properties from pile A in table 3.2

Table 3.1 shows that there is good agreement between the present model and literature, slight variation of the eigenfrequencies is expected since different shell theories are used.

By solving the eigenvalue problem, a series of unique and non-trivial solutions is found. The normal modes of the structure are per definition orthogonal to each other. The orthogonality condition is applied

File	Length L [m]	Radius R [m]	Thickness h [m]	Density ρ [kg m ⁻³]	Young's Modulus E [N m ⁻²]	Poisson's Ratio ν [-]
A	20	1	0.005	7850	$2.1 \cdot 10^{11}$	0.3
B	60	2.5	0.03	7850	$2.1 \cdot 10^{11}$	0.28

Table 3.2: Pile properties

by substituting an arbitrary mode into the equation of motion, pre-multiplying with a different mode and integrating over the domain. After some simple manipulations, the relation as shown in eq. (3.1.6) is obtained [16].

$$\iint_{E_P} (\underline{\mathbf{R}}_l(\theta) \hat{\mathbf{u}}_{P,k}(z))^T \underline{\mathbf{M}} (\underline{\mathbf{R}}_n(\theta) \hat{\mathbf{u}}_{P,m}(z)) dA = \pi \rho h R \Gamma_{nm}^P \delta_{nl} \delta_{mk} \quad (3.1.6)$$

$$\text{with: } E_P = \{(z, \theta) \mid 0 \leq z \leq L, 0 \leq \theta \leq 2\pi\}$$

The modes are normalized such that the factor Γ_m^P is equal to one for every mode m . This is done to ensure a more stable linear system in the modematching process. The modematching is further elaborated in chapter 4.

As mentioned before, the complete motion of the pile is described in terms of a modal summation over both the circular mode numbers n and the axial mode numbers m , as seen in eq. (3.1.7). The expanded expressions for the internal forces $N_{P,\{zz;\theta\theta\}}$, $Q_{P,\{zr;\theta r\}}$, and $M_{P,\{zz;\theta\theta;z\theta\}}$ are obtained by substituting eq. (3.1.7) into the expressions found in appendix A.1. The expanded expressions are stated in appendix A.3.

$$\tilde{\mathbf{u}}_P(z, \theta, \omega) = \sum_{n=0}^{\infty} \sum_{m=1}^{\infty} C_{P,nm} \underline{\mathbf{R}}_n(\theta) \hat{\mathbf{u}}_{P,nm}(z) \quad (3.1.7)$$

In fig. 3.3 the degrees of freedom are shown for the first three modes of a pile with the properties of pile B shown in table 3.2.

3.1.3 Displacement and stress field

Finally, the displacement field of the pile can be expressed through the superposition of the obtained modes:

$$\tilde{\mathbf{u}}_P(z, \theta, \omega) = \sum_{n=0}^{\infty} \sum_{m=1}^{\infty} C_{P,nm} \underline{\mathbf{R}}_n(\theta) \hat{\mathbf{u}}_{P,nm}(z) e^{i\omega t} \quad (3.1.8)$$

$$\text{with: } \hat{\mathbf{u}}_{P,m}(z) = [\hat{u}_{P,r,m}(z) \quad \hat{u}_{P,\theta,m}(z) \quad \hat{u}_{P,m,p}(z) \quad \hat{\beta}_{P,r,m}(z) \quad \hat{\beta}_{P,\theta,m}(z)]^T$$

$$\underline{\mathbf{R}}_n(\theta) = \text{diag} \left([\cos(n\theta) \quad -\sin(n\theta) \quad \cos(n\theta) \quad \cos(n\theta) \quad -\sin(n\theta)]^T \right)$$

The displacements for the first three modes are plotted in section 3.1.3 for both the symmetric and non-symmetric case. From this figure, it is also apparent that the azimuthal components of the modes are zero in the symmetric case.

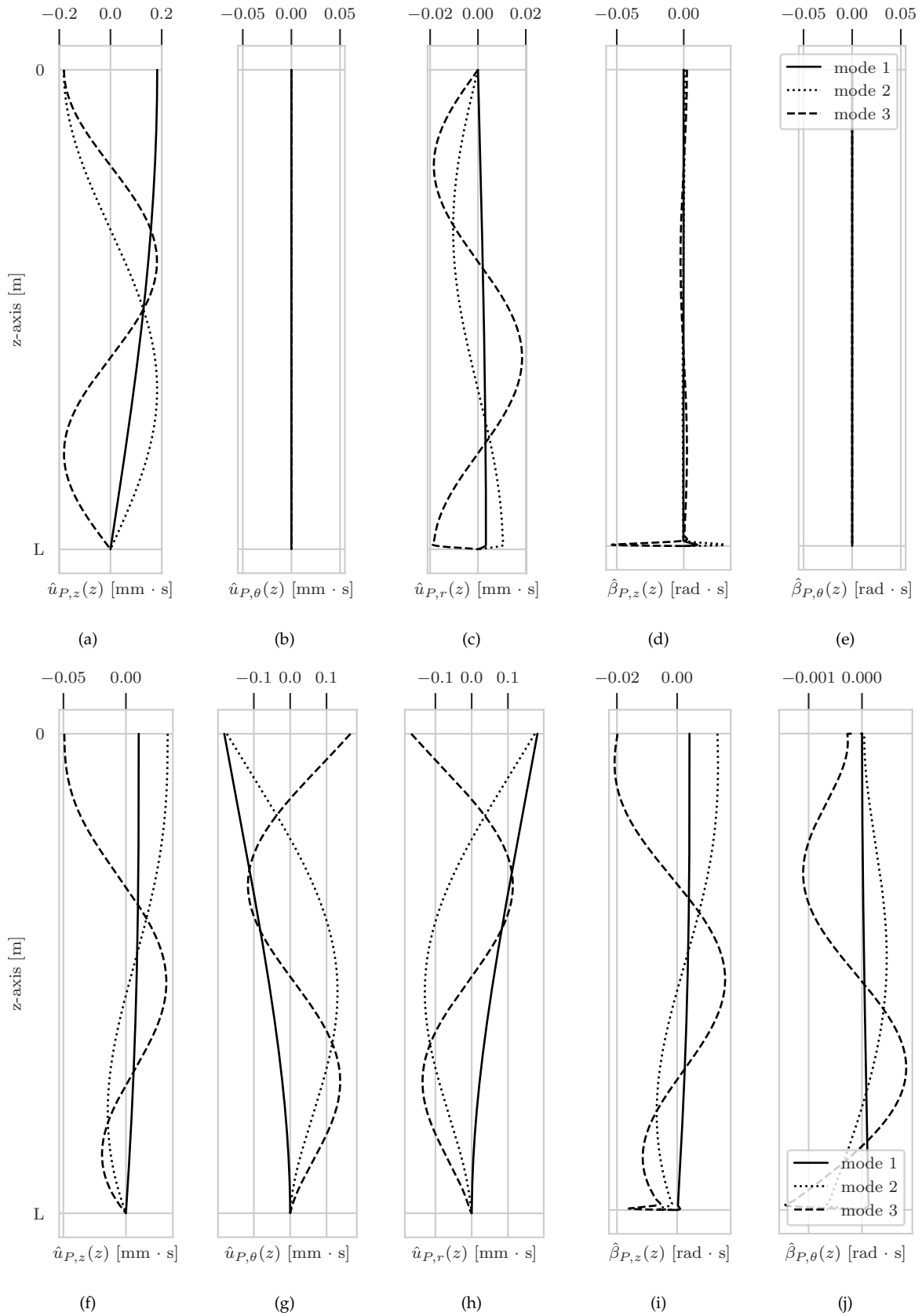


Figure 3.3: Displacements for the first three modes of pile B in table 3.2 with a F-C configuration. Figures (a)-(e) display the degrees of freedom for $n = 0$, while (f)-(j) show $n = 1$

3.1.4 Forcing

As mentioned in [chapter 2](#), a detailed model of the GDP-shaker is not yet used in current modelling approaches. The driving force is thus simplified to a distributed load along the circumference of the pile top, which is decomposed of three components $f_{e,z}(\theta, \omega)$, $f_{e,\theta}(\theta, \omega)$, and $f_{e,r}(\theta, \omega)$ in the vector notation $\underline{f}_e(z, \theta)$. This force is linearly decomposed in forces that are cylindrical symmetric and anti-symmetric, using a Fourier series, as shown in [eq. \(3.1.9\)](#).

The frequency response functions (FRF) are obtained for the four basic forcing configurations, which are depicted in [fig. 5.1](#). Note that a vertical point load ([fig. 3.4a](#)), used to model impact pile driving, is described by the 0th order component of the external force, [eq. \(3.1.10a\)](#), while a moment M_y around the y -axis ([fig. 3.4b](#)) is described by the 1st order component, [eq. \(3.1.10b\)](#). Furthermore, a horizontal point load ([fig. 3.4c](#)) is the 1st order component, as shown in [eq. \(3.1.10c\)](#). The 0th order horizontal load is uniform pressure and is not relevant for the application at hand. Similarly, the 1st order defines a uniform torsional moment, which is irrelevant, therefore, only a higher order torsional moment ([fig. 3.4d](#)) is considered, see [eq. \(3.1.10d\)](#).

$$\underline{f}_e(z, \theta) = \sum_{n=0}^{\infty} \underline{f}_{e,n}(z, \theta) = \sum_{n=0}^{\infty} \delta(z) \overbrace{\underline{\mathbf{R}}_n(\theta)}^{f_{e,n}(\theta)} \hat{\underline{f}}_e \quad \text{with} \quad \underline{\mathbf{R}}_n(\theta) = \text{diag} \left(\begin{bmatrix} \cos(n\theta) \\ -\sin(n\theta) \\ \cos(n\theta) \end{bmatrix} \right) \quad (3.1.9)$$

The magnitude F of an arbitrary point load is related to the distributed load as shown in [fig. 5.1](#). The magnitude can be solved using the incomplete elliptic integral of the 2nd kind. For the application at hand, however, only a few cases are of relevance, which can be simplified without using the aforementioned integral. The cases being both an uniform vertical F_z and horizontal F_x point load, and a normal M_y and torsional M_z moment.

Note that an uniform horizontal load requires the azimuthal and radial component of $\hat{\underline{f}}_e$ to be equal, as seen in [eq. \(3.1.10c\)](#). Furthermore, a non-zero angular phase φ is required to define the magnitude T of a torsional moment, [eq. \(3.1.10d\)](#).

Uniform vertical force: $n = 0, \hat{\underline{f}}_e = \hat{f}_{e,z} \underline{e}_z$	→	$F_z = 2\pi R \hat{f}_{e,z}$	(3.1.10a)
Moment on the y-axis: $n = 1, \hat{\underline{f}}_e = \hat{f}_{e,z} \underline{e}_z$	→	$M_y = 2\pi R^2 \hat{f}_{e,z}$	(3.1.10b)
Uniform horizontal force: $n = 1, \hat{\underline{f}}_e = \hat{f}_0 (\underline{e}_\theta + \underline{e}_r)$	→	$F_x = 2\pi R \hat{f}_0$	(3.1.10c)
2nd order torsional moment: $n = 2, \hat{\underline{f}}_e = \hat{f}_{e,\theta} \underline{e}_\theta$	→	$T = 2\pi R^2 \hat{f}_{e,\theta} \sin(\varphi)$	(3.1.10d)

Where $\underline{e}_{\{z;\theta;r\}}$ denote the unit vectors in the cylindrical coordinate-system.

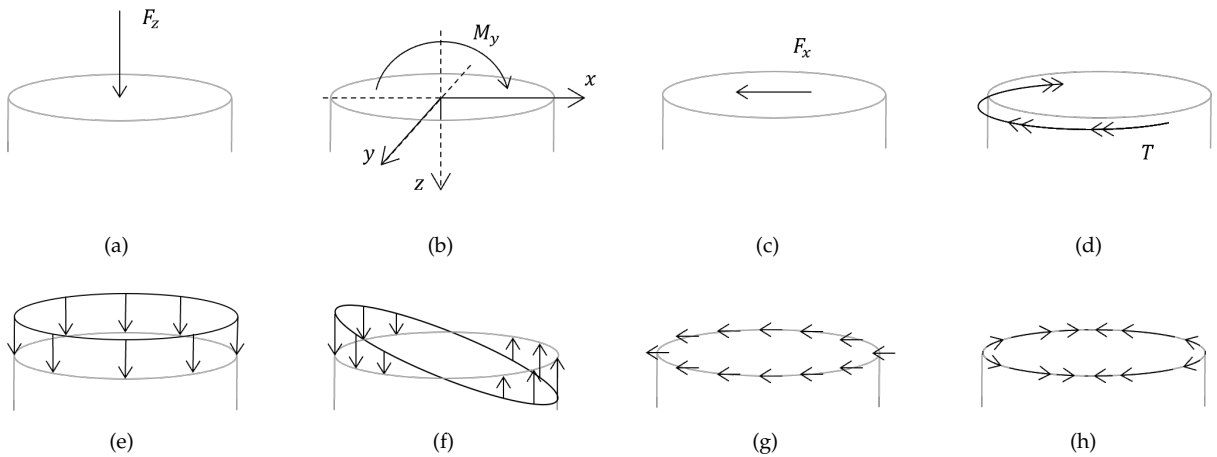


Figure 3.4: Basic force configurations

3.1.5 In-vacuo response

The in-vacuo response of the pile to an arbitrary external force f_e is obtained by substituting the solution form and the forcing into the equation of motion eq. (3.1.1) and multiplying by an arbitrary mode $u_{P,k}(z, \theta)$ and integrating over the domain E_P . An expression for the modal amplitude can then be obtained with the help of the orthogonality condition, eq. (3.1.6):

$$C_{P,nm} = \frac{1}{(\omega_{nm}^2 - \omega^2) \pi \rho h R \Gamma_{nm}^P} \iint_{E_P} u_{P,nm}^T f_{e,n} dA = \frac{(\hat{u}_{P,m}|_{z=0})^T \hat{f}_e}{(\omega_{nm}^2 - \omega^2) \rho h R \Gamma_{nm}^P} \quad (3.1.11)$$

$$\text{with: } E_P = \{(z, \theta) \mid 0 \leq z \leq L, 0 \leq \theta \leq 2\pi\}$$

Truncation

The infinite summation over the number of modes needs to be truncated at a certain point. The number of modes taken into account are based on their contribution, which is directly observed from the absolute value of the amplitude $C_{P,nm}$.

The modal amplitudes are normalized to the maximum amplitude per frequency, conform eq. (3.1.12), and are plotted in figs. 3.5a to 3.5d for the response to the 0th and 1st order vertical and horizontal force.

$$\tilde{C}_{P,nm} = \left| \frac{C_{P,nm}}{\max(C_{P,n1}; \dots; C_{P,n200})} \right| \quad (3.1.12)$$

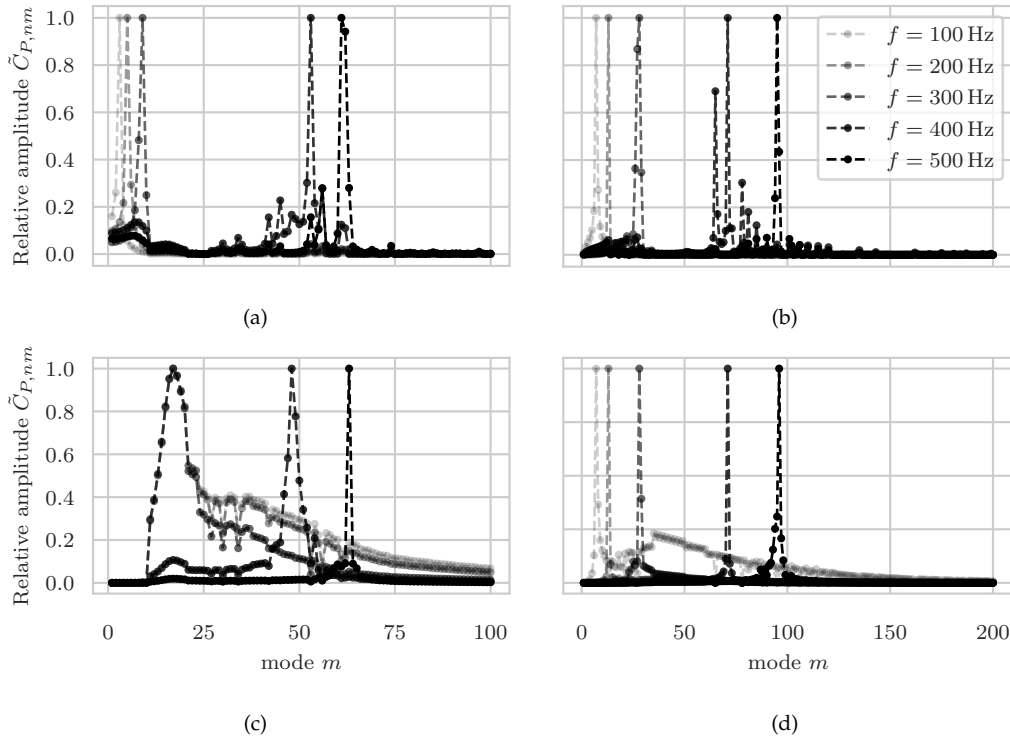


Figure 3.5: The normalized amplitudes of the response to (a) the 0th order vertical force (uniform vertical load) (b) the 1st order vertical force (moment on the y -axis) (c) the 0th order horizontal force (d) the 1st order horizontal force (uniform horizontal load)

For higher frequencies, the response tends to consist of modes with a higher mode-number m , as is seen for the darker lines in the plots. Therefore, the truncation of the modal summation is based on the contribution of the modes at the highest frequency within the scope of this work. In the present model, the number of

modes N_P taken into account for the pile is set to 80 and 100 for the symmetric and non-symmetric case respectively.

$$u_{P,n} = \sum_{m=1}^{\infty} u_{P,nm} \approx \sum_{m=1}^{N_P} u_{P,nm} \quad \text{with} \quad \begin{cases} N_P = 80 & \text{for } n = 0 \\ N_P = 100 & \text{for } n = 1 \end{cases} \quad (3.1.13)$$

3.2 The fluid & soil domain: An acousto-elastic medium

3.2.1 Modal Decomposition

The fluid-soil domain is modeled as an acousto-elastic medium, as mentioned in [chapter 2](#). The motion \underline{u}_s of an elastic continuum is described by the equation of motion shown in [eq. \(3.2.1\)](#), while the fluid domain is described by the wave-equation [eq. \(3.2.2\)](#) using the fluid potential ϕ_f .

$$\mu_s \nabla^2 \underline{u}_s + (\lambda_s + \mu_s) \nabla \nabla \underline{u} - \rho_s \omega^2 \underline{u}_s = \underline{0} \quad (3.2.1)$$

$$\nabla^2 \phi_f(r, \theta, z, \omega) + \frac{\omega^2}{c_f^2} \phi_f(r, \theta, z, \omega) = 0 \quad (3.2.2)$$

Decomposition in potentials

The equation of motion of the soil domain breaks up into three separate differential equations according to Lamé's theorem [17]. To achieve this the displacement vector is parsed conform Lamb's decomposition using three potentials, namely ϕ_s , ψ_s and χ_s as shown in [eq. \(3.2.3\)](#). Each of these potentials reflects a specific set of waves that describe the final response of the system. The type of waves are respectively the pressure (P), vertical (SV) and horizontal (SH) shear waves.

When considering the symmetric response of the system any derivatives with respect to θ are equal to zero, since, there is no azimuthal dependence. This results in the decoupling of the azimuthal displacement $u_{s,\theta}$ from the radial- and vertical displacement $u_{s,r}$ and $u_{s,z}$. The non-azimuthal displacements however, stay coupled through the P- and SV-components.

$$\underline{u} = \underbrace{\nabla \phi_s}_{\text{P-component}} + \underbrace{\nabla \times \nabla \times \begin{bmatrix} 0 \\ 0 \\ \psi_s \end{bmatrix}}_{\text{SV-component}} + \underbrace{\nabla \times \begin{bmatrix} 0 \\ 0 \\ \chi_s \end{bmatrix}}_{\text{SH-component}} \quad (3.2.3)$$

Substituting the decomposed expressions into the equation of motion will result in a wave equation for each potential. The motion of the acousto-elastic domain can, thus, be described with the four wave equations given in [eqs. \(3.2.4a\) to \(3.2.4d\)](#)

$$\nabla^2 \phi_s(r, \theta, z, \omega) + \frac{\omega^2}{c_L^2} \phi_s(r, \theta, z, \omega) = 0 \quad (3.2.4a)$$

$$\nabla^2 \psi_s(r, \theta, z, \omega) + \frac{\omega^2}{c_T^2} \psi_s(r, \theta, z, \omega) = 0 \quad (3.2.4b)$$

$$\nabla^2 \chi_s(r, \theta, z, \omega) + \frac{\omega^2}{c_T^2} \chi_s(r, \theta, z, \omega) = 0 \quad (3.2.4c)$$

$$\nabla^2 \phi_f(r, \theta, z, \omega) + \frac{\omega^2}{c_f^2} \phi_f(r, \theta, z, \omega) = 0 \quad (3.2.4d)$$

$$\text{with: } c_L^2 = \frac{\lambda_s + 2\mu_s}{\rho_s} \quad \text{and} \quad c_T^2 = \frac{\mu_s}{\rho_s}$$

With c_L and c_T being the speed of compressional and shear waves respectively, while c_f is the speed of sound in the fluid.

The above wave equations are known as the Helmholtz' equations, these can be solved in different ways. One of which is the method of separation of variables, which is further elaborated upon in [appendix B.2](#), resulting in the expressions [eqs. \(3.2.5a\) to \(3.2.5d\)](#).

$$\phi_s = \overbrace{\cos(n\theta)}^{\Theta(\theta)} \overbrace{H_n^{(2)}(k_{\phi_s} r)}^{R(r)} \overbrace{(A_1 e^{\alpha_s z} + B_1 e^{-\alpha_s z})}^{Z_i(z)} \quad (3.2.5a)$$

$$\psi_s = \cos(n\theta) H_n^{(2)}(k_{\psi_s} r) (A_2 e^{\beta_s z} + B_2 e^{-\beta_s z}) \quad (3.2.5b)$$

$$\chi_s = -\sin(n\theta) H_n^{(2)}(k_{\chi_s} r) (A_3 e^{\beta_s z} + B_3 e^{-\beta_s z}) \quad (3.2.5c)$$

$$\phi_f = \cos(n\theta) H_n^{(2)}(k_{\phi_f} r) (A_4 e^{\alpha_f z} + B_4 e^{-\alpha_f z}) \quad (3.2.5d)$$

$$\text{with: } \alpha_s^2 = k_{\phi_s}^2 - \left(\frac{\omega}{c_L}\right)^2, \quad \beta_{s,\psi}^2 = k_{\psi_s}^2 - \left(\frac{\omega}{c_T}\right)^2$$

$$\alpha_f^2 = k_{\phi_f}^2 - \left(\frac{\omega}{c_f}\right)^2, \quad \beta_{s,\chi}^2 = k_{\chi_s}^2 - \left(\frac{\omega}{c_T}\right)^2$$

Note that the wavenumbers $k_{\{\phi_s, \psi_s, \chi_s, \phi_f\}}$ have to be equal to ensure that the continuity conditions between the different layers ¹ are satisfied for all r . The subscripts for k are, therefore, omitted in the rest of this report.

It should be mentioned that in the solution-form as shown in [eq. \(3.2.5\)](#) a few choices have been made to comply with the application at hand.

The initial phase angle of the general solution is set to zero, this way displacements for any arbitrary initial phase are found by a matter of rotation.

Second the radial dependence is described by use of Bessel functions. The Bessel function of choice is the second Hankel function. Sommer's radiation condition is fulfilled by this choice as well.

Substituting the decided upon solution-form back into [eq. \(3.2.3\)](#), results in the displacement expressions for a single circular mode $\underline{u}_{s,n}$. The vertical $\underline{\sigma}_{s,z,n}$ and radial stresses $\underline{\sigma}_{s,r,n}$ of the modes can then be obtained with the use of the kinematic relations as found in [appendix B.1](#).

These circular modes are dependant on the circular mode number n , which couples the r - and θ -dependency of the mode. The vertical functions $Z_i(z)$, however, are independent of this circular mode number. For the displacement and vertical stress vector this results in a clear separation of variables, which can be seen best in the matrix-form as shown in the box below. The radial stresses are constructed differently, but all three cylindrical variables can still be separated, leaving the expressions coupled in r and θ through the circular mode number n and coupled in r and z through the vertical wave-numbers k .

Note that the solution of the symmetric case corresponds to substituting zero for n , which causes the expression [eq. \(3.2.5\)](#) of the χ_s -potential, which describes the SH-motion, to be decoupled and, therefore, not contribute to the acoustic field.

$$\underline{u}_s(r, \theta, z, \omega) = \sum_{n=1}^{\infty} C_n \underline{u}_{s,n}(r, \theta, z, \omega) \quad (3.2.6)$$

$$\tilde{\underline{u}}_{s,n}(z, \theta, r) = \underline{\mathbf{R}}_n(\theta) \underline{\mathbf{H}}_n(kr) \hat{\underline{u}}_s(z) \quad (3.2.7)$$

¹ These interface- and boundary conditions are introduced in [section 3.2.2](#)

Stress- & displacement modes

The displacement and stress field is expanded using the circular modal field of the acousto-elastic medium.

$$\underline{u}_{\{f,s\}}(r, \theta, z, \omega) = \sum_{n=1}^{\infty} C_n \underline{u}_{\{f,s\},n}(r, \theta, z, \omega) \quad (3.2.8a)$$

$$p_f(r, \theta, z, \omega) = \sum_{n=1}^{\infty} C_n p_{f,n}(r, \theta, z, \omega) \quad (3.2.8b)$$

$$\underline{\sigma}_{s,z}(r, \theta, z, \omega) = \sum_{n=1}^{\infty} C_n \underline{\sigma}_{s,z,n}(r, \theta, z, \omega) \quad (3.2.8c)$$

$$\underline{\sigma}_{s,r}(r, \theta, z, \omega) = \sum_{n=1}^{\infty} C_n \underline{\sigma}_{s,r,n}(r, \theta, z, \omega) \quad (3.2.8d)$$

$$\text{with: } \underline{u}_{\{f,s\}} = \begin{bmatrix} \tilde{u}_{\{f,s\},r} \\ \tilde{u}_{\{f,s\},\theta} \\ \tilde{u}_{\{f,s\},z} \end{bmatrix}, \quad \underline{\sigma}_{s,z} = \begin{bmatrix} \tilde{\sigma}_{s,zr} \\ \tilde{\sigma}_{s,z\theta} \\ \tilde{\sigma}_{s,zz} \end{bmatrix} \quad \text{and} \quad \underline{\sigma}_{s,r} = \begin{bmatrix} \tilde{\sigma}_{s,rr} \\ \tilde{\sigma}_{s,r\theta} \\ \tilde{\sigma}_{s,rz} \end{bmatrix}$$

When considering the soil layer, the expressions for a single displacement mode $\underline{u}_{s,n}$ and vertical stress mode $\underline{\sigma}_{s,z,n}$ are quite similarly constructed, as both can be expressed by using the same matrices, namely $\underline{R}_n(\theta)$ and $\underline{H}_n(kr)$, which are the rotational matrix and Hankel-matrix respectively [18].

$$\tilde{\underline{u}}_{s,n}(z, \theta, r) = \underline{R}_n(\theta) \underline{H}_n(kr) \hat{\underline{u}}_s(z) \quad (3.2.8e)$$

$$\tilde{\underline{\sigma}}_{s,z,n}(z, \theta, r) = \underline{R}_n(\theta) \underline{H}_n(kr) \hat{\underline{\sigma}}_{s,z}(z) \quad (3.2.8f)$$

With the matrices being:

$$\underline{R}_n(\theta) = \begin{bmatrix} \cos(n\theta) & 0 & 0 \\ 0 & -\sin(n\theta) & 0 \\ 0 & 0 & \cos(n\theta) \end{bmatrix} \quad (3.2.8g)$$

$$\underline{H}_n(kr) = \begin{bmatrix} \frac{1}{k} \partial_r H_n^{(2)}(kr) & \frac{n}{kr} H_n^{(2)}(kr) & 0 \\ \frac{n}{kr} H_n^{(2)}(kr) & \frac{1}{k} \partial_r H_n^{(2)}(kr) & 0 \\ 0 & 0 & -H_n^{(2)}(kr) \end{bmatrix} \quad (3.2.8h)$$

The expressions of the radial soil stresses $\underline{\sigma}_{s,r}(z, \theta, r, \omega)$ and the fluid displacement $\underline{u}_{f,n}$ are found in [appendices B.4.1](#) and [B.4.2](#) for the non-symmetrical ($n \neq 0$) and symmetrical ($n = 0$) case respectively. Expressions for the vertical functions $\hat{\underline{u}}_{\{s,f\},\{z;\theta;r\}}(z)$, $\hat{\underline{\sigma}}_{s,\{z;\theta;r\}}(z)$ and $\hat{p}_f(z)$ are included in the same sections.

3.2.2 Boundary Value Problem

In this thesis, the configuration is limited to just one fluid layer and one soil layer, as mentioned in the scope (section 1.2). However, adding more soil layers would simply expand the system with three potentials per layer to describe its motion. The additional interface conditions are the continuity of displacements ($\underline{u}_{s1} = \underline{u}_{s2}$) and equilibrium of vertical stresses ($\underline{\sigma}_{s1,z} = \underline{\sigma}_{s2,z}$) between two adjacent soil layers.

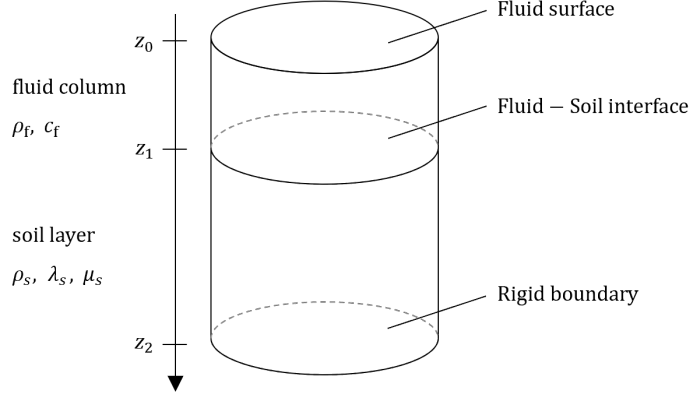


Figure 3.6: Geometry of the soil-fluid media (F1S1 configuration)

The fluid surface acts as a pressure release boundary, giving one of the two of the necessary equations for the wave-equation of the fluid potential.

$$\text{Fluid surface at } z = z_0 \quad \rightarrow \quad \hat{p}_{f,n}(z_0) = 0 \quad (3.2.9a)$$

Since, the soil- and fluid-layer are stacked vertically, both the continuity of displacement and equilibrium of stresses in the vertical direction should be satisfied. Note that the acoustic fluid has no shear stiffness, as a result all shear stresses in the soil will, thus, become zero at this interface.

$$\text{Fluid-Soil interface at } z = z_1 \quad \rightarrow \quad \hat{u}_{s,z,n}(z_1) - \hat{u}_{f,z,n}(z_1) = 0 \quad (3.2.9b)$$

$$\rightarrow \quad \hat{\sigma}_{s,zz,n}(z_1) + \hat{p}_{f,n}(z_1) = 0 \quad (3.2.9c)$$

$$\rightarrow \quad \hat{\sigma}_{s,z\theta,n}(z_1) = 0 \quad (3.2.9d)$$

$$\rightarrow \quad \hat{\sigma}_{s,zr,n}(z_1) = 0 \quad (3.2.9e)$$

Finally the soil is cut off by a rigid boundary condition, where no displacements are allowed. The assumption of a rigid boundary condition does have an effect on the generated waves in the far-field. However, in the scope of the thesis, only the near-field is considered, and here this effect is minimal, especially when a sufficient amount of soil is considered between the pile and the rigid boundary condition [3].

$$\text{Rigid boundary condition at } z = z_2 \quad \rightarrow \quad \hat{u}_{s,z,n}(z_2) = 0 \quad (3.2.9f)$$

$$\rightarrow \quad \hat{u}_{s,\theta,n}(z_2) = 0 \quad (3.2.9g)$$

$$\rightarrow \quad \hat{u}_{s,r,n}(z_2) = 0 \quad (3.2.9h)$$

The coefficient matrix is now obtained by substituting the expressions of relevant stresses and displacements, eqs. (3.2.8e) and (3.2.8f) into the boundary conditions eqs. (3.2.9a) to (3.2.9h). This results two decoupled eigenvalue problems corresponding to the SH and P-SV problems separately. The individual elements of the matrices in eqs. (3.2.10b) and (3.2.10c) are found in appendix B.3

Both eigenvalue problems are solved relative to one amplitude A_i or B_i . However, it must be mentioned that the P-SV problem contains both the amplitudes of the fluid and soil response, and that these can differ greatly in order size. The system is thus best solved by imposing an unit displacement of the seabed to obtain the relative amplitudes.

Solving the eigenvalue problems will result in Rayleigh modes (consisting of P- and S-waves) and Love

modes (consisting of SH-waves). In the rest of this thesis, these will be referred to as the P-SV and SH modes respectively.

$$\underline{\underline{D}} \underline{x} = \underline{0} \quad (3.2.10a)$$

$$\hookrightarrow \underline{\underline{D}}_{PSV} \underline{x}_{PSV} = \underline{0} \quad \text{with} \quad \underline{x}_{PSV} = [A_1 \ B_1 \ A_2 \ B_2 \ A_4 \ B_4]^T \quad (3.2.10b)$$

$$\hookrightarrow \underline{\underline{D}}_{sH} \underline{x}_{sH} = \underline{0} \quad \underline{x}_{sH} = [A_3 \ B_3]^T \quad (3.2.10c)$$

Dispersion relations

When assessing an undamped soil-layer, the eigenvalue problem of the SH modes consists of two unknowns and its dispersion relation [eq. \(3.2.11a\)](#) is analytically solvable considering both its size and the fact that only pure imaginary or pure real roots are found. The analytical derivation of the roots of this problem, the SH wavenumbers [eq. \(3.2.11a\)](#), are found in [appendix B.3](#).

The P-SV problem, however, gives a rather sizeable dispersion relation ([eq. \(3.2.11b\)](#)) for which both real and complex roots exist. The complex rootfinder described in [section 2.3.1](#) is used to find these P-SV wavenumbers.

The roots of both dispersion relations are shown in [fig. 3.7](#) for the values in [table 3.3](#).

$$\det(\underline{\underline{D}}_{sH}) = \sum_{j=0}^1 c_j (k)^{2j} = 0 \quad \xrightarrow{\text{appendix B.3}} \quad k_q^{\text{SH}} \quad \text{with: } p, q \in \mathbb{N} \quad (3.2.11a)$$

$$\det(\underline{\underline{D}}_{PSV}) = \sum_{j=0}^5 c_j (k)^{2j} = 0 \quad \xrightarrow{\text{Rootfinder}} \quad k_p^{\text{PSV}} \quad (3.2.11b)$$

Layer	Depth [m]	Density ρ [kg m ⁻³]	Compressional wavespeed c_L [m s ⁻¹]	Shear wavespeed c_T [m s ⁻¹]	Compressional damping α_c [%]	Shear damping α_s [%]
Soil (Undamped)	60	1700	1800	300	0	0
Soil (Damped)	60	1700	1800	300	1	1
Fluid	22	1000	1500	-	-	-

Table 3.3: Properties of the acousto-elastic medium per layer

Damping

A soil-layer, in which damping is considered, is characterized by having complex Lamè parameters instead of real Lamè parameters λ_s and μ_s . This results in complex-valued wavespeeds, which causes a transformation of the wavenumbers, which corresponds to a slight rotation of the numbers in the complex plane, as can be seen in [fig. 3.7](#).

The damping in a soil layer can be defined in different ways, which are found in [\[13\]](#). In this thesis, the damping will be defined terms of percentages of the Lamè parameters, conform [eq. \(3.2.12a\)](#).

$$\lambda_{s,\text{damped}} = \lambda_{s,\text{undamped}} \left(1 - \frac{\alpha_c}{100} \cdot i\right) \quad \text{with } \alpha_c \text{ in } [\%] \quad (3.2.12a)$$

$$\mu_{s,\text{damped}} = \mu_{s,\text{undamped}} \left(1 - \frac{\alpha_s}{100} \cdot i\right) \quad \text{with } \alpha_s \text{ in } [\%] \quad (3.2.12b)$$

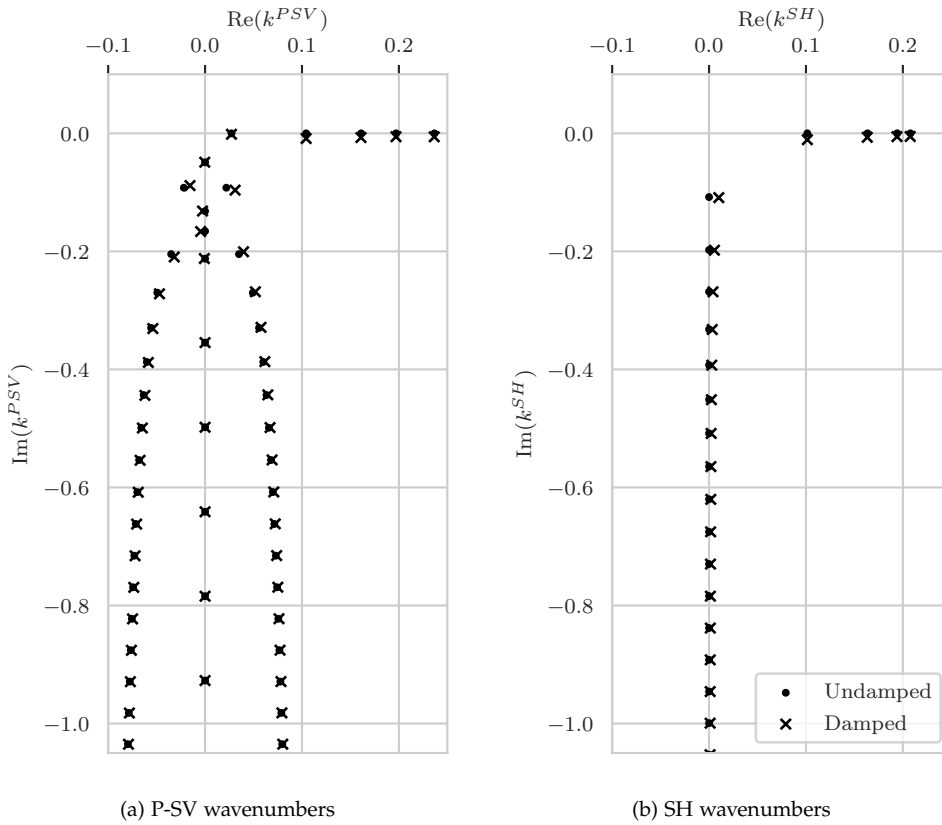


Figure 3.7: Wavenumbers for the damped and undamped case plotted in the complex plane for $f = 10$ Hz.

Propagating & evanescent modes

Each wavenumber represents a single mode. Note that for the undamped system, the complex P-SV wavenumbers come in conjugate pairs ($k = k^{\text{Re}} \pm k^{\text{Im}}$). Such wavenumbers correspond to what are called the evanescent modes, which decay rather fast, with increasing radial distance r , due to the relatively small real part k^{Re} [4]. These modes do not contribute significantly to the total energy of the response.

Contrastingly, the real wavenumbers correspond to so-called propagating modes, which are characterised by their slow decaying. Naturally, they also carry most of the energy of the response. Thus, these propagating modes are of high importance to convey the acoustic response. Since, the number of real wavenumbers is finite, it is possible to include the complete propagating spectrum into the modal superposition.

However, the evanescent spectrum consists of an infinite number of modes, the modal summation will, thus, be truncated within this spectrum. The truncation criteria is introduced in [chapter 4](#).

Orthogonality relations

The relation between two modes can be derived using the reciprocity theorem, [eq. \(3.2.13\)](#). Note that since the P-SV and SH problem are decoupled, and give two unique sets of modes, the reciprocity condition holds between the individual modes within a set, but also between an individual P-SV and SH mode [3, 17, 19].

For two P-SV modes, the reciprocity theorem leads to the orthogonality relation in [eq. \(3.2.14a\)](#). These are essentially the same and can be derived from one another.

For two SH modes a more straight forward relation [eq. \(3.2.15\)](#) is obtained from the same starting point.

$$\iint_S \mathbf{u}_{s,1}^T \underline{\sigma}_{s,z,2} - \mathbf{u}_{s,2}^T \underline{\sigma}_{s,z,1} dS \quad (3.2.13)$$

$$-\frac{1}{k_p} \int_{z_0}^{z_1} \frac{\hat{v}_{i,r,p}}{i\omega} \hat{p}_{i,l} dz + \frac{1}{k_p} \int_{z_1}^{z_2} \hat{\alpha}_{s,l}^I(z) \hat{u}_{s,r,p}(z) - \hat{u}_{s,z,l}(z) \hat{\sigma}_{s,zr,p}(z) dz = \Gamma_l^{\text{PSV}} \delta_{pl} \quad (3.2.14a)$$

with: $\hat{\alpha}_{s,l}^I(z) = \zeta_s k_l \hat{u}_{s,r,l}(z) + \eta_s \hat{\sigma}_{s,zz,l}(z)$

$$-\frac{1}{k_p} \int_{z_0}^{z_1} \frac{\hat{v}_{t,r,p}}{i\omega} \hat{p}_{t,l} dz + \frac{1}{k_p} \int_{z_1}^{z_2} \hat{\sigma}_{s,rr,l}^{PSV,1} \hat{u}_{s,r,p} - \hat{\sigma}_{s,zr,p} \hat{u}_{s,z,l} dz = \Gamma_l^{PSV} \delta_{pl} \quad (3.2.14b)$$

$$\int_{z_2}^L \mu k_j^2 \hat{u}_{s,\theta,j} \hat{u}_{s,\theta,q} dz = \Gamma_j^{SH} \delta_{qj} \quad (3.2.15)$$

These orthogonality relations are used in [chapter 4](#) to match the soil-fluid modes with the pile modes. For this procedure large systems of linear equations will be constructed. A way to improve the stability of such systems is to reduce the difference in order size between the different elements. This is done by normalizing both the P-SV modes as well as the SH modes such that Γ_l^{PSV} and Γ_j^{SH} are equal to one.

The above relations can also be used to check whether the set of modes at hand is indeed an orthogonal set. This is visualised in [fig. 3.8](#) using the properties from [table 3.3](#)

Finally, as mentioned before, the P-SV and SH modes are two distinctive solutions to the same problem, thus, these must comply with the reciprocity theorem. Bostock derived such a relation ([eq. \(3.2.16\)](#)) in [19]. However, this relation was not applied within this work.

$$\int_{z_1}^{z_2} \left[\hat{\alpha}_{s,i}^{II}(z) \hat{u}_{s,\theta,q}(z) - \mu \hat{u}_{s,r,i}(z) k_q \hat{u}_{s,\theta,q}(z) + \mu k_i \hat{u}_{s,z,i}(z) \frac{d\hat{u}_{s,\theta,q}}{dz} \right] dz \quad (3.2.16)$$

with: $\hat{\alpha}_{s,i}^{II} = (\lambda_s + 2\mu_s) \hat{u}_{s,r,i}(z) k_i^2 - k_i \lambda_s \frac{d\hat{u}_{s,z,i}}{dz}$

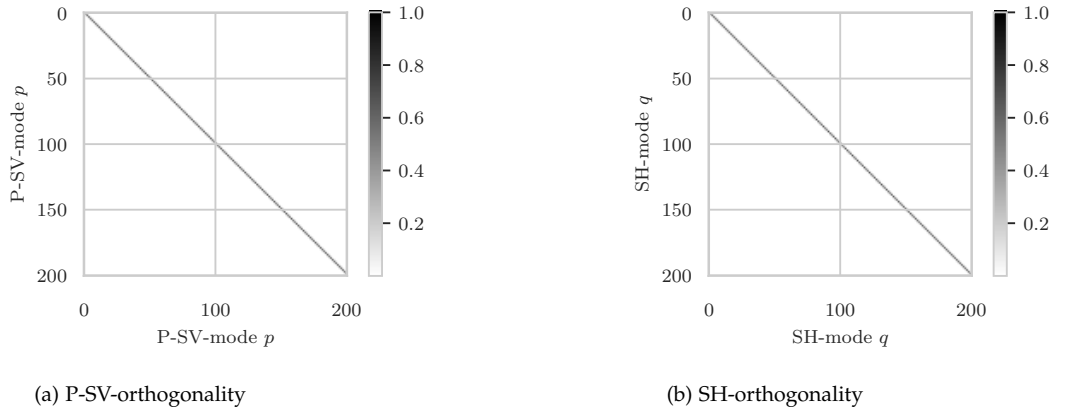


Figure 3.8: Orthogonality conditions for $f = 10\text{Hz}$ for the undamped values from [table 3.3](#)

3.2.3 Displacement and stress field

Once the eigenmodes are obtained the displacement field can be described by a modal expansion, as shown in [eq. \(3.2.17\)](#). With use of the kinematic and constitutive relations the vertical stress-field can be expanded the same way, see [eq. \(B.4.8\)](#).

The expanded expressions for \underline{u}_f , $\underline{\hat{p}}_f$ and $\underline{\sigma}_{s,r}$ are found in [appendix B.4](#)

$$\underline{u}_{s,n}(z, \theta, r) = \underline{\mathbf{R}}_n(\theta) \left(\sum_{p=1}^{\infty} C_{PSV,np} \underline{\mathbf{H}}_n(k_p r) \hat{\underline{u}}_{s,p}^{PSV}(z) + \sum_{q=1}^{\infty} C_{SH,nq} \cdot \underline{\mathbf{H}}_n(k_q r) \hat{\underline{u}}_{s,q}^{SH}(z) \right) \quad (3.2.17)$$

$$\underline{v}_{f,n}(z, \theta, r) = \underline{\mathbf{R}}_n(\theta) \sum_{p=1}^{\infty} C_{PSV,np} \underline{\mathbf{R}}_n(\theta) \text{diag} \left(\begin{bmatrix} -\frac{\partial H_n^{(2)}(\rho)}{\partial \rho} \Big|_{\rho=k_p r} \\ \frac{n}{r} H_n^{(2)}(k_p r) \\ H_n^{(2)}(k_p r) \end{bmatrix} \right) \hat{\underline{v}}_{f,p}^{PSV}(z) \quad (3.2.18)$$

$$\text{with: } \hat{\underline{u}}_{s,p}^{\text{PSV}}(z) = \begin{bmatrix} \hat{u}_{s,r,p}(z) & 0 & \hat{u}_{s,z,p}(z) \end{bmatrix}^T$$

$$\hat{\underline{u}}_{s,q}^{\text{SH}}(z) = \begin{bmatrix} 0 & \hat{u}_{s,\theta,q}(z) & 0 \end{bmatrix}^T$$

The displacement- and stress-field for the first 3 modes are shown in [figs. 3.9a](#) to [3.9f](#). These figures show that the imposed boundary and interface conditions are satisfied.

The plots for the vertical modes of the radial stresses $\underline{\sigma}_r$ are found in [appendix B.4](#)

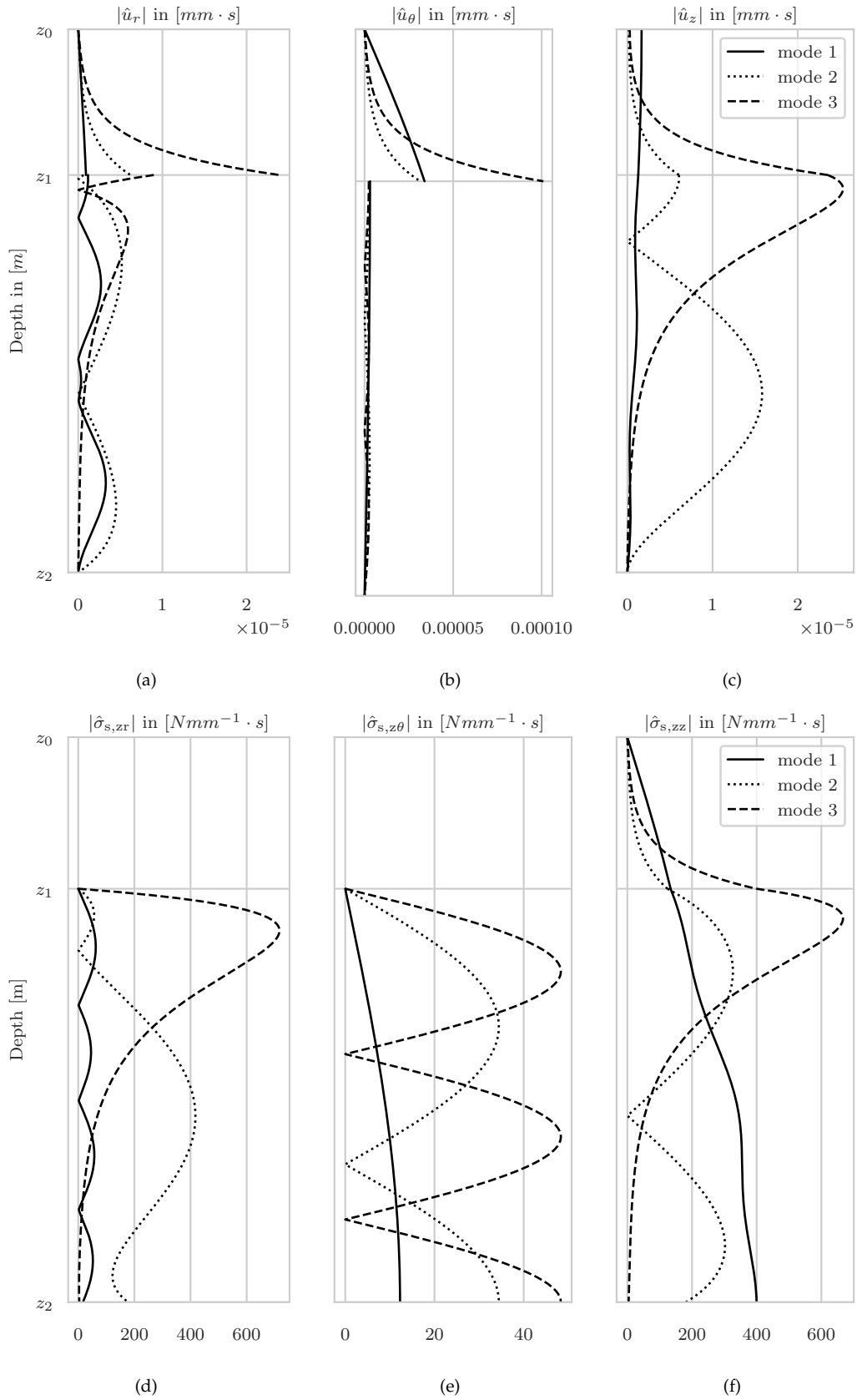


Figure 3.9: Displacement and stress field for the first three modes for $f = 10\text{Hz}$ for the undamped values from [table 3.3](#)

Chapter 4

Mode-matching

To get the total response of the system, and by extension the resulting acoustic field, the pile and acousto-elastic medium need to be coupled. This coupling occurs through the interface conditions, ensuring both displacement continuity and stress equilibrium in radial direction along the total length and circumference of the pile, these conditions are enforced by matching the modes of both subsystems this interface ¹using a mode-matching method to obtain the modal amplitudes for both dynamical system, and by extension the final coupled response.

In the work of Tsouvalas and Metrikine [3] a mode-matching method based on the orthogonality relations of the acousto-elastic medium is developed for the symmetric case. In this thesis a similar method is developed for the non-symmetric case, where the weight functions are chosen such that the final system can be simplified using the orthogonality relations of the acousto-elastic medium, this method can be read upon in [section 4.2](#). A more elaborate derivation, similar to the work of [3], of this method is given in [appendix C.2](#).

However, the main goal of this thesis, and this chapter in particular, is to develop a method alternative to the previous one. The so-called point-collocation method, where the matching of the modes is done with systematically chosen weight functions. Not necessarily taking into account the orthogonality relations of the acousto-elastic medium. This method is further elaborated in [section 4.3](#).

4.1 Method description

Just like any mode matching method, in essence the interface conditions between the pile and the acousto-elastic medium will be enforced in a weaker form. In the methods described in this chapter the weak form is obtained by use of the (partial) expressions of the radial soil stresses $\tilde{\sigma}_{s,r}$ and the fluid pressure \tilde{p}_f as weight functions.

Eventually, from the weak form the modal participation factors (or: amplitudes) of the modes will be acquired, which are then used to modally expand the stress- and displacement fields of the acousto-elastic medium.

As briefly mentioned before, two types of interface conditions between the pile and the adjacent acousto-elastic media are considered for this method:

1. Kinematic interface conditions: Displacement continuity
2. Dynamic interface conditions: Stress equilibrium

Displacement continuity

The mode-matching method centers around the condition of displacement continuity, which is imposed through four equations for the non-symmetric case, and three equations for the symmetric one, since the continuity in azimuthal direction, [eq. \(4.1.1c\)](#), is not relevant.

¹ The interface covers the region $\{(r, \theta, z) \mid r = R, 0 \leq \theta \leq 2\pi, 0 \leq z \leq L\}$, where R and L are the radius and length of the pile respectively.

$$u_{P,r}(z, \theta) = u_{f,r}(z, \theta, R) \quad \text{for} \quad z_1 \leq z \leq z_2 \quad (4.1.1a)$$

$$u_{P,r}(z, \theta) = u_{s,r}(z, \theta, R) \quad \text{for} \quad z_2 \leq z \leq L \quad (4.1.1b)$$

$$u_{P,\theta}(z, \theta) = u_{s,\theta}(z, \theta, R) \quad \text{for} \quad z_2 \leq z \leq L \quad (4.1.1c)$$

$$u_{P,z}(z, \theta) = u_{s,z}(z, \theta, R) \quad \text{for} \quad z_2 \leq z \leq L \quad (4.1.1d)$$

Note that the interface conditions do not involve the additional angles $\beta_{P,\{z,\theta\}}$, which reduces any pile vectors in the mode-matching process to 3 elements instead of the 5 elements initially introduced in [section 3.1](#). Furthermore, it is worth noting that for the mode-matching the vector notation conform [section 3.2](#) are used, i.e. $[\hat{e}_r \ \hat{e}_\theta \ \hat{e}_z]^T$.

After modally expanding the pile, fluid and soil expressions, conform [eqs. \(3.1.8\)](#) and [\(3.2.17\)](#), it shows that the non-symmetric problem deals with three sets of unknown modal amplitudes, namely $\underline{C}_{P,n}$, $\underline{C}_{PSV,n}$ and $\underline{C}_{SH,n}$. For this reason two weight vectors $\hat{\underline{w}}_s^{PSV}$ and $\hat{\underline{w}}_s^{SH}$ are defined next to the weight function $\hat{w}_f(z, \theta, R)$ used for the displacement continuity in the fluid.

$$\iint_E \hat{w}_f(z) u_{P,r}(z, \theta) dA = \iint_E \hat{w}_f(z) u_{f,r}(z, \theta, R) dA \quad (4.1.2a)$$

$$\iint_E \left(\hat{\underline{w}}_s^{PSV} \right)^T \underline{u}_P dA = \iint_E \left(\hat{\underline{w}}_s^{PSV} \right)^T \underline{u}_s \Big|_{r=R} dA \quad (4.1.2b)$$

$$\iint_E \left(\hat{\underline{w}}_s^{SH} \right)^T \underline{u}_P dA = \iint_E \left(\hat{\underline{w}}_s^{SH} \right)^T \underline{u}_s \Big|_{r=R} dA \quad (4.1.2c)$$

$$\text{with:} \quad E = \{(\theta, z) | 0 \leq \theta \leq 2\pi, 0 \leq z \leq z_2\}$$

$$\underline{u}_P = \underline{u}_P(z, \theta) = [u_{P,r} \quad u_{P,\theta} \quad u_{P,z}]^T$$

$$\underline{u}_s = \underline{u}_s(z, \theta, r) = [u_{s,r} \quad u_{s,\theta} \quad u_{s,z}]^T$$

$$\hat{\underline{w}}_s = \hat{\underline{w}}_s(z) = [\hat{w}_{s,r} \quad \hat{w}_{s,\theta} \quad \hat{w}_{s,z}]^T$$

In general weight functions are chosen to somewhat comply with the dynamics of the system at hand. Thus opting for (part of) arbitrary normal modes of the system as weight functions. As is the case in this work. For this reason the weight functions are henceforth displayed with the appropriate subscripts.

When N_{PSV} number of PSV-modes are considered, there are N_{PSV} possible weight functions $\hat{\underline{w}}_{s,ni}^{PSV}$ (i being the PSV-mode number). Thus matching the number of equations with the number of unknown constants in $\underline{C}_{PSV,n}$. The same holds for the number of SH-modes in relation to $\hat{\underline{w}}_{s,nj}^{SH}$.

Procedure

To obtain the necessary system of equations the following manipulations are performed:

1. Substituting the weight functions $\hat{\underline{w}}_{\{f;PSV;SH\}}$ native to the method into the weekend interface conditions [eqs. \(4.1.2a\)](#) to [\(4.1.2c\)](#).
2. Modally expanding the expressions of the displacements $vectu_{\{P;f;s\}}$ conform the displacement fields derived in [sections 3.1.3](#) and [3.2.3](#)
3. Summing [eqs. \(4.1.2a\)](#) and [\(4.1.2b\)](#), since these both contain the unknown \underline{C}_{PSV}
4. Re-arranging the resulting expressions gives two sets of equations, shown in generic form in [eqs. \(4.1.3a\)](#) and [\(4.1.4a\)](#).

$$\sum_{m=1}^{\infty} C_{P,nm} \hat{F}_{1,nlm} = \sum_{p=1}^{\infty} C_{PSV,np} \hat{F}_{2,nlp} + \sum_{q=1}^{\infty} C_{SH,nq} \hat{F}_{3,nlq} \quad \text{with} \quad l = 1, \dots, N_{PSV} \quad (4.1.3a)$$

$$(4.1.3b)$$

$$\hat{F}_{1,nlm} = \left\langle \hat{u}_{P,r,m}(z); \hat{w}_{s,r,l}^{PSV}(z) \right\rangle + \left\langle \hat{u}_{P,\theta,m}(z); \hat{w}_{s,\theta,l}^{PSV}(z) \right\rangle + \left\langle \hat{u}_{P,z,m}(z); \hat{w}_{s,z,l}^{PSV}(z) \right\rangle + \left\langle \hat{u}_{P,r,m}(z); \hat{w}_{f,l}(z) \right\rangle \quad (4.1.3c)$$

$$\hat{F}_{2,nlp} = \left\langle u_{s,r,np}^{PSV}(z, R); \hat{w}_{s,r,l}^{PSV}(z) \right\rangle + \left\langle u_{s,\theta,np}^{PSV}(z, R); \hat{w}_{s,\theta,l}^{PSV}(z) \right\rangle + \left\langle u_{s,z,np}^{PSV}(z, R); \hat{w}_{s,z,l}^{PSV}(z) \right\rangle + \left\langle u_{f,r,np}(z, R); \hat{w}_{f,l}(z) \right\rangle \quad (4.1.3d)$$

$$\hat{F}_{3,nlq} = \left\langle \hat{u}_{s,r,nq}^{SH}(z, R); \hat{w}_{s,r,l}^{PSV}(z) \right\rangle + \left\langle \hat{u}_{s,\theta,nq}^{SH}(z, R); \hat{w}_{s,\theta,l}^{PSV}(z) \right\rangle \quad (4.1.3e)$$

$$\sum_{m=1}^{\infty} C_{P,nm} \hat{F}_{4,njm} = \sum_{p=1}^{\infty} C_{PSV,np} \hat{F}_{5,njp} + \sum_{q=1}^{\infty} C_{SH,nq} \hat{F}_{6,njq} \quad \text{with} \quad j = 1, \dots, N_{SH} \quad (4.1.4a)$$

$$(4.1.4b)$$

$$\hat{F}_{4,njm} = \left\langle \hat{u}_{P,r,m}(z); \hat{w}_{s,r,j}^{SH}(z) \right\rangle + \left\langle \hat{u}_{P,\theta,m}(z); \hat{w}_{s,\theta,j}^{SH}(z) \right\rangle + \left\langle \hat{u}_{P,z,m}(z); \hat{w}_{s,z,j}^{SH}(z) \right\rangle \quad (4.1.4c)$$

$$\hat{F}_{5,njp} = \left\langle u_{s,r,np}^{PSV}(z, R); \hat{w}_{s,r,j}^{SH}(z) \right\rangle + \left\langle u_{s,\theta,np}^{PSV}(z, R); \hat{w}_{s,\theta,j}^{SH}(z) \right\rangle + \left\langle u_{s,z,np}^{PSV}(z, R); \hat{w}_{s,z,j}^{SH}(z) \right\rangle \quad (4.1.4d)$$

$$\hat{F}_{6,njq} = \left\langle \hat{u}_{s,r,nq}^{SH}(z, R); \hat{w}_{s,r,j}^{SH}(z) \right\rangle + \left\langle \hat{u}_{s,\theta,nq}^{SH}(z, R); \hat{w}_{s,\theta,j}^{SH}(z) \right\rangle \quad (4.1.4e)$$

For the sake of clarity the inner-product notation is used to display integrals: $\left\langle f(z); g(z) \right\rangle$ represents the integral of the product $f(z) \cdot g(z)$ over the domain in which both $f(z)$ and $g(z)$ exist. Therefore, the interval of the integral is omitted in this notation. The derivation with the traditional integral notation can be found in [appendix C.1](#).

Stress equilibrium

The equilibrium of stresses is enforced through the equation of motion of the pile. The response of the pile can be expressed in terms of the modal field of the acousto-elastic domain by following the same procedure as described in [section 3.1.5](#) to get the in-vacuo response of the pile.

$$\left(\omega_{nm} - \omega^2 \right) \underline{\underline{M}} \underline{u}_{P,n}(z, \theta) = \underline{\sigma}_{s,r,n}(z, \theta, R) - \underline{p}_{f,n}(z, \theta, R) + \underline{f}_{e,n}(z, \theta) \quad (4.1.5)$$

In this case the right-hand side consists of the external force $\underline{f}_{e,n}$, the exerted soil stresses $\underline{\sigma}_{s,r}$ and fluid pressure $-\underline{p}_{f,n}$ (eqs. (4.1.6a) and (4.1.6b)). After expanding the expressions it is immediately apparent that trigonometric functions $\underline{R}_n(\theta)$ cancel out. The equation of motion is then pre-multiplied by an arbitrary pile mode $\hat{u}_{P,k}(z)$ and integrated over the z -axis. Using the orthogonality condition of the pile, [eq. \(3.1.6\)](#), and

re-arranging results in the sets of equations shown in eq. (4.1.7a). Where $\hat{F}_{10,k}$ are the elements of the modal forcing vector.

$$\underline{\sigma}_{s,r,n}(z, \theta, R) = \underline{\mathbf{R}}_n(\theta) \left(\sum_{p=1}^{\infty} C_{\text{PSV},np} \underline{\mathbf{H}}_n^*(k_p R) \hat{\sigma}_{s,r,p}^{\text{PSV}}(z) + \sum_{q=1}^{\infty} C_{\text{SH},nq} \underline{\mathbf{H}}_n^{**}(k_q R) \hat{\sigma}_{s,r,q}^{\text{SH}}(z) \right) \quad (4.1.6a)$$

$$p_{f,n}(z, \theta, R) = \cos(n\theta) \left(\sum_{p=1}^{\infty} C_{\text{PSV},np} H_n^{(2)}(k_p R) \hat{p}_{f,n}(z) \right) \quad (4.1.6b)$$

The matrices $\underline{\mathbf{R}}_n(\theta)$, $\underline{\mathbf{H}}_n^*(k_p R)$, $\underline{\mathbf{H}}_n^{**}(k_q R)$ and vectors $\hat{\sigma}_{s,r,p}^{\text{PSV}}(z)$, $\hat{\sigma}_{s,r,q}^{\text{SH}}(z)$ are defined in appendix B.4

$$\sum_{m=1}^{\infty} C_{P,nm} \hat{F}_{7,nkm} = \sum_{p=1}^{\infty} C_{\text{PSV},np} \hat{F}_{8,nkp} + \sum_{q=1}^{\infty} C_{\text{SH},nq} \hat{F}_{9,nkq} + \hat{F}_{10,k} \quad \text{with} \quad k = 1, \dots, N_P \quad (4.1.7a)$$

$$\hat{F}_{7,nkm} = (\omega_{nm}^2 - \omega^2) \rho h R \Gamma_{nm}^P \delta_{mk} \quad (4.1.7b)$$

$$\hat{F}_{8,nkp} = \left\langle \hat{u}_{P,r,k}(z); \underbrace{\left[-H_n^{(2)}(k_p R) \hat{p}_{f,p}(z) \right]}_{p_{f,np}(z,R)} \right\rangle \quad (4.1.7c)$$

$$+ \left\langle \hat{u}_{P,r,k}(z); \underbrace{\left[-\hat{\sigma}_{s,rr,p}^{\text{PSV},1}(z) \cdot H_n^{(2)}(k_p R) + \hat{\sigma}_{s,rr,p}^{\text{PSV},2}(z) \cdot h_{1,n}(k_p R) \right]}_{\sigma_{s,rr,np}^{\text{PSV}}(z,R)} \right\rangle$$

$$+ \left\langle \hat{u}_{P,\theta,k}(z); \underbrace{\left[\hat{\sigma}_{s,rr,p}^{\text{PSV},2}(z) \cdot h_{2,n}(k_p R) \right]}_{\sigma_{r\theta,np}^{\text{PSV}}(z,R)} \right\rangle + \left\langle \hat{u}_{P,z,k}(z); \underbrace{\left[\hat{\sigma}_{s,zr,p}(z) \cdot \frac{1}{k_p} \partial_r H_n^{(2)}(k_p R) \right]}_{\sigma_{s,rz,np}^{\text{PSV}}(z,R)} \right\rangle$$

$$\hat{F}_{9,nkq} = \left\langle \hat{u}_{P,r,k}(z); \underbrace{\left[-\hat{\sigma}_{s,rr,q}^{\text{SH}}(z) \cdot h_{2,n}(k_q R) \right]}_{\sigma_{s,rr,nq}^{\text{SH}}(z,R)} \right\rangle + \left\langle \hat{u}_{P,\theta,k}(z); \underbrace{\left[\hat{\sigma}_{s,rr,q}^{\text{SH}}(z) \cdot h_{3,n}(k_q R) \right]}_{\sigma_{r\theta,nq}^{\text{SH}}(z,R)} \right\rangle \quad (4.1.7d)$$

$$+ \left\langle \hat{u}_{P,z,k}(z); \underbrace{\left[\hat{\sigma}_{s,z\theta,q}(z) \cdot \frac{n}{k_q r} H_n^{(2)}(k_q R) \right]}_{\sigma_{s,rz,nq}^{\text{SH}}(z,R)} \right\rangle$$

$$\hat{F}_{10,k} = \int_0^L \hat{\mathbf{u}}_{P,k}^T \hat{\mathbf{f}}_e \delta(z) dz = \hat{u}_{P,r,k}(0) \hat{f}_{e,r} + \hat{u}_{P,\theta,k}(0) \hat{f}_{e,\theta} + \hat{u}_{P,z,k}(0) \hat{f}_{e,z} \quad (4.1.7e)$$

In this work it was opted to include eq. (4.1.7a) in the final system of equations, resulting in a linear system with $(N_{\text{PSV}} + N_{\text{SH}} + N_P)$ unknowns and equations. Whereas in the work of [3] the pile amplitudes were substituted back into the weakend interface conditions, eqs. (4.1.2a) to (4.1.2c), proceeding with only the modal amplitudes of the acousto-elastic amplitudes as unknowns.

However, when it comes to the programming of the latter, extra steps are involved as nested summations occur, in contrast to the method chosen in this work, where the implementation is straight-forward and easily modified.

Symmetric case For the symmetric case it suffices to substitute $n = 0$ into the equations, which results in the decoupling of the azimuthal terms, i.e. the SH-problem separates from the PSV-problem. After simplifying and re-naming the modes, conform appendix B.4.2, the required two sets of equations become eqs. (4.1.8) and (4.1.9a).

$$\sum_{m=1}^{\infty} C_{P,0m} \hat{F}_{1,lm} = \sum_{p=1}^{\infty} C_{PSV,0p} \hat{F}_{2,lp} \quad \text{with} \quad l = 1, \dots, N_{PSV} \quad (4.1.8a)$$

$$\hat{F}_{1,lm} = \left\langle \hat{u}_{P,r,m}(z); \hat{w}_{f,l}(z) \right\rangle + \left\langle \hat{u}_{P,r,m}(z); \hat{w}_{s,r,l}^{PSV}(z) \right\rangle + \left\langle \hat{u}_{P,z,m}(z); \hat{w}_{s,z,l}^{PSV}(z) \right\rangle \quad (4.1.8b)$$

$$\hat{F}_{2,lp} = \left\langle u_{f,r,p}(z, R); \hat{w}_{f,l}(z) \right\rangle + \left\langle u_{s,r,p}(z, R); \hat{w}_{s,r,l}^{PSV}(z) \right\rangle + \left\langle u_{s,z,p}(z, R); \hat{w}_{s,z,l}^{PSV}(z) \right\rangle \quad (4.1.8c)$$

$$\sum_{m=1}^{\infty} C_{P,0m} \hat{F}_{3,km} = \sum_{p=1}^{\infty} C_{PSV,0p} \hat{F}_{4,kp} + \hat{F}_{5,k} \quad \text{with} \quad k = 1, \dots, N_P \quad (4.1.9a)$$

$$\hat{F}_{3,km} = \left(\omega_{0m}^2 - \omega^2 \right) \rho h R \Gamma_{0m}^P \delta_{mk} \quad (4.1.9b)$$

$$\begin{aligned} \hat{F}_{4,kp} = & \left\langle \hat{u}_{P,r,k}(z); \underbrace{\left[-\hat{p}_{f,p}(z) H_0^{(2)}(k_p R) \right]}_{p_{f,0p}(z,R)} \right\rangle + \left\langle \hat{u}_{P,z,k}(z); \underbrace{\left[\hat{\sigma}_{s,zr,p}^{H_1}(z) H_1^{(2)}(k_p R) \right]}_{\sigma_{s,rz,0p}(z,R)} \right\rangle \\ & + \left\langle \hat{u}_{P,r,k}(z); \underbrace{\left[\hat{\sigma}_{s,rr,p}^{H_0}(z) H_0^{(2)}(k_p R) + \hat{\sigma}_{s,rr,p}^{H_1}(z) H_1^{(2)}(k_p R) \right]}_{\sigma_{s,rr,0p}(z,R)} \right\rangle \end{aligned} \quad (4.1.9c)$$

$$\hat{F}_{5,k} = \hat{u}_{P,r,k}(0) \hat{f}_{e,r} + \hat{u}_{P,z,k}(0) \hat{f}_{e,z} \quad (4.1.9d)$$

Final system of equations

In sections 4.2 and 4.3 a second and third ² set of equations similar to eqs. (4.1.7a) and (4.1.9a) are obtained. Collecting the unknown amplitudes into a single vector results in a linear system as depicted in eqs. (4.1.10) and (4.1.11) for the non-symmetric and symmetric case respectively.

Note that $\hat{\underline{F}}_{1,lp}$ is a matrix where the element (l, p) is the scalar expression $\hat{F}_{1,lp}$. Since l and p denote the pile and PSV-mode numbers respectively this particular matrix has a size of $N_P \times N_{PSV}$, where $N_{\{P, PSV, SH\}}$ is the number of modes that are considered. section 4.4.3 elaborates further upon the truncation of these modes and choice for $N_{\{PSV, SH\}}$

$$\begin{bmatrix} \hat{\underline{F}}_{2,nlp} & \hat{\underline{F}}_{3,nlq} & -\hat{\underline{F}}_{1,nlm} \\ \hat{\underline{F}}_{5,njp} & \hat{\underline{F}}_{6,njq} & -\hat{\underline{F}}_{4,njm} \\ \hat{\underline{F}}_{8,nkp} & \hat{\underline{F}}_{9,nkq} & -\hat{\underline{F}}_{7,nkm} \end{bmatrix} \begin{bmatrix} \underline{C}_{PSV} \\ \underline{C}_{SH} \\ \underline{C}_P \end{bmatrix} = \begin{bmatrix} \underline{0} \\ \underline{0} \\ -\hat{\underline{F}}_{10,k} \end{bmatrix} \quad \text{with} \quad \begin{cases} p, l & \in [1, N_{PSV}] \\ q, j & \in [1, N_{SH}] \\ m, k & \in [1, N_P] \end{cases} \quad (4.1.10)$$

$$\begin{bmatrix} \hat{\underline{F}}_{2,lp} & -\hat{\underline{F}}_{1,lm} \\ \hat{\underline{F}}_{3,kp} & -\hat{\underline{F}}_{4,km} \end{bmatrix} \begin{bmatrix} \underline{C}_{PSV} \\ \underline{C}_P \end{bmatrix} = \begin{bmatrix} \underline{0} \\ -\underline{F}_{5,k} \end{bmatrix} \quad (4.1.11)$$

Differences

Two main differences between the developed method and Tsouvalas' method, hereinafter referred to as the orthogonality method, are first and foremost regarding the choice of weight functions, which are used to weaken the imposed conditions.

The orthogonality method opts for the use of arbitrary modes, eq. (4.1.12a), as weight functions. While the

² A third equation is obtained only for the non-symmetric cases.

method at hand uses the point-located radial as weight functions, which include the Hankel-function evaluated at the interface $r = R$, eq. (4.1.12b).

$$\text{arbitrary mode } l: \hat{\sigma}_{s,zr,l}(z) \quad (4.1.12a)$$

$$\text{point-located mode } l: \sigma_{s,zz,nl}(z, R) = -H_n^{(2)}(k_l R) \hat{\sigma}_{s,zz,l}(z) \quad (4.1.12b)$$

Note that in the point-located modes the θ -dependant part is not considered, since these do not influence the weakened form, as the trigonometric functions are cancelled out before integration. Henceforth when integration over the domain is mentioned in this chapter this only concerns the vertical domain, i.e. the z -axis. Furthermore, in the Orthogonality-method the weight functions are chosen such that the expressions can be simplified by use of the orthogonality relations of the acousto-elastic modes ³.

The advantage of the alternative method is that the resulting matrix is diagonally dominant, increasing its computational efficiency. However, the derivation of the matrix elements consists of many derivation steps and is, therefore, prone to error, both in deriving the equations and programming them. The methods presented in sections 4.2 and 4.3 avoid this by having straight forward weight functions, making the method less liable to error but more time robust at the same time.

4.2 The Orthogonality-method

As mentioned before, the Orthogonality-method that is derived in [3] will be further extended for higher circular mode numbers $n > 0$. The main difference between the axi-symmetric and non-axi-symmetric case is the coupling that exists between the PSV-waves the horizontal shear SH-waves for the non-symmetric case, i.e. the previously derived Rayleigh and Love modes.

In this section the weight functions of the Orthogonality-method are shown for both the non-symmetric and symmetric case in section 4.2 respectively. Note that the weight-functions for the symmetric case are retrieved from [3], and are briefly mentioned for the purpose of validating the developed method.

Non-symmetric case ($n > 0$)

Similar to the Orthogonality-method for the symmetric case, the aim is to choose the weight functions such that the resulting expressions can be simplified using the orthogonality relations of the acousto-elastic medium. These relations are introduced in section 3.2 and are revisited here:

$$-\frac{1}{k_p} \int_{z_1}^{z_2} \frac{\hat{\sigma}_{f,x,p}}{i\omega} \hat{p}_{f,l} dz + \frac{1}{k_p} \int_{z_2}^{z_3} \hat{\alpha}_{s,l}^I(z) \hat{u}_{s,x,p}(z) - \hat{u}_{s,z,l}(z) \hat{\sigma}_{s,zr,p}(z) dz = \Gamma_l^{\text{PSV}} \delta_{pl} \quad (3.2.14a \text{ revisited})$$

$$\text{with: } \hat{\alpha}_{s,l}^I(z) = \zeta_s k_l \hat{u}_{s,x,l}(z) + \eta_s \hat{\sigma}_{s,zz,l}(z)$$

$$\int_{z_2}^{z_3} \mu k_j^2 \hat{u}_{s,\theta,j} \hat{u}_{s,\theta,q} dz = \Gamma_j^{\text{SH}} \delta_{qj} \quad (3.2.15 \text{ revisited})$$

Weight functions The weight functions that allow for simplification in the non-symm case are shown in eq. (4.2.2). The subscripts l and j respectively denote an arbitrary PSV- and SH-mode.

An extended derivation is found in appendix C.2, where the final expressions are simplified using the orthogonality conditions. Note, however, that these simplifications are not applied in the model at hand, for the sake of having a straight forward model where adjustments to the weight functions are easily implemented.

³ The simplifying of the expressions is excluded in this thesis but can be found in [3]

$$\hat{w}_{f,l}(z) = -\hat{p}_{f,l}(z) \quad (4.2.2a)$$

$$\hat{w}_{s,l}^{\text{PSV}} = \begin{bmatrix} \zeta_s k_l \hat{u}_{s,r,l}(z) + \eta_s \hat{\sigma}_{s,zz,l}(z) \\ 0 \\ -\frac{1}{k_l} \hat{\sigma}_{s,zr,l}^{\text{PSV}}(z) \end{bmatrix} \quad (4.2.2b)$$

$$\hat{w}_{s,j}^{\text{SH}} = \begin{bmatrix} 0 \\ \mu k_j^2 \hat{u}_{s,\theta,j}^{\text{SH}} \\ 0 \end{bmatrix} \quad (4.2.2c)$$

The aforementioned procedure (page 26) is applied with the chosen weight functions, eq. (4.2.2). This results in the following two sets of equations:

$$\sum_{m=1}^{\infty} C_{P,nm} \hat{F}_{1,nlm} = \sum_{p=1}^{\infty} C_{\text{PSV},np} \hat{F}_{2,nlp} + \sum_{q=1}^{\infty} C_{\text{SH},nq} \hat{F}_{3,nlq} \quad (4.2.3a)$$

$$\begin{aligned} \hat{F}_{1,nlm} = & \left\langle \hat{u}_{P,r,m}(z); [-\hat{p}_{f,l}(z)] \right\rangle + \left\langle \hat{u}_{P,r,m}(z); \underbrace{[\zeta_s k_l \hat{u}_{s,r,l}(z) + \eta_s \hat{\sigma}_{s,zz,l}(z)]}_{\hat{w}_{s,r,l}^{\text{PSV}}(z)} \right\rangle \\ & + \left\langle \hat{u}_{P,z,m}(z); \underbrace{\left[-\frac{1}{k_l} \hat{\sigma}_{s,zr,l}^{\text{PSV}}(z) \right]}_{\hat{w}_{s,z,l}^{\text{PSV}}(z)} \right\rangle \end{aligned} \quad (4.2.3b)$$

$$\begin{aligned} \hat{F}_{2,nlp} = & \left\langle \underbrace{\left[\hat{u}_{f,r,p}(z) \cdot \partial_r H_n^{(2)}(k_p R) \right]}_{u_{f,r,np}^{\text{PSV}}(z,R)}; [-\hat{p}_{f,l}(z)] \right\rangle \\ & + \left\langle \underbrace{\left[\hat{u}_{s,r,p}(z) \cdot \frac{1}{k_p} \partial_r H_n^{(2)}(k_p R) \right]}_{u_{s,r,np}^{\text{PSV}}(z,R)}; [\zeta_s k_l \hat{u}_{s,r,l}(z) + \eta_s \hat{\sigma}_{s,zz,l}(z)] \right\rangle \\ & + \left\langle \underbrace{\left[\hat{u}_{s,z,p}(z) \cdot -H_n^{(2)}(k_p R) \right]}_{u_{s,z,np}^{\text{PSV}}(z,R)}; \left[-\frac{1}{k_l} \hat{\sigma}_{s,zr,l}^{\text{PSV}}(z) \right] \right\rangle \end{aligned} \quad (4.2.3c)$$

$$\hat{F}_{3,nlq} = \left\langle \underbrace{\left[\hat{u}_{s,\theta,q}(z) \cdot \frac{n}{k_q r} H_n^{(2)}(k_q R) \right]}_{u_{s,\theta,nq}^{\text{SH}}(z,R)}; [\zeta_s k_l \hat{u}_{s,r,l}(z) + \eta_s \hat{\sigma}_{s,zz,l}(z)] \right\rangle \quad (4.2.3d)$$

$$\sum_{m=1}^{\infty} C_{P,nm} \hat{F}_{4,njm} = \sum_{p=1}^{\infty} C_{PSV,np} \hat{F}_{5,njp} + \sum_{q=1}^{\infty} C_{SH,nq} \hat{F}_{6,njq} \quad (4.2.4a)$$

$$\hat{F}_{4,njm} = \left\langle \hat{u}_{P,\theta,m}(z); \underbrace{\left[\mu k_j^2 \hat{u}_{s,\theta,j}^{SH} \right]}_{\hat{w}_{s,\theta,j}^{SH}(z)} \right\rangle \quad (4.2.4b)$$

$$\hat{F}_{5,njp} = \left\langle \underbrace{\left[\hat{u}_{s,r,p}(z) \cdot \frac{n}{k_p r} H_n^{(2)}(k_p R) \right]}_{u_{s,\theta,np}^{PSV}(z,R)}; \left[\mu k_j^2 \hat{u}_{s,\theta,j}^{SH} \right] \right\rangle \quad (4.2.4c)$$

$$\hat{F}_{6,njq} = \left\langle \underbrace{\left[\hat{u}_{s,\theta,q}(z) \cdot \frac{1}{k_q} \partial_r H_n^{(2)}(k_q R) \right]}_{u_{s,\theta,nq}^{SH}(z,R)}; \left[\mu k_j^2 \hat{u}_{s,\theta,j}^{SH} \right] \right\rangle \quad (4.2.4d)$$

Symmetric case ($n = 0$)

Since the SH- and PSV-modes are decoupled for the symmetric case ($n = 0$) and only the response of the system in terms of PSV-waves is of interest the system reduces to two unknown sets of modal amplitudes $\underline{C}_{\{P,PSV\}}$. Thus, the additional set of weakend equations eq. (4.1.2c), as well as the vector-element corresponding to the azimuthal direction is scrapped.

Weight functions

$$\hat{w}_{f,l}(z) = -\hat{p}_{f,l}(z) \quad (4.2.5a)$$

$$\hat{w}_{s,l}^{PSV} = \begin{bmatrix} \zeta_s k_l \hat{u}_{s,r,l}(z) + \eta_s \hat{\sigma}_{s,zz,l}(z) \\ -\frac{1}{k_l} \hat{\sigma}_{s,zr,l}(z) \end{bmatrix} \quad (4.2.5b)$$

Following the procedure described section 4.1 in on page 26 results in the following set of equations:

$$\sum_{m=1}^{\infty} C_{P,0m} \hat{F}_{1,nlm} = \sum_{p=1}^{\infty} C_{PSV,0p} \hat{F}_{2,nlp} \quad (4.2.6a)$$

$$\begin{aligned} \hat{F}_{1,nlm} &= \left\langle \hat{u}_{P,r,m}(z); \underbrace{\left[-\hat{p}_{f,l}(z) \right]}_{\hat{w}_{f,l}(z)} \right\rangle + \left\langle \hat{u}_{P,r,m}(z); \underbrace{\left[\zeta_s k_l \hat{u}_{s,r,l}(z) + \eta_s \hat{\sigma}_{s,zz,l}(z) \right]}_{\hat{w}_{s,r,l}^{PSV}(z)} \right\rangle \\ &+ \left\langle \hat{u}_{P,z,m}(z); \underbrace{\left[-\frac{1}{k_l} \hat{\sigma}_{s,zr,l}(z) \right]}_{\hat{w}_{s,z,l}^{PSV}(z)} \right\rangle \end{aligned} \quad (4.2.6b)$$

$$\begin{aligned} \hat{F}_{2,nlp} &= \left\langle \underbrace{\left[H_1^{(2)}(k_p r) \hat{u}_{f,r,p}(z) \right]}_{u_{f,r,np}(z,R)}; \left[-\hat{p}_{f,l}(z) \right] \right\rangle \\ &+ \left\langle \underbrace{\left[H_1^{(2)}(k_p r) \hat{u}_{s,r,p}(z) \right]}_{u_{s,r,np}(z,R)}; \left[\zeta_s k_l \hat{u}_{s,r,l}(z) + \eta_s \hat{\sigma}_{s,zz,l}(z) \right] \right\rangle + \left\langle \underbrace{\left[H_0^{(2)}(k_p r) \hat{u}_{s,z,p}(z) \right]}_{u_{z,r,np}(z,R)}; \left[-\frac{1}{k_l} \hat{\sigma}_{s,zr,l}(z) \right] \right\rangle \end{aligned} \quad (4.2.6c)$$

4.3 The Point Collocation-method

As previously mentioned the weightfunctions for the Point Collocation-method are chosen more systematically. For the interface conditions between the pile and soil the weight function is set to the radial stress in the relevant direction. So, for example, for the continuity of vertical displacement the weight functions $\hat{w}_{s,r,nl}^{PSV}$ and $\hat{w}_{s,r,nl}^{SH}$ are the arbitrary modes $\sigma_{s,zr,nl}^{PSV}(z, R)$ and $\sigma_{s,zr,nl}^{SH}(z, R)$ respectively.

The weight functions for the Point Collocation-method are shown for both the non-symmetric and symmetric case in [section 4.3](#) respectively.

Non-symmetric case ($n > 0$)

Weight functions

$$\hat{w}_{t,nl}(z) = -\hat{p}_{t,l}(z) H_n^{(2)}(k_l R) \quad (4.3.1a)$$

$$\hat{w}_{s,nl}^{\text{PSV}} = \underline{\sigma}_{s,r,nl}^{\text{PSV}}(z, R) = \begin{bmatrix} -\hat{\sigma}_{s,rr,l}^{\text{PSV},1}(z) H_n^{(2)}(k_l R) + \hat{\sigma}_{s,rr,l}^{\text{PSV},2}(z) h_{1,n}(k_l R) \\ \hat{\sigma}_{s,rr,l}^{\text{PSV},2}(z) h_{2,n}(k_l R) \\ \hat{\sigma}_{s,zr,l}(z) \frac{1}{k_l} \partial_r H_n^{(2)}(k_l R) \end{bmatrix} \quad (4.3.1b)$$

$$\hat{w}_{s,nj}^{\text{SH}} = \underline{\sigma}_{s,r,nj}^{\text{SH}}(z, R) = \begin{bmatrix} -\hat{\sigma}_{s,rr,j}^{\text{SH}}(z) h_{2,n}(k_j R) \\ \hat{\sigma}_{s,rr,j}^{\text{SH}}(z) h_{3,n}(k_j R) \\ \hat{\sigma}_{s,z\theta,j}^{\text{SH}}(z) \frac{n}{k_j R} H_n^{(2)}(k_j R) \end{bmatrix} \quad (4.3.1c)$$

Following the procedure described in [section 4.1](#) on [page 26](#) results in the following two sets of equations:

$$\sum_{m=1}^{\infty} C_{P,nm} \hat{F}_{1,nlm} = \sum_{p=1}^{\infty} C_{PSV,np} \hat{F}_{2,nlp} + \sum_{q=1}^{\infty} C_{SH,nq} \hat{F}_{3,nlq} \quad (4.3.2a)$$

$$\hat{F}_{1,nlm} = \left\langle \hat{u}_{P,r,m}(z); \underbrace{\left[-\hat{p}_{\ell,l}(z) \cdot H_n^{(2)}(k_l R) \right]}_{\hat{w}_{\ell,l}^{PSV}(z)} \right\rangle \quad (4.3.2b)$$

$$+ \left\langle \hat{u}_{P,r,m}(z); \underbrace{\left[-\hat{\sigma}_{s,rr,p}^{PSV,1}(z) \cdot H_n^{(2)}(k_p R) + \hat{\sigma}_{s,rr,p}^{PSV,2}(z) \cdot h_{1,n}(k_p R) \right]}_{\hat{w}_{s,r,l}^{PSV}(z)} \right\rangle$$

$$+ \left\langle \hat{u}_{P,\theta,m}(z); \underbrace{\left[\hat{\sigma}_{s,rr,l}^{PSV,2}(z) \cdot h_{2,n}(k_l R) \right]}_{\hat{w}_{s,\theta,l}^{PSV}(z)} \right\rangle + \left\langle \hat{u}_{P,z,m}(z); \underbrace{\left[\hat{\sigma}_{s,zr,l}(z) \cdot \frac{1}{k_l} \partial_r H_n^{(2)}(k_l R) \right]}_{\hat{w}_{s,z,l}^{PSV}(z)} \right\rangle$$

$$\hat{F}_{2,nlp} = \left\langle \underbrace{\left[\hat{u}_{f,r,p}(z) \cdot \partial_r H_n^{(2)}(k_p R) \right]}_{u_{f,r,np}(z,R)}; \left[-\hat{p}_{\ell,l}(z) H_n^{(2)}(k_l R) \right] \right\rangle \quad (4.3.2c)$$

$$+ \left\langle \underbrace{\left[\hat{u}_{s,r,p}(z) \cdot \frac{1}{k_p} \partial_r H_n^{(2)}(k_p R) \right]}_{u_{s,r,np}^{PSV}(z,R)}; \left[-\hat{\sigma}_{s,rr,l}^{PSV,1}(z) H_n^{(2)}(k_l R) + \hat{\sigma}_{s,rr,l}^{PSV,2}(z) h_{1,n}(k_l R) \right] \right\rangle$$

$$+ \left\langle \underbrace{\left[\hat{u}_{s,\theta,p}(z) \cdot \frac{n}{k_p r} H_n^{(2)}(k_p R) \right]}_{u_{s,\theta,np}^{PSV}(z,R)}; \left[\hat{\sigma}_{s,rr,l}^{PSV,2}(z) h_{2,n}(k_l R) \right] \right\rangle$$

$$+ \left\langle \underbrace{\left[\hat{u}_{s,z,p}(z) \cdot -H_n^{(2)}(k_p R) \right]}_{u_{s,z,np}^{PSV}(z,R)}; \left[\hat{\sigma}_{s,zr,l}(z) \frac{1}{k_l} \partial_r H_n^{(2)}(k_l R) \right] \right\rangle$$

$$\hat{F}_{3,nlq} = \left\langle \underbrace{\left[\hat{u}_{s,\theta,q}(z) \cdot \frac{n}{k_q R} H_n^{(2)}(k_q R) \right]}_{u_{s,\theta,nq}^{SH}(z,R)}; \left[-\hat{\sigma}_{s,rr,l}^{PSV,1}(z) H_n^{(2)}(k_l R) + \hat{\sigma}_{s,rr,l}^{PSV,2}(z) h_{1,n}(k_l R) \right] \right\rangle \quad (4.3.2d)$$

$$+ \left\langle \underbrace{\left[\hat{u}_{s,\theta,q}(z) \cdot \frac{1}{k_q} \partial_r H_n^{(2)}(k_q R) \right]}_{u_{s,\theta,nq}^{SH}(z,R)}; \left[\hat{\sigma}_{s,rr,l}^{PSV,2}(z) h_{2,n}(k_l R) \right] \right\rangle$$

$$\sum_{m=1}^{\infty} C_{P, nm} \hat{F}_{4, njm} = \sum_{p=1}^{\infty} C_{PSV, np} \hat{F}_{5, njp} + \sum_{q=1}^{\infty} C_{SH, nq} \hat{F}_{6, njq} \quad (4.3.3a)$$

$$\hat{F}_{4, njm} = \left\langle \hat{u}_{P, r, m}(z); \underbrace{\left[-\hat{\sigma}_{s, rr, j}^{SH}(z) h_{2, n}(k_j R) \right]}_{\hat{w}_{s, r, j}^{SH}(z)} \right\rangle \quad (4.3.3b)$$

$$+ \left\langle \hat{u}_{P, \theta, m}(z); \underbrace{\left[\hat{\sigma}_{s, rr, j}^{SH}(z) h_{3, n}(k_j R) \right]}_{\hat{w}_{s, \theta, j}^{SH}(z)} \right\rangle + \left\langle \hat{u}_{P, z, m}(z); \underbrace{\left[\hat{\sigma}_{s, z\theta, j}^{SH}(z) \frac{n}{k_j R} H_n^{(2)}(k_j R) \right]}_{\hat{w}_{s, z, j}^{SH}(z)} \right\rangle$$

$$\hat{F}_{5, njp} = \left\langle \underbrace{\left[\hat{u}_{s, r, p}(z) \cdot \frac{1}{k_p} \partial_r H_n^{(2)}(k_p R) \right]}_{u_{s, r, np}^{PSV}(z, R)}; \left[-\hat{\sigma}_{s, rr, j}^{SH}(z) h_{2, n}(k_j R) \right] \right\rangle \quad (4.3.3c)$$

$$+ \left\langle \underbrace{\left[\hat{u}_{s, \theta, p}(z) \cdot \frac{n}{k_p r} H_n^{(2)}(k_p R) \right]}_{u_{s, \theta, np}^{PSV}(z, R)}; \left[\hat{\sigma}_{s, rr, j}^{SH}(z) h_{3, n}(k_j R) \right] \right\rangle$$

$$+ \left\langle \underbrace{\left[\hat{u}_{s, z, p}(z) \cdot -H_n^{(2)}(k_p R) \right]}_{u_{s, z, np}^{PSV}(z, R)}; \left[\hat{\sigma}_{s, z\theta, j}^{SH}(z) \frac{n}{k_j R} H_n^{(2)}(k_j R) \right] \right\rangle$$

$$\hat{F}_{6, njq} = \left\langle \underbrace{\left[\hat{u}_{s, \theta, q}(z) \cdot \frac{n}{k_q R} H_n^{(2)}(k_q R) \right]}_{u_{s, r, nq}^{SH}(z, R)}; \left[-\hat{\sigma}_{s, rr, j}^{SH}(z) h_{2, n}(k_j R) \right] \right\rangle \quad (4.3.3d)$$

$$+ \left\langle \underbrace{\left[\hat{u}_{s, \theta, q}(z) \cdot \frac{1}{k_q} \partial_r H_n^{(2)}(k_q R) \right]}_{u_{s, \theta, nq}^{SH}(z, R)}; \left[\hat{\sigma}_{s, rr, j}^{SH}(z) h_{3, n}(k_j R) \right] \right\rangle$$

Symmetric case ($n = 0$)

Similar to [section 4.2](#) the problem reduces for the symmetric case. Naturally the same set of equations can be obtained by substituting $n = 0$ into [eq. \(4.3.2\)](#)

Weight functions

$$\hat{w}_{f, l}(z) = -\hat{p}_{f, l}(z) H_0^{(2)}(k_l R) \quad (4.3.4a)$$

$$\hat{w}_{s, l}^{PSV} = \begin{bmatrix} \hat{\sigma}_{s, rr, l}^{H_0}(z) H_0^{(2)}(k_l R) + \hat{\sigma}_{s, rr, l}^{H_1}(z) \frac{1}{R} H_1^{(2)}(k_l R) \\ \hat{\sigma}_{s, zr, l}(z) H_1^{(2)}(k_l R) \end{bmatrix} \quad (4.3.4b)$$

Following the procedure described [section 4.1](#) in on page [26](#) results in the following set of equations:

$$\sum_{m=1}^{\infty} C_{P,0m} \hat{F}_{1,lm} = \sum_{p=1}^{\infty} C_{PSV,0p} \hat{F}_{2,lp} \quad (4.3.5a)$$

$$\begin{aligned} \hat{F}_{1,lm} = & \left\langle \hat{u}_{P,r,0m}(z); \underbrace{\left[-\hat{p}_{f,l}(z) H_0^{(2)}(k_l R) \right]}_{\hat{w}_{f,l}(z)} \right\rangle + \left\langle \hat{u}_{P,z,0m}(z); \underbrace{\left[\hat{\sigma}_{s,zr,l}^{H_1}(z) H_1^{(2)}(k_l R) \right]}_{\hat{w}_{s,z,l}^{PSV}(z)} \right\rangle \\ & + \left\langle \hat{u}_{P,r,0m}(z); \underbrace{\left[\hat{\sigma}_{s,rr,l}^{H_0}(z) H_0^{(2)}(k_l R) + \hat{\sigma}_{s,rr,l}^{H_1}(z) \frac{1}{R} H_1^{(2)}(k_l R) \right]}_{\hat{w}_{s,r,l}^{PSV}(z)} \right\rangle \end{aligned} \quad (4.3.5b)$$

$$\begin{aligned} \hat{F}_{2,lp} = & \left\langle \underbrace{\left[\hat{u}_{f,r,p}(z) H_1^{(2)}(k_p R) \right]}_{p_{f,0p}(z,R)}; \left[-\hat{p}_{f,l}(z) H_0^{(2)}(k_l R) \right] \right\rangle \\ & + \left\langle \underbrace{\left[\hat{u}_{s,r,p}(z) H_1^{(2)}(k_p R) \right]}_{u_{s,r,0p}(z,R)}; \left[\hat{\sigma}_{s,rr,l}^{H_0}(z) H_0^{(2)}(k_l R) + \hat{\sigma}_{s,rr,l}^{H_1}(z) \frac{1}{R} H_1^{(2)}(k_l R) \right] \right\rangle \\ & + \left\langle \underbrace{\left[\hat{u}_{s,z,p}(z) H_0^{(2)}(k_p R) \right]}_{u_{s,z,0p}(z,R)}; \left[\hat{\sigma}_{s,zr,l}^{H_1}(z) H_1^{(2)}(k_l R) \right] \right\rangle \end{aligned} \quad (4.3.5c)$$

4.4 Numerical considerations

In this section the stability and solvability of the assembled linear system is briefly touched upon in [section 4.4.1](#).

Furthermore, an uniform error definition is set to systematically assess the convergence of the different methods, this definition is found in [section 4.4.2](#). The truncation of the modal summation of the fluid-soil medium is elaborated upon in [section 4.4.3](#).

4.4.1 Stability of the system

The assembled linear system, of size $(N_P + N_{PSV})$ for the symmetric case and $(N_P + N_{PSV} + N_{SH})$ for the non-symmetric case, is solved by inverting the coefficient matrix $\underline{\underline{A}}$. Depending on the truncation, which is further elaborated on in [section 4.4.3](#), the size of $\underline{\underline{A}}$ can become quite big and is not necessarily prominent diagonal, resulting in an ill-conditioned matrix. Hence the stability of the system is questioned.

The stability of the matrix is monitored through the relative error of the outcome during the solving process. This process is shown in [eq. \(4.4.1\)](#), where $\underline{\underline{x}}$ consists of the unknowns $\underline{\underline{C}}_{\{P,PSV,SH\}}$ and vectors $\underline{\underline{b}}_0$ and $\underline{\underline{b}}_1$ are the original and re-calculated right-hand side respectively.

A sample check shows that the obtained amplitude do satisfy the equation for with the tolerance of 10^{-10} , therefore, no extra measures were taken. If the threshold was exceeded one could pre-condition the matrix to increase its stability.

$$\begin{aligned} \underline{\underline{x}} = \underline{\underline{A}}^{-1} \underline{\underline{b}}_0 & \longrightarrow \Delta \underline{\underline{b}} = \underline{\underline{b}}_1 - \underline{\underline{b}}_0 \\ \underline{\underline{b}}_1 = \underline{\underline{A}} \underline{\underline{x}} & \end{aligned} \quad (4.4.1a)$$

$$\text{Absolute error: } \left| \sqrt{\Delta \underline{\underline{b}}^T \Delta \underline{\underline{b}}} \right| \quad (4.4.1b)$$

$$\text{Relative error: } \frac{\text{Absolute error}}{\underline{\underline{b}}_0^T \underline{\underline{b}}_0} \leq \varepsilon_{\text{tol}} = 10^{-10} \quad (4.4.1c)$$

4.4.2 Matching error

Once the amplitudes $\underline{C}_{\{P,PSV,SH\}}$ the extent to which they comply with the kinematic interface conditions is checked through the absolute mismatch between the displacement of the pile and the adjacent acousto-elastic medium at $r = R$. The mismatch in radial direction is shown in [fig. 4.1a](#). This error is greatly influenced by the number of (evanescent) acousto-elastic modes taken into account, therefore, the truncation of the modal summation is based on a threshold for the mean mismatch error, further elaboration on this process is found in [section 4.4.3](#).

For the purpose of having a uniform threshold test the relative mismatch error is defined in [eq. \(4.4.2b\)](#), where the $\langle f(z) \rangle$ depicts the averaging process along the z -axis.

Due to the oscillatory nature of the displacement the relative error reaches rather high values when the displacement in the acousto-elastic medium becomes small, see the unbroken line in [fig. 4.1b](#), when this is not accounted for in the relative error this results in non-credible error-values. This is omitted by filtering the values of $\hat{u}_{\{s,f\},\{z;\theta;r\}}$ that are smaller than 10% of the mean displacement. After applying the filtering procedure the peaks in the relative error becomes much smaller, see the dashed line in [fig. 4.1b](#), however, the peaks near the boundary are inevitable, and are attributed to Gibbs phenomenon, which is clearly seen in the mismatch at $z = z_0$ and $z = z_1$ in [fig. 4.1a](#).

$$\text{Filtering: } \left| \hat{u}_{\{P;s,f\},\{z;\theta;r\}}^* \right| \geq 0.1 \cdot \text{mean} \left(\left| \hat{u}_{\{s,f\},\{z;\theta;r\}}^* \right| \right) \quad (4.4.2a)$$

$$\text{Error per medium: } \delta_{\{s,f\},\{z;\theta;r\}} = \left\langle \frac{\left| \hat{u}_{P,\{z;\theta;r\}}^* - \hat{u}_{\{s,f\},\{z;\theta;r\}}^* \right|}{\left| \hat{u}_{\{s,f\},\{z;\theta;r\}}^* \right|} \right\rangle \quad (4.4.2b)$$

$$\text{Overall error: } \delta_{\text{total}} = \frac{\sum_i \gamma_i \delta_{\{s,f\},\{z;\theta;r\}}}{\sum_i \gamma_i} \quad \text{with} \quad \begin{cases} \gamma_{f,r} = \sum \gamma_{s,\{z;\theta;r\}} \\ \text{for } n = 1: & \gamma_{s,\{z;\theta;r\}} = 1 \\ \text{for } n = 0: & \gamma_{s,\{z;r\}} = 1 \end{cases} \quad (4.4.2c)$$

Finally an overall relative error is obtained by taking the weighted average of the relative errors for the different interface conditions. Since the waveradiation in the fluid-medium is of interest, the corresponding interface condition is weighted twice as heavy as the others, conform [eq. \(4.4.2c\)](#).

Geometry	Pile	Soil	Fluid
Pile top $z_{\text{pile top}}$	0 m	ρ_P 7850 kg m ⁻³	ρ_f 1000 kg m ⁻³
Sea surface z_0	8 m	E 2.1 · 10 ¹¹ kg m ⁻³	d_f 22 m
Sea bed z_1	30 m	R 2.5 m	c_f 1500 m s ⁻¹
Pile bottom z_L	60 m	h 0.03 m	c_L 366.06 m s ⁻¹
Rigid boundary condition z_2	90 m	ν 0.28	E_s 1.0 · 10 ⁸ kg m ⁻³
		L 60 m	$P_{\{\lambda,\mu\}}$ 1 %

Table 4.1: Properties of the system

4.4.3 Truncation

Unlike the truncation of the pile modes, which is based on the excited modes for the highest frequency used in the scope of this thesis (as described in [section 3.1.5](#)), the number of evanescent PSV- and SH-modes that satisfy the interface conditions up to a certain threshold for a higher frequency do not necessarily meet the same threshold for a lower frequency. One may say that there exists an optimum combination of the numbers of PSV- and SH-modes that are considered for each frequency. When the ideal number of modes is exceeded the solution starts to diverge for some cases, [fig. 4.2](#). The extra added modes seem to cause "noise" in the linear system ⁴, as a result of which the local requirement (kinematic conditions at $r = R$) is not met. This effect

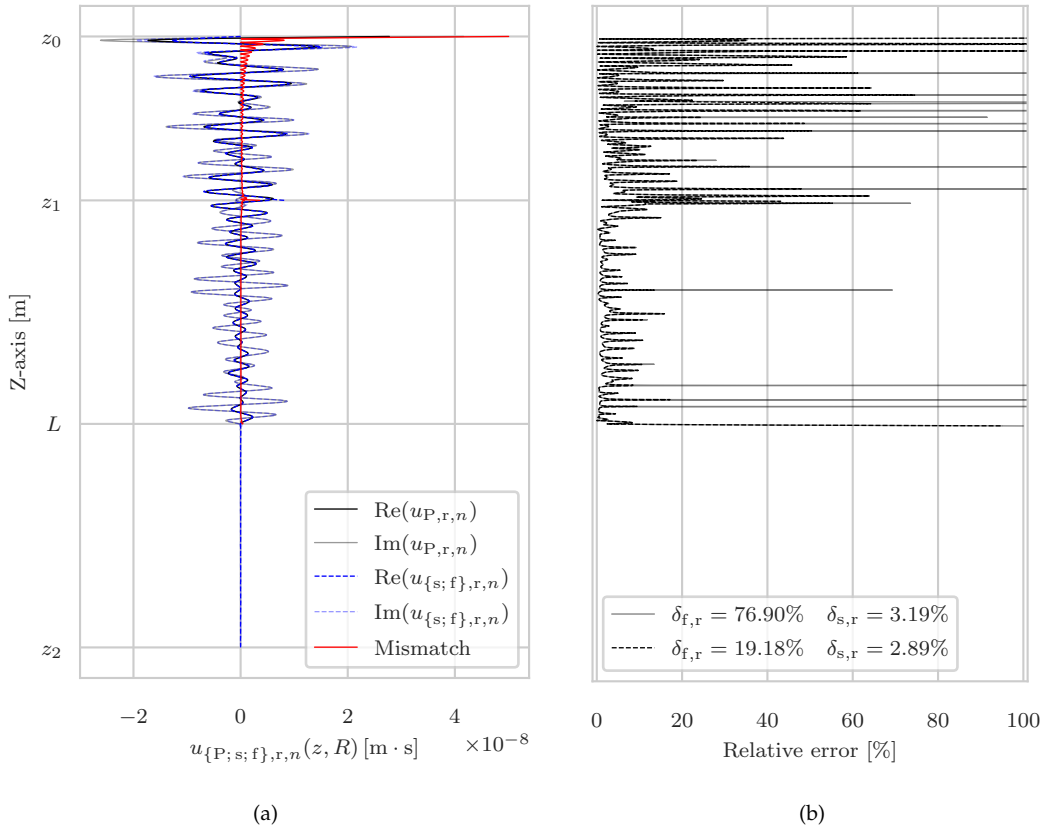


Figure 4.1: (a) Mismatch and (b) relative error, both filtered (dashed line) and unfiltered (unbroken line), in radial direction for a system with the properties in table 4.1 at $f = 200$ Hz and for $N_{\{PSV;SH\}} = (297, 275)$

seems to be related to the matching method, since it seems to be more prominent in the Orthogonality-method.

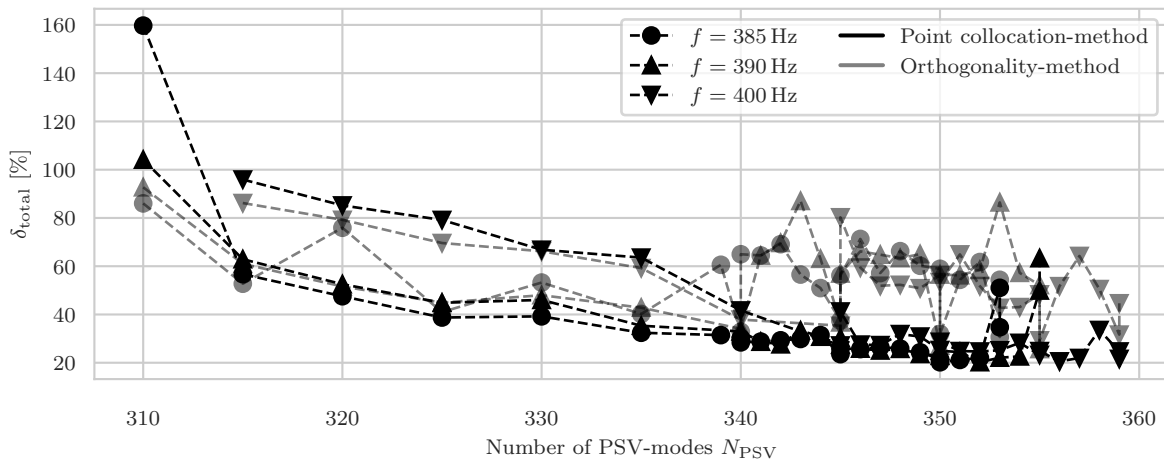


Figure 4.2: The convergence of the response to a uniform vertical force shown by plotting δ_{total} against N_{PSV} for several frequencies.

The ideal number of modes to obtain the response to a uniform horizontal and vertical force are depicted in figs. 4.3 and 4.4 respectively.

⁴ A possible explanation for the "noise" in the linear system, is that the additional modes enlarge the linear systems and since large systems are prone to being ill-conditioned this may result in less accurate solutions.

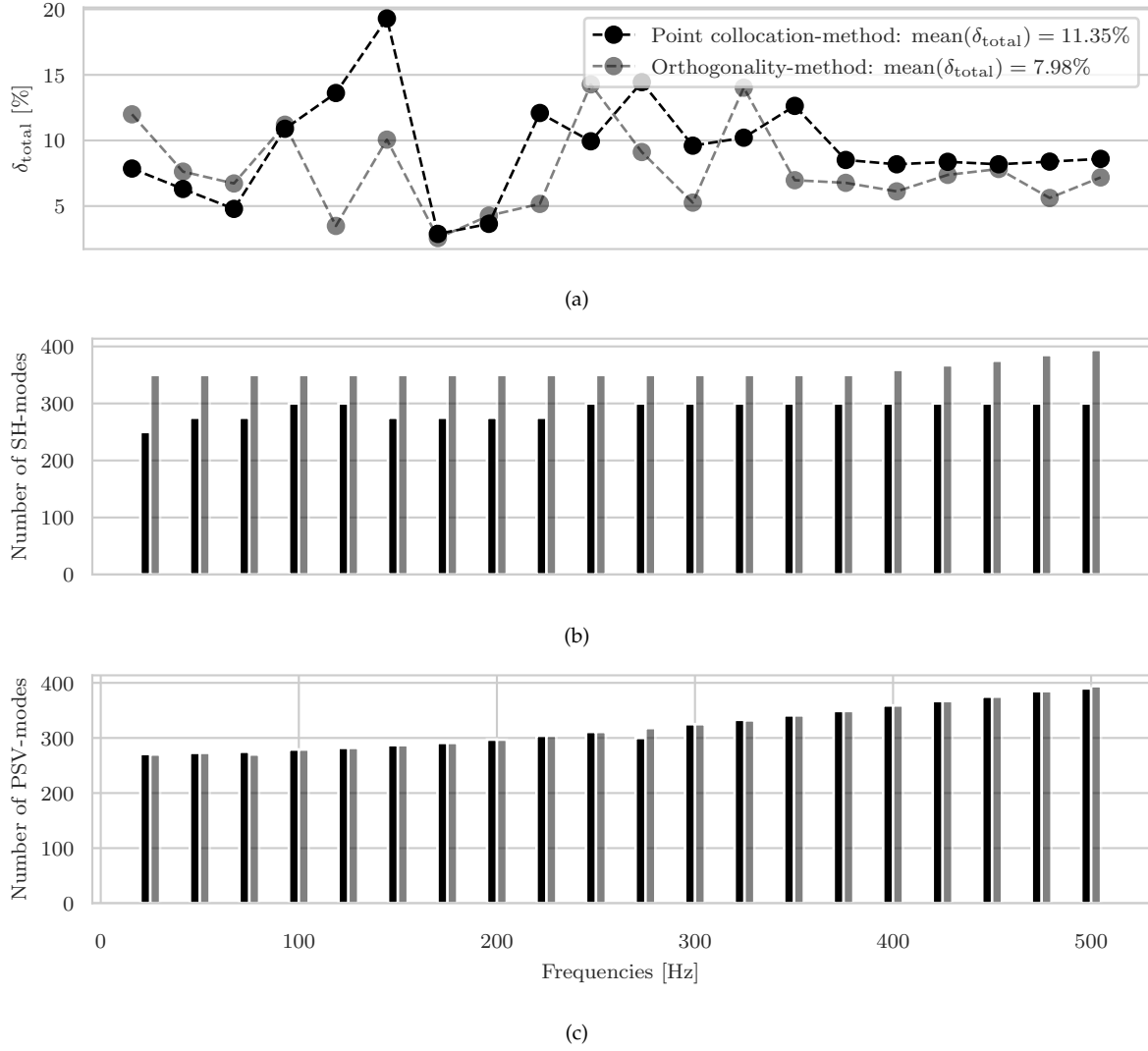


Figure 4.3: (b)-(c) The ideal number of modes $N_{\{\text{PSV};\text{SH}\}}$ for the response to a uniform horizontal force and (a) the corresponding error

Finding the optimum

In the case of an undamped system the modes corresponding to real wavenumbers k^{PSV} are always taken into account, after which evanescent modes are added with increments of dN_{PSV}

The mode-matching procedure is iterated for different combinations of $N_{\{\text{PSV};\text{SH}\}}$. This is done starting from a higher number of modes and decreasing the number of modes with increments of $dN_{\{\text{PSV};\text{SH}\}}$, while taking into account the fact that the (complex) evanescent modes come in pairs⁵. The minimum number of modes is pre-set to a hundred, this ensures that any modes corresponding to real wavenumbers (in the undamped state) are taken into account. For the non-symmetric case this translates to a nested loop where the algorithm checks for and stores the combination of $N_{\{\text{PSV};\text{SH}\}}$ that results in the smallest error δ_{IC} .

Convergence

Naturally, it is interesting to see how quickly the algorithm converges. To demonstrate this, the error analysis, as described above, is run once to get the response to a vertical force and a moment on the y -axis, allowing for a maximum of 10 and 20 iterations respectively. The error analysis is set-up to start from the maximum available PSV-modes and 400 SH-modes and decreasing with increments of $dN_{\text{SH}} = 50$ and $dN_{\text{PSV}} = 10$. The

⁵ Tip for optimization of the model: Currently the user can set the increment-size $dN_{\{\text{PSV};\text{SH}\}}$ and an upper and lower limit for $N_{\{\text{PSV};\text{SH}\}}$ which is looped through to look for the ideal combination of $N_{\{\text{PSV};\text{SH}\}}$. The behaviour of the error in relation to $N_{\{\text{PSV};\text{SH}\}}$ can be studied per frequency, so that when a trend is visible this can be implemented in the algorithm.

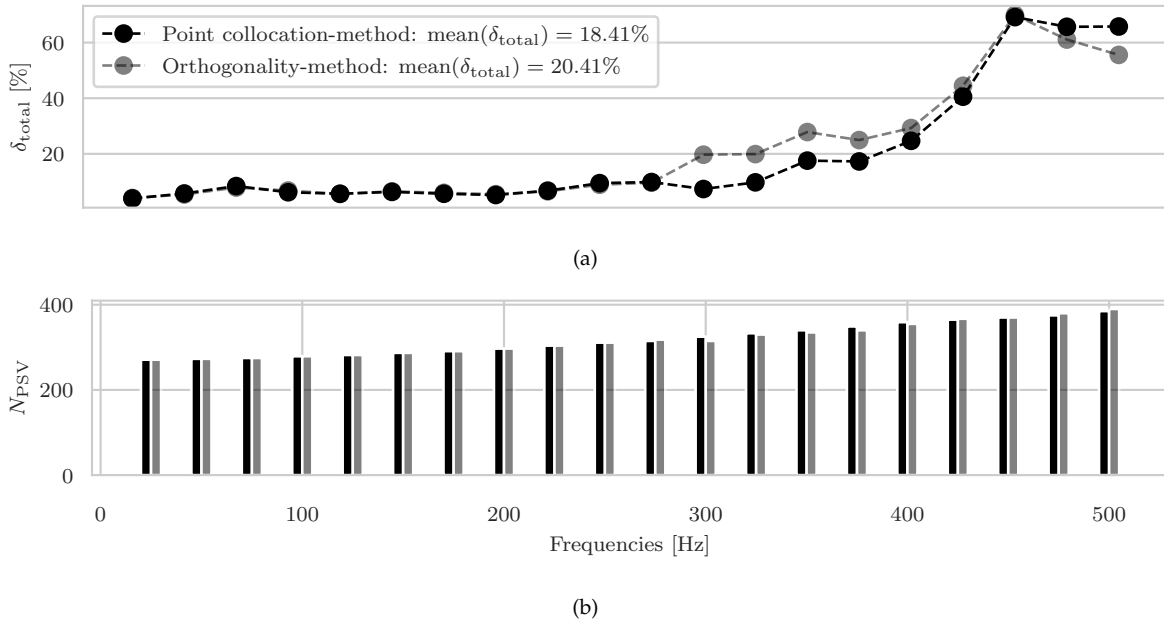


Figure 4.4: (b) The ideal number of modes N_{PSV} for the response to a uniform vertical force and (a) the corresponding error

threshold for both analysis was set to $\delta_{\text{total}} \leq 10\%$. From [fig. 4.5](#) it can be concluded that the higher frequencies have trouble meeting the threshold with this set-up. For the higher order responses refining the step-size dN_{SH} would result in better convergence, as the solution seems to converge drastically for high numbers of SH-modes. One should be critical of running the algorithm for more iterations, since it essentially takes less and less modes into account, which doesn't bode well for a better convergence.

Last but not least, it is noticeable that the symmetric case has more difficulty converging for higher frequencies, in contrast to the 1st order response, where this difference in convergence between high and low frequencies is not directly visible.

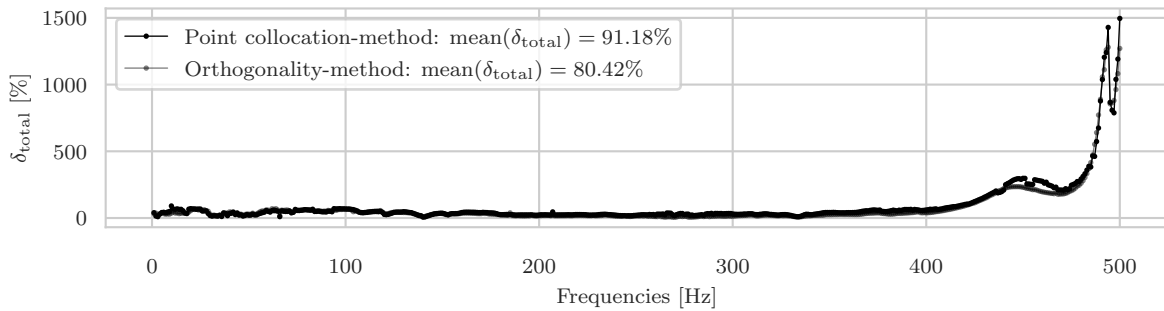


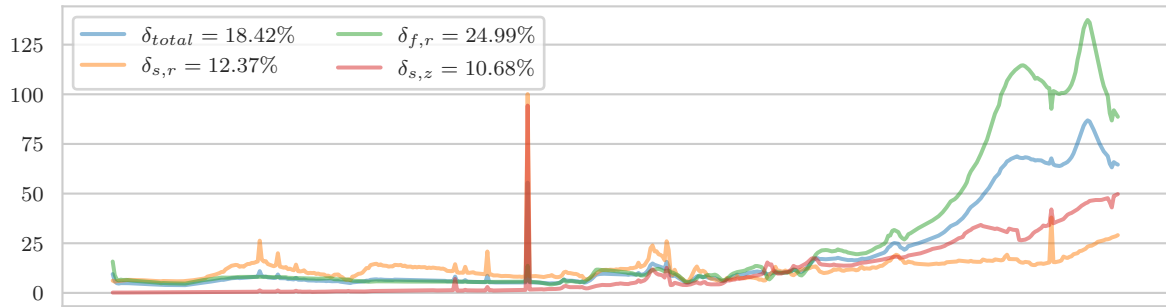
Figure 4.5: The local error per frequency for the response to a uniform horizontal force.

Error per continuity condition

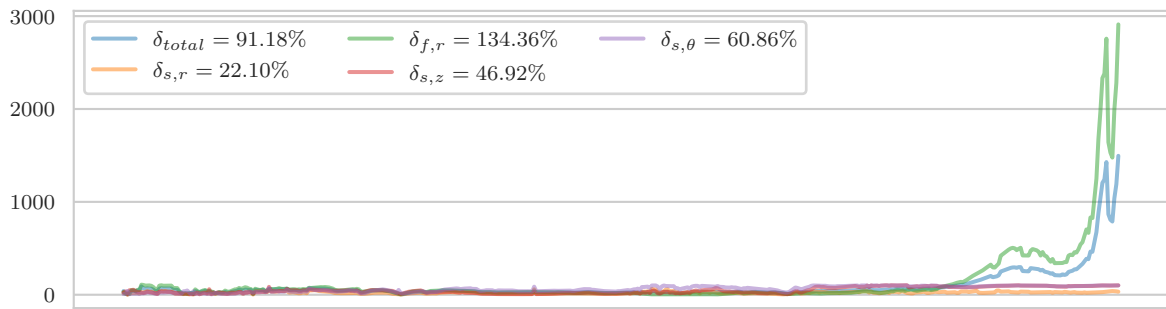
[Figure 4.6](#) illustrates the contribution to the error per continuity condition. As is evident the error in the radial direction of the fluid medium is relatively large, and this is independent of the larger weight factor $\gamma_{f,r}$.

[Figure 4.7](#) shows the mismatch in the radial direction at the pile interface ($r = R$). It is evident that the fluid displacement is loosely following the pile displacement, despite the highly oscillatory behaviour. The modal expansion to express the fluid displacement needs more modes to converge to such a function. The difficulty in convergence can thus be attributed to the lack of available evanescent modes.

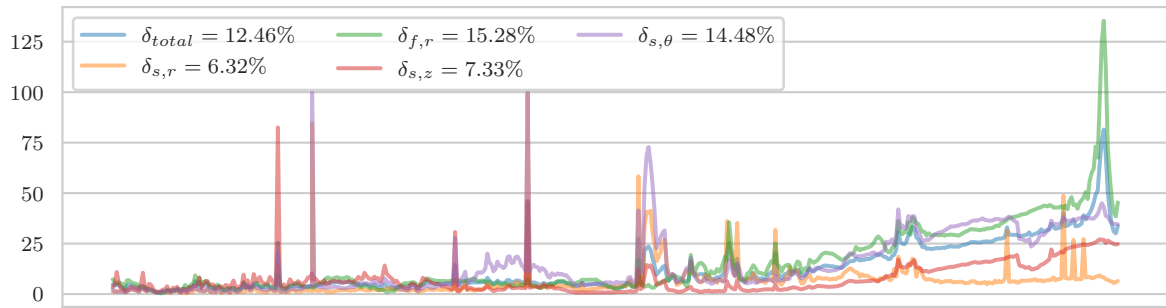
Note that both [figs. 4.6](#) and [4.7](#) show results obtained with the Point-Collocation method. The results from the Orthogonality method are omitted, since the convergence is fairly similar the



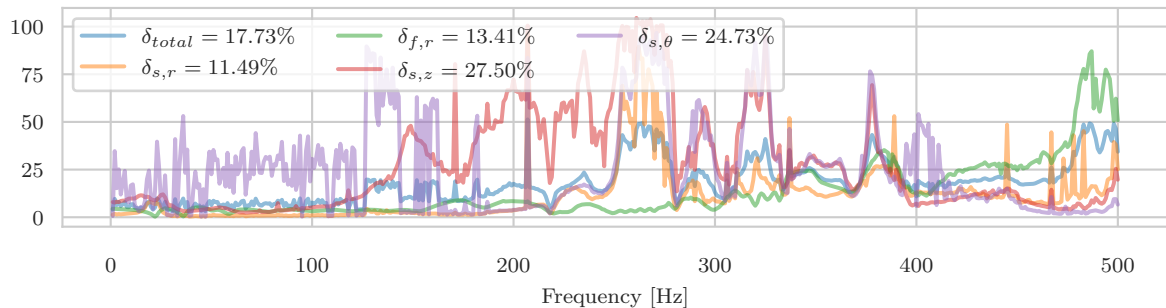
(a)



(b)



(c)



(d)

Figure 4.6: The local error per continuity condition for the response to (a) a vertical force, (b) horizontal force, (c) moment on the y -axis and (d) 2nd-order torsional moment

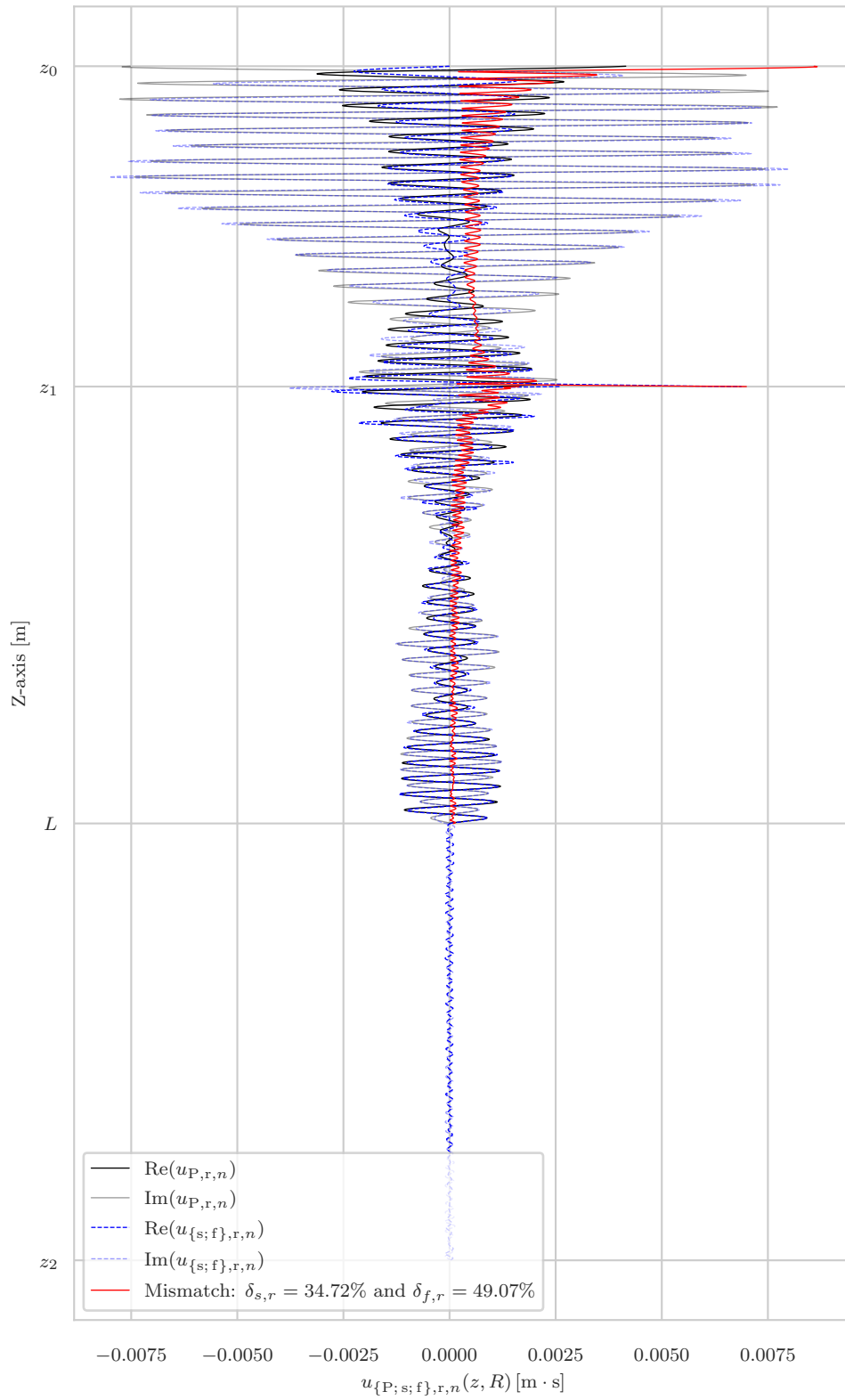


Figure 4.7: Mismatch in the radial direction for a system with the properties in table 4.1 at $f = 420$ Hz and for $N_{\{\text{PSV};\text{SH}\}} = (365, 200)$

Chapter 5

A case study

In the previous chapter, [chapter 4](#), the method for obtaining the displacement fields, that fulfill the local kinematic conditions at the interface $r = R$, [eq. \(4.1.1\)](#), is described per frequency. The response of the model in the frequency domain can thus be obtained by repeating the described routine for various frequencies. The response in time is then obtained by use of the inverse Fourier transform. Note, however, that the analysis still takes place per circular modenumber n , which describes simple forcing configurations, such as the ones depicted in [fig. 5.1](#). More complex forcing configurations can be obtained by superposition of the simple ones.

In this chapter a realistic casestudy will be conducted. The desired output and required input are mentioned thoroughly in the chapter, before discussing the obtained results.

Input: forcing configurations, spectrum and amplitudes

As mentioned earlier in [section 2.1](#), in practice it is common for higher order modes of the shell to be activated when performing symmetric impact pile-driving. A likely reason for this are imperfections in the symmetry. Such as a small eccentricity e of the point of application of the force or the action line having a small angle φ with the normal, i.e. the force isn't perfectly vertical, as shown in [fig. 5.1a](#).

Note that decomposing the aforementioned imperfect vertical configuration would lead to a combination of three basic loading configurations, namely a vertical (F_z , [fig. 5.1b](#)) and horizontal (F_x , [fig. 5.1d](#)) load due to the small angle, and a moment (M_y , [fig. 5.1c](#)) due to the eccentricity of the vertical load.

Furthermore, it is interesting to assess the response of the system to higher order torsional moments (M_z).

The geometry and material parameters are similar to the ones used in previous chapters, all values are summarized again in [table 5.1](#). Furthermore, for the sake of a clear synopsis, the different cases are shown in [table 5.2](#) together with a few pre-set properties of the system.

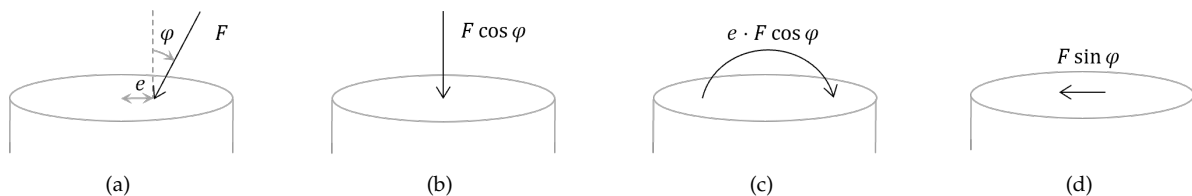


Figure 5.1: (a) An imperfect impact load F , with an eccentricity e and angle to the vertical φ is a combination of (b) a vertical load, (c) a moment on the y -axis and (d) a horizontal load.

In the following sections the response to the three basic forcing configurations is evaluated. The normalized amplitude spectrum and corresponding timesignal of the force is given in [fig. 5.2](#). Note that the forcing amplitude has been proportioned as if a vertical load of 1 MN has been placed with an eccentricity e of 3 cm and tilted by an angle φ of 3° to the normal of the pile.

Note that [fig. 5.2](#) shows distributed forces, with a normalized amplitude $\hat{f}_{\{z,0,r\}}$ of the timesignal. The amplitudes of the components of a unit force F that is tilted from the normal by 3° and eccentric by 3 cm are shown in [table 5.3](#).

Geometry		Pile		Soil		Fluid	
Pile top	0 m	ρ_P	7850 kg m^{-3}	ρ_s	1600 kg m^{-3}	ρ_f	1000 kg m^{-3}
Sea surface z_0	8 m	E	$2.1 \cdot 10^{11} \text{ kg m}^{-3}$	d_s	60 m	d_f	22 m
Sea bed z_1	30 m	R	2.5 m	c_T	149.373 m s^{-1}	c_f	1500 m s^{-1}
Pile bottom L	60 m	h	0.03 m	c_L	366.06 m s^{-1}		
Rigid boundary condition z_2	90 m	ν	0.28	E_s	$1.0 \cdot 10^8 \text{ kg m}^{-3}$		
		L	60 m	$\alpha_{\{\lambda,\mu\}}$	1 %		

Table 5.1: Properties of the system

Basic force configuration	Circular modenumber n	Force vector \hat{f}_e [N]	Force amplitude \hat{f}_0 [N]	Number of pile modes N_P
Uniform vertical load (F_z)	0	$\hat{f}_0 [1 \ 0 \ 0]^T$	$1 \cdot 10^6$	80
Uniform horizontal load (F_x)	1	$\hat{f}_0 [0 \ 1 \ 1]^T$	$1 \cdot 10^6$	100
1 st order normal moment (M_y)	1	$\hat{f}_0 [1 \ 0 \ 0]^T$	$1 \cdot 10^6$	100
2 nd order torsional moment (M_z)	2	$\hat{f}_0 [0 \ 1 \ 0]^T$	$1 \cdot 10^6$	100

Table 5.2: Pre-set properties of the basic forcing configurations, displayed in [fig. 5.1](#)

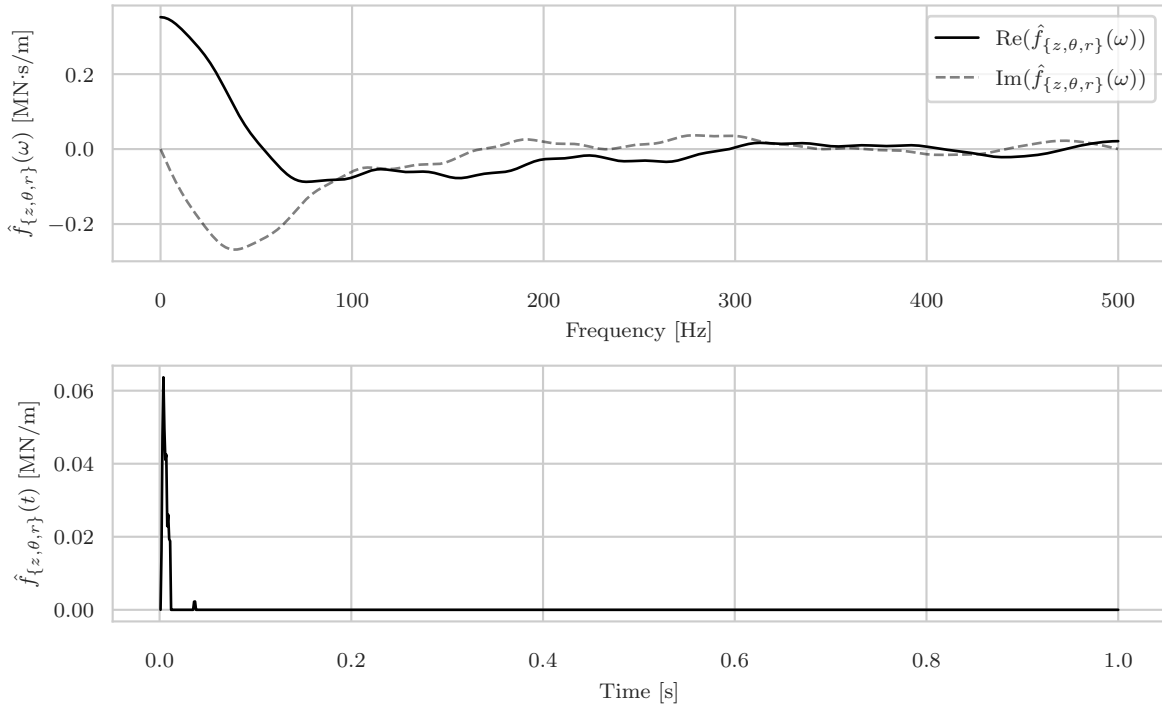


Figure 5.2: The frequency spectrum and corresponding time signal of the components of a unit impact force of 1 MN.

Output: domain, spectra and metrics

As far as the output goes one is most interested in the response in the frequency domain, since the obtainable response in the time domain is minimal when the reach of the frequency is limited to a maximum of 500 Hz with steps of 1 Hz.

As mentioned in [section 2.1](#) various noise metrics are used conform the codes issued by American National Standards Institute, in this thesis the various responses will be assessed through the sound exposure level

Force	$\hat{f}_{z,\max}$ MN/m	$\hat{f}_{\theta,\max}$ MN/m	$\hat{f}_{r,\max}$ MN/m
Vertical unit force	-	-	0.06366
Vertical component	-	-	0.06357
Horizontal component	0.00333	0.00333	-
Moment component (incl. φ)	-	-	0.01528
Moment component (excl. φ)	-	-	0.01526

Table 5.3: The amplitudes of the force spectrum of a unit force and the forces per component of an imperfect impact load.

$$\text{Note } \hat{f}_{\{z,\theta,r\},\max} = \max(\hat{f}_{\{z,\theta,r\}}(t))$$

(SEL, eq. (5.0.2)) and the zero-to-peak pressure level (L_{peak} , eq. (5.0.3)). Furthermore, the fluid pressure is assessed through the sound pressure level (SPL, eq. (5.0.1))

$$\text{SPL} = 20 \cdot \log_{10} \left(\frac{1}{2} \sqrt{2} \frac{|\hat{p}_f(r, \theta, z, \omega)|}{10^{-6}} \right) \quad \text{in} \quad \text{dB re } 1 \mu\text{Pa s} \quad (5.0.1)$$

$$\text{SEL} = 10 \log_{10} \left(\frac{1}{t_0} \int_{t_5}^{t_{95}} \frac{p_f^2(r, \theta, z, t)}{10^{-12}} dt \right) \quad \text{in} \quad \text{dB re } 1 \mu\text{Pa}^2 \text{ s} \quad (5.0.2)$$

$$L_{\text{peak}} = 20 \log_{10} \left(\frac{|p_{\text{peak}}(r, \theta, z)|}{10^{-6}} \right) \quad \text{in} \quad \text{dB re } 1 \mu\text{Pa} \quad (5.0.3)$$

$$\text{with} \quad p_{\text{peak}}(r, \theta, z) = \max(p_f(r, \theta, z, t))$$

5.1 Basic forcing configurations

5.1.1 A vertical force

First a perfectly symmetric driving force F_x is assumed at the top of the pile, with a magnitude of 0.9986 MN, conform the gradient of [fig. 5.2](#).

Local mismatch

Before assessing the post-processed data the local error at $r = R$ is shown per frequency, to illustrate any discrepancies in the modal amplitudes.

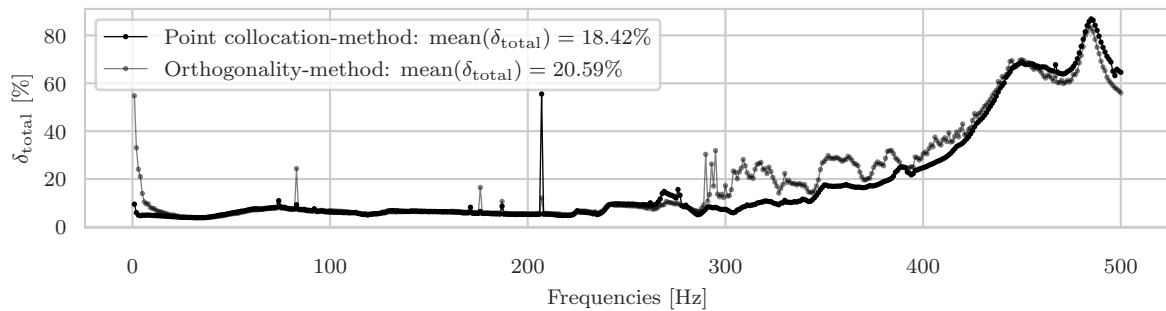


Figure 5.3: Local mismatch error δ_{Total} in the response to a vertical force per frequency

Amplitude spectra

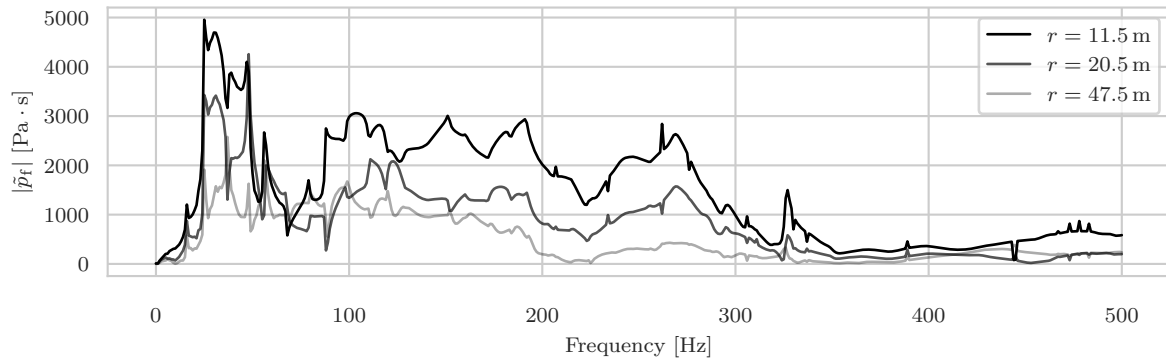


Figure 5.4: The amplitude spectra of the fluid pressure at a depth of 13.5 m at various distances from the pile.

- In [fig. 5.4](#) two separate bands of peaks can be distinguished, namely the peaks between 20 and 50 Hz and the set of peaks between 80 and 300 Hz.
- In the frequency spectra of both the radial ([fig. 5.5b](#)) and vertical ([fig. 5.5d](#)) soil displacements a peak occurs around 30 Hz.
- In the frequency spectrum of the vertical fluid displacement ([fig. 5.5c](#)) a single significant peak occurs at ≈ 10 Hz, contrary to the spectrum of the radial fluid displacement ([fig. 5.5a](#)), where two separate peaks can be distinguish at 10 and 30 Hz respectively. The latter corresponds with the peaks found in the spectra of the soil displacements.

Time signals

- [Figure 5.6](#) shows that the fluid pressure behaves conform the attenuation law, i.e. the amplitude of the peak reduces for larger horizontal distances r . Furthermore, the delay in the arrival time is clearly visible for larger horizontal distances.

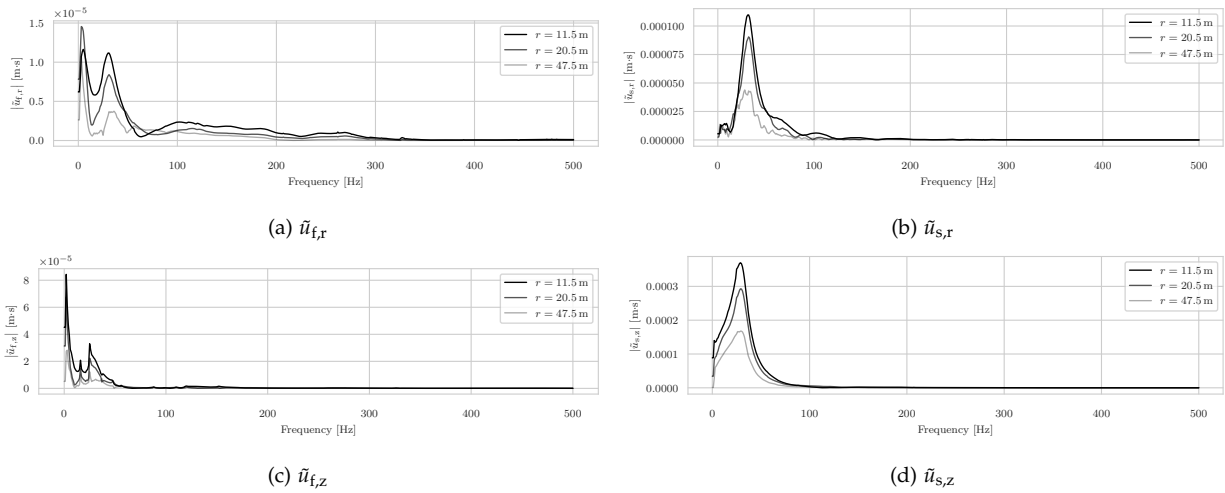


Figure 5.5: The amplitude spectra of the (a, c) fluid and (b, d) soil displacements at a depth of 13.5 m and 32 m respectively.

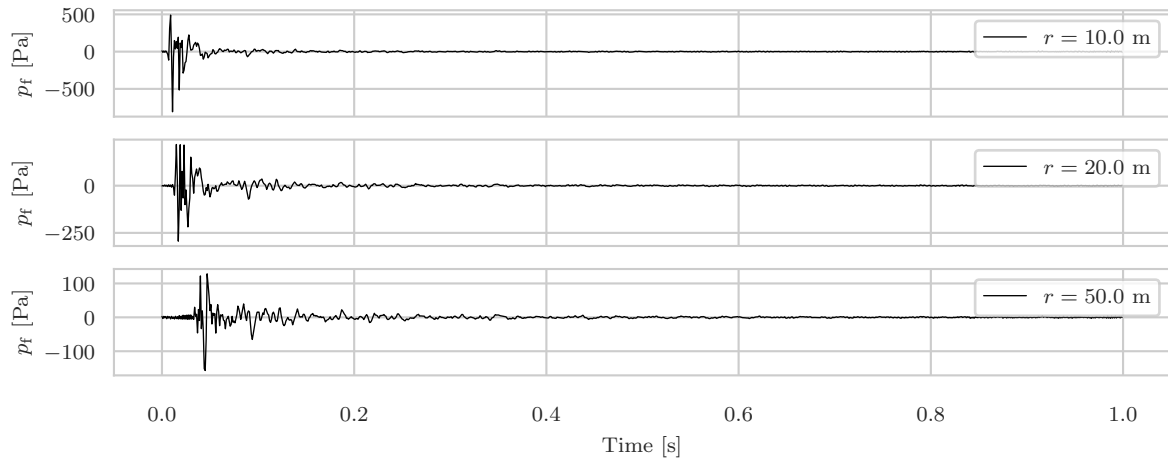


Figure 5.6: The time signal of the fluid pressure at various distances from the pile measured at a depth of 3 m below the sea-surface.

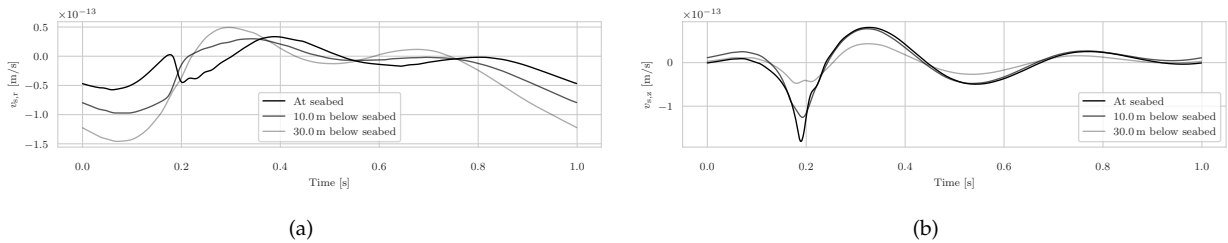


Figure 5.7: The unfiltered time signal of the (a) azimuthal and (b) vertical velocity in the soil at various depths, measured at a distance of 50 m from the pile

- In [figs. 5.7a](#) and [5.7b](#) the time signals of the radial and vertical velocities in the soil appear to be governed by just a few frequencies, which follows from the almost perfect periodic graph.
- [Figures 5.8a](#) and [5.8b](#) show the filtered timesignals. The filtered graphs are obtained by replacing the highest peaks in [figs. 5.5b](#) and [5.5d](#) by the value of the second highest peak. The same operation is used for filtered time signals shown further along.

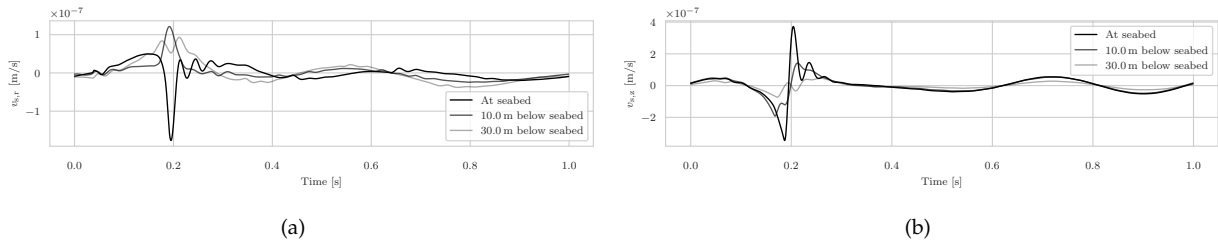


Figure 5.8: The filtered time signal of the (a) azimuthal and (b) vertical velocity in the soil at various depths, measured at a distance of 50 m from the pile. (Note: the highest peak has been replaced by the next highest peak of the signal)

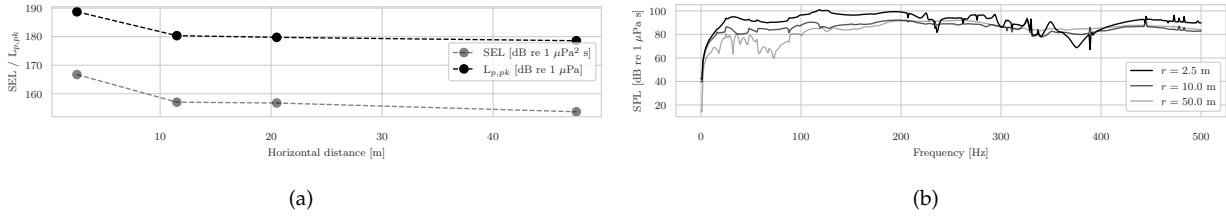


Figure 5.9: (a) The SEL and L_{peak} values along the horizontal axis and (b) SPL spectrum at various horizontal distances from the pile.

Noise metrics

Contour plots

- [Figure D.5](#) shows a pressure wave in the fluid that propagates quicker than the shockwave in the soil. This is clearly visible in the plot for $t = 60$ ms. Where the fluid pressure is back to an almost complete equilibrium, while the displacementnorm still appears to be at 20 % of the maximum value.

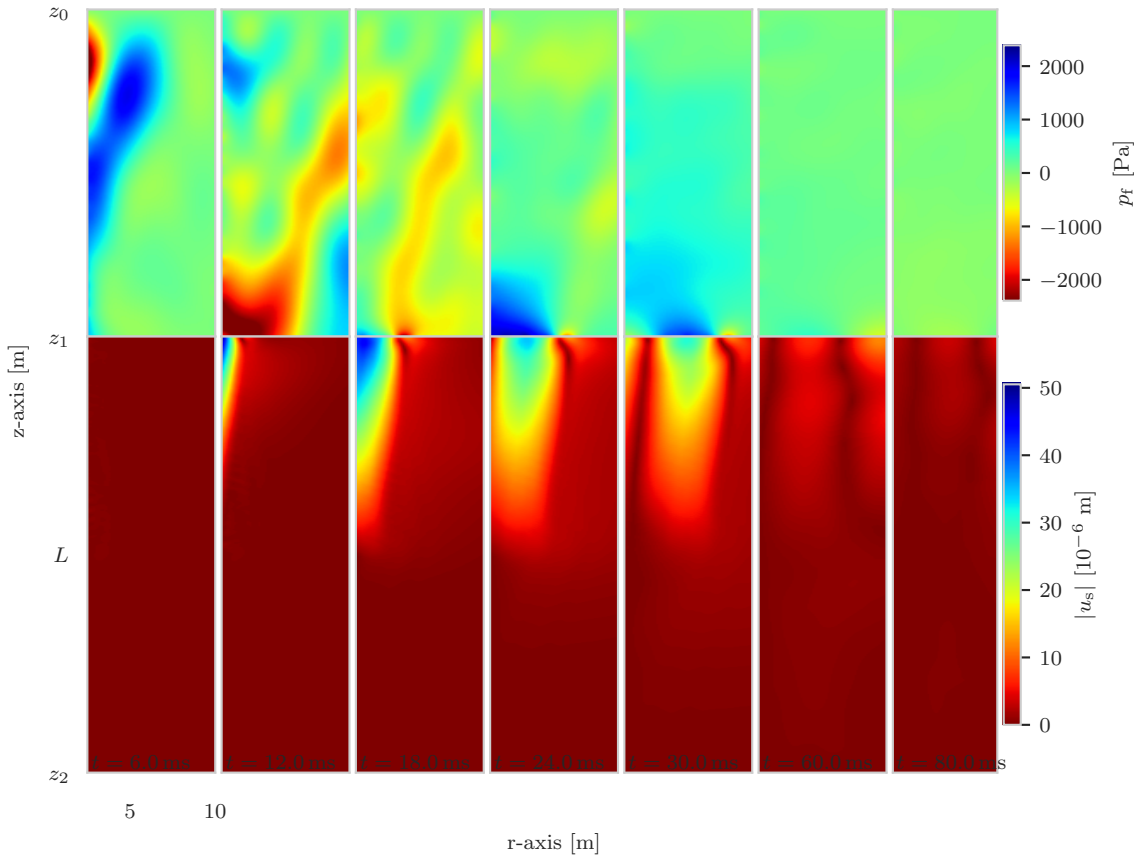


Figure 5.10: Fluid pressure and displacement norm of the soil resulting from an uniform vertical load at $t = 6, 12, 18, 24, 30, 60$ and 80 ms respectively (Note: the colour bars do not convey the maximum values in the contour plots)

5.1.2 A horizontal force

Similar to the horizontal force F_x , the moment M_y occurring due to the eccentricity of the vertical force has a rather small amplitude of 0.03 MN m, thus significantly less energy is put into the system from this specific component of the imperfect force, this should be taken into consideration when considering the total response of the system.

Local mismatch

Before assessing the post-processed data the local error at $r = R$ is shown per frequency, to illustrate any discrepancies in the modal amplitudes. Note that

Amplitude spectra

- The graph in [fig. 5.13](#) shows that the fluid pressure is activated mostly at the frequencies between 150 and 300 Hz. Furthermore, the maximum amplitude of the pressure is approximately 475 Hz, which
- [Figures 5.14a, 5.14c and 5.14e](#) show that the unfiltered amplitude spectra of the fluid displacement all contain a single emphasized peak at 30 Hz, which is likely to be caused by a discrepancy in the obtained amplitudes C_{PSV} . After filtering the highest peak of the amplitude spectra, the graphs in [figs. 5.15a, 5.15c and 5.15e](#) show a more common development of the frequency spectrum in the fluid-medium.
- The same peaks appear in the unfiltered amplitude spectra of the soil displacements, [figs. 5.14b, 5.14d and 5.14f](#), however, the height of the first peak doesn't minimize the complete spectrum like it does for the fluid spectra.
- The unfiltered graphs in [figs. 5.15a and 5.15e](#) show that, similar to the fluid pressure in [fig. 5.13](#), the frequencies 150 to 300 Hz do influence the fluid displacements in the radial and vertical direction, while

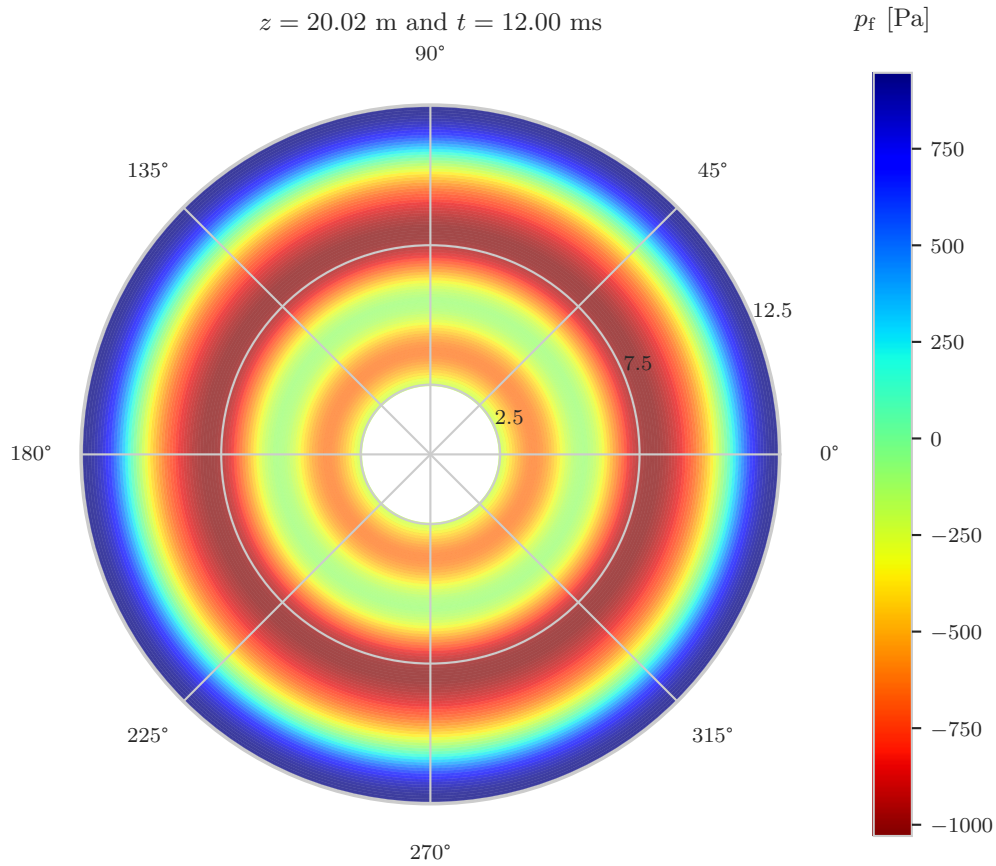


Figure 5.11: A top view of the fluid pressure (fig. D.5) at a depth of $z = 20$ m due to an uniform vertical load at $t = 12$ ms.

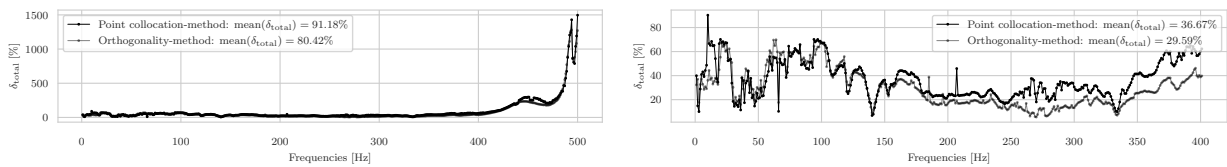


Figure 5.12: Local mismatch error δ_{Total} in the response to a horizontal force per frequency.

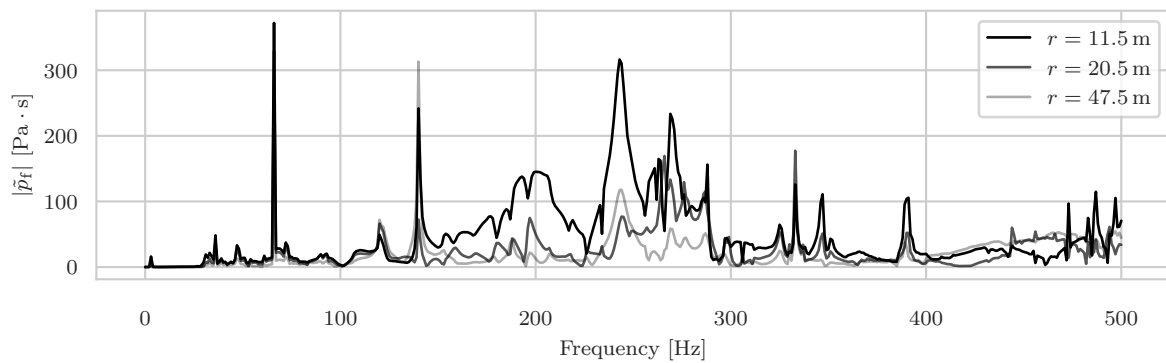


Figure 5.13: The amplitude spectra of the fluid pressure at a depth of 13.5 m.

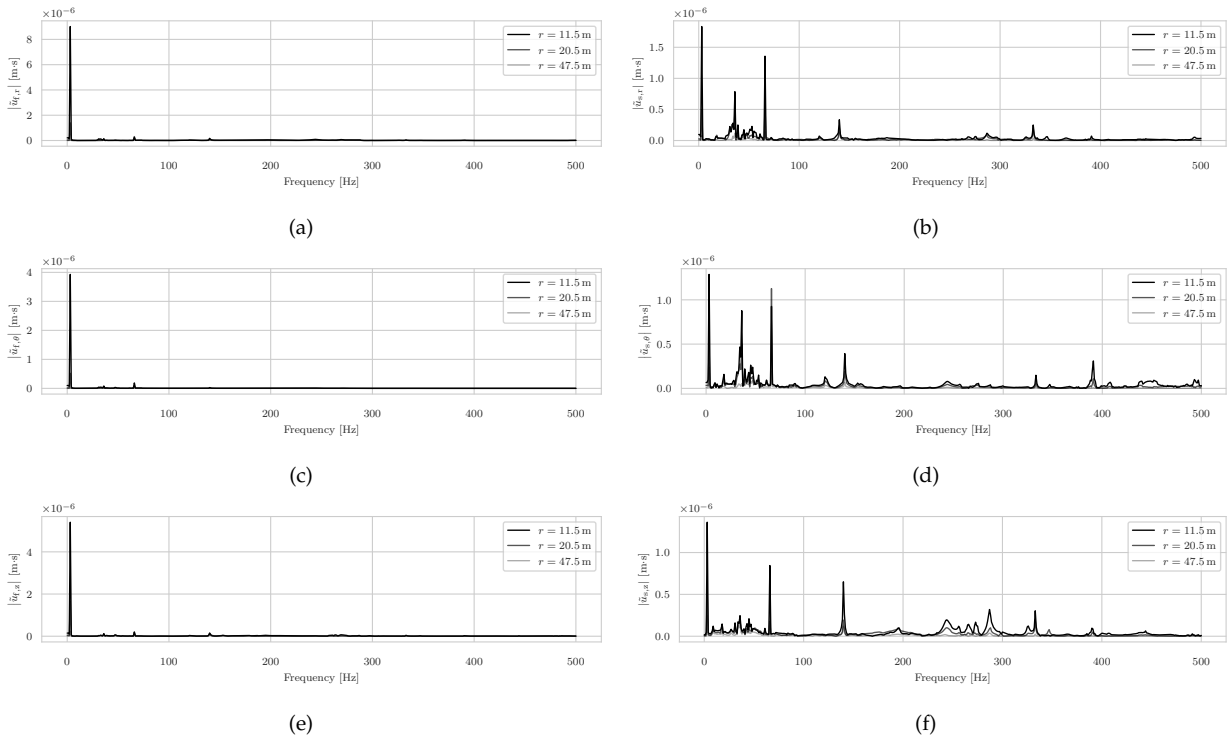


Figure 5.14: The unfiltered amplitude spectra of the (a,c,e) fluid and (b,d,f) soil displacements at a depth of 13.5 m and 32 m respectively.

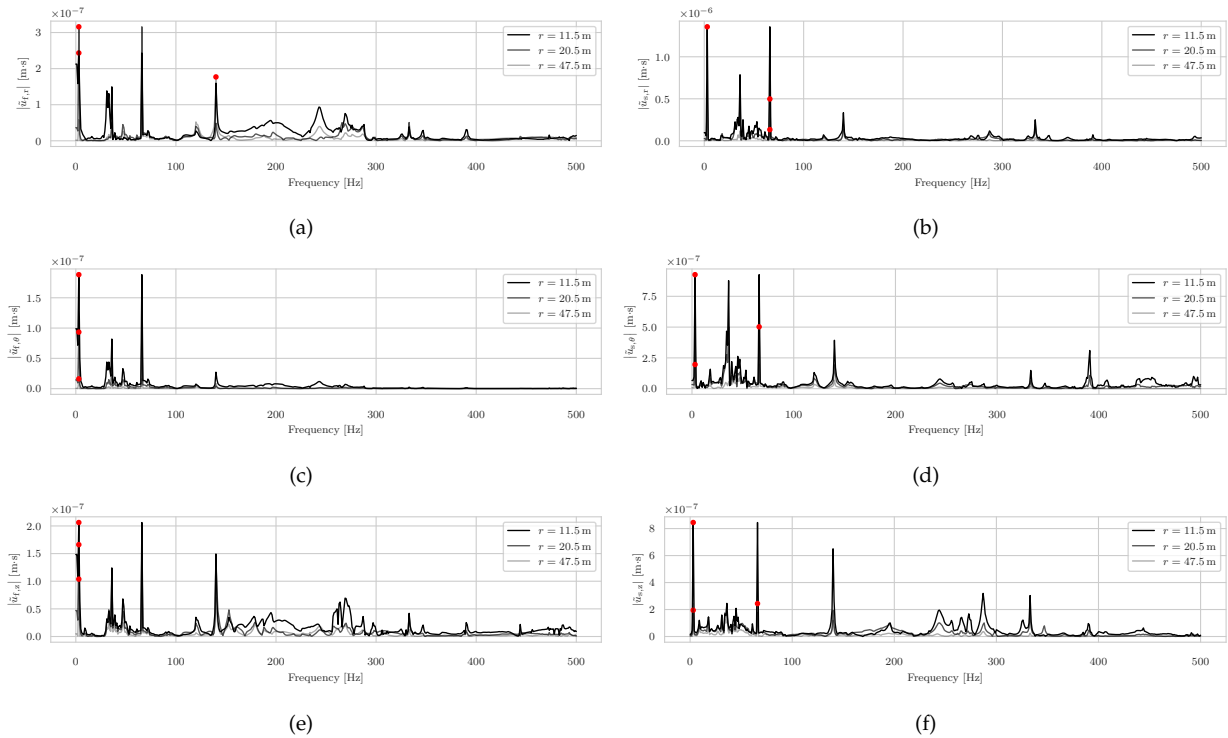


Figure 5.15: The filtered amplitude spectra of the (a,c,e) fluid and (b,d,f) soil displacements at a depth of 13.5 m and 32 m respectively. (Note: the highest peak has been replaced by the next highest peak of the signal)

for the azimuthal displacement [fig. 5.15c](#) the amplitudes at these frequencies are negligible compared to those at the lower frequencies.

Time signals

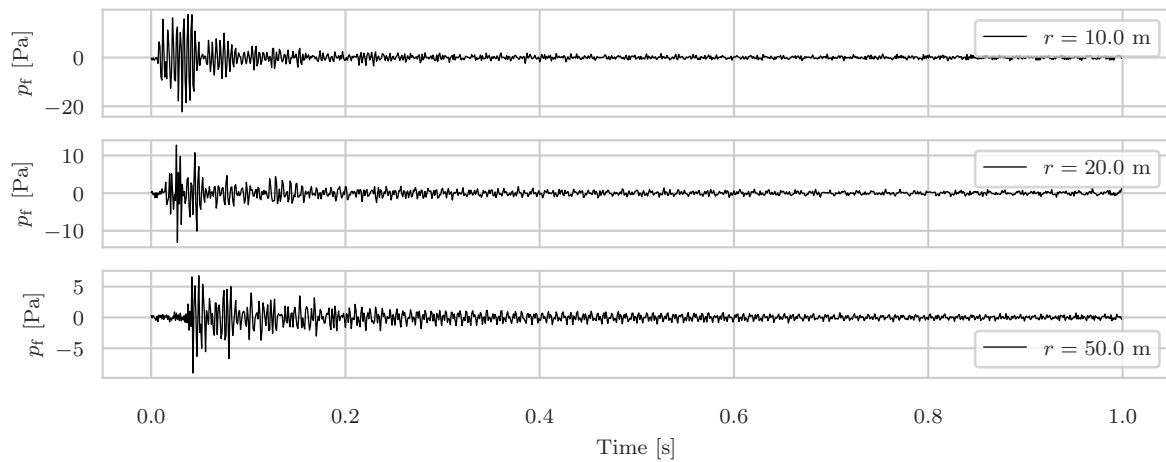


Figure 5.16: The time signal of the fluid pressure at various distances from the pile measured at a depth of 3 m below the seafloor.

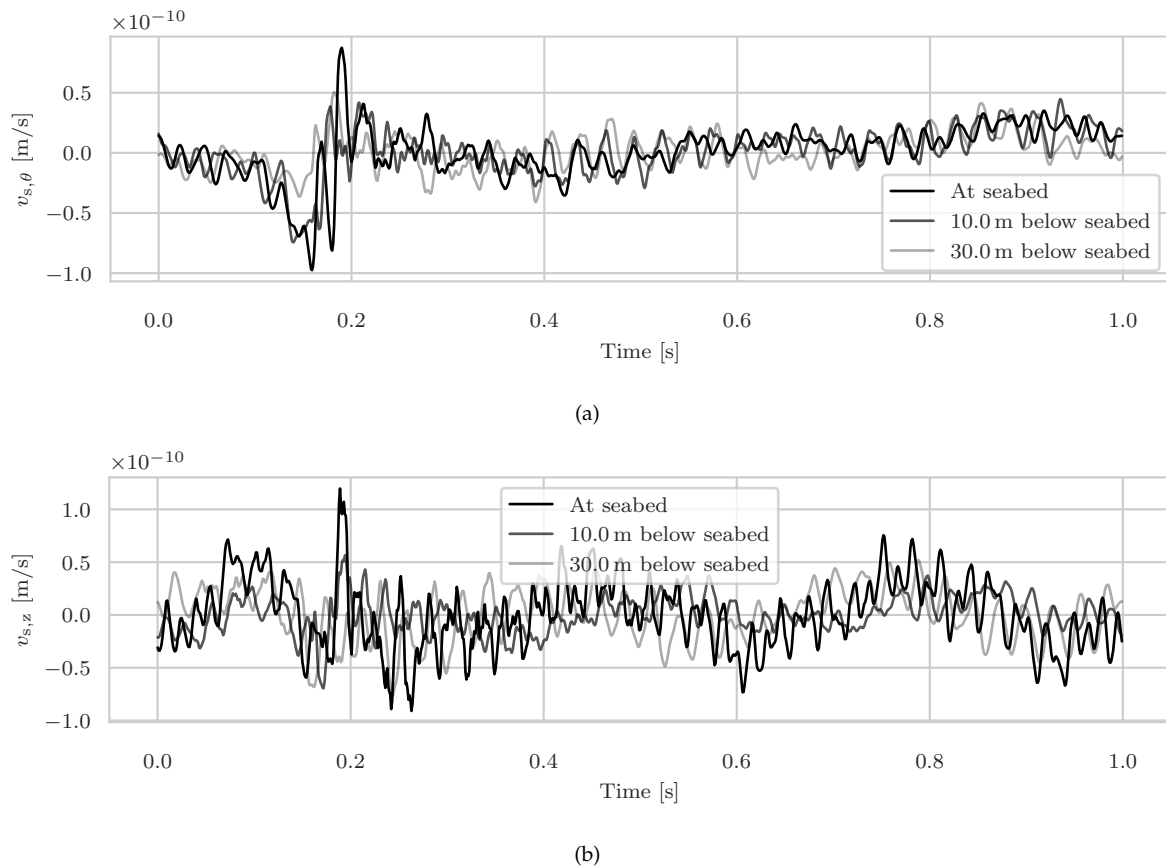


Figure 5.17: The time signal of the (a) azimuthal and (b) vertical velocity in the soil at various depths, measured at a distance of 50 m from the pile. (Note: the highest peak has been replaced by the next highest peak of the signal)

- The graphs in [fig. 5.13](#) show a slight peak at the time of impact, which is delayed in time the further we are from the pile. Unlike the first two graphs, a small damping can be noticed in the third graph at $r = 50$ m.

- Despite the oscillatory behaviour of the graphs in [figs. 5.17a](#) and [5.17b](#) a gradient similar to the [figs. 5.8a](#) and [5.8b](#) is vaguely visible, especially the peak around $t = 2$ ms.
- [fig. 5.17b](#)

Noise metrics

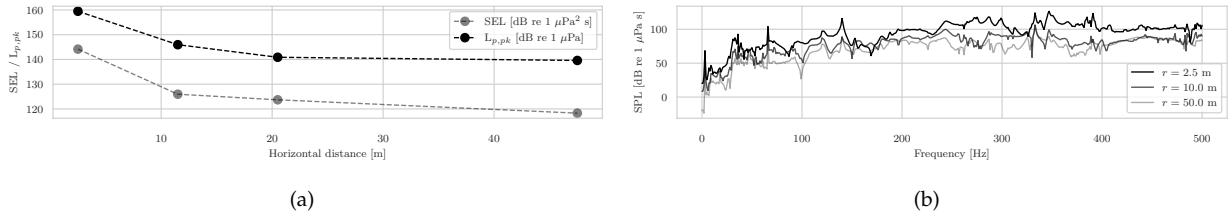


Figure 5.18: (a) The SEL and L_{peak} values along the horizontal axis and (b) SPL spectrum at various horizontal distances from the pile.

Contour plots

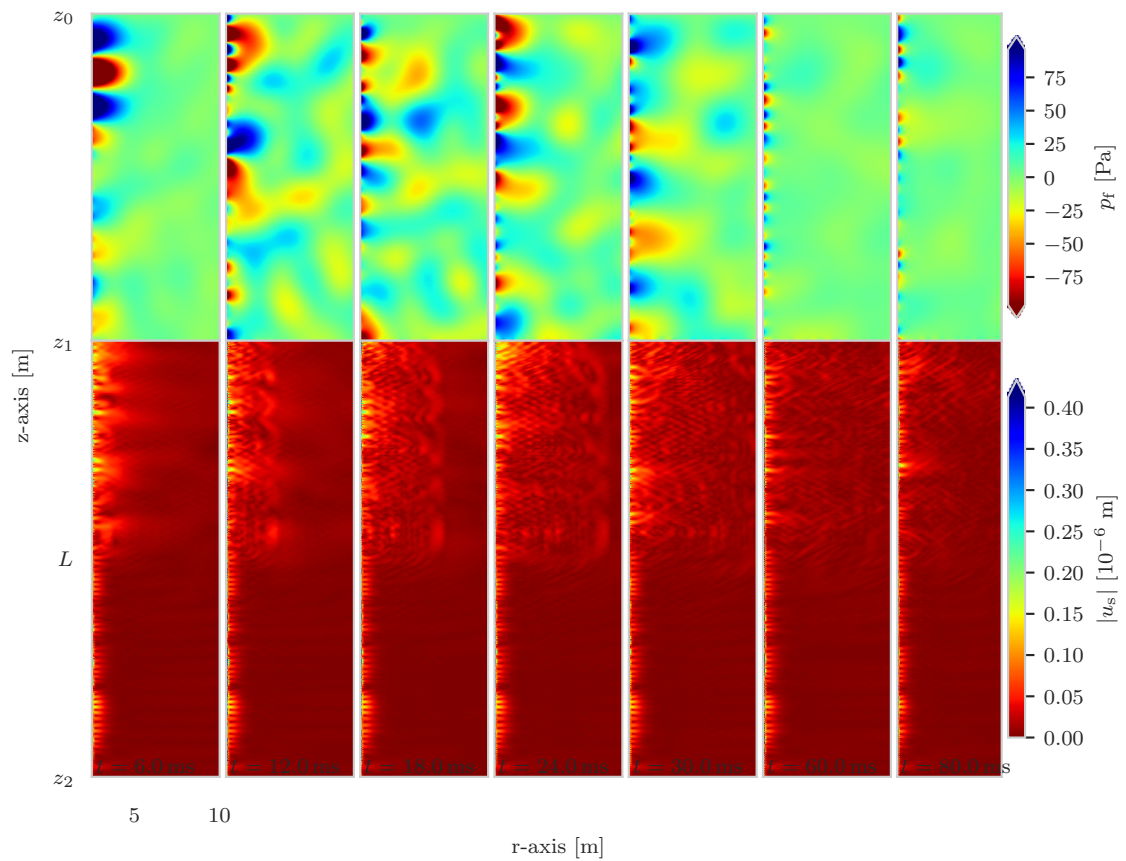


Figure 5.19: Fluid pressure and displacement norm of the soil resulting from an uniform horizontal load at $t = 6, 12, 18, 24, 30, 60$ and 80 ms respectively (Note: the colour bars do convey 33% of the maximum value in the contour plots)

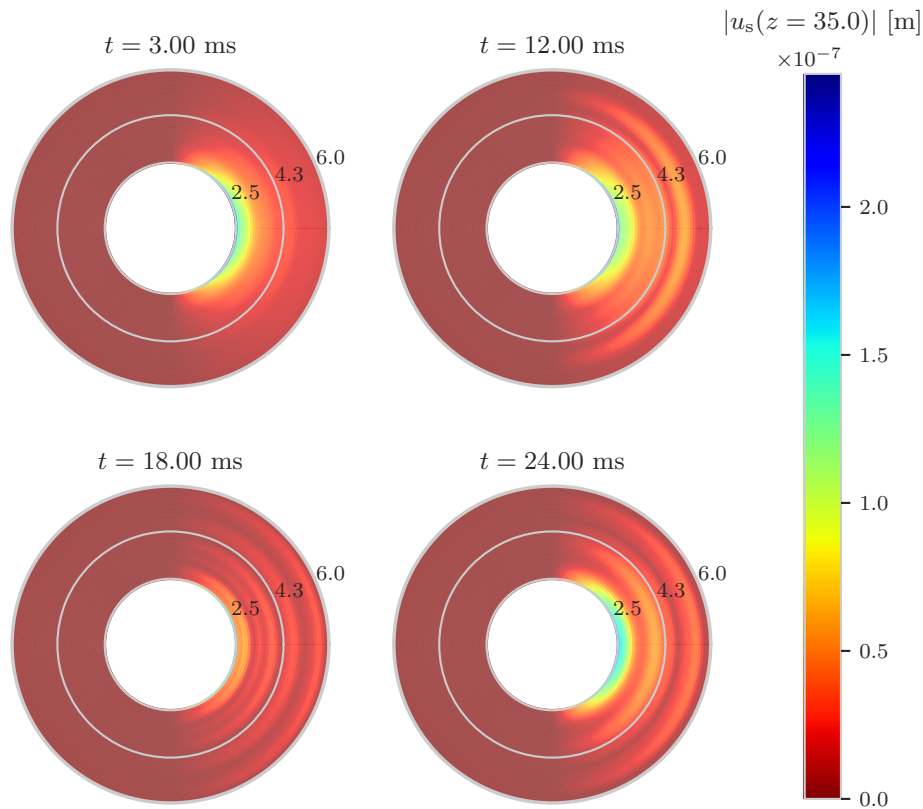


Figure 5.20: A top view of the displacement norm in the soil (fig. D.7) at a depth of $z = 35$ m due to an uniform vertical load at $t = 3, 12, 18$ and 24 ms.

5.1.3 A moment on the y -axis

Similar to the horizontal force F_x , the moment M_y occurring due to the eccentricity of the vertical force has a rather small amplitude of 0.03 MN m, thus less energy is put into the system from this specific component of the imperfect force, this should be taken into consideration when considering the response of the system.

Local mismatch

Before assessing the post-processed data the local error at $r = R$ is shown per frequency, to illustrate any discrepancies in the modal amplitudes.

Amplitude spectra

Time signals

- On first sight the time signals shown in fig. 5.25 show no damping as time goes on. But for larger horizontal distances ($r = 50$ m) there clearly appears to be some sort of damping in time. Furthermore, the time of arrival is difficult to determine via these figures. However, one can see that for greater distance the damping can be seen.
- The frequency spectra of the displacements in the fluid and soil (fig. 5.23) caused by a moment on the y -axis are governed by just one or two frequencies, therefore, the time signals of the accompanying velocities are almost perfect sines. The filtering process (fig. 5.24) could not change this, without filtering too many peaks from the spectra. For this reason, the velocities are not shown in this part.

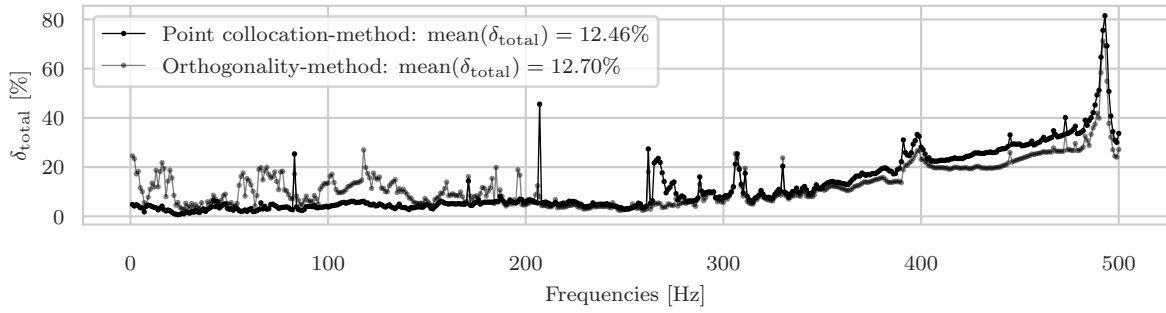


Figure 5.21: Local mismatch error δ_{Total} in the response to a moment on the y -axis per frequency

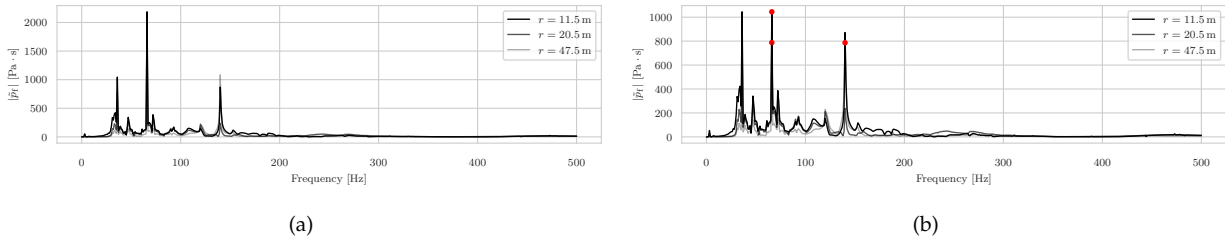


Figure 5.22: The (a) unfiltered and (b) filtered amplitude spectra of the fluid pressure at a depth of 13.5 m. (Note: the highest peak has been replaced by the next highest peak of the signal)

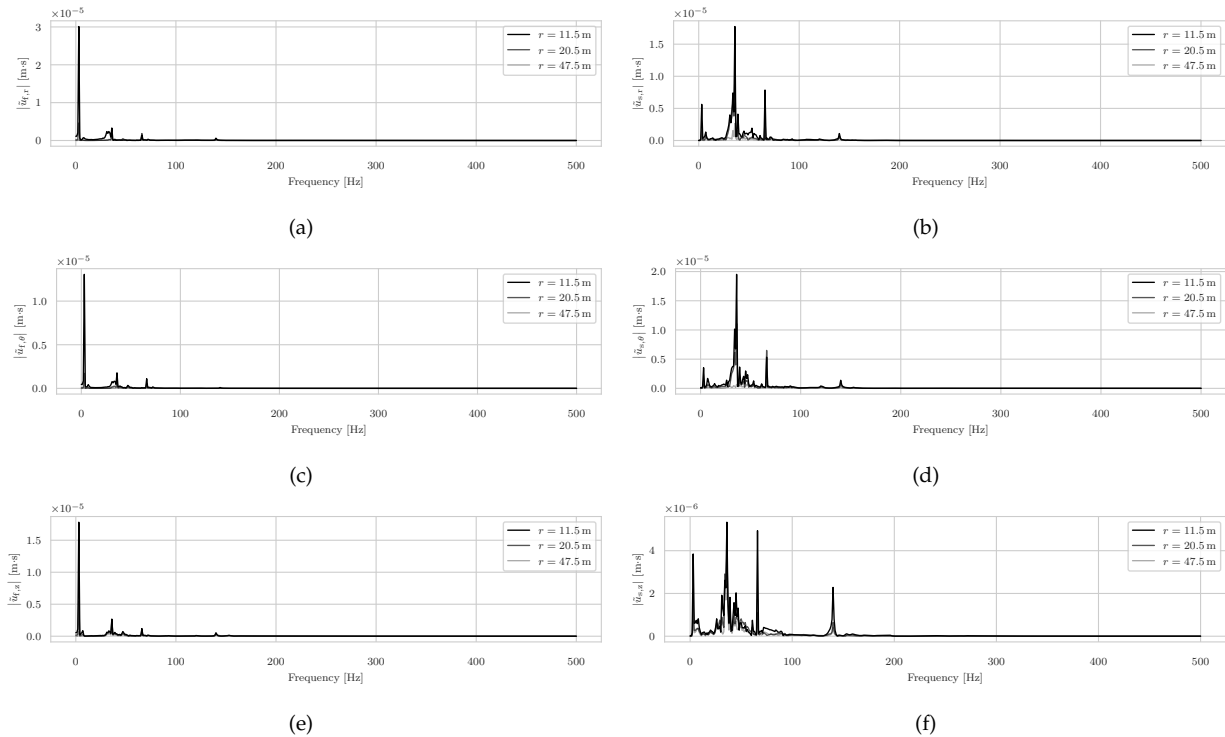


Figure 5.23: The unfiltered amplitude spectra of the (a,c,e) fluid and (b,d,f) soil displacements at a depth of 13.5 m and 32 m respectively.

Noise metrics

Contour plots

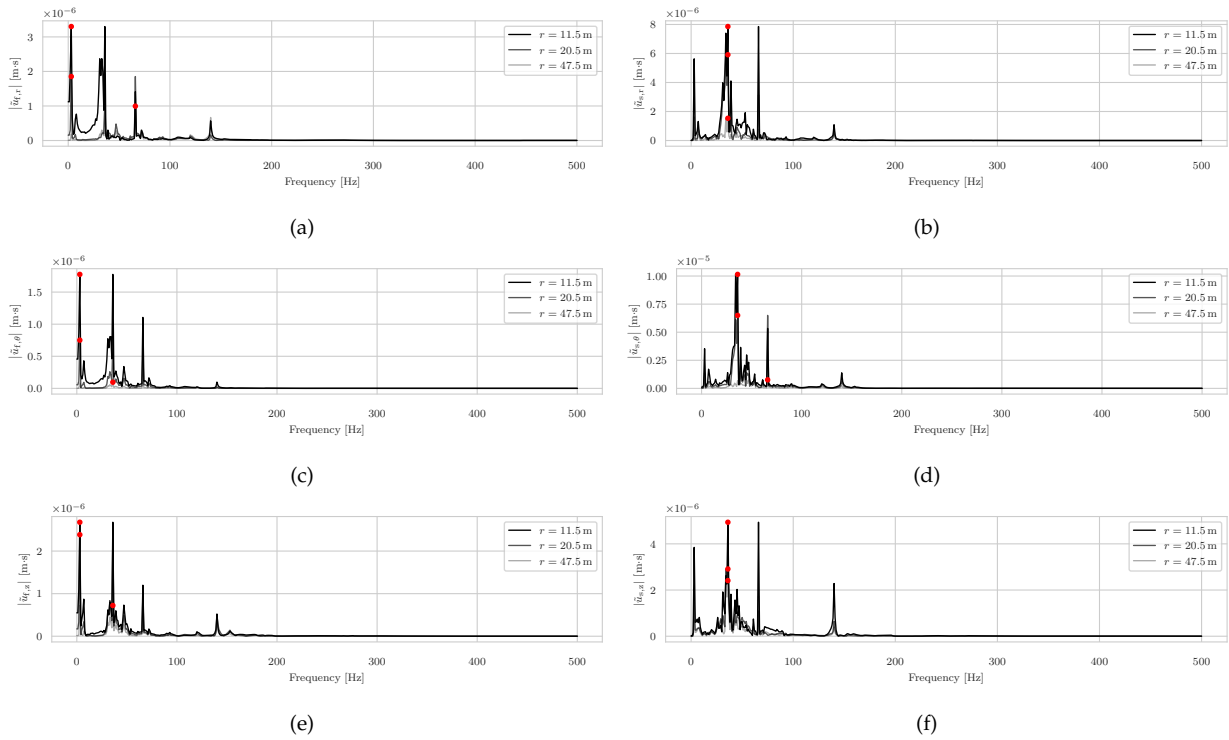


Figure 5.24: The unfiltered amplitude spectra of the (a,c,e) fluid and (b,d,f) soil displacements at a depth of 13.5 m and 32 m respectively. (Note: the highest peak has been replaced by the next highest peak of the signal)

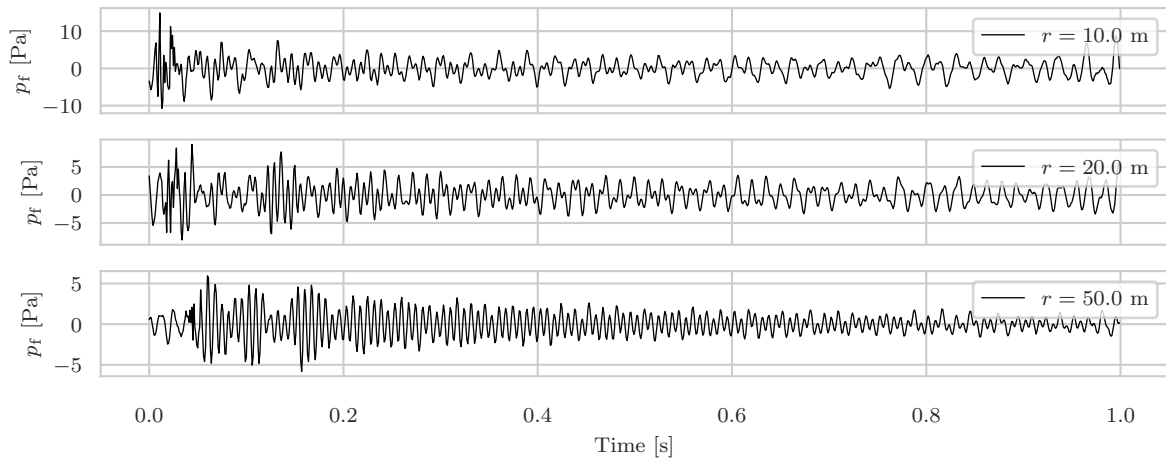


Figure 5.25: The time signal of the fluid pressure at various distances from the pile measured at a depth of 3 m below the seasurface.

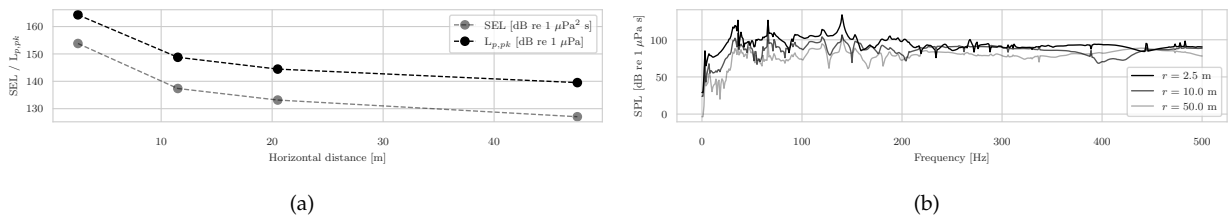


Figure 5.26: (a) The SEL and L_{peak} values along the horizontal axis and (b) SPL spectrum at various horizontal distances from the pile.

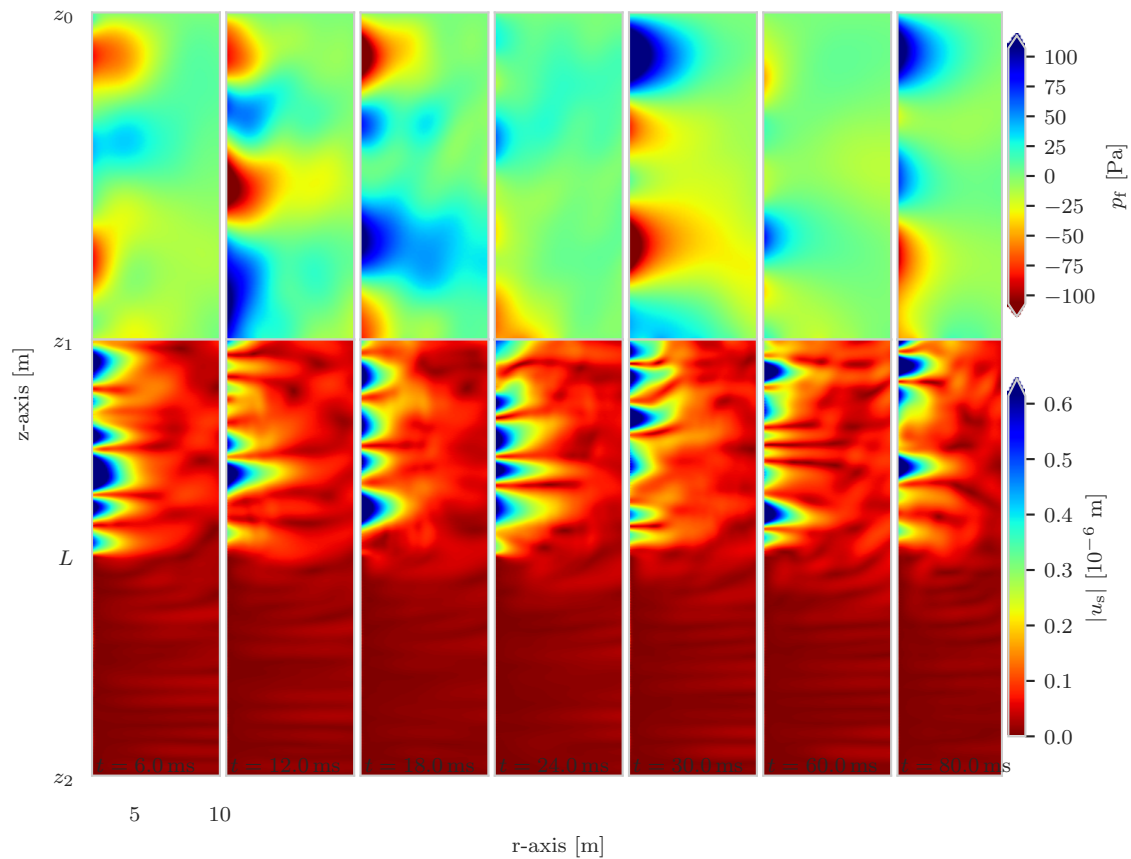


Figure 5.27: Fluid pressure and displacement norm of the soil resulting from a moment on the y -axis at $t = 6, 12, 18, 24, 30, 60$ and 80 ms respectively (Note: the colour bars do convey 50 % of the maximum value in the contour plots)

5.2 Imperfect vertical force

The response of eccentric and tilted forces (and combinations thereof) consists of the same forcing components, with slight differences in the amplitudes, the results turn out to be very similar because of this. Thus the section is shortened and will only contain the results of an eccentric force and an eccentric force that is also slightly tilted. This way all possible components are shown in the graphs.

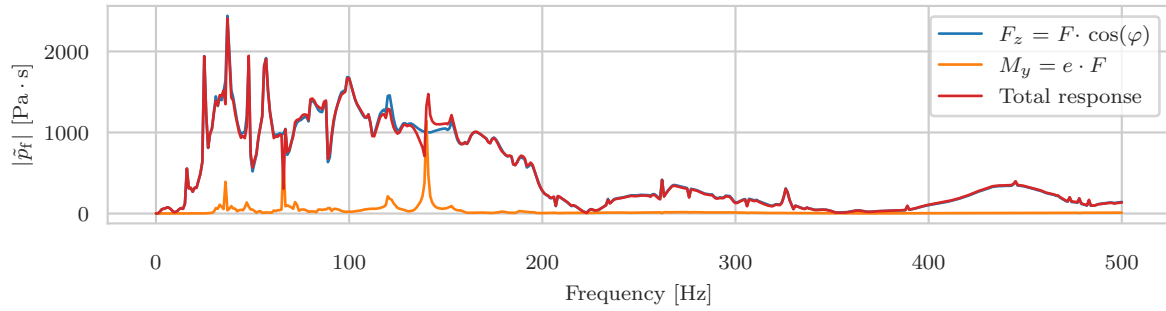
Amplitude spectra

- [fig. 5.28a](#) shows that the spectrum of the fluid pressure due to the vertical force is dominating. Only in the region between 100 and 150 Hz does the total response deviate a little bit from the response of F_z
- [fig. 5.28b](#) shows the same behaviour additional to a slight decrease and increase at $f = 250$ Hz and between 400 – 500 Hz respectively.

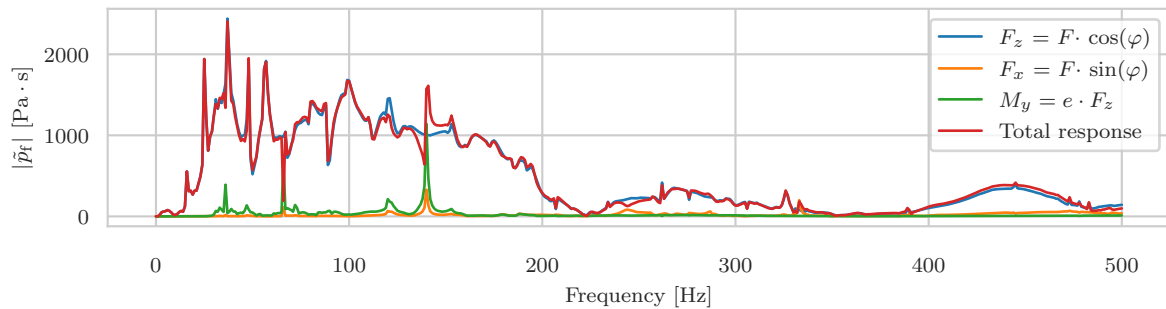
Time signals

- [fig. 5.31](#) shows that the course of the fluid pressure for an imperfect vertical force in time is almost equal to that of a perfect force, [fig. 5.4](#). Despite the deviations previously seen for a horizontal force, [fig. 5.13](#). The vertical force dominates, this is as expected when looking at the amplitudes of the forcing spectra in [table 5.3](#).

Noise metrics

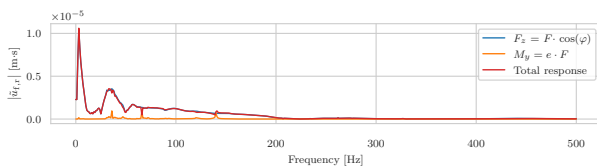


(a)

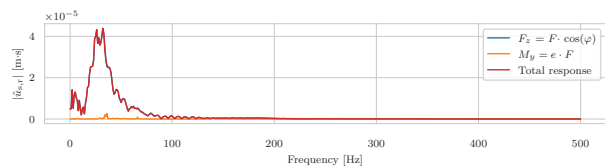


(b)

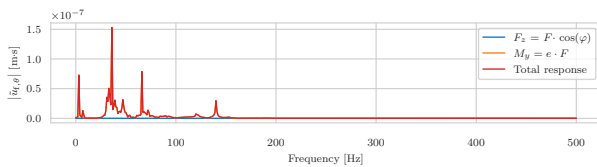
Figure 5.28: The amplitude spectra of the fluid pressure due to an eccentric (a) vertical and (b) tilted force at a depth of 13.5 m.



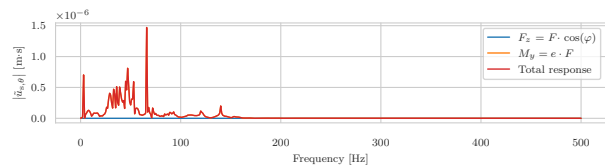
(a)



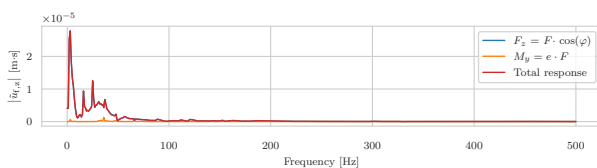
(b)



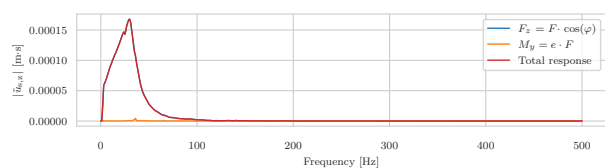
(c)



(d)



(e)



(f)

Figure 5.29: The amplitude spectra of the (a,c,e) fluid and (b,d,f) soil displacements at a depth of 13.5 m and 32 m respectively for an eccentric force. ($\varphi = 0^\circ, e = 3$ cm)

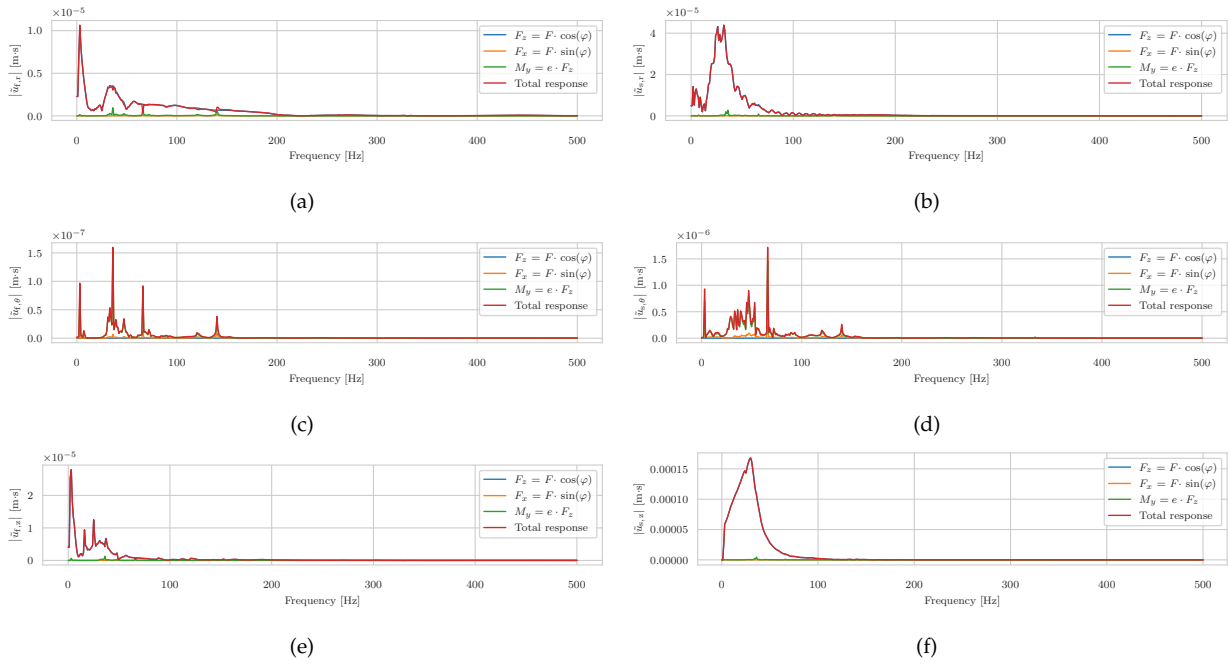


Figure 5.30: The amplitude spectra of the (a,c,e) fluid and (b,d,f) soil displacements at a depth of 13.5 m and 32 m respectively for an eccentric force. ($\varphi = 3^\circ, e = 3$ cm)

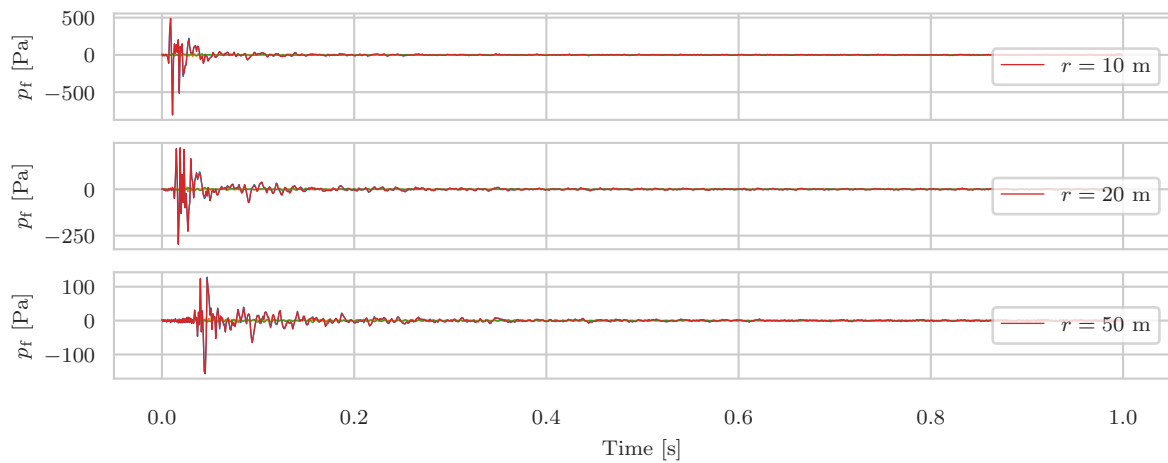
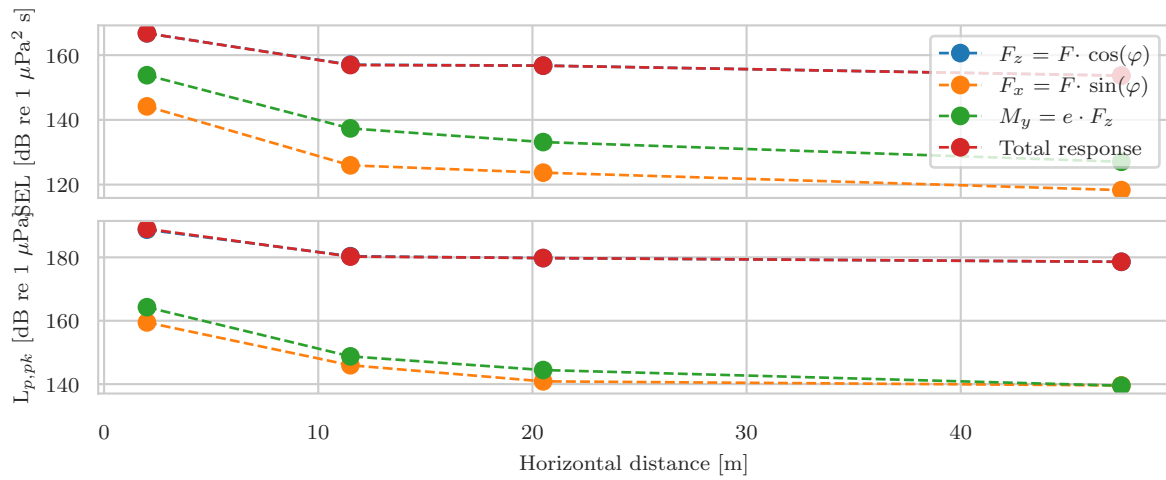
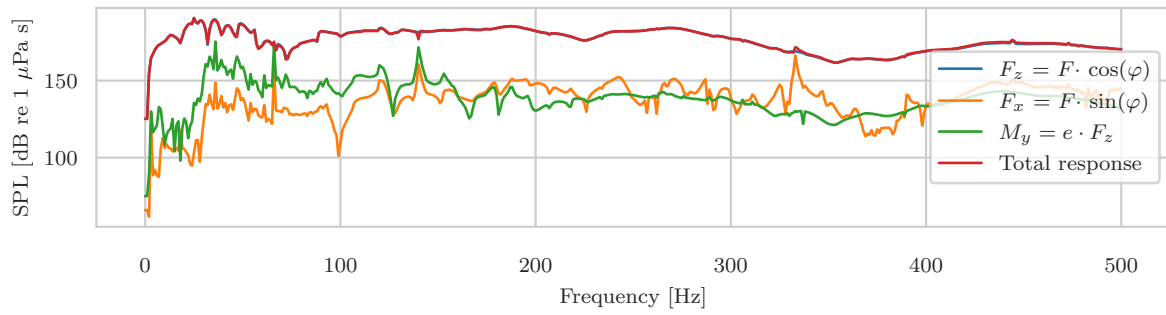


Figure 5.31: The time signal of the fluid pressure at various distances from the pile measured at a depth of 3 m below the seasurface ($\varphi = 3^\circ, e = 3$ cm).



(a)



(b)

Figure 5.32: (a) The SEL and L_{peak} values along the horizontal axis and (b) SPL spectrum at various horizontal distances from the pile.

Chapter 6

Discussion

In this chapter two separate discussions will be held. In [section 6.1](#) the methods described in [chapter 4](#) will be discussed, while [section 6.2](#) focusses on the casestudy executed in [chapter 5](#).

6.1 The method

In this section, discussion points are cited based on the findings in [chapter 4](#), where two modematching methods are derived, namely the Point-Collocation method ([section 4.3](#)) and the Orthogonality method ([section 4.2](#)). The implementation of the methods in the developed model and any numerical considerations are shed light on in [section 4.4](#).

The pile module In this work the pile is described by a circular cylindrical shell using a higher order shell theory. The shell is considered to have 5 degrees of freedom, including the two angles $\beta_{P,\{r\}}$. However, for the application at hand a lower order theory might suffice, where at least the minimum 3 degrees of freedom are considered. The pile module could easily be switched or adapted to further research the influence of the shell theory on the results of the model.

Furthermore, the truncation of the modal summation of the pile ([section 3.1.5](#)) is currently based on an impact load with an infinite amplitude (i.e. Dirac delta function), of which the frequency spectrum is a constant. Note that the excited modes might differ for a more realistic spectrum, a hard-coded number of pile modes N_p is not recommended for obtaining the response to any arbitrary force.

Last but not least, the forcing on the pile has been simplified in this work. When it comes to the GDP-technique, there is still an opportunity for more in-depth modelling of the driving force, closer to the reality of the GDP-device.

Point-Collocation method The Point-Collocation method is developed with an eye on the reciprocity theorem. The weight-functions are thus chosen to be physical quantities, in this case: the radial stresses and fluid pressures.

Orthogonality method This method is developed keeping the orthogonality relations of the *P-SV* and *SH* modes in mind. The weight-functions are chosen such that the final equations can be reduced using the orthogonality relations. This method is deemed computationally efficient since it results in diagonally dominant systems of equations.

Rayleigh-Love orthogonality During the earlier stages of deriving the Orthogonality method ([appendix C.2](#)), it was opted to use the orthogonality relation between Love and Rayleigh waves, as derived from Betti's identity by [Bostock \[19\]](#). However, this work did not result in a functional orthogonality condition between the *P-SV* and *SH* modes. Since it is certain that an orthogonality relation does exist between these two mode-types, it would be valuable to put more effort into obtaining it, in order to improve the Orthogonality method

Coupling of the modal amplitudes One of the three matching equations (eq. (C.1.3a) in appendix C.1) is the forced equation of motion of the pile. Solving the equation of motion would result in a coupling between the modal amplitudes of the pile and those of the P - SV and SH waves, so that a final system of equations with only the SH - and P - SV amplitudes is obtained. This method is applied in the extended derivation in appendix C.2 but resulted in too many nested expressions. For the sake of a straightforward script this method is thus disregarded.

The current method includes the pile amplitudes into the set of unknowns: \underline{C}_P , \underline{C}_{PSV} and \underline{C}_{SH} . one could argue that this unnecessarily increases the size of the system and, therefore, endangering its stability.

Less algebraic reduction Another choice that might affect the numerical error is not simplifying the implemented matching equations (eqs. (C.1.6), (C.1.9) and (C.1.10a)), and opting for numerical evaluation of the integrals. Because of this choice the code could be written such that the weight-functions are easily accessible, so that an alternative modematching methods can be included without changing much to the algorithm. This is deemed more valuable than the negligible numerical error that numerical evaluation may cause.

Stability Various of the points quoted have to do with the numerical error and/or stability of the system. Since this is not necessarily self-evident for the Point-Collocation method, the obtained amplitudes are checked as described in section 4.4.1.

Optimum number of modes For many frequencies an optimum exists for the number of modes taken into account, finding this optimum for the non-symmetrical case has been done in a trial-and-error fashion, from which we learned that the local error was less sensitive to the changes in N_{SH} , as opposed to N_{PSV} . Because of this the increments dN_{SH} were kept quite large (≈ 50), while dN_{PSV} has been set to 10. Despite this bigger grid the error analysis has to repeat the matching procedure ≈ 180 times per frequency.

The reduced insensitivity to changes in N_{SH} could also be linked to the fact that the SH -waves only appear in the radial and azimuthal displacements of the soil, which contribute only $1/2 \cdot 2/3 \approx 33\%$ to the local error (see eq. (4.4.2c) in section 4.4.2) in contrast to N_{PSV} which is used in all the expressions of the acousto-elastic displacement field.

Less evanescent modes Figures 6.3c and 6.4b show that the ideal number of P - SV modes gets higher for higher frequencies, which is expected. However, note that despite the increasing total number of modes N_{PSV} the number of available evanescent modes decreases for higher frequencies. This is due to the limit set in the complex rootfinder in SILINCE, from which the P - SV wavenumbers are obtained (section 2.3.1). Keeping this in mind the fact that the model has trouble converging for higher frequencies is comprehensible, fig. 6.4a. Figure 6.2 reassures that the fluid displacement does try to follow the highly oscillatory response of the pile.

Differences between the matching methods As mentioned before the Point-Collocation method does not necessarily result in diagonally dominant algebraic systems, making stability not self-evident. In contrast to the Orthogonality method which ensures a diagonally dominant system to solve, despite this difference the convergence of the two methods seems to be fairly equal overall, see appendix D.1.

For the response to a vertical unit-load ($n = 0$) the Point-Collocation method appears to converge more than the Orthogonality method, fig. D.1. However, fig. 6.1 shows that the Orthogonality method tends to diverge more after the ideal number of modes is exceeded, unlike the Point-Collocation method, which converges in a stable manner. On the other hand, for the response to a horizontal unit-force ($n = 1$) the Orthogonality method converges better, especially for frequencies higher than 150 Hz, see fig. D.2

The local error for the response to a horizontal unit-load ($n = 1$, fig. 6.3a) combined with the number of modes $N_{\{PSV,SH\}}$ (figs. 6.3b and 6.3c) show that the optimum number of SH -modes lies consistently higher for the Orthogonality method. There is no obvious explanation for this. However, it is striking that the Orthogonality method only includes the SH -modes once in each matching equations (eqs. (C.1.6) and (C.1.7a)), in contrast to the Point-Collocation method, where the SH -modes are included twice in each equation (eqs. (C.1.9) and (C.1.10a)).

Based on the mean local error the Point-Collocation method converges better than the Orthogonality method for the symmetric case (fig. 6.4a), while the the opposite is true for the non-symmetric case (fig. 6.3a), where the mean total error of the orthogonality-method is significantly better. It could be that the diagonally dominant matrices of the Orthogonality method are an advantage that excels with larger systems.

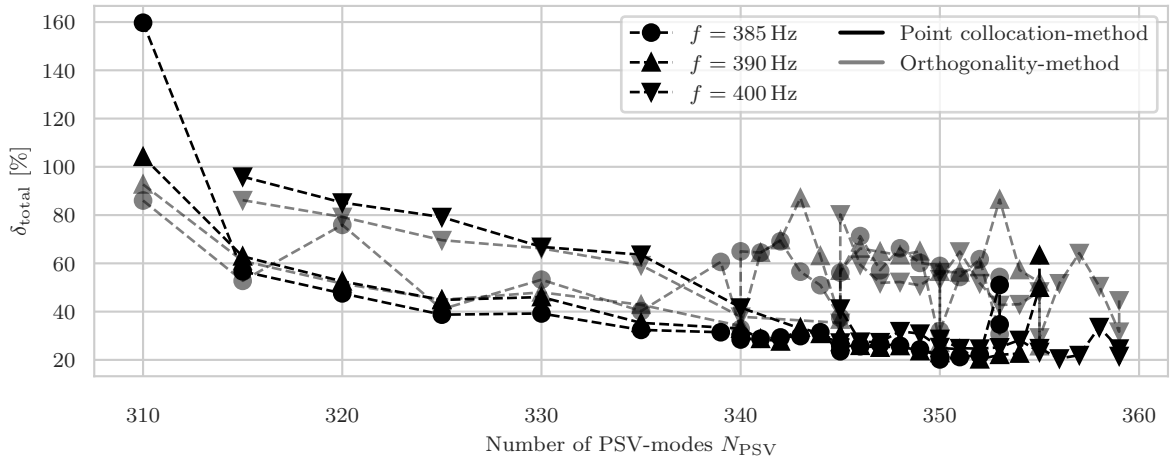


Figure 6.1: The convergence of the response to an uniform vertical force shown by plotting δ_{total} against $N_{\{\text{PSV};\text{SH}\}}$ for several frequencies.

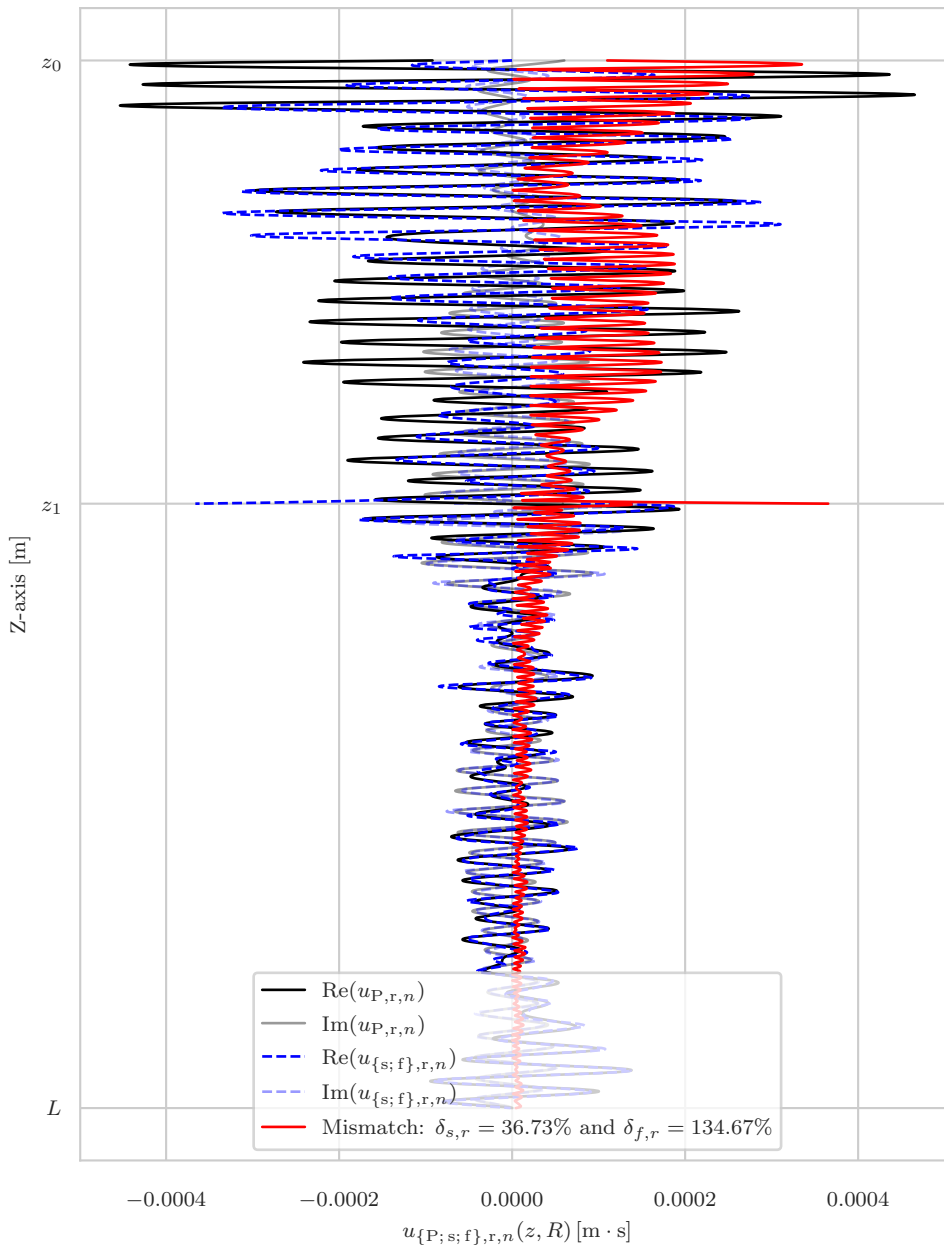


Figure 6.2: Mismatch in the radial direction for a system with the properties in table 4.1 at $f = 420$ Hz and for $N_{\{\text{PSV};\text{SH}\}} = (365, 200)$

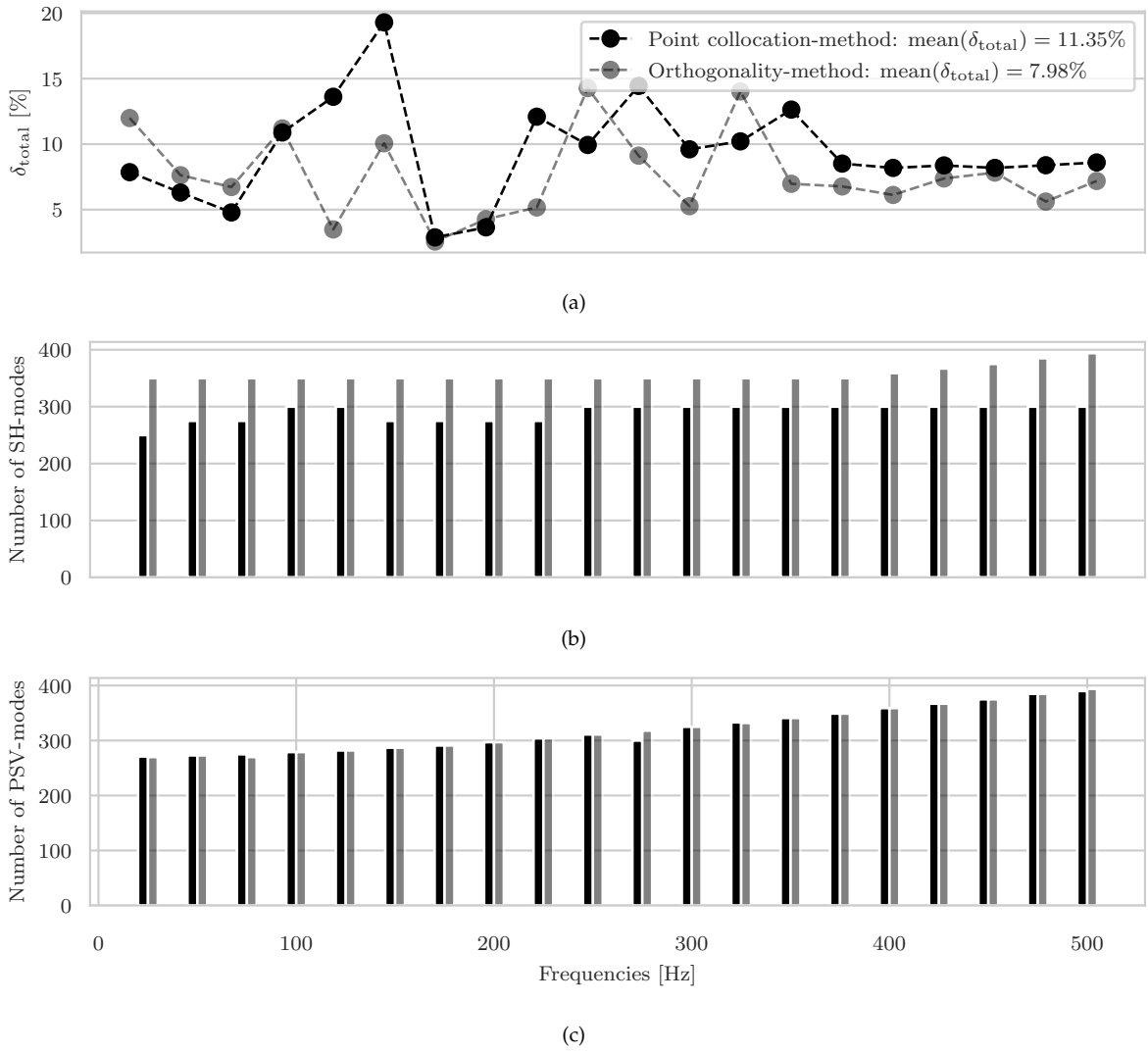


Figure 6.3: (b)-(c) The ideal number of modes $N_{\{PSV;SH\}}$ for the response to a uniform force and (a) the corresponding error

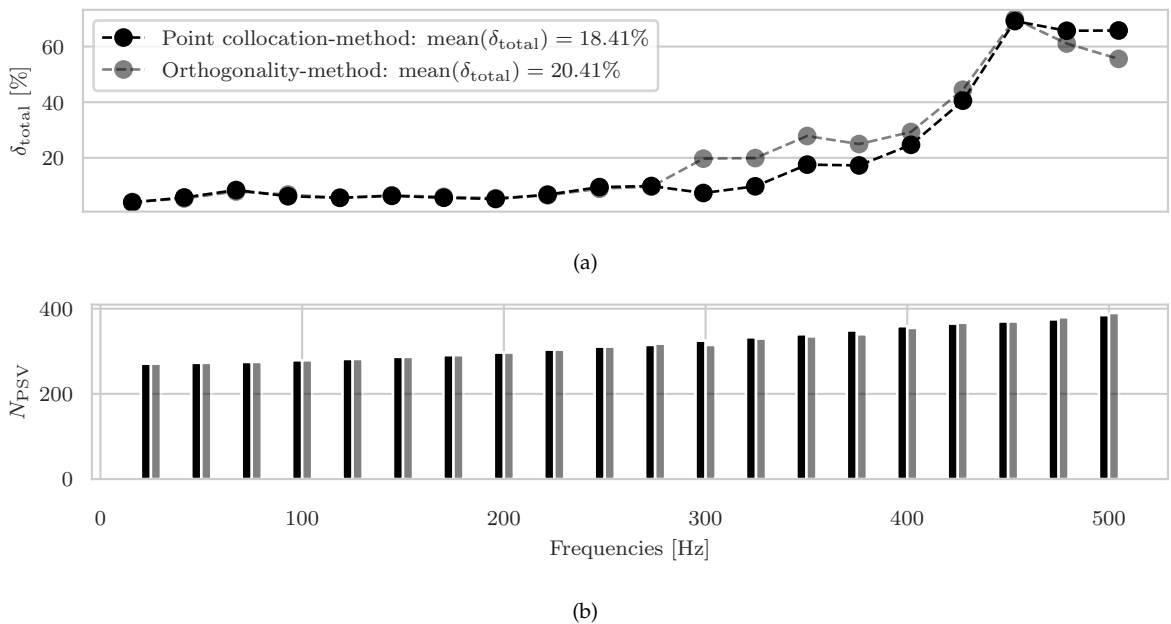


Figure 6.4: (b) The ideal number of modes N_{PSV} for the response to a uniform vertical force and (a) the corresponding error

6.2 The case study

In this section, discussion points are cited based on the results of the case study conducted in [chapter 5](#).

One case only It was decided to work with only one geometry case, in order to focus on the effect of the different forcing configurations. Especially focusing on the non-symmetric forcing fields since this is supposed to be the novice part of this model.

Furthermore, we chose to focus on the components of an imperfect vertical force compared to a perfect vertical force.

The analysis has been carried out for a higher order torsional force as well, these results are not included in this report due to lack of comparison material.

Fluid pressure The frequency spectra of the fluid pressures \bar{p}_f for the non-symmetric ($n = 1$, [figs. 6.5b](#) and [6.5c](#)) configurations show dominant peaks that are missing in the response to the symmetric force ($n = 0$, [fig. 6.5a](#))¹. These peaks are accredited to the fact that the eigen-frequencies of the pile are much smaller and denser for higher order circular modes n , as seen in the eigenvalue analysis in [fig. 6.6](#). For example three of the distinct peaks in [fig. 6.5b](#) correspond to the eigen-frequencies of the first three modes of the pile. Note that the peaks might be shifted a little due to the stiffness of the soil surrounding the pile.

After superposition of the spectra of the various components it shows that the vertical force F_z is governing, which is expected for realistic imperfections of this small a scale (i.e. an eccentricity of $0.03 \cdot R$ and an angle to the normal of 3°).

Despite the small amplitude of F_x and M_z , the third pile mode seems to influence the spectrum of the total response still, [fig. 6.5d](#).

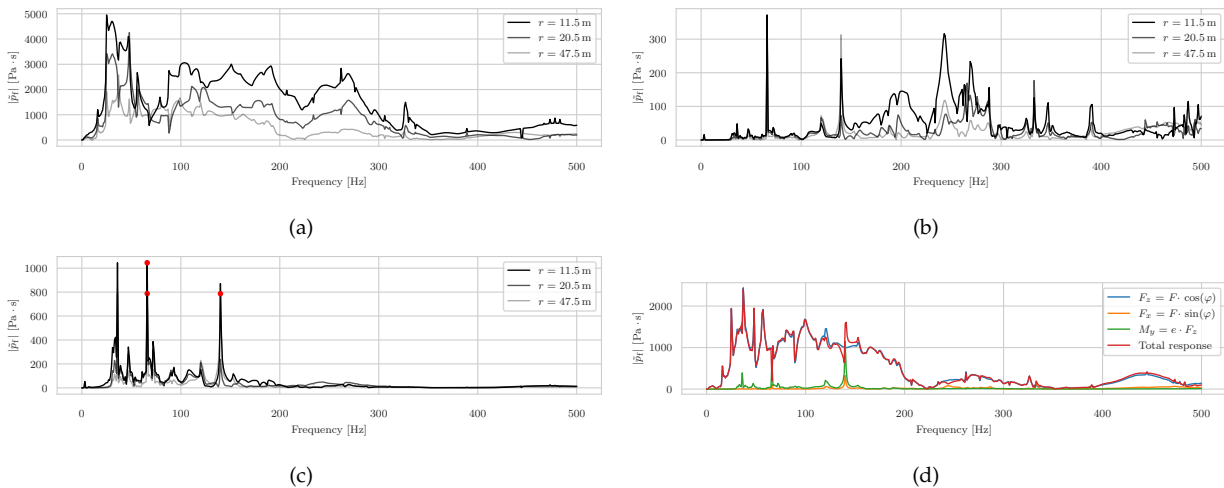


Figure 6.5: The amplitude spectra of the fluid pressure at a depth of 13.5 m at various distances from the pile due to (a) a vertical (b) a horizontal force and (c) a moment on the y-axis (d) imperfect vertical force.

Time signals Obtaining reasonable time signals requires more than 500 frequencies, this is also clearly visible in the graphs of the soil velocities ([figs. 5.7a](#) and [5.7b](#)), which are governed by a single dominant peak in the frequency spectra. An attempt was made to somewhat correct this by filtering out outliers from the frequency spectrum, resulting in slightly finer results ([figs. 5.8a, 5.8b, 5.17a](#) and [5.17b](#)).

Furthermore, the time signals of the fluid pressure clearly show a time of arrival as well as the decrease of the pressure with increasing distance ([figs. 5.6](#) and [5.16](#)).

¹ Note that the amplitudes in [fig. 6.5](#) are the response to already proportioned forcing components of the total forcing. As a result, the amplitudes of the aforementioned graphs cannot be compared fairly.

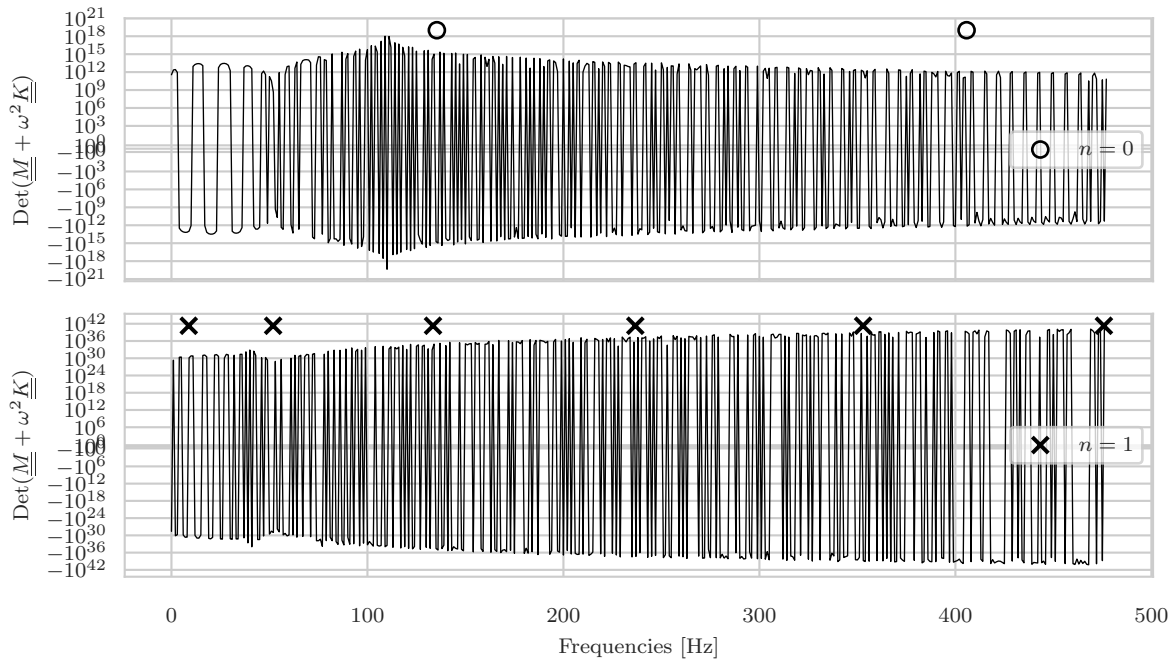


Figure 6.6: Eigenvalue analysis of the pile up to 500 Hz for $n = 0$ and $n = 1$

Soil medium Figures 6.7a and 6.7b show regular smooth frequency spectra that are within the expected outcome. In contrast to the response to a horizontal force (figs. 6.7c and 6.7d) which shows that the spectrum is governed by a few dominant peaks. The three most prominent peaks again occur at eigen-frequencies of the pile.

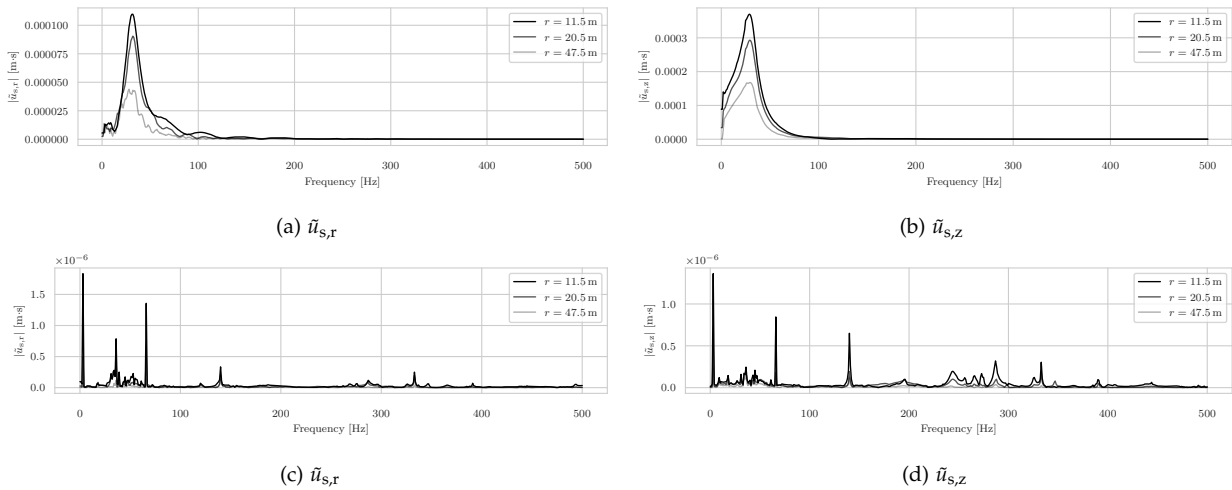


Figure 6.7: The amplitude spectra of the soil displacements at a depth of 32 m due to (a,b) a vertical and (c,d) a horizontal force

Arrival shear waves Figure 6.8 shows the time evolution of the fluid pressure and the displacement norm of the soil. Despite the scatter in the contour plot, the arrival of the shearwave in the soil can be recognized at 18 ms. Assuming a shear wave speed in the pile of $(\frac{1}{3}\sqrt{\frac{2.1 \cdot 10^{11}}{7850}} \approx) 1683 \text{ m s}^{-1}$, the shear wave will indeed have traveled $(1683 \cdot 18 \cdot 10^{-3} \approx) 30 \text{ m}$ after 18 ms, and thus arrive at the soil layer.

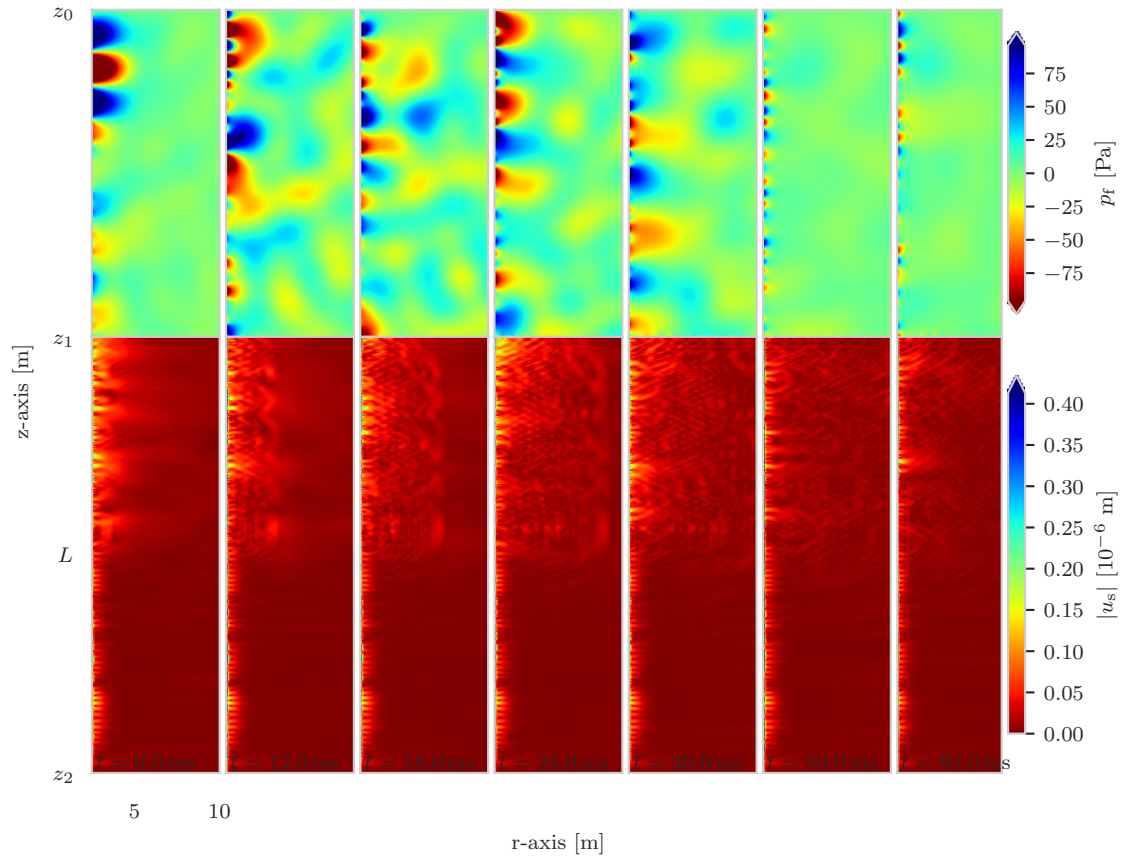


Figure 6.8: Fluid pressure and displacement norm of the soil resulting from an uniform horizontal load at $t = 6, 12, 18, 24, 30, 60$ and 80 ms respectively (Note: the colour bars do convey 33% of the maximum value in the contour plots)

Chapter 7

Conclusions & Recommendations

The concluding chapter of this thesis contains conclusions that are drawn based upon the findings in the report. [Section 7.1](#) summarizes all method related conclusions, while [section 7.2](#) focuses on the case study. Finally, in [section 7.3](#) some recommendations for future research is stated.

7.1 The method

Convergence When comparing the convergence of the two different modematching methods, as presented in [chapter 4](#), there is no clear frontrunner. The Point-Collocation method seems to converge better than the orthogonality-method for the symmetric case ($n = 0$), while the orthogonality-method performs better in the higher order cases ($n = 1$). This is accredited to the diagonally dominant matrices that are characteristic to the Orthogonality method.

Straightforward The implementation of the Point-Collocation method is favored due to its straightforward nature, which makes its programming also clear-cut and less prone to programming errors. This resulted in a generic script that is highly customizable, where alternative weight-functions are easily included to conduct future studies on matching methods.

Time The execution of the developed model is quite time consuming. The culprit is the error analysis that takes up to 24 hours per case per forcing configuration, depending on the convergence. On the upside the error analysis stores the modal amplitudes for every case, which makes them easily accessible for any post-processing procedures. The latter is significantly faster, for example it takes a little less than 30 minutes to get the acousto-elastic displacement field and the fluid pressures, in both the frequency and time domain, for a 600×100 (z, r)-grid for 500 frequencies.

Finding the optimum number of modes The procedure to find the ideal number of P - SV and SH modes is quite robust and time consuming. Due to a lack of time and computing power an extensive study on the behaviour of the error with smaller increments $dN_{\{PSV,SH\}}$ has not been carried out. Researching this more thoroughly and possibly optimizing this procedure would be an interesting objective for future work.

7.2 The case study

Model validation Due to lack of time and computation power extensive model validation could not take place within this work. This model could be validated by running several symmetric case studies with the existing SILENCE program. Furthermore, existing data from small-scale experiments could be used to validate the response to non-symmetric forcing configurations. Only after such studies can the model be tweaked and possibly perfected to give results that suffice.

Higher order torsional moments Despite the error-analysis being carried out for the higher order torsional moments (fig. D.4), post-processing the results and assessing the response was disregarded, since the model could not be validated. The obtained results would not be reliable.

Convergence & azimuthal direction The model seems to have extensive convergence issues with the case of the horizontal force, even after limiting the frequencies higher than 400 Hz, fig. D.2. When the radial component of the force is removed (i.e. higher order torsional moment fig. D.4), the model converges much better. Because of this we can exclude the possibility that the convergence difficulty is due to the azimuthal direction of the model. However, to date, there is no plausible explanation for this issue.

Eigenfrequencies of the pile The eigenfrequencies of the pile for higher order circular modes ($n > 1$) are smaller than for the symmetric case. The possibility of resonance must, therefore, be taken into account more than was the case for the symmetric case. In the case study the eigenfrequencies show up as peaks in the frequency spectra of the fluid and soil displacements.

7.3 Recommendations

A few pointers are made for research that follows up the work in this thesis. These are both things that could have been done differently in this thesis, as well as follow-up topics to look at.

Coupling of the modal amplitudes The model can be optimized by implementing the coupling of the modal vectors, as mentioned in the fifth discussion-point on page 62.

The pile module Since the pile was not the main objective in this work, the current model leaves room for improvement in this area. One of instance of this is the truncation of the modal summation, which is currently hard-coded in the script based on the presumption elaborated in the discussion-point on page 62.

Functional Rayleigh-Love orthogonality During the earlier stages of deriving the Orthogonality method (appendix C.2), it was opted to use the orthogonality relation between Love and Rayleigh waves, as derived from Betti's identity by Bostock [19]. However, this work did not result in a functional orthogonality condition between the P - SV and SH modes. Since it is certain that an orthogonality relation does exist between these two mode-types, it would be valuable to put more effort into obtaining it. With this condition the Orthogonality method could be further improved.

Finding optimum number of modes If after improvements the methods still seem to be highly sensitive to the number of modes taken into account, one could further study the influence of the number of P - SV and SH modes on the local error, in order to find a more efficient algorithm that finds the optimum number of modes for a minimal local matching-error.

Higher order torsional moments A case study, where the driving force is modelled with higher order torsional moment could be carried out. Since this is essentially a simplification of the GDP-shaker. The results from the case study can be compared to and/or validated by data obtained from GDP measuring campaigns, which should be available in the near future.

Driving force The pile driving device is currently modelled by means of various distributed loads. This may suffice when it concerns an hydraulic hammer, but when looking at the vibratory GDP-device, a extensive model of the device, including its geometry and the vibrating technique, could give interesting insight.

Bibliography

- [1] Andrei Metrikine. Gentle driving of piles (gdp) — grow offshore wind, 2022. URL <https://www.grow-offshorewind.nl/project/gentle-driving-of-piles#modalTrigger3>.
- [2] Apostolos Tsouvalas, Özkan Sertlek, Jun Tang, Yaxi Peng, and Timo Molenkamp. Silence, 2022. URL <http://ua.citg.tudelft.nl/SILENCE.html>.
- [3] A. Tsouvalas and A.V. Metrikine. A three-dimensional vibroacoustic model for the prediction of underwater noise from offshore pile driving. *Journal of Sound and Vibration*, 333:2283–2311, 4 2014. ISSN 0022460X. DOI: [10.1016/j.jsv.2013.11.045](https://doi.org/10.1016/j.jsv.2013.11.045).
- [4] Apostolos Tsouvalas. Underwater noise generated by offshore pile driving, 2015.
- [5] Jennifer L. Amaral, James H. Miller, Gopu R. Potty, Kathleen J. Vigness-Raposa, Adam S. Frankel, Ying-Tsong Lin, Arthur E. Newhall, Daniel R. Wilkes, and Alexander N. Gavrilov. Characterization of impact pile driving signals during installation of offshore wind turbine foundations. *The Journal of the Acoustical Society of America*, 147, 2020. ISSN 0001-4966. DOI: [10.1121/10.0001035](https://doi.org/10.1121/10.0001035).
- [6] Apostolos Tsouvalas, Yaxi Peng, and Andrei V. Metrikine. Influence of the seabed conditions on the near-and far-field propagation of noise in impact piling. 2021. ISBN 9788378807995.
- [7] Apostolos Tsouvalas. Underwater noise emission due to offshore pile installation: A review. *Energies*, 13: 3037, 6 2020. ISSN 1996-1073. DOI: [10.3390/en13123037](https://doi.org/10.3390/en13123037).
- [8] Tristan Lippert, Michael A. Ainslie, and Otto von Estorff. Pile driving acoustics made simple: Damped cylindrical spreading model. *The Journal of the Acoustical Society of America*, 143, 2018. ISSN 0001-4966. DOI: [10.1121/1.5011158](https://doi.org/10.1121/1.5011158).
- [9] Technical committee: Iso/tc 43/sc 3 underwater acoustics., 2017. URL <http://ua.citg.tudelft.nl/SILENCE.html>.
- [10] Xue-Qin Li, Wei Zhang, Xiao-Dong Yang, and Lu-Kai Song. A unified approach of free vibration analysis for stiffened cylindrical shell with general boundary conditions. *Mathematical Problems in Engineering*, 2019:1–14, 7 2019. ISSN 1024-123X. DOI: [10.1155/2019/4157930](https://doi.org/10.1155/2019/4157930).
- [11] Werner Soedel and Mohamad S. Qatu. Vibrations of shells and plates, third edition. *The Journal of the Acoustical Society of America*, 117:1683–1683, 4 2005. ISSN 0001-4966. DOI: [10.1121/1.1873932](https://doi.org/10.1121/1.1873932). jbr/i.
- [12] Yaxi Peng, Apostolos Tsouvalas, and Andrei Metrikine. A coupled modelling approach for the fast computation of underwater noise radiation from offshore pile driving. volume 2, pages 2427–2436, 2020. DOI: [10.47964/1120.9196.18574](https://doi.org/10.47964/1120.9196.18574).
- [13] Finn B. Jensen, William A. Kuperman, Michael B. Porter, Henrik Schmidt, and James F. Bartram. Computational ocean acoustics. *The Journal of the Acoustical Society of America*, 97:3213–3213, 5 1995. ISSN 0001-4966. DOI: [10.1121/1.411832](https://doi.org/10.1121/1.411832).
- [14] Apostolos Tsouvalas, Karel N. van Dalen, and Andrei V. Metrikine. The significance of the evanescent spectrum in structure-waveguide interaction problems. *The Journal of the Acoustical Society of America*, 138: 2574–2588, 10 2015. ISSN 0001-4966. DOI: [10.1121/1.4932016](https://doi.org/10.1121/1.4932016).

- [15] Haijun Zhou, Wanyou Li, Binglin Lv, and W.L. Li. Free vibrations of cylindrical shells with elastic-support boundary conditions. *Applied Acoustics*, 73:751–756, 8 2012. ISSN 0003682X. DOI: [10.1016/j.apacoust.2012.02.008](https://doi.org/10.1016/j.apacoust.2012.02.008). jbr/¿.
- [16] Joe G. Easley and Anthony M. Waas. *Analysis of Structures*. 2011. DOI: [10.1002/9781119993278](https://doi.org/10.1002/9781119993278).
- [17] Keiiti Aki and Paul G. Richards. *Quantitative seismology*, 2nd ed. *quse*, 68, 2002.
- [18] E. Kausel and J.M. Roesset. Stiffness matrices for layered soils. *International Journal of Rock Mechanics and Mining Sciences & Geomechanics Abstracts*, 20:A7, 2 1983. ISSN 01489062. DOI: [10.1016/0148-9062\(83\)91665-0](https://doi.org/10.1016/0148-9062(83)91665-0).
- [19] M. G. Bostock. On the orthogonality of surface wave eigenfunctions in cylindrical coordinates. *Geophysical Journal International*, 103:763–767, 12 1990. ISSN 0956540X. DOI: [10.1111/j.1365-246X.1990.tb05688.x](https://doi.org/10.1111/j.1365-246X.1990.tb05688.x).
- [20] Eduardo Kausel. *Fundamental Solutions in Elastodynamics*. Cambridge University Press, 2006. ISBN 9780511546112. DOI: [10.1017/CBO9780511546112](https://doi.org/10.1017/CBO9780511546112).

Appendix A

The Pile

A.1 Constitutive & kinematic relations

Kinematic relation

The relation between the strains and displacement for an arbitrary (deep) shell are given by the following equations. For the sake of brevity we will use these relations as a starting point for our derivation of the shell motion. A more thorough derivation of the shell equations can be found in existing literature [11].

$$\varepsilon_{11} = \frac{1}{f_1(\alpha_3)} \left(\frac{\partial U_1}{\partial \alpha_1} + \frac{U_2}{A_2} \frac{\partial A_1}{\partial \alpha_2} + U_3 \frac{A_1}{R_1} \right) \quad (\text{A.1.1a})$$

$$\varepsilon_{22} = \frac{1}{f_1(\alpha_3)} \left(\frac{\partial U_2}{\partial \alpha_2} + \frac{U_1}{A_1} \frac{\partial A_2}{\partial \alpha_1} + U_3 \frac{A_2}{R_2} \right) \quad (\text{A.1.1b})$$

$$\varepsilon_{33} = \frac{\partial U_3}{\partial \alpha_3} \quad (\text{A.1.1c})$$

$$\varepsilon_{12} = \varepsilon_{21} = \frac{f_1(\alpha_3)}{f_2(\alpha_3)} \frac{\partial}{\partial \alpha_2} \left(\frac{U_1}{f_1(\alpha_3)} \right) + \frac{f_2(\alpha_3)}{f_1(\alpha_3)} \frac{\partial}{\partial \alpha_1} \left(\frac{U_2}{f_2(\alpha_3)} \right) \quad (\text{A.1.1d})$$

$$\varepsilon_{13} = \varepsilon_{31} = f_1(\alpha_3) \frac{\partial}{\partial \alpha_3} \left(\frac{U_1}{f_1(\alpha_3)} \right) + \frac{1}{f_1(\alpha_3)} \frac{\partial U_3}{\partial \alpha_1} \quad (\text{A.1.1e})$$

$$\varepsilon_{23} = \varepsilon_{32} = f_2(\alpha_3) \frac{\partial}{\partial \alpha_3} \left(\frac{U_1}{f_2(\alpha_3)} \right) + \frac{1}{f_2(\alpha_3)} \frac{\partial U_3}{\partial \alpha_2} \quad (\text{A.1.1f})$$

$$\text{With: } f_i(\alpha_3) = A_i \left(1 + \frac{\alpha_3}{R_i} \right) \quad \text{for } i = 1, 2$$

In the case of a cylindrical shell the coordinates are as shown in the box below. With R being the radius of the cylinder.

$\alpha_1 \equiv z,$	$\alpha_2 \equiv \theta$
$\beta_1 \equiv \beta_z,$	$\beta_2 \equiv \beta_\theta$
$A_1 = 1,$	$A_2 = R$
$R_1 = \infty,$	$R_2 = R$

Substituting these coordinates and radii into the strain-displacement relations yields eq. (A.1.2). For thin shells it holds that $\frac{\alpha_3}{R_i}$ is negligible.

$$\varepsilon_{zz} = \frac{\partial u_z}{\partial z} + r \cdot \frac{\partial \beta_z}{\partial z} \quad (\text{A.1.2a})$$

$$\varepsilon_{\theta\theta} = \frac{1}{R} \left(\frac{\partial u_\theta}{\partial \theta} + u_r \right) + r \cdot \frac{1}{R} \frac{\partial \beta_\theta}{\partial \theta} \quad (\text{A.1.2b})$$

$$\varepsilon_{rr} = 0 + r \cdot 0 \quad (\text{A.1.2c})$$

$$\varepsilon_{z\theta} = \frac{\partial u_\theta}{\partial z} + \frac{1}{R} \frac{\partial u_z}{\partial \theta} + r \cdot \left(\frac{\partial \beta_\theta}{\partial z} + \frac{1}{R} \frac{\partial \beta_z}{\partial \theta} \right) \quad (\text{A.1.2d})$$

$$\varepsilon_{zr} = \frac{\partial u_r}{\partial z} + \beta_z + r \cdot 0 \quad (\text{A.1.2e})$$

$$\varepsilon_{\theta r} = \frac{1}{R} \left(\frac{\partial u_r}{\partial \theta} - u_\theta \right) + \beta_\theta + r \cdot 0 \quad (\text{A.1.2f})$$

displacement strain ε_{ij}^0
bending strains k_{ij}

As mentioned before for the application at hand thin shells are used to model the pile. The deformation of the pile is assumed to be non-dependent on the radial coordinate r , conform Love's simplifications.

Consistutive relation

The consistutive relation is then obtained with Hooke's law for a three dimensional element [11]:

$$\sigma_{zz} = \frac{\partial u_z}{\partial z} + r \cdot \frac{\partial \beta_z}{\partial z} \quad (\text{A.1.4a})$$

$$\sigma_{\theta\theta} = \frac{1}{R} \left(\frac{\partial u_\theta}{\partial \theta} + u_r \right) + r \cdot \frac{1}{R} \frac{\partial \beta_\theta}{\partial \theta} \quad (\text{A.1.4b})$$

$$\sigma_{rr} = 0 + r \cdot 0 \quad (\text{A.1.4c})$$

$$\sigma_{z\theta} = \frac{\partial u_\theta}{\partial z} + \frac{1}{R} \frac{\partial u_z}{\partial \theta} + r \cdot \left(\frac{\partial \beta_\theta}{\partial z} + \frac{1}{R} \frac{\partial \beta_z}{\partial \theta} \right) \quad (\text{A.1.4d})$$

$$\sigma_{zr} = \frac{\partial u_r}{\partial z} + \beta_z + r \cdot 0 \quad (\text{A.1.4e})$$

$$\sigma_{\theta r} = \frac{1}{R} \left(\frac{\partial u_r}{\partial \theta} - u_\theta \right) + \beta_\theta + r \cdot 0 \quad (\text{A.1.4f})$$

displacement strain ε_{ij}^0
bending strains k_{ij}

Internal forces

The relation between the strains and the internal forces are obtained by substituting the consistutive and kinematic relations in the equilibrium equations of the deep shell, these can be found in various literature and will not be shown here for abbrivaty. Doing this results in expressions A.1.5

$$N_{zz} = K \left(\varepsilon_{zz}^0 + \mu \varepsilon_{\theta\theta}^0 \right) \quad (\text{A.1.5a})$$

$$N_{\theta\theta} = K \left(\varepsilon_{\theta\theta}^0 + \mu \varepsilon_{zz}^0 \right) \quad (\text{A.1.5b})$$

$$N_{\theta z} = N_{z\theta} = G h \varepsilon_{z\theta}^0 \quad (\text{A.1.5c})$$

$$Q_{zr} = Q_{rz} = k' G h \varepsilon_{zr}^0 \quad (\text{A.1.5d})$$

$$Q_{r\theta} = Q_{\theta r} = k' G h \varepsilon_{\theta r}^0 \quad (\text{A.1.5e})$$

$$M_{zz} = D (k_{zz} + \mu k_{\theta\theta}) \quad (\text{A.1.5f})$$

$$M_{\theta\theta} = D (k_{\theta\theta} + \mu k_{zz}) \quad (\text{A.1.5g})$$

$$M_{\theta z} = M_{z\theta} = D \frac{1-\mu}{2} k_{z\theta} \quad (\text{A.1.5h})$$

$$\text{With: } K = \frac{Eh}{1-\mu^2}, \quad G = \frac{K}{2h}(1-\mu) \quad \text{and} \quad D = \frac{Eh^3}{12(1-\mu^2)}$$

Where K and D are the membrane and bending stiffness respectively. While the shear modulus is represented by G .

The factor k' is used to specify the distribution of the shear stress along the shell thickness. A parabolic distribution is assumed, which complies with $k' = \frac{2}{3}$

A.2 Coefficient matrix & Characteristic relation

Coefficient matrix

The the coefficient matrix $\underline{\underline{K}}$ and $\underline{\underline{M}}$ of the pile equations have been introduced in eq. (3.1.1) in section 3.1.1. The stiffness matrix $\underline{\underline{K}}$ is symmetric conform the assumption of a linear elastic material. While the mass matrix $\underline{\underline{M}}$ is a lumped one.

$$\underline{\underline{K}} = \begin{bmatrix} K_{11} & \cdots & K_{15} \\ \vdots & \ddots & \vdots \\ K_{15} & \cdots & K_{55} \end{bmatrix} \quad \text{and} \quad \underline{\underline{M}} = \rho_P R h \cdot \text{diag} \left(\begin{bmatrix} 1 \\ 1 \\ 1 \\ \frac{1}{12}h^2 \\ \frac{1}{12}h^2 \end{bmatrix} \right) \quad (\text{A.2.1})$$

$$K_{11} = \frac{\rho h c_L^2}{R} \left(R^2 k^2 + \frac{n^2 (\nu + 1)}{2} \right) \quad (\text{A.2.2a})$$

$$K_{12} = -\frac{1}{2} \rho h (\nu + 1) n k c_L^2 \quad (\text{A.2.2b})$$

$$K_{13} = c_L^2 h k \nu \rho \quad (\text{A.2.2c})$$

$$K_{14} = K_{15} = 0 \quad (\text{A.2.2d})$$

$$K_{22} = \frac{h (k^2 (\nu + 1) R^2 + (1 - \nu) k' + 2 n^2) c_L^2 \rho}{2 R} \quad (\text{A.2.2e})$$

$$K_{23} = \frac{1}{2} R n (-2 + (\nu + 1) k') c_L^2 \rho h \quad (\text{A.2.2f})$$

$$K_{24} = 0 \quad (\text{A.2.2g})$$

$$K_{25} = \frac{1}{2} (\nu + 1) k' c_L^2 \rho h \quad (\text{A.2.2h})$$

$$K_{33} = \frac{1}{2} R h (2 + (Rk - n) (Rk + n) (-1 + \nu) k') c_L^2 \rho \quad (\text{A.2.2i})$$

$$K_{34} = \frac{1}{2} h R k (-1 + \nu) k' c_L^2 \rho \quad (\text{A.2.2j})$$

$$K_{35} = -\frac{1}{2} n (\nu + 1) k' c_L^2 \rho h \quad (\text{A.2.2k})$$

$$K_{44} = \frac{1}{2} \rho h \left(2 \beta^2 R^2 k^2 + \beta^2 n^2 \nu - \beta^2 n^2 + k' \nu - k' \right) c_L^2 R \quad (\text{A.2.2l})$$

$$K_{44} = \frac{1}{2} \rho h \left(2 \beta^2 R^2 k^2 + (\beta^2 n^2 k') (-1 + \nu) \right) c_L^2 R \quad (\text{A.2.2m})$$

$$K_{45} = -\frac{1}{2} R^2 n (\nu + 1) \beta^2 k c_L^2 \rho h \quad (\text{A.2.2n})$$

$$K_{55} = \frac{1}{2} \left((k^2 (\nu + 1) R^2 + 2 n^2) \beta^2 - (\nu + 1) k' \right) h \rho R c_L^2 \quad (\text{A.2.2o})$$

A.3 Displacement & stress field

Pile displacements

$$\mathbf{u}_{P,n}(z, \theta, r) = \sum_{m=1}^{\infty} C_{P,nm} \underline{\mathbf{R}}_n(\theta) \hat{\mathbf{u}}_{P,m}(z) \quad (\text{A.3.1})$$

$$\begin{aligned} \text{with: } \hat{\mathbf{u}}_{P,m}(z) &= [\hat{u}_{P,r,m}(z) \quad \hat{u}_{P,\theta,m}(z) \quad \hat{u}_{P,z,m}(z) \quad \hat{\beta}_{P,r,m}(z) \quad \hat{\beta}_{P,\theta,m}(z)]^T \\ \underline{\mathbf{R}}_n(\theta) &= \text{diag} \left([\cos(n\theta) \quad -\sin(n\theta) \quad \cos(n\theta) \quad \cos(n\theta) \quad -\sin(n\theta)]^T \right) \end{aligned}$$

$$\hat{u}_{P,r,m}(z) = \sum_{i=1}^{10} \gamma_{z,i} e^{k_i z} \quad \text{with} \quad k_i = k_i(\omega_m) \quad \text{and} \quad \underline{\gamma}_i = \underline{\gamma}_i(\omega_m) \quad (\text{A.3.2a})$$

$$\hat{u}_{P,\theta,m}(z) = \sum_{i=1}^{10} \gamma_{\theta,i} e^{k_i z} \quad (\text{A.3.2b})$$

$$\hat{u}_{P,z,m}(z) = \sum_{i=1}^{10} \gamma_{r,i} e^{k_i z} \quad (\text{A.3.2c})$$

$$\hat{u}_{P,r,m}(z) = \sum_{i=1}^{10} \gamma_{\beta_z,i} e^{k_i z} \quad (\text{A.3.2d})$$

$$\hat{u}_{P,\theta,m}(z) = \sum_{i=1}^{10} \gamma_{\beta_\theta,i} e^{k_i z} \quad (\text{A.3.2e})$$

Internal forces & bending moments

$$\underline{\mathbf{N}}_{P,n}(z, \theta, r) = \sum_{m=1}^{\infty} C_{P,nm} \cdot \underline{\mathbf{R}}_n(\theta) \begin{bmatrix} \hat{N}_{P,zz,n}(z) \\ \hat{N}_{P,z\theta,n}(z) \\ \hat{Q}_{P,zr,n}(z) \end{bmatrix} \quad (\text{A.3.3})$$

$$\underline{\mathbf{M}}_{P,n}(z, \theta, r) = \sum_{m=1}^{\infty} C_{P,nm} \cdot \text{diag} \left(\begin{bmatrix} \cos(n\theta) \\ -\sin(n\theta) \end{bmatrix} \right) \begin{bmatrix} \hat{M}_{P,zz,m}(z) \\ \hat{M}_{P,z\theta,m}(z) \end{bmatrix} \quad (\text{A.3.4})$$

$$\hat{N}_{P,zz,n}(z) = \sum_{i=1}^{10} \frac{K}{R} (vn \hat{u}_{P,\theta,m}(z) + k_i R \hat{u}_{P,z}(z)) e^{-k_i z} \quad (\text{A.3.5a})$$

$$\hat{N}_{P,z\theta,m}(z) = \sum_{i=1}^{10} \frac{K(v-1)}{2R} (-k_i R \hat{u}_{P,\theta,m}(z) + n \hat{u}_{P,z,m}(z)) e^{-k_i z} \quad (\text{A.3.5b})$$

$$\hat{Q}_{P,zr,m}(z) = \sum_{i=1}^{10} \frac{D}{2R^2} \left(2R^2 k_i^2 \hat{\beta}_{P,z}(z) + n k_i R (v+1) \hat{\beta}_{P,\theta,m}(z) + n^2 (v-1) \hat{\beta}_{P,z,m}(z) \right) e^{-k_i z} \quad (\text{A.3.5c})$$

$$\hat{M}_{P,zz,m}(z) = \sum_{i=1}^{10} \frac{C}{R} (nv \hat{\beta}_{P,\theta,m}(z) + k_i R \hat{\beta}_{P,z,m}(z)) e^{-k_i z} \quad (\text{A.3.5d})$$

$$\hat{M}_{P,z\theta,m}(z) = \sum_{i=1}^{10} \frac{D(v-1)}{2R} (-k_i R \hat{\beta}_{P,\theta,m}(z) + n \hat{\beta}_{P,z,m}(z)) e^{-k_i z} \quad (\text{A.3.5e})$$

Appendix B

Fluid & soil domain

B.1 Constitutive & kinematic relations

The kinematic relation inside a elastic medium in cartesian coordinates can be presented in a compact manner as: $\varepsilon_{ij} = \frac{1}{2}(\partial_j u_i + \partial_i u_j)$, with i and j being the cartesian coordinates x, y and z . Since the application at hand will be determined conform the cylindrical coordinate system the displacement-strain in the different directions are shown in eq. (B.1.1). These relations are assumed to be common knowlegde and can be found in many fundamental literature. [13, 17, 20]

$$\varepsilon_{s,rr} = \frac{\partial u_{s,r}}{\partial r} \quad (\text{B.1.1a})$$

$$\varepsilon_{s,\theta\theta} = \frac{1}{r} \left(u_{s,r} - \frac{\partial u_{s,\theta}}{\partial \theta} \right) \quad (\text{B.1.1b})$$

$$\varepsilon_{s,zz} = \frac{\partial u_{s,z}}{\partial z} \quad (\text{B.1.1c})$$

$$\varepsilon_{s,r\theta} = \varepsilon_{s,\theta r} = \frac{1}{2} \left(\frac{1}{r} \left(\frac{\partial u_{s,r}}{\partial \theta} - u_{s,\theta} \right) + \frac{\partial u_{s,\theta}}{\partial r} \right) \quad (\text{B.1.1d})$$

$$\varepsilon_{s,rz} = \varepsilon_{s,zr} = \frac{1}{2} \left(\frac{\partial u_{s,r}}{\partial z} + \frac{\partial u_{s,z}}{\partial r} \right) \quad (\text{B.1.1e})$$

$$\varepsilon_{s,\theta z} = \varepsilon_{s,z\theta} = \frac{1}{2} \left(\frac{\partial u_{s,\theta}}{\partial z} + \frac{1}{r} \frac{\partial u_{s,z}}{\partial \theta} \right) \quad (\text{B.1.1f})$$

The constitutive relation inside a elastic medium in can be presented in a compact manner too as shown in eq. (B.1.2), where ε_{vol} is the volumetric strain.

$$\sigma_{ij} = \lambda \varepsilon_{vol} \delta_{ij} + \mu(\varepsilon_{ij} + \varepsilon_{ji}) \quad (\text{B.1.2})$$

$$\varepsilon_{vol} = \nabla \cdot \mathbf{u} = \frac{\partial u_r}{\partial r} + \frac{u_r}{r} + \frac{1}{r} \frac{\partial u_\theta}{\partial \theta} + \frac{\partial u_z}{\partial z} \quad (\text{B.1.3})$$

Substituting the kinematic equations [B.1.1](#) into the stress definition gives the relation between the displacements and stresses in different direction, as shown in [Equations \(B.1.4a\) to \(B.1.4f\)](#).

$$\tilde{\sigma}_{s,rr} = (2\mu + \lambda) \frac{\partial u_{s,r}}{\partial r} + \lambda \left(\frac{u_{s,r}}{r} + \frac{1}{r} \frac{\partial u_{s,\theta}}{\partial \theta} + \frac{\partial u_{s,z}}{\partial z} \right) \quad (\text{B.1.4a})$$

$$\tilde{\sigma}_{s,\theta\theta} = (2\mu + \lambda) \frac{\partial u_{s,r}}{\partial r} + \lambda \left(\frac{u_{s,r}}{r} + \frac{1}{r} \frac{\partial u_{s,\theta}}{\partial \theta} + \frac{\partial u_{s,z}}{\partial z} \right) \quad (\text{B.1.4b})$$

$$\tilde{\sigma}_{s,zz} = (2\mu + \lambda) \frac{\partial u_{s,z}}{\partial z} + \lambda \left(\frac{\partial u_{s,r}}{\partial r} + \frac{u_{s,r}}{r} + \frac{1}{r} \frac{\partial u_{s,\theta}}{\partial \theta} \right) \quad (\text{B.1.4c})$$

$$\tilde{\sigma}_{s,r\theta} = \tilde{\sigma}_{s,\theta r} = \mu \left(\frac{1}{r} \frac{\partial u_{s,r}}{\partial \theta} - \frac{1}{r} u_{s,\theta} + \frac{\partial u_{s,\theta}}{\partial r} \right) \quad (\text{B.1.4d})$$

$$\tilde{\sigma}_{s,rz} = \tilde{\sigma}_{s,zr} = \mu \left(\frac{\partial u_{s,r}}{\partial z} + \frac{\partial u_{s,z}}{\partial r} \right) \quad (\text{B.1.4e})$$

$$\tilde{\sigma}_{s,\theta z} = \tilde{\sigma}_{s,z\theta} = \mu \left(\frac{\partial u_{s,\theta}}{\partial z} + \frac{1}{r} \frac{\partial u_{s,z}}{\partial \theta} \right) \quad (\text{B.1.4f})$$

B.2 Solution to the Helmholtz equation

The wave equations as presented in [section 3.2](#) is simply the cylindrical Helmholtz equation. The solution-forms are obtained by separating the variables. The derivation is shown in this appendix.

$$\nabla^2 \phi(r, \theta, z, \omega) + \frac{\omega^2}{c^2} \phi(r, \theta, z, \omega) = 0 \quad (\text{B.2.1})$$

Note that ϕ is the amplitude of the fourier transform and ∇^2 is the Laplace operator in cylindrical coordinates, i.e.: $\nabla^2 = \partial_r^2 + \frac{1}{r} \partial_r + \frac{1}{r^2} \partial_\theta^2 + \partial_z^2$

First the solution is assumed to be in the form $\phi(r, \theta, z, \omega) = R(r) \Theta(\theta) Z(z)$. Substituting the solution form into the PDE, [eq. \(B.2.1\)](#), gives:

$$R'' \Theta Z + \frac{1}{r} R' \Theta Z + \frac{1}{r^2} R \Theta'' Z + R \Theta Z'' + \frac{\omega^2}{c^2} R \Theta Z = 0$$

$$\underbrace{\frac{R''(r)}{R(r)} + \frac{1}{r} \frac{R'(r)}{R(r)} + \frac{1}{r^2} \frac{\Theta''(\theta)}{\Theta(\theta)}}_{f(\theta,r) = -k^2} + \underbrace{\frac{Z''(z)}{Z(z)} + \frac{\omega^2}{c^2}}_{f_1(z) = k^2} = 0 \quad (\text{B.2.2})$$

The above can only hold if both functions are constant, in this case the arbitrary separation constant k^2 is used. The partial differential equation is now split into one ODE and one PDE. The latter is again separable, thus a second and third ODE are obtained using the same analogy.

$$\underbrace{r^2 \frac{R''(r)}{R(r)} + r \frac{R'(r)}{R(r)} + r^2 k^2}_{f_3(r) = n^2} + \underbrace{\frac{\Theta''(\theta)}{\Theta(\theta)}}_{f_2(\theta) = -n^2} = 0 \quad (\text{B.2.3})$$

The vertical function $Z(z)$ is assumed to be non-oscillatory, as the waves are supposed to dissipate with increasing depth.

$$\frac{Z''(z)}{Z(z)} + \frac{\omega^2}{c^2} = k^2$$

$$Z''(z) - \alpha^2 Z(z) = 0 \quad \longrightarrow \quad Z(z) = C_1 e^{\alpha z} + C_2 e^{-\alpha z} \quad (\text{B.2.4})$$

with: $\alpha^2 = k^2 - \frac{\omega^2}{c^2}$

The azimuthal function $\Theta(\theta)$ however is supposed to be oscillatory to satisfy the continuity condition at $\theta = 0$ and $\theta = 2\pi$

$$\frac{\Theta''(\theta)}{\Theta(\theta)} = -n^2 \quad \longrightarrow \quad \Theta(\theta) = C_3 \cos(n\theta) + C_4 \sin(n\theta) \quad \text{or} \quad \Theta(\theta) = C_3 \cos(n\theta + \varphi) \quad (\text{B.2.5})$$

$$\Theta''(\theta) + n^2 \Theta(\theta) = 0$$

Finally the ODE of the radial function $R(r)$ is examined. When writing this equation one can immediately see this is the form of a Bessel differential equation

$$\begin{aligned}
 r^2 \frac{R''(r)}{R(r)} + r \frac{R'(r)}{R(r)} + r^2 k^2 &= n^2 \\
 \frac{1}{k^2} R''(r) + \frac{1}{k^2 r} R'(r) + \left(1 - \frac{n^2}{k^2 r^2}\right) R(r) &= 0 \\
 \downarrow \\
 \begin{aligned}
 kr &= \rho \\
 \frac{1}{k} \frac{dR}{dr} &= \frac{dR}{d\rho} \\
 \frac{1}{k^2} \frac{d^2 R}{dr^2} &= \frac{d^2 R}{d\rho^2}
 \end{aligned} \\
 \downarrow \\
 \frac{d^2 R}{d\rho^2} + \frac{1}{\rho} \frac{dR}{d\rho} + \left(1 - \frac{n^2}{\rho^2}\right) R(\rho) &= 0 \\
 \downarrow \\
 R(kr) &= C_5 H_n^{(1)}(kr) + C_6 H_n^{(2)}(kr)
 \end{aligned} \tag{B.2.6}$$

Since we are only interested in waves that propagate away from the origin only the second Hankelfunction fits in the definition of $R(r)$, therefore $C_5 \equiv 0$.

Combining the above results in the general solution (eq. (B.2.7)) as used in the thesis.

$$\phi = H_n^{(2)}(kr) \cdot \cos(n\theta + \varphi) \cdot (C_1 e^{\alpha z} + C_2 e^{-\alpha z}) \tag{B.2.7}$$

B.3 Coefficient matrix & Dispersion relation

Coefficient matrix

The SH- and PSV-coefficient matrices are introduced in section 3.2.2 (eqs. (3.2.11a) and (3.2.11b) respectively).

PS-V coefficient matrix

$$\underline{\underline{D}}_{PSV} = \begin{bmatrix} D_{11}^{PSV} & \dots & D_{16}^{PSV} \\ \vdots & \ddots & \vdots \\ D_{61}^{PSV} & \dots & D_{66}^{PSV} \end{bmatrix} \tag{B.3.1}$$

$$\begin{aligned}
 D_{11}^{PSV} &= 0 & D_{21}^{PSV} &= -2 \mu k \alpha_{\phi_s} e^{-\alpha_{\phi_s} z_1} & D_{31}^{PSV} &= - \left((-2 \mu - \lambda) \alpha_{\phi_s}^2 + k^2 \lambda \right) e^{-\alpha_{\phi_s} z_1} \\
 D_{12}^{PSV} &= 0 & D_{22}^{PSV} &= 2 \mu k \alpha_{\phi_s} e^{\alpha_{\phi_s} z_1} & D_{32}^{PSV} &= - \left((-2 \mu - \lambda) \alpha_{\phi_s}^2 + k^2 \lambda \right) e^{\alpha_{\phi_s} z_1} \\
 D_{13}^{PSV} &= 0 & D_{23}^{PSV} &= \mu k \left(k^2 + \beta_{\psi}^2 \right) e^{-\beta_{\psi} z_1} & D_{33}^{PSV} &= -2 k^2 \mu \beta_{\psi} e^{-\beta_{\psi} z_1} \\
 D_{14}^{PSV} &= 0 & D_{24}^{PSV} &= \mu k \left(k^2 + \beta_{\psi}^2 \right) e^{\beta_{\psi} z_1} & D_{34}^{PSV} &= 2 e^{\beta_{\psi} z_1} k^2 \mu \beta_{\psi} \\
 D_{15}^{PSV} &= -i \omega \rho_f e^{-\alpha_{\phi_f} z_0} & D_{25}^{PSV} &= 0 & D_{35}^{PSV} &= -i e^{-\alpha_{\phi_f} z_1} \omega \rho_f \\
 D_{16}^{PSV} &= -i e^{\alpha_{\phi_f} z_0} \omega \rho_f & D_{26}^{PSV} &= 0 & D_{36}^{PSV} &= -i e^{\alpha_{\phi_f} z_1} \omega \rho_f
 \end{aligned}$$

$$\begin{aligned}
 D_{41}^{PSV} &= -\alpha_{\phi_s} e^{-\alpha_{\phi_s} z_1} & D_{51}^{PSV} &= e^{-\alpha_{\phi_s} z_2} k & D_{61}^{PSV} &= -e^{-\alpha_{\phi_s} z_2} \alpha_{\phi_s} \\
 D_{42}^{PSV} &= \alpha_{\phi_s} e^{\alpha_{\phi_s} z_1} & D_{52}^{PSV} &= e^{\alpha_{\phi_s} z_2} k & D_{62}^{PSV} &= e^{\alpha_{\phi_s} z_2} \alpha_{\phi_s} \\
 D_{43}^{PSV} &= e^{-\beta_{\psi} z_1} k^2 & D_{53}^{PSV} &= -e^{-\beta_{\psi} z_2} \beta_{\psi} k & D_{63}^{PSV} &= e^{-\beta_{\psi} z_2} k^2 \\
 D_{44}^{PSV} &= e^{\beta_{\psi} z_1} k^2 & D_{54}^{PSV} &= e^{\beta_{\psi} z_2} k \beta_{\psi} & D_{64}^{PSV} &= e^{\beta_{\psi} z_2} k^2 \\
 D_{45}^{PSV} &= \frac{-ie^{-\alpha_{\phi_f} z_1} \alpha_{\phi_f}}{\omega} & D_{55}^{PSV} &= 0 & D_{65}^{PSV} &= 0 \\
 D_{46}^{PSV} &= \frac{ie^{\alpha_{\phi_f} z_1} \alpha_{\phi_f}}{\omega} & D_{56}^{PSV} &= 0 & D_{66}^{PSV} &= 0
 \end{aligned}$$

SH coefficient matrix

$$\underline{\underline{D}}_{SH} = \begin{bmatrix} D_{11}^{SH} & D_{12}^{SH} \\ D_{21}^{SH} & D_{22}^{SH} \end{bmatrix} \quad (B.3.2)$$

$$\begin{aligned}
 D_{11}^{SH} &= e^{-\beta_{\chi} z_1} & D_{21}^{SH} &= -e^{-\beta_{\chi} z_2} k \\
 D_{12}^{SH} &= -e^{\beta_{\chi} z_1} & D_{22}^{SH} &= -e^{\beta_{\chi} z_2} k
 \end{aligned} \quad (B.3.3)$$

Roots of the SH dispersion relation

$$\underline{\underline{D}}_{SH} \underline{\underline{x}}_{SH} = \underline{\underline{0}} \quad \rightarrow \quad \begin{bmatrix} e^{-\beta_{\chi} z_1} & -e^{-\beta_{\chi} z_1} \\ e^{-\beta_{\chi} z_2} & e^{\beta_{\chi} z_2} \end{bmatrix} \begin{bmatrix} A_3 \\ B_3 \end{bmatrix} = \begin{bmatrix} 0 \\ 0 \end{bmatrix} \quad (B.3.4)$$

The roots of the determinant of the coefficientmatrix can be found with use of Eulers identity $e^{i\pi} = -1$ and the definition of $\beta_{s,\chi}$ as defined on page [page 16](#)

$$\det(\underline{\underline{D}}_{SH}) = e^{\beta_{\chi} (L-z_2)} + e^{-\beta_{\chi} (L-z_2)} = e^{2\beta_{\chi} (L-z_2)} + 1 = 0 \quad (B.3.5)$$

$$\begin{aligned}
 2\beta_{\chi} (L-z_2) &= (2q-1) i \pi \\
 \beta_{\chi} &= \sqrt{k^2 - \left(\frac{\omega}{c_T}\right)^2} = \frac{(2q-1) i \pi}{2(L-z_2)} \\
 k_q &= \sqrt{\left(\frac{\omega}{c_T}\right)^2 - \frac{\pi^2 (2q-1)^2}{4(L-z_2)^2}} \quad \text{with: } q = 1, 2, 3, \dots \quad (B.3.6)
 \end{aligned}$$

B.4 Displacement & stress field

B.4.1 For the non-symmetric case ($n > 0$)

The displacement and stress fields are constructed with the trigonometric functions, [eq. \(B.4.1\)](#), and Hankel function, [eq. \(B.4.2\)](#), of the second kind, which describe the azimuthal and radial dependence respectively. The vertical dependence of the fields is described with the exponential functions $Z_i(z)$, shown in [eq. \(B.4.3\)](#)

For the radial stresses two variations on the Hankel-matrix, [eqs. \(B.4.12\)](#) and [\(B.4.13\)](#), are introduced to be able to write the radial stresses in vector form.

$$\text{Rotational matrix: } \underline{\underline{R}}_n(\theta) = \begin{bmatrix} \cos(n\theta) & 0 & 0 \\ 0 & -\sin(n\theta) & 0 \\ 0 & 0 & \cos(n\theta) \end{bmatrix} \quad (B.4.1)$$

$$\text{Hankel-matrix: } \underline{\underline{H}}_n(\rho) = \begin{bmatrix} \partial_{\rho} H_n^{(2)}(\rho) & \frac{n}{\rho} H_n^{(2)}(\rho) & 0 \\ \frac{n}{\rho} H_n^{(2)}(\rho) & \partial_{\rho} H_n^{(2)}(\rho) & 0 \\ 0 & 0 & -H_n^{(2)}(\rho) \end{bmatrix} \quad \text{with } \rho = kr \quad (B.4.2)$$

$$\begin{aligned}
 Z_1(z) &= A_1 e^{\alpha_s z} + B_1 e^{-\alpha_s z} & Z_3(z) &= A_3 e^{\beta_s z} + B_3 e^{-\beta_s z} \\
 Z_2(z) &= A_2 e^{\beta_s z} + B_2 e^{-\beta_s z} & Z_4(z) &= A_4 e^{\alpha_f z} + B_4 e^{-\alpha_f z}
 \end{aligned} \tag{B.4.3}$$

$$\text{with: } \alpha_s^2 = k^2 - \left(\frac{\omega}{c_L}\right)^2, \quad \beta_s^2 = k^2 - \left(\frac{\omega}{c_T}\right)^2 \quad \text{and} \quad \alpha_f^2 = k^2 - \left(\frac{\omega}{c_f}\right)^2$$

Fluid velocities & pressure

$$v_{f,r,n}(z, \theta, r) = \cos(n\theta) \cdot \sum_{p=1}^{\infty} C_{PSV,np} \cdot \partial_r H_n^{(2)}(\rho_p) \cdot \hat{v}_{f,r,p}(z) \quad \text{with: } \hat{v}_{f,r,p}(z) = -k_p Z_4(z) \tag{B.4.4a}$$

$$v_{f,\theta,n}(z, \theta, r) = -\sin(n\theta) \cdot \sum_{p=1}^{\infty} C_{PSV,np} \cdot \frac{n}{r} H_n^{(2)}(k_p r) \cdot \hat{v}_{f,\theta,p}(z) \quad \hat{v}_{f,\theta,p}(z) = Z_4(z) \tag{B.4.4b}$$

$$v_{f,z,n}(z, \theta, r) = \cos(n\theta) \cdot \sum_{p=1}^{\infty} C_{PSV,np} \cdot H_n^{(2)}(k_p r) \cdot \hat{v}_{f,z,p}(z) \quad \hat{v}_{f,z,p}(z) = \frac{dZ_4(z)}{dz} \tag{B.4.4c}$$

$$p_{f,n}(z, \theta, r) = \cos(n\theta) \cdot \sum_{p=1}^{\infty} C_{PSV,np} \cdot H_n^{(2)}(k_p r) \cdot \hat{p}_{f,p}(z) \quad \hat{p}_{f,p}(z) = -i\omega\rho_f Z_4(z) \tag{B.4.4d}$$

Soil displacements

$$\underline{u}_{s,n}(z, \theta, r) = \underline{R}_n(\theta) \left(\sum_{p=1}^{\infty} C_{PSV,np} \underline{H}_n(k_p r) \hat{\underline{u}}_{s,p}^{PSV}(z) + \sum_{q=1}^{\infty} C_{SH,nq} \underline{H}_n(k_q r) \hat{\underline{u}}_{s,q}^{SH}(z) \right) \tag{B.4.5}$$

$$\text{with: } \hat{\underline{u}}_{s,p}^{PSV}(z) = \begin{bmatrix} \hat{u}_{s,r,p}(z) & 0 & \hat{u}_{s,z,p}(z) \end{bmatrix}^T \\
 \hat{\underline{u}}_{s,q}^{SH}(z) = \begin{bmatrix} 0 & \hat{u}_{s,\theta,q}(z) & 0 \end{bmatrix}^T$$

$$u_{s,r,n}(z, \theta, r) = \sum_{p=1}^{\infty} C_{PSV,np} \frac{1}{k_p} \partial_r H_n^{(2)}(k_p r) \hat{u}_{s,r,p} + \sum_{q=1}^{\infty} C_{SH,nq} \frac{n}{k_q r} H_n^{(2)}(k_q r) \hat{u}_{s,\theta,q} \tag{B.4.6a}$$

$$u_{s,\theta,n}(z, \theta, r) = \sum_{p=1}^{\infty} C_{PSV,np} \frac{n}{k_p r} H_n^{(2)}(k_p r) \hat{u}_{s,r,p} + \sum_{q=1}^{\infty} C_{SH,nq} \frac{1}{k_q} \partial_r H_n^{(2)}(\rho_q) \hat{u}_{s,\theta,q} \tag{B.4.6b}$$

$$u_{s,z,n}(z, \theta, r) = \sum_{p=1}^{\infty} C_{PSV,np} \cdot -H_n^{(2)}(k_p r) \hat{u}_{s,z,p} \tag{B.4.6c}$$

$$\hat{u}_{s,r,p}(z) = k_p \left(Z_1(z) + \frac{dZ_2(z)}{dz} \right) \tag{B.4.7a}$$

$$\hat{u}_{s,\theta,q}(z) = -k_q Z_3(z) \tag{B.4.7b}$$

$$\hat{u}_{s,z,p}(z) = -k_p^2 Z_2(z) - \frac{dZ_1(z)}{dz} \tag{B.4.7c}$$

Soil stresses (Vertical)

$$\underline{\sigma}_{s,z,n}(z, \theta, r) = \underline{\mathbf{R}}_n(\theta) \left(\sum_{p=1}^{\infty} C_{\text{PSV},np} \underline{\mathbf{H}}_n(k_p r) \underline{\hat{\sigma}}_{s,z,p}^{\text{PSV}}(z) + \sum_{q=1}^{\infty} C_{\text{SH},nq} \underline{\mathbf{H}}_n(k_q r) \underline{\hat{\sigma}}_{s,z,q}^{\text{SH}}(z) \right) \quad (\text{B.4.8})$$

$$\text{with: } \underline{\hat{\sigma}}_{s,z,p}^{\text{PSV}}(z) = \begin{bmatrix} \hat{\sigma}_{s,zr,p}(z) & 0 & \hat{\sigma}_{s,zz,p}(z) \end{bmatrix}^T$$

$$\underline{\hat{\sigma}}_{s,z,q}^{\text{SH}}(z) = \begin{bmatrix} 0 & \hat{\sigma}_{s,z\theta,q}(z) & 0 \end{bmatrix}^T$$

$$\sigma_{s,zr,n}(z, \theta, r) = \sum_{p=1}^{\infty} C_{\text{PSV},np} \frac{1}{k_p} \partial_r H_n^{(2)}(k_p r) \hat{\sigma}_{s,zr,p}(z) + \sum_{q=1}^{\infty} C_{\text{SH},nq} \frac{n}{k_q r} H_n^{(2)}(k_q r) \hat{\sigma}_{s,z\theta,q}(z) \quad (\text{B.4.9a})$$

$$\sigma_{s,z\theta,n}(z, \theta, r) = \sum_{p=1}^{\infty} C_{\text{PSV},np} \frac{n}{k_p r} H_n^{(2)}(k_p r) \hat{\sigma}_{s,zr,p}(z) + \sum_{q=1}^{\infty} C_{\text{SH},nq} \frac{1}{k_q} \partial_r H_n^{(2)}(\rho_q) \hat{\sigma}_{s,z\theta,q}(z) \quad (\text{B.4.9b})$$

$$\sigma_{s,zz,n}(z, \theta, r) = \sum_{p=1}^{\infty} C_{\text{PSV},np} \cdot -H_n^{(2)}(k_p r) \hat{\sigma}_{s,zz,p}(z) \quad (\text{B.4.9c})$$

$$\hat{\sigma}_{s,zr,p}(z) = \mu \left(\frac{d\hat{u}_{s,r,p}(z)}{dz} - k_p \hat{u}_{s,z,p}(z) \right) \quad (\text{B.4.10a})$$

$$\hat{\sigma}_{s,z\theta,q}(z) = \mu \frac{d\hat{u}_{s,\theta,q}(z)}{dz} \quad (\text{B.4.10b})$$

$$\hat{\sigma}_{s,zz,p}(z) = \lambda k_p \hat{u}_{s,r,p}(z) + (2\mu + \lambda) \frac{d\hat{u}_{s,z,p}(z)}{dz} \quad (\text{B.4.10c})$$

Soil stresses (Radial & other)

$$\underline{\sigma}_{s,r,n}(z, \theta, r) = \underline{\mathbf{R}}_n(\theta) \left(\sum_{p=1}^{\infty} C_{\text{PSV},np} \underline{\mathbf{H}}_n^*(k_p r) \underline{\hat{\sigma}}_{s,r,p}^{\text{PSV}}(z) + \sum_{q=1}^{\infty} C_{\text{SH},nq} \underline{\mathbf{H}}_n^{**}(k_q r) \underline{\hat{\sigma}}_{s,r,q}^{\text{SH}}(z) \right) \quad (\text{B.4.11})$$

$$\text{with: } \underline{\hat{\sigma}}_{s,r,p}^{\text{PSV}}(z) = \begin{bmatrix} \hat{\sigma}_{s,rr,p}^{\text{PSV},1}(z) & \hat{\sigma}_{s,rr,p}^{\text{PSV},2}(z) & \hat{\sigma}_{s,zr,p}(z) \end{bmatrix}^T$$

$$\underline{\hat{\sigma}}_{s,r,q}^{\text{SH}}(z) = \begin{bmatrix} \hat{\sigma}_{s,rr,q}^{\text{SH}}(z) & \hat{\sigma}_{s,z\theta,q}(z) \end{bmatrix}^T$$

$$\underline{\mathbf{H}}_n^*(\rho) = \begin{bmatrix} -H_n^{(2)}(\rho) & h_{1,n}(\rho) & 0 \\ 0 & h_{2,n}(\rho) & 0 \\ 0 & 0 & \partial_\rho H_n^{(2)}(\rho) \end{bmatrix} \quad \text{with } \rho = kr \quad (\text{B.4.12})$$

$$\underline{\mathbf{H}}_n^{**}(\rho) = \begin{bmatrix} -h_{2,n}(\rho) & 0 \\ h_{3,n}(\rho) & 0 \\ 0 & \frac{n}{\rho} H_n^{(2)}(\rho) \end{bmatrix} \quad (\text{B.4.13})$$

$$\sigma_{s,rr,n}(z, \theta, r) = \cos(n\theta) \left(\sum_{p=1}^{\infty} C_{PSV,np} \left[-\hat{\sigma}_{s,rr,p}^{PSV,1}(z) \cdot H_n^{(2)}(k_p r) + \hat{\sigma}_{s,rr,p}^{PSV,2}(z) \cdot h_{1,n}(k_p r) \right] \right. \\ \left. + \sum_{q=1}^{\infty} C_{SH,nq} \left[-\hat{\sigma}_{s,rr,q}^{SH}(z) \cdot h_{2,n}(k_q r) \right] \right) \quad (\text{B.4.14a})$$

$$\sigma_{s,r\theta,n}(z, \theta, r) = -\sin(n\theta) \left(\sum_{p=1}^{\infty} C_{PSV,np} \left[\hat{\sigma}_{s,rr,p}^{PSV,2}(z) \cdot h_{2,n}(k_p r) \right] \right. \\ \left. + \sum_{q=1}^{\infty} C_{SH,nq} \left[\hat{\sigma}_{s,rr,q}^{SH}(z) \cdot h_{3,n}(k_q r) \right] \right) \quad (\text{B.4.14b})$$

$$\sigma_{s,\theta\theta,n}(z, \theta, r) = \cos(n\theta) \left(\sum_{p=1}^{\infty} C_{PSV,np} \left[-\hat{\sigma}_{s,rr,p}^{PSV,1}(z) \cdot H_n^{(2)}(k_p r) + \hat{\sigma}_{s,rr,p}^{PSV,2}(z) \cdot \frac{1}{k_p^2} \partial_r^2 H_n^{(2)}(k_p r) \right] \right. \\ \left. + \sum_{q=1}^{\infty} C_{SH,nq} \left[\hat{\sigma}_{s,rr,q}^{SH}(z) \cdot h_{2,n}(k_q r) \right] \right) \quad (\text{B.4.14c})$$

With:

$$h_{1,n}(\rho) = \frac{n^2}{\rho^2} H_n^{(2)}(\rho) - \frac{1}{\rho} \partial_\rho H_n^{(2)}(\rho) \quad \hat{\sigma}_{s,rr,p}^{PSV,1}(z) = \lambda \frac{d\hat{u}_{s,z,p}(z)}{dz} + k_p (2\mu + \lambda) \hat{u}_{s,r,p}(z) \quad (\text{B.4.15a})$$

$$h_{2,n}(\rho) = \partial_\rho \left(\frac{n}{\rho} H_n^{(2)}(\rho) \right) \quad \hat{\sigma}_{s,rr,p}^{PSV,2}(z) = 2\mu k_p \hat{u}_{s,r,p}(z) \quad (\text{B.4.15b})$$

$$h_{3,n}(\rho) = -\partial_\rho^2 H_n^{(2)}(\rho) - \frac{1}{2} H_n^{(2)}(\rho) \quad \hat{\sigma}_{s,rr,q}^{SH}(z) = -2\mu k_q \hat{u}_{s,\theta,q}(z) \quad (\text{B.4.15c})$$

with: $\rho = kr$

B.4.2 For the axi-symmetric case ($n = 0$)

In this subsection an overview is given of the modal expansions of the stresses and displacements. The expressions in this appendix are directly retrieved from [3]. Note that these expressions are equal to the expressions of the non-symmetrical case in [appendix B.4.1](#) when $n = 0$ is substituted into the latter.

Fluid velocities & pressure

$$v_{f,r} = \sum_{p=1}^{\infty} C_{\text{PSV},0p} H_1^{(2)}(k_p r) \hat{v}_{f,r,p}(z) \quad \text{with:} \quad \hat{v}_{f,r,p}(z) = -k_p Z_4(z) \quad (\text{B.4.16a})$$

$$v_{f,z} = \sum_{p=1}^{\infty} C_{\text{PSV},0p} H_0^{(2)}(k_p r) \hat{v}_{f,z,p}(z) \quad \hat{v}_{f,z,p}(z) = \frac{dZ_4(z)}{dz} \quad (\text{B.4.16b})$$

$$p_f = \sum_{p=1}^{\infty} C_{\text{PSV},0p} H_0^{(2)}(k_p r) \hat{p}_{f,p}(z) \quad \hat{p}_{f,p}(z) = -\omega \rho_f Z_4(z) \quad (\text{B.4.16c})$$

Soil displacements & stresses

$$u_{s,r} = \sum_{p=1}^{\infty} C_{\text{PSV},0p} H_1^{(2)}(k_p r) \hat{u}_{s,r,p}(z) \quad \text{with:} \quad \hat{u}_{s,r,p}(z) = - \left(k Z_1(z) + \frac{dZ_2(z)}{dz} \right) \quad (\text{B.4.17a})$$

$$u_{s,z} = \sum_{p=1}^{\infty} C_{\text{PSV},0p} H_0^{(2)}(k_p r) \hat{u}_{s,z,p}(z) \quad \hat{u}_{s,z,p}(z) = \frac{dZ_1(z)}{dz} + Z_2(z) \quad (\text{B.4.17b})$$

$$\sigma_{s,zr} = \sum_{p=1}^{\infty} C_{\text{PSV},0p} H_1^{(2)}(k_p r) \hat{\sigma}_{s,zr,p}(z) \quad \text{with:} \quad \hat{\sigma}_{s,zr,p}(z) = \mu \left(\frac{d\hat{u}_{s,r,p}(z)}{dz} - k_p \hat{u}_{s,z,p}(z) \right) \quad (\text{B.4.18a})$$

$$\sigma_{s,zz} = \sum_{p=1}^{\infty} C_{\text{PSV},0p} H_0^{(2)}(k_p r) \hat{\sigma}_{s,zz,p}(z) \quad \hat{\sigma}_{s,zz,p}(z) = k_p \lambda \hat{u}_{s,r,p} + \rho c_L^2 \frac{d\hat{u}_{s,z,p}(z)}{dz} \quad (\text{B.4.18b})$$

$$\sigma_{s,rr} = \sum_{p=1}^{\infty} C_{\text{PSV},0p} \left(H_0^{(2)}(k_p r) \hat{\sigma}_{s,rr,p}^{H_0}(z) \right) \quad \hat{\sigma}_{s,rr,p}^{H_0}(z) = k_p \rho_s c_L^2 \hat{u}_{s,r,p}(z) + \lambda \frac{d\hat{u}_{s,z,p}(z)}{dz} \quad (\text{B.4.18c})$$

$$+ \frac{1}{r} H_1^{(2)}(k_p r) \hat{\sigma}_{s,rr,p}^{H_1}(z) \quad \hat{\sigma}_{s,rr,p}^{H_1}(z) = -2 \mu \hat{u}_{s,r,p}(z) \quad (\text{B.4.18d})$$

Vertical modes

Displacement modes

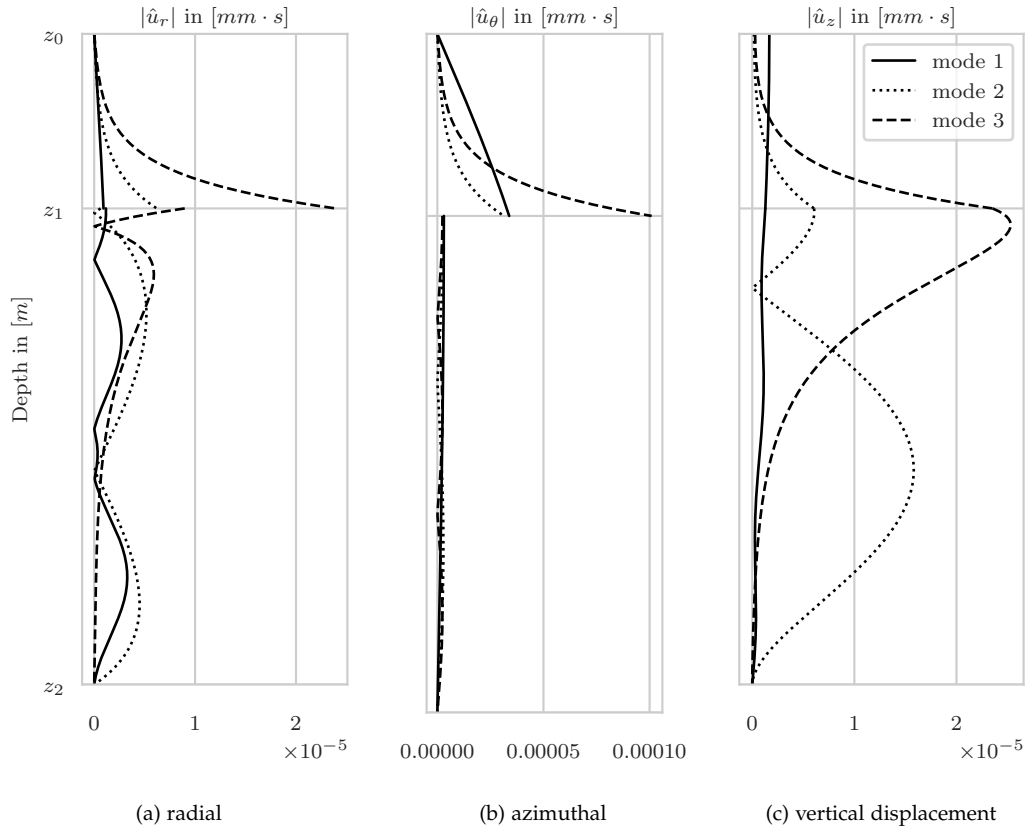


Figure B.1: First three displacement modes for $n > 0$ and $f = 10$ Hz

Figure B.2: First three displacement modes for $n = 0$ and $f = 10$ Hz

Vertical stress modes

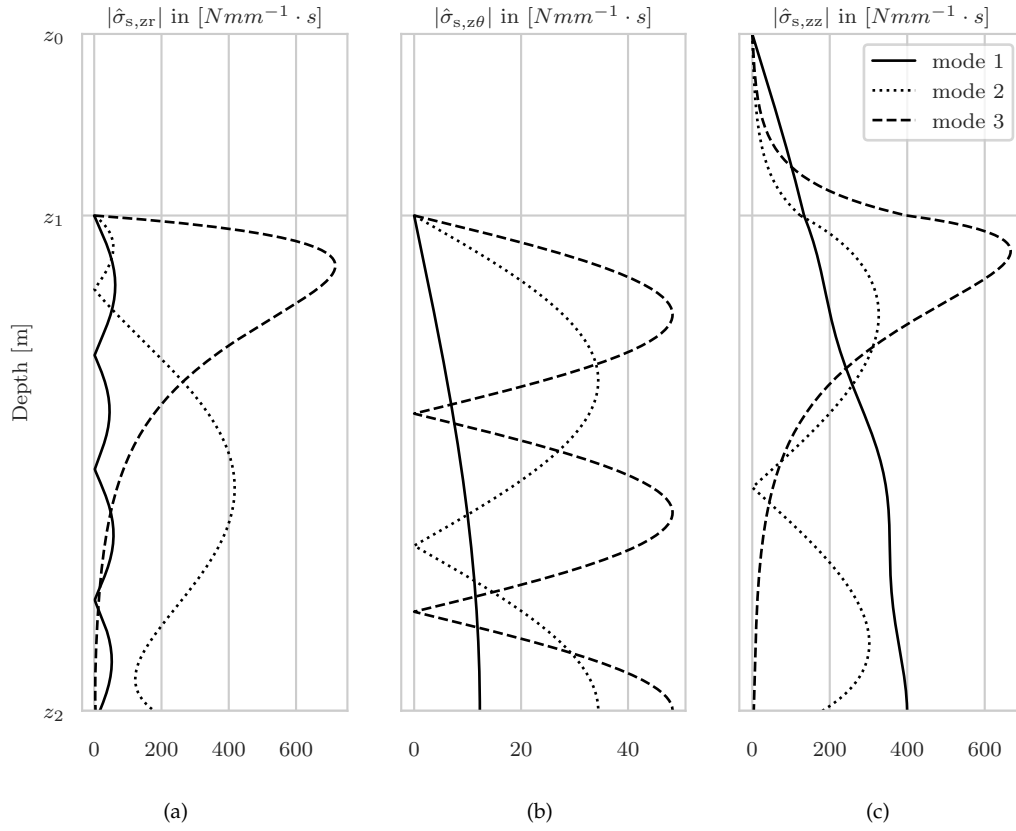


Figure B.3: First three vertical stress modes for $n > 0$ and $f = 10$ Hz, in subfigure (c) p_f is plotted above σ_{zz}

Figure B.4: First three vertical stress modes for $n = 0$ and $f = 10$ Hz, in subfigure (c) p_f is plotted above σ_{zz}

Radial stress modes

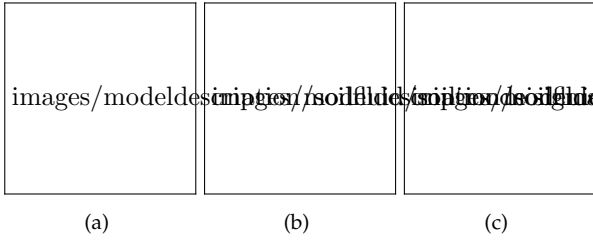


Figure B.5: First three radial stress modes for $n > 0$ and $f = 10$ Hz

Figure B.6: First three radial stress modes for $n = 0$ and $f = 10$ Hz

Appendix C

Modematching

C.1 Overview matching equations

This appendix contains the mode-matching equations introduced in [chapter 4](#). Note that in the body of the thesis the inner-product notation is used, while in this appendix the traditional integral notation is used. The integral limits are related to the geometry as illustrated in the modeloverview [fig. C.1](#).

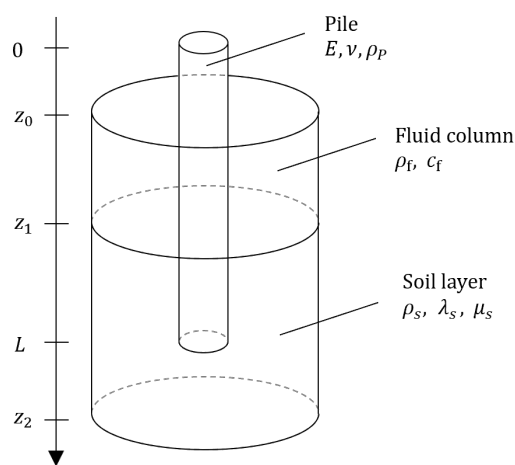


Figure C.1: Model overview

C.1.1 Generic equations

Non-symmetric case

The following equations are alternative notations to eqs. (4.1.3a), (4.1.4a) and (4.1.7a) respectively.

$$\sum_{m=1}^{\infty} C_{P,nm} \hat{F}_{1,nlm} = \sum_{p=1}^{\infty} C_{PSV,np} \hat{F}_{2,nlp} + \sum_{q=1}^{\infty} C_{SH,nq} \hat{F}_{3,nlq} \quad (\text{C.1.1a})$$

$$\begin{aligned} \hat{F}_{1,nlm} = & \int_{z_0}^{z_1} \hat{u}_{P,r,m}(z) \cdot \hat{w}_{s,r,l}^{\text{PSV}}(z) + \hat{u}_{P,\theta,m}(z) \cdot \hat{w}_{s,\theta,l}^{\text{PSV}}(z) \, dz + \text{hat}u_{P,z,m}(z) \cdot \hat{w}_{s,z,l}^{\text{PSV}}(z) \, dz \\ & + \int_{z_1}^L \hat{u}_{P,r,m}(z) \cdot \hat{w}_{f,l}(z) \, dz \end{aligned} \quad (\text{C.1.1b})$$

$$\begin{aligned} \hat{F}_{2,nlp} = & \int_{z_1}^{z_2} u_{s,r,np}^{\text{PSV}}(z, R) \cdot \hat{w}_{s,r,l}^{\text{PSV}}(z) \, dz + u_{s,\theta,np}^{\text{PSV}}(z, R) \cdot \hat{w}_{s,\theta,l}^{\text{PSV}}(z) \, dz + u_{s,z,np}^{\text{PSV}}(z, R) \cdot \hat{w}_{s,z,l}^{\text{PSV}}(z) \, dz \\ & + \int_{z_0}^{z_1} u_{f,r,np}(z, R) \cdot \hat{w}_{f,l}(z) \, dz \end{aligned} \quad (\text{C.1.1c})$$

$$\hat{F}_{3,nlq} = \int_{z_1}^{z_2} \hat{u}_{s,r,nq}^{\text{SH}}(z, R) \cdot \hat{w}_{s,r,l}^{\text{PSV}}(z) + \hat{u}_{s,\theta,nq}^{\text{SH}}(z, R) \cdot \hat{w}_{s,\theta,l}^{\text{PSV}}(z) \, dz \quad (\text{C.1.1d})$$

$$\sum_{m=1}^{\infty} C_{P,nm} \hat{F}_{4,njm} = \sum_{p=1}^{\infty} C_{PSV,np} \hat{F}_{5,njp} + \sum_{q=1}^{\infty} C_{SH,nq} \hat{F}_{6,njq} \quad (\text{C.1.2a})$$

$$\hat{F}_{4,njm} = \int_{z_1}^L \hat{u}_{P,r,m}(z) \cdot \hat{w}_{s,r,j}^{\text{SH}}(z) + \hat{u}_{P,\theta,m}(z) \cdot \hat{w}_{s,\theta,j}^{\text{SH}}(z) + \hat{u}_{P,z,m}(z) \cdot \hat{w}_{s,z,j}^{\text{SH}}(z) \, dz \quad (\text{C.1.2b})$$

$$\hat{F}_{5,njp} = \int_{z_1}^{z_2} u_{s,r,np}^{\text{PSV}}(z, R) \cdot \hat{w}_{s,r,j}^{\text{SH}}(z) + u_{s,\theta,np}^{\text{PSV}}(z, R) \cdot \hat{w}_{s,\theta,j}^{\text{SH}}(z) + u_{s,z,np}^{\text{PSV}}(z, R) \cdot \hat{w}_{s,z,j}^{\text{SH}}(z) \, dz \quad (\text{C.1.2c})$$

$$\hat{F}_{6,njq} = \int_{z_1}^{z_2} \hat{u}_{s,r,nq}^{\text{SH}}(z, R) \cdot \hat{w}_{s,r,j}^{\text{SH}}(z) + \hat{u}_{s,\theta,nq}^{\text{SH}}(z, R) \cdot \hat{w}_{s,\theta,j}^{\text{SH}}(z) \, dz \quad (\text{C.1.2d})$$

$$\sum_{m=1}^{\infty} C_{P,nm} \hat{F}_{7,nkm} = \sum_{p=1}^{\infty} C_{PSV,np} \hat{F}_{8,nkp} + \sum_{q=1}^{\infty} C_{SH,nq} \hat{F}_{9,nkq} + \hat{F}_{10,k} \quad \text{with} \quad k = 1, \dots, N_P \quad (\text{C.1.3a})$$

$$\hat{F}_{7,nkm} = (\omega_{nm}^2 - \omega^2) \rho h R \Gamma_{P,nm} \delta_{mk} \quad (\text{C.1.3b})$$

$$\hat{F}_{8,nkp} = \int_{z_0}^{z_1} \hat{u}_{P,r,k}(z) \cdot \underbrace{\left[-H_n^{(2)}(k_p R) \hat{p}_{f,p}(z) \right]}_{p_{f,np}(z,R)} dz \quad (\text{C.1.3c})$$

$$+ \int_{z_1}^L \left(\hat{u}_{P,r,k}(z) \cdot \underbrace{\left[-\hat{\sigma}_{s,rr,p}^{\text{PSV},1}(z) \cdot H_n^{(2)}(k_p R) + \hat{\sigma}_{s,rr,p}^{\text{PSV},2}(z) \cdot h_{1,n}(k_p R) \right]}_{\sigma_{s,rr,np}^{\text{PSV}}(z,R)} \right. \\ \left. + \hat{u}_{P,\theta,k}(z) \cdot \underbrace{\left[\hat{\sigma}_{s,rr,p}^{\text{PSV},2}(z) \cdot h_{2,n}(k_p R) \right]}_{\sigma_{r\theta,np}^{\text{PSV}}(z,R)} + \hat{u}_{P,z,k}(z) \cdot \underbrace{\left[\hat{\sigma}_{s,zr,p}(z) \cdot \frac{1}{k_p} \partial_r H_n^{(2)}(k_p R) \right]}_{\sigma_{s,rz,np}^{\text{PSV}}(z,R)} \right) dz$$

$$\hat{F}_{9,nkq} = \int_{z_1}^{z_2} \left(\hat{u}_{P,r,k}(z) \cdot \underbrace{\left[-\hat{\sigma}_{s,rr,q}^{\text{SH}}(z) \cdot h_{2,n}(k_q R) \right]}_{\sigma_{s,rr,nq}^{\text{SH}}(z,R)} + \hat{u}_{P,\theta,k}(z) \cdot \underbrace{\left[\hat{\sigma}_{s,rr,q}^{\text{SH}}(z) \cdot h_{3,n}(k_q R) \right]}_{\sigma_{r\theta,nq}^{\text{SH}}(z,R)} \right. \\ \left. + \hat{u}_{P,z,k}(z) \cdot \underbrace{\left[\hat{\sigma}_{s,z\theta,q}(z) \cdot \frac{n}{k_q r} H_n^{(2)}(k_q R) \right]}_{\sigma_{s,rz,nq}^{\text{SH}}(z,R)} \right) dz \quad (\text{C.1.3d})$$

$$\hat{F}_{10,k} = \int_0^L \hat{\mathbf{u}}_{P,k}^T \hat{\mathbf{f}}_e \delta(z) dz = \hat{u}_{P,r,k}(0) \hat{f}_{e,r} + \hat{u}_{P,\theta,k}(0) \hat{f}_{e,\theta} + \hat{u}_{P,z,k}(0) \hat{f}_{e,z} \quad (\text{C.1.3e})$$

Symmetric case

The following equations are alternative notations to eqs. (4.1.8) and (4.1.9a) respectively.

$$\sum_{m=1}^{\infty} C_{P,0m} \hat{F}_{1,lm} = \sum_{p=1}^{\infty} C_{PSV,0p} \hat{F}_{2,lp} \quad (\text{C.1.4a})$$

$$\hat{F}_{1,lm} = \int_{z_0}^{z_1} \hat{u}_{P,r,m}(z) \cdot \hat{w}_{f,l}(z) dz + \int_{z_1}^L \hat{u}_{P,r,m}(z) \cdot \hat{w}_{s,r,l}^{\text{PSV}}(z) + \hat{u}_{P,z,m}(z) \cdot \hat{w}_{s,z,l}^{\text{PSV}}(z) dz \quad (\text{C.1.4b})$$

$$\hat{F}_{2,lp} = \int_{z_1}^{z_2} u_{f,r,p}(z, R) \cdot \hat{w}_{f,l}(z) + u_{s,r,p}(z, R) \cdot \hat{w}_{s,r,l}^{\text{PSV}}(z) + u_{s,z,p}(z, R) \cdot \hat{w}_{s,z,l}^{\text{PSV}}(z) dz \quad (\text{C.1.4c})$$

$$\sum_{m=1}^{\infty} C_{P,0m} \hat{F}_{3,km} = \sum_{p=1}^{\infty} C_{PSV,0p} \hat{F}_{4,kp} + \hat{F}_{5,k} \quad \text{with} \quad k = 1, \dots, N_P \quad (\text{C.1.5a})$$

$$\hat{F}_{3,km} = (\omega_{0m}^2 - \omega^2) \rho h R \Gamma_{P,0m} \delta_{mk} \quad (\text{C.1.5b})$$

$$\hat{F}_{4,kp} = \int_{z_0}^{z_1} \hat{u}_{P,r,k}(z) \cdot \underbrace{\left[-\hat{p}_{f,p}(z) H_0^{(2)}(k_p R) \right]}_{p_{\ell,0p}(z,R)} dz \quad (\text{C.1.5c})$$

$$+ \int_{z_1}^L \hat{u}_{P,z,k}(z) \cdot \underbrace{\left[\hat{\sigma}_{s,zr,p}^{H_1}(z) H_1^{(2)}(k_p R) \right]}_{\sigma_{s,rz,0p}(z,R)} \hat{u}_{P,r,k}(z) \cdot \underbrace{\left[\hat{\sigma}_{s,rr,p}^{H_0}(z) H_0^{(2)}(k_p R) + \hat{\sigma}_{s,rr,p}^{H_1}(z) H_1^{(2)}(k_p R) \right]}_{\sigma_{s,rr,0p}(z,R)} dz$$

$$\hat{F}_{5,k} = \hat{u}_{P,r,k}(0) \hat{f}_{e,r} + \hat{u}_{P,z,k}(0) \hat{f}_{e,z} \quad (\text{C.1.5d})$$

C.1.2 Orthogonality method

Non-symmetric case

The following equations are alternative notations to eqs. (4.2.3) and (4.2.4a) respectively.

$$\sum_{m=1}^{\infty} C_{P,nm} \hat{F}_{1,nlm} = \sum_{p=1}^{\infty} C_{PSV,np} \hat{F}_{2,nlp} + \sum_{q=1}^{\infty} C_{SH,nq} \hat{F}_{3,nlq} \quad (\text{C.1.6a})$$

$$\hat{F}_{1,nlm} = \int_{z_0}^{z_1} \hat{u}_{P,r,m}(z) \cdot [-\hat{p}_{\ell,l}(z)] dz \quad (\text{C.1.6b})$$

$$+ \int_{z_1}^L \left(\hat{u}_{P,r,m}(z) \cdot \underbrace{\left[\zeta_s k_l \hat{u}_{s,r,l}(z) + \eta_s \hat{\sigma}_{s,zz,l}(z) \right]}_{\hat{w}_{s,r,l}^{\text{PSV}}(z)} + \hat{u}_{P,z,m}(z) \cdot \underbrace{\left[-\frac{1}{k_l} \hat{\sigma}_{s,zr,l}^{\text{PSV}}(z) \right]}_{\hat{w}_{s,z,l}^{\text{PSV}}(z)} \right) dz$$

$$\hat{F}_{2,nlp} = \int_{z_0}^{z_1} \left(\underbrace{\left[\hat{u}_{f,r,p}(z) \cdot \partial_r H_n^{(2)}(k_p R) \right]}_{u_{\ell,r,np}^{\text{PSV}}(z,R)} \cdot [-\hat{p}_{\ell,l}(z)] \right) dz \quad (\text{C.1.6c})$$

$$+ \int_{z_1}^{z_2} \left(\underbrace{\left[\hat{u}_{s,r,p}(z) \cdot \frac{1}{k_p} \partial_r H_n^{(2)}(k_p R) \right]}_{u_{s,r,np}^{\text{PSV}}(z,R)} \cdot \left[\zeta_s k_l \hat{u}_{s,r,l}(z) + \eta_s \hat{\sigma}_{s,zz,l}(z) \right] \right.$$

$$\left. + \underbrace{\left[\hat{u}_{s,z,p}(z) \cdot -H_n^{(2)}(k_p R) \right]}_{u_{s,z,np}^{\text{PSV}}(z,R)} \cdot \left[-\frac{1}{k_l} \hat{\sigma}_{s,zr,l}^{\text{PSV}}(z) \right] \right) dz$$

$$\hat{F}_{3,nlq} = \int_{z_1}^{z_2} \left(\underbrace{\left[\hat{u}_{s,\theta,q}(z) \cdot \frac{n}{k_q r} H_n^{(2)}(k_q R) \right]}_{u_{s,r,nq}^{\text{SH}}(z,R)} \left[\zeta_s k_l \hat{u}_{s,r,l}(z) + \eta_s \hat{\sigma}_{s,zz,l}(z) \right] \right) dz \quad (\text{C.1.6d})$$

$$\sum_{m=1}^{\infty} C_{P,nm} \hat{F}_{4,njm} = \sum_{p=1}^{\infty} C_{PSV,np} \hat{F}_{5,njp} + \sum_{q=1}^{\infty} C_{SH,nq} \hat{F}_{6,njq} \quad (\text{C.1.7a})$$

$$\hat{F}_{4,njm} = \int_{z_1}^L \left(\hat{u}_{P,\theta,m}(z) \cdot \underbrace{\left[\mu k_j^2 \hat{u}_{s,\theta,j}^{\text{SH}} \right]}_{\hat{w}_{s,\theta,j}^{\text{SH}}(z)} \right) dz \quad (\text{C.1.7b})$$

$$\hat{F}_{5,njp} = \int_{z_1}^{z_2} \left(\underbrace{\left[\hat{u}_{s,r,p}(z) \cdot \frac{n}{k_p r} H_n^{(2)}(k_p R) \right]}_{u_{s,\theta,np}^{\text{PSV}}(z,R)} \cdot \left[\mu k_j^2 \hat{u}_{s,\theta,j}^{\text{SH}} \right] \right) dz \quad (\text{C.1.7c})$$

$$\hat{F}_{6,njq} = \int_{z_1}^{z_2} \left(\underbrace{\left[\hat{u}_{s,\theta,q}(z) \cdot \frac{1}{k_q} \partial_r H_n^{(2)}(k_q R) \right]}_{u_{s,\theta,nq}^{\text{SH}}(z,R)} \cdot \left[\mu k_j^2 \hat{u}_{s,\theta,j}^{\text{SH}} \right] \right) dz \quad (\text{C.1.7d})$$

Symmetric case

The following equation is alternative notations to eq. (4.2.6a).

$$\sum_{m=1}^{\infty} C_{P,0m} \hat{F}_{1,nlm} = \sum_{p=1}^{\infty} C_{PSV,0p} \hat{F}_{2,nlp} \quad (\text{C.1.8a})$$

$$\hat{F}_{1,nlm} = \int_{z_0}^{z_1} \left(\hat{u}_{P,r,m}(z) \cdot \underbrace{\left[-\hat{p}_{\ell,l}(z) \right]}_{\hat{w}_{\ell,l}(z)} \right) dz \quad (\text{C.1.8b})$$

$$+ \int_{z_1}^L \left(\hat{u}_{P,r,m}(z) \cdot \underbrace{\left[\zeta_s k_l \hat{u}_{s,r,l}(z) + \eta_s \hat{\sigma}_{s,zz,l}(z) \right]}_{\hat{w}_{s,r,l}^{\text{PSV}}(z)} + \hat{u}_{P,z,m}(z) \cdot \underbrace{\left[-\frac{1}{k_l} \hat{\sigma}_{s,zr,l}(z) \right]}_{\hat{w}_{s,z,l}^{\text{PSV}}(z)} \right) dz$$

$$\hat{F}_{2,nlp} = \int_{z_0}^{z_1} \left(\underbrace{\left[H_1^{(2)}(k_p r) \hat{u}_{\ell,r,p}(z) \right]}_{u_{\ell,r,np}(z,R)} \cdot \left[-\hat{p}_{\ell,l}(z) \right] \right) dz \quad (\text{C.1.8c})$$

$$+ \int_{z_1}^{z_2} \left(\underbrace{\left[H_1^{(2)}(k_p r) \hat{u}_{s,r,p}(z) \right]}_{u_{s,r,np}(z,R)} \cdot \left[\zeta_s k_l \hat{u}_{s,r,l}(z) + \eta_s \hat{\sigma}_{s,zz,l}(z) \right] \right)$$

$$+ \underbrace{\left[H_0^{(2)}(k_p r) \hat{u}_{s,z,p}(z) \right]}_{u_{z,r,np}(z,R)} \cdot \left[-\frac{1}{k_l} \hat{\sigma}_{s,zr,l}(z) \right] \right) dz$$

C.1.3 Point-Collocation method

Non-symmetric case

The following equations are alternative notations to eqs. (4.3.3a) and (4.3.2) respectively.

$$\sum_{m=1}^{\infty} C_{P,nm} \hat{F}_{1,nlm} = \sum_{p=1}^{\infty} C_{PSV,np} \hat{F}_{2,nlp} + \sum_{q=1}^{\infty} C_{SH,nq} \hat{F}_{3,nlq} \quad (\text{C.1.9a})$$

$$\hat{F}_{1,nlm} = \int_{z_0}^{z_1} \left(\hat{u}_{P,r,m}(z) \cdot \underbrace{\left[-\hat{p}_{f,l}(z) \cdot H_n^{(2)}(k_l R) \right]}_{\hat{w}_{f,l}^{\text{PSV}}(z)} \right) dz \quad (\text{C.1.9b})$$

$$+ \int_{z_1}^L \left(\hat{u}_{P,r,m}(z) \cdot \underbrace{\left[-\hat{\sigma}_{s,rr,p}^{\text{PSV},1}(z) \cdot H_n^{(2)}(k_p R) + \hat{\sigma}_{s,rr,p}^{\text{PSV},2}(z) \cdot h_{1,n}(k_p R) \right]}_{\hat{w}_{s,r,l}^{\text{PSV}}(z)} \right. \\ \left. + \hat{u}_{P,\theta,m}(z) \cdot \underbrace{\left[\hat{\sigma}_{s,rl}^{\text{PSV},2}(z) \cdot h_{2,n}(k_l R) \right]}_{\hat{w}_{s,\theta,l}^{\text{PSV}}(z)} + \hat{u}_{P,z,m}(z) \cdot \underbrace{\left[\hat{\sigma}_{s,zr,l}(z) \cdot \frac{1}{k_l} \partial_r H_n^{(2)}(k_l R) \right]}_{\hat{w}_{s,z,l}^{\text{PSV}}(z)} \right) dz$$

$$\hat{F}_{2,nlp} = \int_{z_0}^{z_1} \left(\underbrace{\left[\hat{u}_{f,r,p}(z) \cdot \partial_r H_n^{(2)}(k_p R) \right]}_{u_{f,r,np}(z,R)} \cdot \left[-\hat{p}_{f,l}(z) H_n^{(2)}(k_l R) \right] \right) dz \quad (\text{C.1.9c})$$

$$+ \int_{z_1}^{z_2} \left(\underbrace{\left[\hat{u}_{s,r,p}(z) \cdot \frac{1}{k_p} \partial_r H_n^{(2)}(k_p R) \right]}_{u_{s,\bar{r},np}^{\text{PSV}}(z,R)} \cdot \left[-\hat{\sigma}_{s,rr,l}^{\text{PSV},1}(z) H_n^{(2)}(k_l R) + \hat{\sigma}_{s,rr,l}^{\text{PSV},2}(z) h_{1,n}(k_l R) \right] \right. \\ \left. + \underbrace{\left[\hat{u}_{s,\theta,p}(z) \cdot \frac{n}{k_p r} H_n^{(2)}(k_p R) \right]}_{u_{s,\theta,np}^{\text{PSV}}(z,R)} \cdot \left[\hat{\sigma}_{s,rl}^{\text{PSV},2}(z) h_{2,n}(k_l R) \right] \right. \\ \left. + \underbrace{\left[\hat{u}_{s,z,p}(z) \cdot -H_n^{(2)}(k_p R) \right]}_{u_{s,z,np}^{\text{PSV}}(z,R)} \cdot \left[\hat{\sigma}_{s,zr,l}(z) \frac{1}{k_l} \partial_r H_n^{(2)}(k_l R) \right] \right) dz$$

$$\hat{F}_{3,nlq} = \int_{z_1}^{z_2} \left(\underbrace{\left[\hat{u}_{s,\theta,q}(z) \cdot \frac{n}{k_q R} H_n^{(2)}(k_q R) \right]}_{u_{s,\bar{r},nq}^{\text{SH}}(z,R)} \cdot \left[-\hat{\sigma}_{s,rr,l}^{\text{PSV},1}(z) H_n^{(2)}(k_l R) + \hat{\sigma}_{s,rr,l}^{\text{PSV},2}(z) h_{1,n}(k_l R) \right] \right. \quad (\text{C.1.9d})$$

$$\left. + \underbrace{\left[\hat{u}_{s,\theta,q}(z) \cdot \frac{1}{k_q} \partial_r H_n^{(2)}(k_q R) \right]}_{u_{s,\theta,nq}^{\text{SH}}(z,R)} \cdot \left[\hat{\sigma}_{s,rl}^{\text{PSV},2}(z) h_{2,n}(k_l R) \right] \right) dz$$

$$\sum_{m=1}^{\infty} C_{P,nm} \hat{F}_{4,njm} = \sum_{p=1}^{\infty} C_{PSV,np} \hat{F}_{5,njp} + \sum_{q=1}^{\infty} C_{SH,nq} \hat{F}_{6,njq} \quad (\text{C.1.10a})$$

$$\begin{aligned} \hat{F}_{4,njm} = \int_{z_1}^L & \left(\hat{u}_{P,r,m}(z) \cdot \underbrace{\left[-\hat{\partial}_{s,rr,j}^{SH}(z) h_{2,n}(k_j R) \right]}_{\hat{w}_{s,r,j}^{SH}(z)} \right. \\ & \left. + \hat{u}_{P,\theta,m}(z) \cdot \underbrace{\left[\hat{\partial}_{s,rr,j}^{SH}(z) h_{3,n}(k_j R) \right]}_{\hat{w}_{s,\theta,j}^{SH}(z)} + \hat{u}_{P,z,m}(z) \cdot \underbrace{\left[\hat{\partial}_{s,z\theta,j}^{SH}(z) \frac{n}{k_j R} H_n^{(2)}(k_j R) \right]}_{\hat{w}_{s,z,j}^{SH}(z)} \right) dz \end{aligned} \quad (\text{C.1.10b})$$

$$\begin{aligned} \hat{F}_{5,njp} = \int_{z_1}^{z_2} & \left[\underbrace{\left[\hat{u}_{s,r,p}(z) \cdot \frac{1}{k_p} \partial_r H_n^{(2)}(k_p R) \right]}_{u_{s,r,np}^{PSV}(z,R)} \cdot \left[-\hat{\partial}_{s,rr,j}^{SH}(z) h_{2,n}(k_j R) \right] \right. \\ & + \left[\underbrace{\left[\hat{u}_{s,\theta,p}(z) \cdot \frac{n}{k_p R} H_n^{(2)}(k_p R) \right]}_{u_{s,\theta,np}^{PSV}(z,R)} \cdot \left[\hat{\partial}_{s,rr,j}^{SH}(z) h_{3,n}(k_j R) \right] \right. \\ & \left. \left. + \left[\underbrace{\left[\hat{u}_{s,z,p}(z) \cdot -H_n^{(2)}(k_p R) \right]}_{u_{s,z,np}^{PSV}(z,R)} \cdot \left[\hat{\partial}_{s,z\theta,j}^{SH}(z) \frac{n}{k_j R} H_n^{(2)}(k_j R) \right] \right] \right) dz \end{aligned} \quad (\text{C.1.10c})$$

$$\begin{aligned} \hat{F}_{6,njq} = \int_{z_1}^{z_2} & \left(\underbrace{\left[\hat{u}_{s,\theta,q}(z) \cdot \frac{n}{k_q R} H_n^{(2)}(k_q R) \right]}_{u_{s,\theta,nq}^{SH}(z,R)} \cdot \left[-\hat{\partial}_{s,rr,j}^{SH}(z) h_{2,n}(k_j R) \right] \right. \\ & \left. + \underbrace{\left[\hat{u}_{s,\theta,q}(z) \cdot \frac{1}{k_q} \partial_r H_n^{(2)}(k_q R) \right]}_{u_{s,\theta,nq}^{SH}(z,R)} \cdot \left[\hat{\partial}_{s,rr,j}^{SH}(z) h_{3,n}(k_j R) \right] \right) dz \end{aligned} \quad (\text{C.1.10d})$$

Symmetric case

The following equation is an alternative notation to [eq. \(4.3.5a\)](#)

$$\sum_{m=1}^{\infty} C_{P,0m} \hat{F}_{1,lm} = \sum_{p=1}^{\infty} C_{PSV,0p} \hat{F}_{2,lp} \quad (\text{C.1.11a})$$

$$\begin{aligned} \hat{F}_{1,lm} = & \int_{z_0}^{z_1} \left(\hat{u}_{P,r,0m}(z) \cdot \underbrace{\left[-\hat{p}_{f,l}(z) H_0^{(2)}(k_l R) \right]}_{\hat{w}_{f,l}(z)} \right) dz \\ & + \int_{z_1}^L \left(\hat{u}_{P,z,0m}(z) \cdot \underbrace{\left[\hat{\sigma}_{s,zr,l}^{H_1}(z) H_1^{(2)}(k_l R) \right]}_{\hat{w}_{s,z,l}^{\text{PSV}}(z)} \right. \\ & \left. + \hat{u}_{P,r,0m}(z) \cdot \underbrace{\left[\hat{\sigma}_{s,rr,l}^{H_0}(z) H_0^{(2)}(k_l R) + \hat{\sigma}_{s,rr,l}^{H_1}(z) \frac{1}{R} H_1^{(2)}(k_l R) \right]}_{\hat{w}_{s,r,l}^{\text{PSV}}(z)} \right) dz \end{aligned} \quad (\text{C.1.11b})$$

$$\begin{aligned} \hat{F}_{2,lp} = & \int_{z_1}^{z_2} \left[\underbrace{\left[\hat{u}_{f,r,p}(z) H_1^{(2)}(k_p R) \right]}_{p_{f,0p}(z,R)} \cdot \left[-\hat{p}_{f,l}(z) H_0^{(2)}(k_l R) \right] \right. \\ & + \underbrace{\left[\hat{u}_{s,r,p}(z) H_1^{(2)}(k_p R) \right]}_{u_{s,r,0p}(z,R)} \cdot \left[\hat{\sigma}_{s,rr,l}^{H_0}(z) H_0^{(2)}(k_l R) + \hat{\sigma}_{s,rr,l}^{H_1}(z) \frac{1}{R} H_1^{(2)}(k_l R) \right] \\ & \left. + \underbrace{\left[\hat{u}_{s,z,p}(z) H_0^{(2)}(k_p R) \right]}_{u_{s,z,0p}(z,R)} \cdot \left[\hat{\sigma}_{s,zr,l}^{H_1}(z) H_1^{(2)}(k_l R) \right] \right) dz \end{aligned} \quad (\text{C.1.11c})$$

C.2 The extended orthogonality method for the non-symmetric case ($n > 0$)

In this chapter the derivation of a previous version of the Orthogonality method is shown. This derivation is extended in the sense that the expressions are simplified. Note that this is not done in the final work.

The process as described in appendix C of Tsouvalas' thesis [4] is loosely followed. The derivation starts on [XXVIII](#), after the recap of relevant equations.

Recap

The needed displacements of the shell, fluid medium and soil medium in the frequency domain are shown in equations [eq. \(C.2.1\)](#), [eq. \(C.2.4\)](#) and [eq. \(C.2.2\)](#) respectively.

$$\hat{\mathbf{u}}_p(z, \theta, \omega) = \sum_{n=0}^{\infty} \sum_{m=1}^{\infty} C_{P,nm} \underline{\mathbf{R}}_n(\theta) \hat{\mathbf{u}}_{p,nm}(z) e^{i\omega t} \quad (\text{C.2.1})$$

$$\tilde{\mathbf{u}}_s(r, \theta, z, \omega) = \sum_{n=0}^{\infty} \left(\sum_{p=1}^{\infty} C_{\text{PSV},np} \underline{\mathbf{R}}_n(\theta) \underline{\mathbf{H}}_n(k_p r) \hat{\mathbf{u}}_{s,\text{PSV},np} \right. \quad (\text{C.2.2})$$

$$\left. + \sum_{q=1}^{\infty} C_{\text{SH},nq} \underline{\mathbf{R}}_n(\theta) \underline{\mathbf{H}}_n(k_q r) \hat{\mathbf{u}}_{s,\text{SH},nq} \right) e^{i\omega t} \quad (\text{C.2.3})$$

$$\tilde{u}_{f,r}(r, \theta, z, \omega) = \sum_{n=0}^{\infty} \sum_{p=1}^{\infty} C_{\text{PSV},np} \frac{\hat{v}_{f,r,p}(z)}{i\omega} \cos(n\theta) e^{i\omega t} \quad (\text{C.2.4})$$

The stress-vectors $\underline{\sigma}_{s,\{r,\theta,z\}}$ are shown in eqs. (C.2.5) to (C.2.7).

$$\tilde{\underline{\sigma}}_{s,r,n}(r, \theta, z) = \underline{\mathbf{R}}_n(\theta) \left(\sum_{p=1}^{\infty} C_{\text{PSV},np} \tilde{\underline{\sigma}}_{s,r,np}^{\text{PSV}}(r, z) + \sum_{q=1}^{\infty} C_{\text{SH},nq} \tilde{\underline{\sigma}}_{s,r,nq}^{\text{SH}}(r, z) \right) \quad (\text{C.2.5})$$

$$\tilde{\underline{\sigma}}_{s,\theta,n}(r, \theta, z) = \underline{\mathbf{R}}_n(-\theta - \pi/2) \left(\sum_{p=1}^{\infty} C_{\text{PSV},np} \tilde{\underline{\sigma}}_{s,\theta,np}^{\text{PSV}}(r, z) + \sum_{q=1}^{\infty} C_{\text{SH},nq} \tilde{\underline{\sigma}}_{s,\theta,nq}^{\text{SH}}(r, z) \right) \quad (\text{C.2.6})$$

$$\tilde{\underline{\sigma}}_{s,z,n}(r, \theta, z) = \underline{\mathbf{R}}_n(\theta) \left(\sum_{p=1}^{\infty} C_{\text{PSV},np} \underline{\mathbf{H}}_n(k_p r) \hat{\underline{\sigma}}_{s,z,np}^{\text{PSV}}(z) + \sum_{q=1}^{\infty} C_{\text{SH},nq} \underline{\mathbf{H}}_n(k_q r) \hat{\underline{\sigma}}_{s,z,nq}^{\text{SH}}(z) \right) \quad (\text{C.2.7})$$

Orthogonality

To achieve a more simplified expression of the relation between the unknown amplitudes the following orthogonality definitions will be used. Equations eq. (C.2.8) and eq. (C.2.9) are the orthogonality conditions for PSV-modes and SH-modes respectively in [4], while eq. (C.2.10) is the orthogonality condition for both Rayleigh and Love modes, as found in [19].

$$-\frac{1}{k_p} \int_{z_1}^{z_2} \frac{\partial_{f,r,p}}{i\omega} \hat{p}_{f,l} dz + \frac{1}{k_p} \int_{z_2}^L \hat{\alpha}_{s,l}^I(z) \hat{u}_{s,r,p}(z) - \hat{u}_{s,z,l}(z) \partial_{s,zr,p}(z) dz = \Gamma_l^{\text{PSV}} \delta_{pl} \quad (\text{C.2.8})$$

with: $\hat{\alpha}_{s,l}^I(z) = \zeta_s k_l \hat{u}_{s,r,l}(z) + \eta_s \partial_{s,zz,l}(z)$

$$\int_{z_2}^L \mu k_j^2 \hat{u}_{s,\theta,j} \hat{u}_{s,\theta,q} dz = \Gamma_j^{\text{SH}} \delta_{qj} \quad (\text{C.2.9})$$

$$\int_0^L \left[\hat{\alpha}_{s,i}^{II}(z) \hat{u}_{s,\theta,q}(z) - \mu \hat{u}_{s,r,i}(z) k_q \hat{u}_{\theta,q}(z) + \mu k_i \hat{u}_{s,z,i}(z) \frac{d\hat{u}_{\theta,q}}{dz} \right] dz = \Gamma_i^{RL} \delta_{qi} \quad (\text{C.2.10})$$

with: $\hat{\alpha}_{s,i}^{II} = (\lambda + 2\mu) \hat{u}_{s,r,i}(z) k_i^2 - k_i \lambda \frac{d\hat{u}_{s,z,i}}{dz}$

The orthogonality of the shell modes is shown in eq. (C.2.11). Where $\underline{\underline{M}}$ is the diagonal mass/inertia matrix.

$$\int_0^L \int_0^{2\pi} (\underline{\underline{R}}_l(\theta) \hat{\underline{\underline{u}}}_{P,lk}(z))^T \underline{\underline{M}} (\underline{\underline{R}}_n(\theta) \hat{\underline{\underline{u}}}_{P,nm}(z)) d\theta dz = N_{nm} \delta_{nl} \delta_{mk} \quad (\text{C.2.11})$$

with: $\underline{\underline{M}} = \rho_P R h \cdot \text{diag} \left(1, 1, 1, \frac{h^2}{12}, \frac{h^2}{12} \right)$

Interface Conditions at $r = R$

The interface conditions between the shell and the acousto-elastic medium can be divided in two subsections, namely equations that come forth out of the displacement continuity (subsection C.2) and the ones as a result of the stress equilibrium (subsection C.2).

Displacement Continuity

$$\tilde{\underline{\underline{u}}}_{P,r} = \tilde{\underline{\underline{u}}}_{f,r} \quad z_1 < z < z_2 \quad (\text{C.2.12})$$

$$\underline{\underline{u}}_P = \underline{\underline{u}}_s \quad z_2 < z < L \quad (\text{C.2.13})$$

First the interface conditions in equation will be expanded using equations eqs. (C.2.1) and (C.2.2)

$$\sum_{m=1}^{\infty} C_{P,nm} \hat{\underline{\underline{u}}}_{P,r,nm} \cos(n\theta) = \sum_{p=1}^{\infty} C_{\text{PSV},np} \frac{\partial_{f,r,p}}{i\omega} \cos(n\theta) \quad (\text{C.2.14})$$

$$\sum_{m=1}^{\infty} C_{P,nm} \underline{\underline{R}}_n(\theta) \hat{\underline{\underline{u}}}_{P,nm} = \underline{\underline{R}}_n(\theta) \left(\sum_{p=1}^{\infty} C_{\text{PSV},np} \underline{\underline{H}}_n(k_p r) \hat{\underline{\underline{u}}}_{s,\text{PSV},p} + \sum_{q=1}^{\infty} C_{\text{SH},nq} \underline{\underline{H}}_n(k_q r) \hat{\underline{\underline{u}}}_{s,\text{SH},q} \right) \quad (\text{C.2.15})$$

With $\underline{\underline{R}}_n(\theta)$ and $\underline{\underline{H}}_n(k_p r)$ being the rotational matrix and Hankel matrix respectively.

$$\underline{\underline{R}}_n(\theta) = \begin{bmatrix} \cos(n\theta) & 0 & 0 \\ 0 & -\sin(n\theta) & 0 \\ 0 & 0 & \cos(n\theta) \end{bmatrix} \quad \text{and} \quad \underline{\underline{H}}_n(k_p r) = \begin{bmatrix} \partial_r H_n^{(2)}(k_p r) & \frac{n}{r} H_n^{(2)}(k_p r) & 0 \\ \frac{n}{r} H_n^{(2)}(k_p r) & \partial_r H_n^{(2)}(k_p r) & 0 \\ 0 & 0 & H_n^{(2)}(k_p r) \end{bmatrix} \quad (\text{C.2.16})$$

Writing out eq. (C.2.15) gives:

$$\sum_{m=1}^{\infty} C_{P,nm} \hat{u}_{P,r,nm} = \sum_{p=1}^{\infty} C_{PSV,np} \partial_r H_n^{(2)}(k_p r) \hat{u}_{s,r,p} + \sum_{q=1}^{\infty} C_{SH,nq} \frac{n}{r} H_n^{(2)}(k_q r) \hat{u}_{s,\theta,q} \quad (\text{C.2.17})$$

$$\sum_{m=1}^{\infty} C_{P,nm} \hat{u}_{P,\theta,nm} = \sum_{p=1}^{\infty} C_{PSV,np} \frac{n}{r} H_n^{(2)}(k_p r) \hat{u}_{s,r,p} + \sum_{q=1}^{\infty} C_{SH,nq} \partial_r H_n^{(2)}(k_q r) \hat{u}_{s,\theta,q} \quad (\text{C.2.18})$$

$$\sum_{m=1}^{\infty} C_{P,nm} \hat{u}_{P,z,nm} = \sum_{p=1}^{\infty} C_{PSV,np} H_n^{(2)}(k_p r) \hat{u}_{s,z,p} \quad (\text{C.2.19})$$

Manipulations

Using PSV orthogonality To obtain a simplified expression in which eq. (C.2.8) is applied the following manipulations are performed:

1. Multiply eq. (C.2.14) by $-\hat{p}_{f,l}$ and integrating over the fluid domain (i.e. $[z_1, z_2]$)

$$\sum_{m=1}^{\infty} C_{P,nm} \left(- \int_{z_1}^{z_2} \hat{u}_{P,r,nm} \hat{p}_{f,l} dz \right) = \sum_{p=1}^{\infty} C_{PSV,np} \left(- \int_{z_1}^{z_2} \frac{\hat{\sigma}_{f,r,p}}{i\omega} \hat{p}_{f,l} dz \right) \quad (\text{C.2.20})$$

2. Multiplying eq. (C.2.17) by $\hat{\alpha}_{s,l}^I$ and integrating over the soil domain (i.e. $[z_2, L]$)

$$\begin{aligned} \sum_{m=1}^{\infty} C_{P,nm} \left(\int_{z_2}^L \hat{u}_{P,r,nm} \hat{\alpha}_l^I dz \right) &= \sum_{p=1}^{\infty} C_{PSV,np} \partial_r H_n^{(2)}(k_p r) \left(\int_{z_2}^L \hat{u}_{s,r,p} \hat{\alpha}_l^I dz \right) \\ &+ \sum_{q=1}^{\infty} C_{SH,nq} \frac{n}{r} H_n^{(2)}(k_q r) \left(\int_{z_2}^L \hat{u}_{s,\theta,q} \hat{\alpha}_l^I dz \right) \end{aligned} \quad (\text{C.2.21})$$

3. Multiplying eq. (C.2.19) by $\frac{\hat{\sigma}_{s,zr,l}}{k_l}$ and integrate over the domain.

$$\sum_{m=1}^{\infty} C_{P,nm} \left(\int_{z_2}^L \hat{u}_{P,z,nm} \frac{\hat{\sigma}_{s,zr,l}}{k_l} dz \right) = \sum_{p=1}^{\infty} C_{PSV,np} H_n^{(2)}(k_p r) \left(\int_{z_2}^L \hat{u}_{s,z,p} \frac{\hat{\sigma}_{s,zr,l}}{k_l} dz \right) \quad (\text{C.2.22})$$

4. Adding up equations eq. (C.2.20), eq. (C.2.21) and eq. (C.2.22).
5. Adding expression eq. (C.2.23) to the right-hand side of the resulting equation and subtracting the same expression again will give us eq. (C.2.24)

$$\sum_{p=1}^{\infty} C_{PSV,np} \partial_r H_n^{(2)}(k_p r) \left(\int_{z_2}^L \hat{u}_{s,z,l} \frac{\hat{\sigma}_{s,zr,p}}{k_l} dz \right) \quad (\text{C.2.23})$$

$$\sum_{m=1}^{\infty} C_{P,nm} \hat{F}_1 = \sum_{p=1}^{\infty} C_{PSV,np} \left[\partial_r H_n^{(2)}(k_p r) \hat{F}_{21} + H_n^{(2)}(k_p r) \hat{F}_{22} \right] + \sum_{q=1}^{\infty} C_{SH,nq} \frac{n}{r} H_n^{(2)}(k_q r) \hat{F}_3 \quad (\text{C.2.24})$$

$$\hat{F}_{1,nml} = - \int_{z_1}^{z_2} \hat{u}_{P,x,nm} \hat{p}_{f,l} dz + \int_{z_2}^L \hat{u}_{P,x,nm} \hat{\alpha}_l^I + \hat{u}_{P,z,nm} \frac{\hat{\sigma}_{s,zr,l}}{k_l} dz \quad (\text{C.2.25})$$

$$\begin{aligned} \hat{F}_{21,npl} &= - \int_{z_1}^{z_2} \hat{u}_{s,r,p} \hat{p}_{f,l} dz + \int_{z_2}^L \hat{u}_{s,r,p} \hat{\alpha}_l^I - \hat{u}_{s,z,l} \frac{\hat{\sigma}_{s,zr,p}}{k_l} dz + \int_{z_2}^L \hat{u}_{s,z,l} \frac{\hat{\sigma}_{s,zr,p}}{k_l} dz \\ &= k_p \Gamma_l^{\text{PSV}} \delta_{pl} + \int_{z_2}^L \hat{u}_{s,z,l} \frac{\hat{\sigma}_{s,zr,p}}{k_l} dz \end{aligned} \quad (\text{C.2.26})$$

$$\hat{F}_{22,npl} = \int_{z_2}^L \hat{u}_{s,z,p} \frac{\hat{\sigma}_{s,zr,l}}{k_l} dz \quad (\text{C.2.27})$$

$$\hat{F}_{3,nql} = \int_{z_2}^L \hat{u}_{s,\theta,q} \hat{\alpha}_l^I dz \quad (\text{C.2.28})$$

6. After rearranging the equation we obtain:

$$\begin{aligned} \sum_{m=1}^{\infty} C_{P,nm} \hat{F}_{1,nml} &= C_{PSV,nl} \partial_r H_n^{(2)}(k_l r) k_l \Gamma_l^{\text{PSV}} \\ &+ \sum_{p=1}^{\infty} C_{PSV,np} \left[\partial_r H_n^{(2)}(k_p r) \hat{F}_{22,nlp} + H_n^{(2)}(k_p r) \hat{F}_{22,npl} \right] \\ &+ \sum_{q=1}^{\infty} C_{SH,nq} \frac{n}{r} H_n^{(2)}(k_q r) \hat{F}_{3,nql} \end{aligned} \quad (\text{C.2.29})$$

Using SH orthogonality An expression for C_{SH} is obtained by multiplying eq. (C.2.18) by $\mu k_j^2 \hat{u}_{s,\theta,j}$ and integrating over the domain.

$$\sum_{m=1}^{\infty} C_{P,nm} \hat{F}_4 = \sum_{p=1}^{\infty} C_{PSV,np} \frac{n}{r} H_n^{(2)}(k_p r) \hat{F}_5 + \sum_{q=1}^{\infty} C_{SH,nq} \partial_r H_n^{(2)}(k_q r) \hat{F}_6 \quad (\text{C.2.30})$$

$$\hat{F}_{4,nmj} = \int_{z_2}^L \hat{u}_{P,\theta,nm} \mu k_j^2 \hat{u}_{s,\theta,j} dz \quad (\text{C.2.31})$$

$$\hat{F}_{5,npj} = \int_{z_2}^L \hat{u}_{s,r,p} \mu k_j^2 \hat{u}_{s,\theta,j} dz \quad (\text{C.2.32})$$

$$\hat{F}_{6,nqj} = \int_{z_2}^L \hat{u}_{s,\theta,q} \mu k_j^2 \hat{u}_{s,\theta,j} dz = \Gamma_j^{\text{SH}} \delta_{qj} \quad (\text{C.2.33})$$

$$\sum_{m=1}^{\infty} C_{P,nm} \hat{F}_{4,nmq} = \sum_{p=1}^{\infty} C_{PSV,np} \frac{n}{r} H_n^{(2)}(k_p r) \hat{F}_{5,npq} + C_{SH,nq} \partial_r H_n^{(2)}(k_q r) \Gamma_q^{\text{SH}} \quad (\text{C.2.34})$$

$$C_{SH,nq} = \frac{\sum_{m=1}^{\infty} C_{P,nm} \hat{F}_{4,nmq} - \sum_{p=1}^{\infty} C_{PSV,np} \frac{n}{r} H_n^{(2)}(k_p r) \hat{F}_{5,npq}}{\partial_r H_n^{(2)}(k_q r) \Gamma_q^{\text{SH}}} \quad (\text{C.2.35})$$

Combining eq. (C.2.35) is substituted into eq. (C.2.29) and all $C_{P,nm}$ are transferred to the left-hand side

$$\begin{aligned}
\sum_{m=1}^{\infty} C_{P,nm} \hat{F}_{1,nml} &= C_{PSV,nl} \partial_r H_n^{(2)}(k_l r) k_l \Gamma_l^{\text{PSV}} \\
&+ \sum_{p=1}^{\infty} C_{PSV,np} \left[\partial_r H_n^{(2)}(k_p r) \hat{F}_{22,nlp} + H_n^{(2)}(kr) \hat{F}_{22,npl} \right] \\
&+ \sum_{q=1}^{\infty} \left(\frac{\sum_{m=1}^{\infty} C_{P,nm} \hat{F}_{4,nmq} - \sum_{p=1}^{\infty} C_{PSV,np} \frac{n}{r} H_n^{(2)}(k_p r) \hat{F}_{5,npq}}{\partial_r H_n^{(2)}(k_q r) \Gamma_q^{\text{SH}}} \right) \frac{n}{r} H_n^{(2)}(k_q r) \hat{F}_{3,nql}
\end{aligned} \tag{C.2.36}$$

$$\begin{aligned}
\sum_{m=1}^{\infty} C_{P,nm} \hat{G}_{1,nmlq} &= C_{PSV,nl} \partial_r H_n^{(2)}(k_l r) k_l \Gamma_l^{\text{PSV}} \\
&+ \sum_{p=1}^{\infty} C_{PSV,np} \left[\partial_r H_n^{(2)}(k_p r) \hat{F}_{22,nlp} + H_n^{(2)}(kr) \hat{F}_{22,npl} - \frac{n}{r} H_n^{(2)}(k_p r) \hat{G}_{2,npql} \right]
\end{aligned} \tag{C.2.37}$$

$$\hat{G}_{1,nmlq} = \hat{F}_{1,nml} - \sum_{p=1}^{\infty} \hat{F}_{4,nmq} \hat{F}_{3,nql} \left(\frac{\frac{n}{r} H_n^{(2)}(k_q r)}{\Gamma_q^{\text{SH}} \partial_r H_n^{(2)}(k_q r)} \right) \tag{C.2.38}$$

$$\hat{G}_{2,npql} = \sum_{p=1}^{\infty} \hat{F}_{5,npq} \hat{F}_{3,nql} \left(\frac{\frac{n}{r} H_n^{(2)}(k_q r)}{\Gamma_q^{\text{SH}} \partial_r H_n^{(2)}(k_q r)} \right) \tag{C.2.39}$$

Using mixed orthogonality To use the mixed orthogonality eq. (C.2.17) is multiplied by $\hat{\alpha}_{s,ni}^{II}$ and integrated over the domain $[z_2, L]$. Then expression eq. (C.2.40) is added to the right-hand side of the resulting equation and subtracted again.

$$\sum_{q=1}^{\infty} C_{SH,nq} \frac{n}{r} H_n^{(2)}(k_q r) \int_{z_2}^L \left[-\mu \hat{u}_{s,r,ni}(z) k_q \hat{u}_{\theta,nq}(z) + \mu k_i \hat{u}_{s,z,ni}(z) \frac{d\hat{u}_{\theta,nq}}{dz} \right] dz \tag{C.2.40}$$

$$\sum_{m=1}^{\infty} C_{P,nm} \hat{F}_{7,nmi} = \sum_{p=1}^{\infty} C_{PSV,np} \partial_r H_n^{(2)}(k_p r) \hat{F}_{8,npi} + \sum_{q=1}^{\infty} C_{SH,nq} \frac{n}{r} H_n^{(2)}(k_q r) \hat{F}_{9,nqi}^* \tag{C.2.41}$$

$$\hat{F}_{7,nmi} = \int_{z_2}^L \hat{u}_{p,x,mm} \hat{\alpha}_{s,ni}^{II} dz \tag{C.2.42}$$

$$\hat{F}_{8,npi} = \int_{z_2}^L \hat{u}_{s,x,p} \hat{\alpha}_{s,ni}^{II} dz \tag{C.2.43}$$

$$\begin{aligned}
\hat{F}_{9,nqi}^* &= \int_{z_2}^L \left[\hat{u}_{s,\theta,q} \hat{\alpha}_{s,ni}^{II} - \mu \hat{u}_{s,r,ni} k_q \hat{u}_{\theta,nq} + \mu k_i \hat{u}_{s,z,ni} \frac{d\hat{u}_{\theta,nq}}{dz} \right] dz \\
&- \int_{z_2}^L \left[-\mu \hat{u}_{s,r,ni} k_q \hat{u}_{\theta,nq} + \mu k_i \hat{u}_{s,z,ni} \frac{d\hat{u}_{\theta,nq}}{dz} \right] dz \\
&= \Gamma_i^{\text{RL}} \delta_{qi} - \hat{F}_{9,nqi}
\end{aligned} \tag{C.2.44}$$

After rearranging we obtain eq. (C.2.69):

$$\begin{aligned} \sum_{m=1}^{\infty} C_{P,nm} \hat{F}_{7,nmi} &= C_{SH,ni} \frac{n}{r} H_n^{(2)}(k_i r) \Gamma_i^{RL} \\ &+ \sum_{p=1}^{\infty} C_{PSV,np} \partial_r H_n^{(2)}(k_p r) \hat{F}_{8,npi} \\ &+ \sum_{q=1}^{\infty} C_{SH,nq} \frac{n}{r} H_n^{(2)}(k_p r) \hat{F}_{9,nqi} \end{aligned} \quad (C.2.45)$$

Stress equilibrium / Forced EOM

$$\tilde{\sigma}_{P,rr} = \tilde{\sigma}_{f,rr} \quad z_1 < z < z_2 \quad (C.2.46)$$

$$\tilde{\sigma}_{P,r} = \tilde{\sigma}_{s,r} \quad z_2 < z < L \quad (C.2.47)$$

This equilibrium equation in the forced equation of motion.

$$\underline{\underline{L}} \underline{\underline{u}}_P = \begin{cases} \underline{\sigma}_{f,r} + \underline{f}_e, & z_1 < z < z_2 \\ \underline{\sigma}_{s,r} + \underline{f}_e, & z_2 < z < z_L \end{cases} \quad (C.2.48)$$

with:

$$\underline{\sigma}_{f,r} = [0 \quad 0 \quad -\tilde{p}_f \quad 0 \quad 0]^T \quad (C.2.49)$$

$$\underline{\sigma}_{s,r} = [\tilde{\sigma}_{s,rz} \quad \tilde{\sigma}_{s,r\theta} \quad \tilde{\sigma}_{s,rr} \quad 0 \quad 0]^T \quad (C.2.50)$$

$$\underline{f}_e = [f_z \quad f_\theta \quad f_r \quad 0 \quad 0]^T \quad (C.2.51)$$

Expanding all expressions

First the forced equation of motion (eq. (C.2.48)) is expanded by substituting eqs. (C.2.1) and (C.2.5).

$$\underline{\underline{L}} \underline{\underline{u}}_P = \sum_{m=1}^{\infty} C_{P,nm} \left(-\omega^2 \underline{\underline{M}} + \underline{\underline{K}}_{nm} \right) \left(\underline{\underline{R}}_n(\theta) \hat{\underline{u}}_{P,nm}(z) \right) \quad (C.2.52)$$

$$\tilde{\sigma}_{s,r,n} = \underline{\underline{R}}_n(\theta) \left(\sum_{p=1}^{\infty} C_{PSV,np} \tilde{\sigma}_{s,r,np}^{\text{PSV}}(r,z) + \sum_{q=1}^{\infty} C_{SH,nq} \tilde{\sigma}_{s,r,nq}^{\text{SH}}(r,z) \right) \quad (C.2.53)$$

$$\tilde{p}_{f,n} = \sum_{p=1}^{\infty} C_{PSV,np} H_n^{(2)}(k_p r) \hat{p}_{f,np}(z) \cos(n\theta) \quad (C.2.54)$$

$$\underline{\underline{f}}_n = [\underline{\underline{a}}_n \cos(n\theta) + \underline{\underline{b}}_n \sin(n\theta)] \delta(z) \quad (C.2.55)$$

$$\underline{\underline{a}}_n = \begin{cases} \frac{1}{\pi} \int_0^{2\pi} [\underline{\underline{f}}(\theta) \cos(n\theta)] d\theta & \text{for } n \neq 0 \\ \frac{1}{2\pi} \int_0^{2\pi} \underline{\underline{f}}(\theta) d\theta & \text{for } n = 0 \end{cases} \quad (C.2.56)$$

$$\underline{\underline{b}}_n = \frac{1}{\pi} \int_0^{2\pi} [\underline{\underline{f}}(\theta) \sin(n\theta)] d\theta \quad (C.2.57)$$

Using shell orthogonality

The equation of motion is then pre-multiplied by an arbitrary mode $(\underline{\underline{R}}_n(\theta) \hat{\underline{u}}_{P,nk}(z))^T$ and integrated over the domain.

$$\begin{aligned} \langle \underline{\underline{R}}_n(\theta) \hat{\underline{u}}_{P,nk}(z), \underline{\underline{L}} \underline{\underline{u}}_P \rangle &= \langle \underline{\underline{R}}_n(\theta) \hat{\underline{u}}_{P,nk}(z), \tilde{\sigma}_{s,r,n} \rangle \\ &+ \langle \underline{\underline{R}}_n(\theta) \hat{\underline{u}}_{P,nk}(z), \tilde{\sigma}_{f,r,n} \rangle \\ &+ \langle \underline{\underline{R}}_n(\theta) \hat{\underline{u}}_{P,nk}(z), \underline{\underline{f}}_n \rangle \end{aligned} \quad (C.2.58)$$

The expanded expressions will become:

$$\begin{aligned}
 \langle \underline{\mathbf{R}}_n(\theta) \hat{\mathbf{u}}_{P,nk}(z), \underline{\mathbf{L}} \underline{\mathbf{u}}_P \rangle &= \sum_{m=1}^{\infty} C_{P,nm} \int_0^L \int_0^{2\pi} (\underline{\mathbf{R}}_n(\theta) \hat{\mathbf{u}}_{P,nk}(z))^T (-\omega^2 \underline{\mathbf{M}} + \underline{\mathbf{K}}_{nm}) (\underline{\mathbf{R}}_n(\theta) \hat{\mathbf{u}}_{P,nm}(z)) d\theta dz \\
 &= \sum_{m=1}^{\infty} C_{P,nm} \int_0^L \int_0^{2\pi} (\underline{\mathbf{R}}_n(\theta) \hat{\mathbf{u}}_{P,nk}(z))^T (\omega_{nm}^2 - \omega^2) \underline{\mathbf{M}} (\underline{\mathbf{R}}_n(\theta) \hat{\mathbf{u}}_{P,nm}(z)) d\theta dz \\
 &= C_{P,nk} (\omega_{nk}^2 - \omega^2) N_{nk}
 \end{aligned} \tag{C.2.59}$$

$$\langle \underline{\mathbf{R}}_n(\theta) \hat{\mathbf{u}}_{P,nk}(z), \tilde{\underline{\mathbf{f}}}_{f,r} \rangle = -\pi (1 + \delta_{n0}) \sum_{p=1}^{\infty} C_{PSV,np} H_n^{(2)}(k_p R) \int_{z_1}^{z_2} \hat{u}_{P,r,nk} \hat{p}_{f,np} dz \tag{C.2.60}$$

$$\langle \underline{\mathbf{R}}_n(\theta) \hat{\mathbf{u}}_{P,nk}(z), \tilde{\underline{\mathbf{f}}}_n \rangle = \pi \left[(\hat{\mathbf{u}}_{P,nk}^{\cos}(0))^T \underline{\mathbf{a}}_n (1 + \delta_{n0}) + (\hat{\mathbf{u}}_{P,nk}^{\sin}(0))^T \underline{\mathbf{b}}_n (1 - \delta_{n0}) \right] \tag{C.2.61}$$

$$\begin{aligned}
 \langle \underline{\mathbf{R}}_n(\theta) \hat{\mathbf{u}}_{P,nk}(z), \tilde{\underline{\mathbf{c}}}_{s,r} \rangle &= \int_{z_2}^L \int_0^{2\pi} (\underline{\mathbf{R}}_n(\theta) \hat{\mathbf{u}}_{P,nk}(z))^T \underline{\mathbf{R}}_n(\theta) \left(\sum_{p=1}^{\infty} C_{PSV,np} \tilde{\underline{\mathbf{c}}}_{s,r,np}^{\text{PSV}}(r, z) + \sum_{q=1}^{\infty} C_{SH,nq} \tilde{\underline{\mathbf{c}}}_{s,r,nq}^{\text{SH}}(r, z) \right) d\theta dz \\
 &= \int_{z_2}^L \sum_{p=1}^{\infty} C_{PSV,np} \left[c_{11,nkp}(z, r) \langle \cos(n\theta), \cos(n\theta) \rangle + c_{12,nkp}(z, r) \langle \sin(n\theta), \sin(n\theta) \rangle \right] \\
 &\quad + \sum_{q=1}^{\infty} C_{SH,nq} \left[c_{21,nkp}(z, r) \langle \cos(n\theta), \cos(n\theta) \rangle + c_{22,nkp}(z, r) \langle \sin(n\theta), \sin(n\theta) \rangle \right] dz \\
 &= \sum_{p=1}^{\infty} C_{PSV,np} \pi \int_{z_2}^L c_{1,nkp}(z, r) dz + \sum_{q=1}^{\infty} C_{SH,nq} \pi \int_{z_2}^L c_{2,nkq}(z, r) dz
 \end{aligned} \tag{C.2.62}$$

with:

$$\begin{aligned}
 c_{1,nkp}(z, r) &= (1 + \delta_{n0}) (\hat{\mathbf{u}}_{P,nk}^{\cos})^T \tilde{\underline{\mathbf{c}}}_{s,r,np}^{\text{PSV},\cos} + (1 - \delta_{n0}) (\hat{\mathbf{u}}_{P,nk}^{\sin})^T \tilde{\underline{\mathbf{c}}}_{s,r,np}^{\text{PSV},\sin} \\
 c_{2,nkq}(z, r) &= (1 + \delta_{n0}) (\hat{\mathbf{u}}_{P,nk}^{\cos})^T \tilde{\underline{\mathbf{c}}}_{s,r,nq}^{\text{SH},\cos} + (1 - \delta_{n0}) (\hat{\mathbf{u}}_{P,nk}^{\sin})^T \tilde{\underline{\mathbf{c}}}_{s,r,nq}^{\text{SH},\sin}
 \end{aligned}$$

$$\begin{aligned}
 \hat{\mathbf{u}}_P^{\cos}(z) &= [\hat{u}_{P,z} \quad 0 \quad \hat{u}_{P,r} \quad \hat{\beta}_{P,z} \quad 0]^T \\
 \hat{\mathbf{u}}_P^{\sin}(z) &= [0 \quad \hat{u}_{P,\theta} \quad 0 \quad 0 \quad \hat{\beta}_{P,\theta}]^T
 \end{aligned}$$

Substituting the expressions back into the equation of motion results in:

$$\begin{aligned}
 C_{P,nk} (\omega_{nk}^2 - \omega^2) N_{nk} &= \sum_{p=1}^{\infty} C_{PSV,np} \pi \int_{z_2}^L c_{1,nkp}(z, r) dz + \sum_{q=1}^{\infty} C_{SH,nq} \pi \int_{z_2}^L c_{2,nkq}(z, r) dz \\
 &\quad - \sum_{p=1}^{\infty} C_{PSV,np} H_n^{(2)}(k_p R) \pi \int_{z_1}^{z_2} \hat{u}_{P,r,nk} \hat{p}_{f,np} dz \\
 &\quad + \pi \left[(\hat{\mathbf{u}}_{P,nk}^{\cos}(0))^T \underline{\mathbf{a}}_n (1 + \delta_{n0}) + (\hat{\mathbf{u}}_{P,nk}^{\sin}(0))^T \underline{\mathbf{b}}_n (1 - \delta_{n0}) \right]
 \end{aligned} \tag{C.2.63}$$

$$C_{p,nk} = \frac{\pi}{(\omega_{nk}^2 - \omega^2) N_{nk}} \left[\hat{G}_{3,nk}^F + \sum_{p=1}^{\infty} C_{PSV,np} \hat{G}_{4,nlp} + \sum_{q=1}^{\infty} C_{SH,nq} \hat{G}_{5,nlq} \right] \quad (\text{C.2.64})$$

$$\hat{G}_{3,nk}^F = (\hat{\mathbf{u}}_{p,nk}^{\cos}(0))^T \mathbf{a}_n (1 + \delta_{n0}) + (\hat{\mathbf{u}}_{p,nk}^{\sin}(0))^T \mathbf{b}_n (1 - \delta_{n0}) \quad (\text{C.2.65})$$

$$\hat{G}_{4,nlp} = \int_{z_2}^L c_{1,nkp}(z, \mathbf{r}) \, dz - H_n^{(2)}(k_p R) \int_{z_1}^{z_2} \hat{u}_{p,r,nk} \hat{p}_{f,np} \, dz \quad (\text{C.2.66})$$

$$\hat{G}_{5,nlq} = \int_{z_2}^L c_{2,nkq}(z, \mathbf{r}) \, dz \quad (\text{C.2.67})$$

Final system of equations

$$\sum_{m=1}^{\infty} C_{P,nm} \hat{G}_{1,nmlq} = C_{PSV,nl} \partial_r H_n^{(2)}(k_l r) k_l \Gamma_l^{\text{PSV}} \quad (\text{C.2.68})$$

$$+ \sum_{p=1}^{\infty} C_{PSV,np} \left[\partial_r H_n^{(2)}(k_p r) \hat{F}_{22,nlp} + H_n^{(2)}(kr) \hat{F}_{22,npl} - \frac{n}{r} H_n^{(2)}(k_p r) \hat{G}_{2,npql} \right]$$

$$\sum_{m=1}^{\infty} C_{P,nm} \hat{F}_{7,nmi} = C_{SH,ni} \frac{n}{r} H_n^{(2)}(k_i r) \Gamma_i^{\text{RL}} \quad (\text{C.2.69})$$

$$+ \sum_{p=1}^{\infty} C_{PSV,np} \partial_r H_n^{(2)}(k_q r) \hat{F}_{8,npi}$$

$$+ \sum_{q=1}^{\infty} C_{SH,nq} \frac{n}{r} H_n^{(2)}(k_p r) \hat{F}_{9,nqi}$$

$$C_{P,nk} = \frac{\pi}{(\omega_{nk}^2 - \omega^2) N_{nk}} \left[\hat{G}_{3,nk}^F + \sum_{p=1}^{\infty} C_{PSV,np} \hat{G}_{4,nlp} + \sum_{q=1}^{\infty} C_{SH,nq} \hat{G}_{5,nlq} \right] \quad (\text{C.2.70})$$

Now that we have expressed the amplitudes of the pile modes C_P in amplitudes of PSV- and SH-modes, we can substitute that back into the two relations, eq. (C.2.68) and eq. (C.2.69), obtained from displacement continuity. Rearranging will give us the following two sets of equations.

$$C_{PSV,nl} A_{nl}^{(1)} + \sum_{p=1}^{\infty} C_{PSV,np} A_{nlp}^{(2)} + \sum_{q=1}^{\infty} C_{SH,nq} A_{nlq}^{(3)} = F_{nl}^{(1)} \quad (\text{C.2.71})$$

$$C_{SH,ni} A_{ni}^{(4)} + \sum_{p=1}^{\infty} C_{PSV,np} A_{nlp}^{(5)} + \sum_{q=1}^{\infty} C_{SH,nq} A_{nlq}^{(6)} = F_{ni}^{(2)} \quad (\text{C.2.72})$$

$$A_{nl}^{(1)} = \partial_r H_n^{(2)}(k_l r) k_l \Gamma_l^{\text{PSV}} \quad (\text{C.2.73})$$

$$A_{nlpq}^{(2)} = \left[\partial_r H_n^{(2)}(k_p r) \hat{F}_{22,nlp} + H_n^{(2)}(kr) \hat{F}_{22,npl} - \frac{n}{r} H_n^{(2)}(k_p r) \hat{G}_{2,npql} \right] \quad (\text{C.2.74})$$

$$- \sum_{m=1}^{\infty} \frac{\pi}{(\omega_{nm}^2 - \omega^2) N_{nm}} \left[\hat{G}_{4,nlp} \hat{G}_{1,nmlq} \right] \quad (\text{C.2.75})$$

$$A_{nlq}^{(3)} = - \sum_{m=1}^{\infty} \frac{\pi}{(\omega_{nm}^2 - \omega^2) N_{nm}} \left[\hat{G}_{5,nlq} \hat{G}_{1,nmlq} \right] \quad (\text{C.2.76})$$

$$A_{ni}^{(4)} = \frac{n}{r} H_n^{(2)}(k_i r) \Gamma_i^{\text{RL}} \quad (\text{C.2.77})$$

$$A_{nlpqi}^{(5)} = \partial_r H_n^{(2)}(k_q r) \hat{F}_{8,npi} - \sum_{m=1}^{\infty} \frac{\pi}{(\omega_{nm}^2 - \omega^2) N_{nm}} \left[\hat{G}_{4,nlp} \hat{F}_{7,nmi} \right] \quad (\text{C.2.78})$$

$$A_{nlpqi}^{(6)} = \frac{n}{r} H_n^{(2)}(k_p r) \hat{F}_{9,nqi} - \sum_{m=1}^{\infty} \frac{\pi}{(\omega_{nm}^2 - \omega^2) N_{nm}} \left[\hat{G}_{5,nlq} \hat{F}_{7,nmi} \right] \quad (\text{C.2.79})$$

$$F_{nlq}^{(1)} = \sum_{m=1}^{\infty} \frac{\pi}{(\omega_{nm}^2 - \omega^2) N_{nm}} \left[\hat{G}_{3,nm}^F \hat{G}_{1,nmlq} \right] \quad (\text{C.2.80})$$

$$F_{ni}^{(2)} = \sum_{m=1}^{\infty} \frac{\pi}{(\omega_{nm}^2 - \omega^2) N_{nm}} \left[\hat{G}_{3,nm}^F \hat{F}_{7,nmi} \right] \quad (\text{C.2.81})$$

$$(\text{C.2.82})$$

$$\underline{\underline{\mathbf{A}}}^{(1)} \underline{\underline{\mathbf{C}}}_{\text{PSV},n} + \underline{\underline{\mathbf{A}}}^{(2)} \underline{\underline{\mathbf{C}}}_{\text{PSV},n} + \underline{\underline{\mathbf{A}}}^{(3)} \underline{\underline{\mathbf{C}}}_{\text{SH},n} = \underline{\underline{\mathbf{F}}}^{(1)} \quad (\text{C.2.83})$$

$$\underline{\underline{\mathbf{A}}}^{(4)} \underline{\underline{\mathbf{C}}}_{\text{SH},n} + \underline{\underline{\mathbf{A}}}^{(5)} \underline{\underline{\mathbf{C}}}_{\text{PSV},n} + \underline{\underline{\mathbf{A}}}^{(6)} \underline{\underline{\mathbf{C}}}_{\text{SH},n} = \underline{\underline{\mathbf{F}}}^{(2)} \quad (\text{C.2.84})$$

$$\begin{bmatrix} \underline{\underline{\mathbf{A}}}^{(1)} + \underline{\underline{\mathbf{A}}}^{(2)} & \underline{\underline{\mathbf{A}}}^{(3)} \\ \underline{\underline{\mathbf{A}}}^{(5)} & \underline{\underline{\mathbf{A}}}^{(4)} + \underline{\underline{\mathbf{A}}}^{(6)} \end{bmatrix} \begin{bmatrix} \underline{\underline{\mathbf{C}}}_{\text{PSV},n} \\ \underline{\underline{\mathbf{C}}}_{\text{SH},n} \end{bmatrix} = \begin{bmatrix} \underline{\underline{\mathbf{F}}}^{(1)} \\ \underline{\underline{\mathbf{F}}}^{(2)} \end{bmatrix} \quad (\text{C.2.85})$$

Response to a unit load

Projecting the force in polar coordinates

The force $\tilde{\underline{\underline{f}}}_e(\theta, z, t)$ is transferred to the frequency domain with a fourier transform

$$\tilde{\underline{\underline{f}}}_e(\theta, z, \omega) = \mathcal{F}\{\underline{\underline{f}}_e(\theta, z, t)\} \quad (\text{C.2.86})$$

$$\underline{\underline{f}}_e(\theta, z, t) \xrightarrow{\text{Fourier-transform}} \tilde{\underline{\underline{f}}}_e(\theta, z, \omega) \quad (\text{C.2.87})$$

$$\tilde{\underline{\underline{f}}}_e(\theta, z, \omega) = \underline{\underline{\mathbf{R}}}_n(\theta) \hat{\underline{\underline{f}}}_e \delta(z) \quad (\text{C.2.88})$$

$$\text{Vertical unit force: } \hat{\underline{\underline{f}}}_e = [1 \ 0 \ 0 \ 0 \ 0]^T \rightarrow \hat{\underline{\underline{G}}}_{3,0m}^{F,ver} = 2\pi \hat{u}_{P,z,0m}(0) \quad (\text{C.2.89})$$

$$\text{Horizontal unit force: } \hat{\underline{\underline{f}}}_e = [0 \ 1 \ 1 \ 0 \ 0]^T \rightarrow \hat{\underline{\underline{G}}}_{3,nm}^{F,hor} = \pi(\hat{u}_{P,\theta,nm}(0) + \hat{u}_{P,r,nm}(0)) \quad (\text{C.2.90})$$

$$\begin{aligned} \hat{\underline{\underline{G}}}_{3,nk}^F &= \langle \underline{\underline{\mathbf{R}}}_n(\theta) \hat{\underline{\underline{u}}}_{P,nm}(z), \tilde{\underline{\underline{f}}}_e \rangle \\ &= \int_0^L \int_0^{2\pi} \left[(\underline{\underline{\mathbf{R}}}_n(\theta) \hat{\underline{\underline{u}}}_{P,nm}(z))^T \underline{\underline{\mathbf{R}}}_n(\theta) \hat{\underline{\underline{f}}}_e \delta(z) \right] d\theta dz \\ &= \pi (\hat{u}_{P,r,nm}(0) \hat{f}_{rr} + \hat{u}_{P,\theta,nm}(0) \hat{f}_{r\theta} + \hat{u}_{P,z,nm}(0) \hat{f}_{zz}) \\ &= \pi \left[(\hat{\underline{\underline{u}}}_{P,nk}^{\cos}(0))^T \underline{\underline{\mathbf{a}}}_n (1 + \delta_{n0}) + (\hat{\underline{\underline{u}}}_{P,nk}^{\sin}(0))^T \underline{\underline{\mathbf{b}}}_n (1 - \delta_{n0}) \right] \\ &= \pi \left[(\hat{u}_{P,z,nk}(0) a_{z,n} + \hat{u}_{P,r,nk}(0) a_{r,n}) (1 + \delta_{n0}) + \hat{u}_{P,\theta,nk}(0) a_{\theta,n} (1 - \delta_{n0}) \right] \\ &= \pi \left[(\hat{u}_{P,z,nk}(0) f_z + \hat{u}_{P,r,nk}(0) f_r) (1 + \delta_{n0}) + \hat{u}_{P,\theta,nk}(0) f_\theta (1 - \delta_{n0}) \right] \end{aligned} \quad (\text{C.2.91})$$

Appendix D

Casestudy

D.1 Error analysis

In this appendix the local error of the displacement fields of the case in [table D.1](#) shown in [Chapter 5](#), where the point-collocation method is used for different forcing configurations. Still the error analysis of the Orthogonality method is included in this appendix too.

Geometry	Pile	Soil	Fluid
Pile top $z_{\text{pile top}}$	0 m	ρ_P 7850 kg m ⁻³	ρ_f 1000 kg m ⁻³
Sea surface z_0	8 m	E 2.1 · 10 ¹¹ kg m ⁻³	d_s 60 m
Sea bed z_1	30 m	R 2.5 m	c_T 149.373 m s ⁻¹
Pile bottom z_L	60 m	h 0.03 m	c_L 366.06 m s ⁻¹
Rigid boundary condition z_2	90 m	ν 0.28	E_s 1.0 · 10 ⁸ kg m ⁻³
		L 60 m	$P_{\{\lambda,\mu\}}$ 1%

Table D.1: Properties of the system

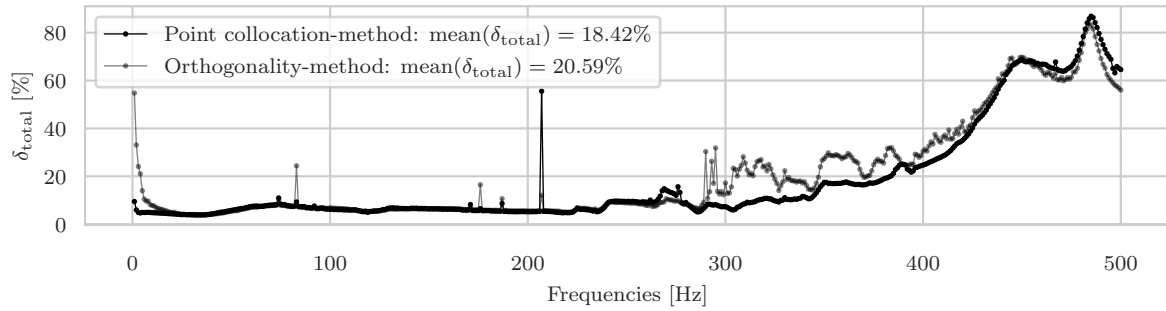


Figure D.1: Local mismatch error δ_{Total} in the response to a vertical force per frequency

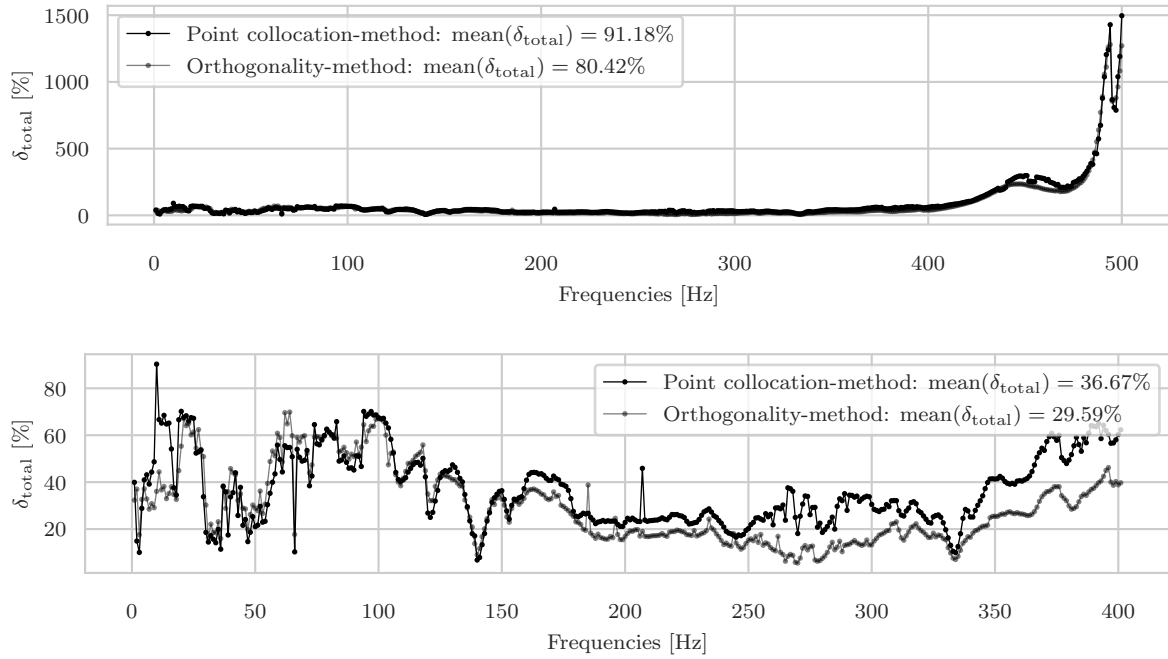


Figure D.2: Local mismatch error δ_{Total} in the response to a horizontal force per frequency. (b) Shows a close up to the errors for frequencies below 400 Hz

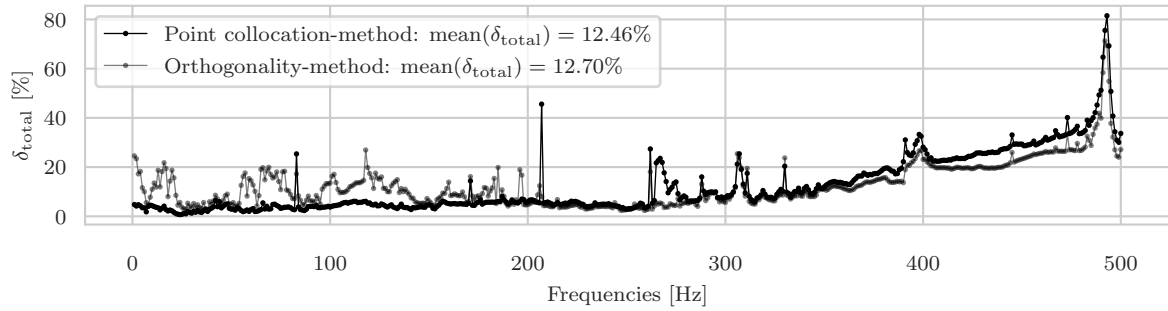


Figure D.3: Local mismatch error δ_{Total} in the response to a moment on the y-axis per frequency

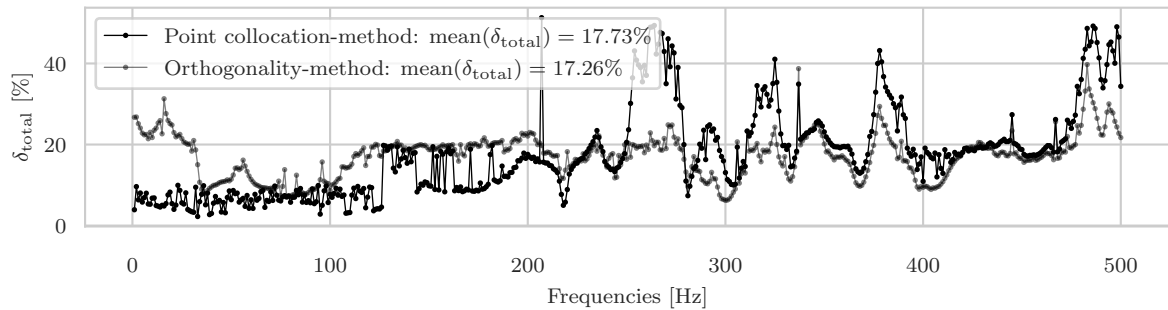


Figure D.4: Local mismatch error δ_{Total} in the response to a higher order torsional moment per frequency.

D.2 Time evolution

In this appendix various contourplots in the (r, θ) - and (z, r) -plane are included to illustrate the time evolution of the acoustic field.

Note that the quantities (eqs. (D.2.1) to (D.2.3)) have been evaluated at different times t , with different time steps dt .

$$\text{Fluid pressure} \quad \rightarrow \quad p_f(r, \theta = \theta_0, z, t = t_0) \quad \text{or} \quad p_f(r, \theta = \theta, z = z_0, t = t_0) \quad (\text{D.2.1})$$

$$\text{Displacement norm} \quad \rightarrow \quad \left| \underline{\mathbf{u}}_{\{\text{P};\text{s};\text{f}\}}(r, \theta = \theta_0, z, t) \right| \quad \text{or} \quad \left| \underline{\mathbf{u}}_{\{\text{P};\text{s};\text{f}\}}(r, \theta, z = z_0, t) \right| \quad (\text{D.2.2})$$

$$\text{Velocity norm} \quad \rightarrow \quad \left| \underline{\mathbf{v}}_{\{\text{P};\text{s};\text{f}\}}(r, \theta = \theta_0, t) \right| \quad \text{or} \quad \left| \underline{\mathbf{v}}_{\{\text{P};\text{s};\text{f}\}}(r, \theta = \theta, z = z_0, t) \right| \quad (\text{D.2.3})$$

D.2.1 A vertical force

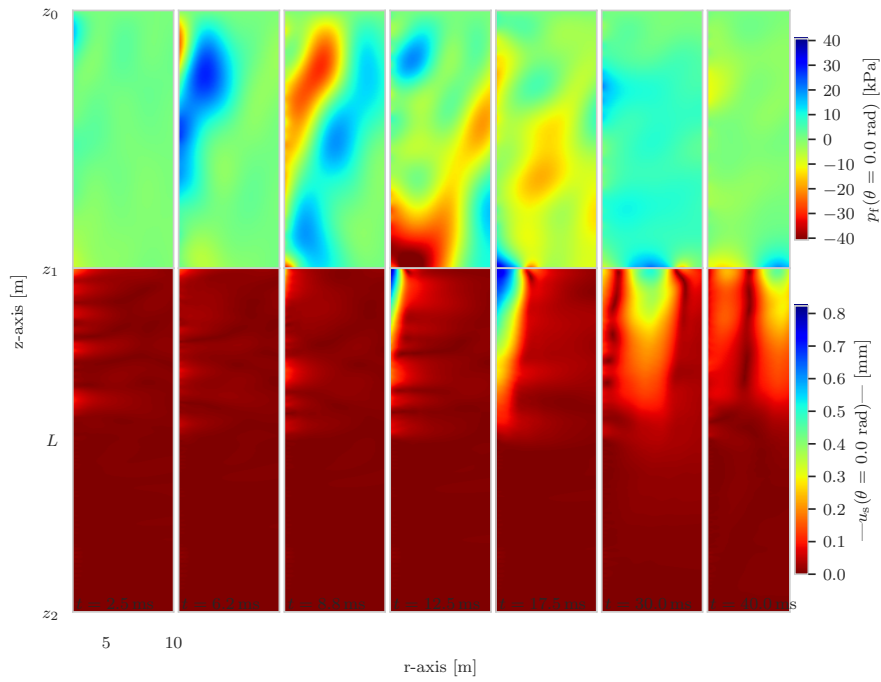


Figure D.5: Fluid pressure and displacement norm of the soil resulting from an uniform vertical load.

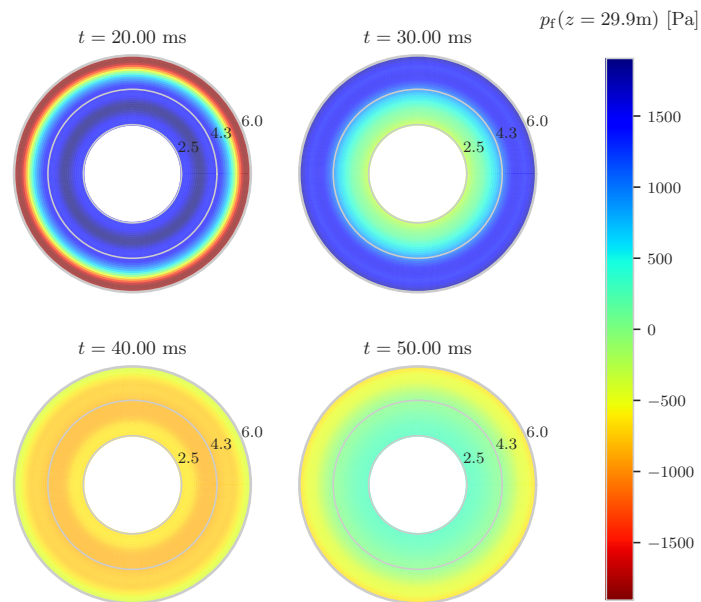


Figure D.6: A top view of the fluid pressure (fig. D.5) at a depth of $z = 29.9$ m due to an uniform vertical load.

D.2.2 A horizontal force

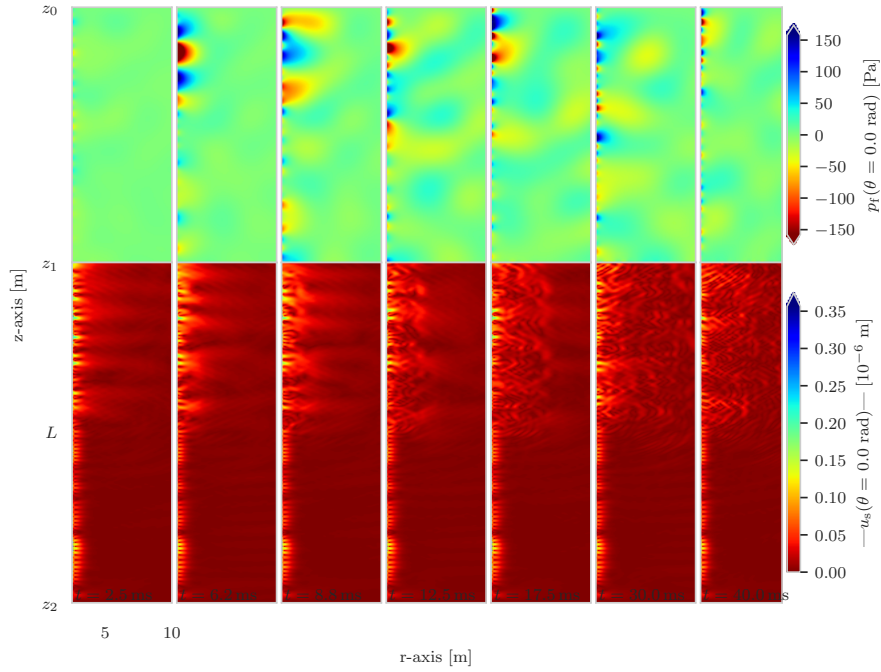


Figure D.7: Fluid pressure and displacement norm of the soil resulting from an uniform horizontal load (Note: the colour bars do convey 50 % of the maximum value in the contour plots)

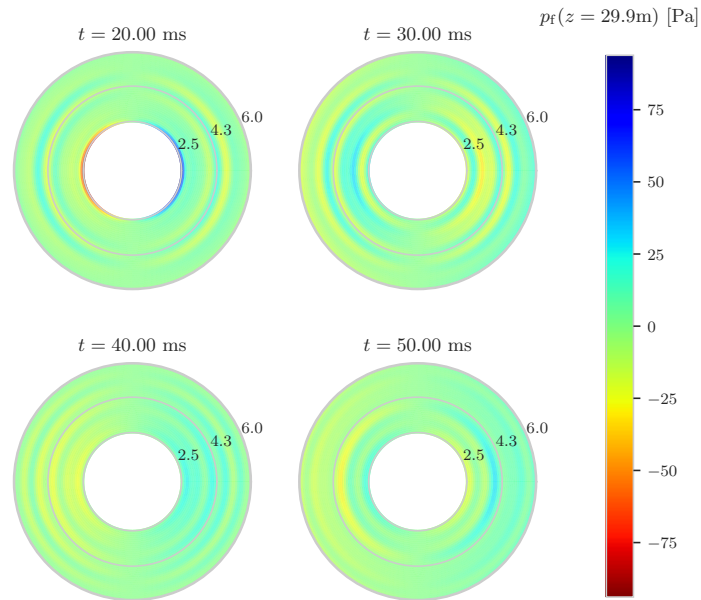


Figure D.8: A top view of the fluid pressure (fig. D.7) at a depth of $z = 29.9$ m due to an uniform horizontal load.

D.2.3 A moment on the y -axis

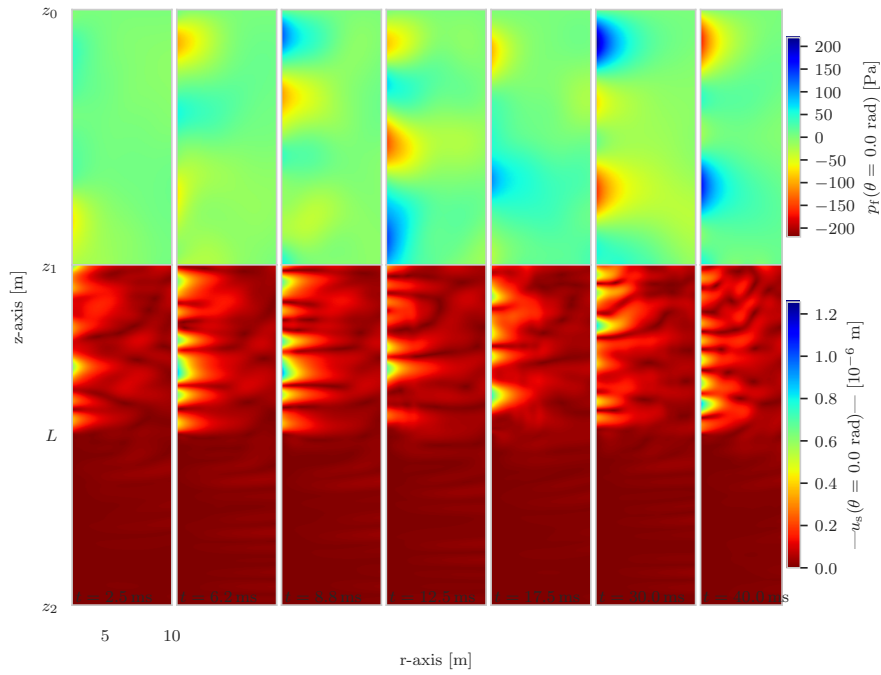


Figure D.9: Fluid pressure and velocity norm of the soil resulting from a moment on the y -axis load.

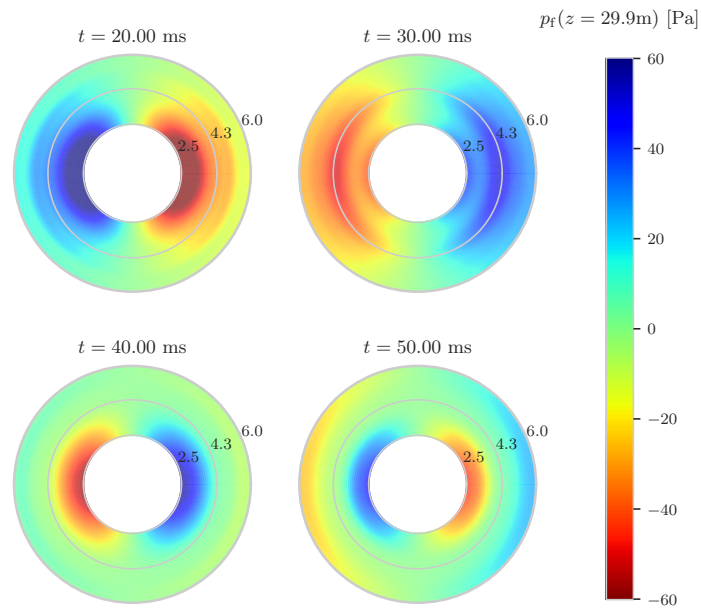


Figure D.10: A top view of the fluid pressure (fig. D.9) at a depth of $z = 29.9$ m due to a moment on the y -axis.

D.2.4 Imperfect vertical force

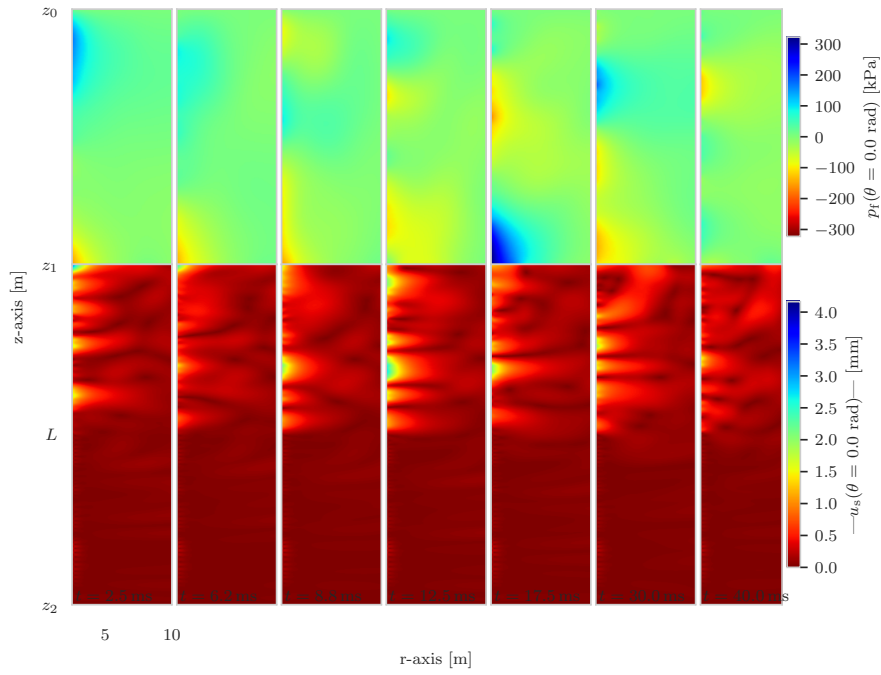


Figure D.11: Fluid pressure and velocity norm of the soil resulting from an imperfect vertical force.

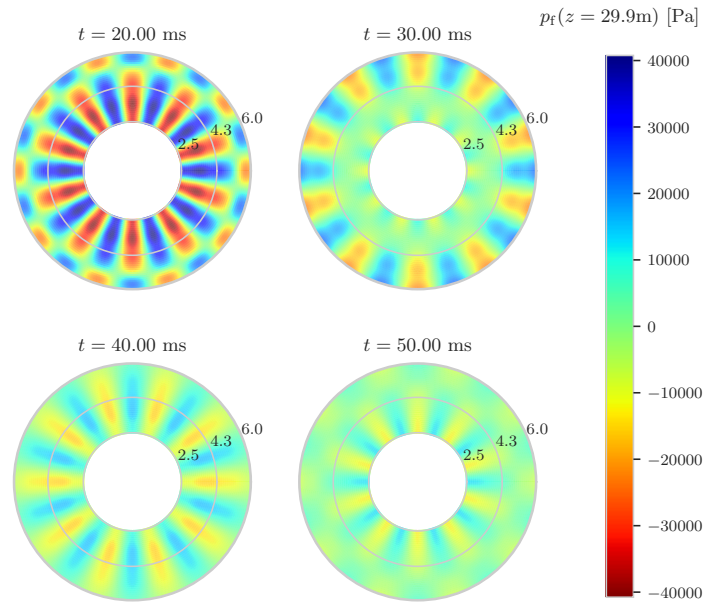


Figure D.12: A top view of the fluid pressure (fig. D.11) at a depth of $z = 20$ m due to an imperfect vertical force ($\varphi = 3^\circ, e = 3$ cm).